ABSTRACT

Title of Dissertation: QUANTUM INFORMATION DYNAMICS IN MANY-BODY SYSTEMS

Subhayan Sahu
Doctor of Philosophy, 2022

Dissertation Directed by: Professor Brian Swingle
Department of Physics

This thesis is a collection of theoretical and numerical studies of the dynamics of quantum information in quantum many-body systems, focused on characterizing the scrambling of information and entanglement dynamics in generic dynamical setups.

In the first part of the thesis I study out-of-time-ordered correlators (OTOCs) as a probe for quantum information scrambling. By computing OTOCs in disordered quantum spin systems we find that disorder leads to distinct patterns of scrambling, and can arrest the information propagation significantly for high enough values of disorder. I also study the generic features of finite temperature OTOCs in gapped local systems, using a combination of numerical and analytical approaches. We find that the role of the thermal regulator significantly affects the behavior of OTOCs at finite temperature, which restricts the applicability of the temperature bound on chaos.

In the second part of the thesis, I study analytically tractable models of measurement-induced entanglement transition. Frequent measurements in a quantum circuit lead to distinct

entanglement phases of the prepared quantum state. Using these models, we find effective field theories describing the entanglement patterns and the entanglement phase transitions. By considering generalizations of these models, we find that long-range interactions in the quantum circuit lead to novel entanglement phases with efficient emergent error-correcting properties.

In the last part of the thesis, I study tensor network states defined on generic sparse graphs. The underlying graphical structure leads to efficient tensor network representation of highly entangled states even with modest classical resources. Using the intuition that generic graphs are locally tree-like, I develop efficient numerical methods to access local information of such states. These methods suggest a pathway for studying quantum many-body physics on sparse graphs beyond lattices.

QUANTUM INFORMATION DYNAMICS IN MANY-BODY SYSTEMS

by

Subhayan Sahu

Dissertation submitted to the Faculty of the Graduate School of the
University of Maryland, College Park in partial fulfillment
of the requirements for the degree of
Doctor of Philosophy
2022

Advisory Committee:
Professor Brian Swingle, Co-Chair/Advisor
Professor Jay D. Sau, Chair
Professor Maissam Barkeshli
Professor Daniel Gottesman
Professor Nicole Yunger Halpern

Dedication

To my mother, Kathika, who started the journey [1], and to you, for being a part of mine.

Acknowledgments

"Which is more important," asked Big Panda,"the journey or the destination?"

"The company," said Tiny Dragon.

- Big Panda and Tiny Dragon, James Norbury.

This dissertation is a reflection of my interactions with many, many people who made my journey with physics possible, exciting, and ultimately enjoyable. As I write, I am reminded of the many occasions when I would look up the acknowledgements section of others' dissertations, to peek into their journey as a graduate student. While reading those sections with a vicarious pleasure, I would often end up feeling struck by the large number of people who end up contributing to the thesis. As I look back at my five years as a graduate student, it becomes obvious: it takes a village to raise a dissertation.

The first person I'd like to thank is Brian Swingle, my advisor. I feel grateful to have had Brian as a guide and a friend, not just for sharing his acumen for physics with me, but for his immense kindness and constant encouragement. I have had several conversations with Brian where I have been blown away by his physical intuition and the uncanny ability to get to the heart of the problem that we were looking at. But, my most memorable interactions have been the even more numerous times when he took effort to create a friendly and fulfilling environment for me to feel comfortable doing physics.

For my pedagogy in physics I am deeply grateful to the professors at the University of

Maryland, among whom I would specifically like to thank Ted Jacobson, Andrew Childs, Maissam Barkeshli, Jay Sau, Victor Galitski, and Christopher Jarzynski for teaching their beautiful courses. I have also learnt a lot through my conversations with many faculty at UMD, and I would like to acknowledge Maissam, Ted, Victor Yakovenko, and Michael Gullans in particular. I am grateful to have had Maissam as a mentor since my first semester, and I have had many wonderfully stimulating conversations with him. I am very thankful to professors Daniel Gottesman, Jay, Maissam, and Nicole Yunger Halpern for agreeing to serve on my dissertation committee. My deep gratitude also goes towards the administrative staff in the Physics Department, especially Jessica, Josiland, and the late Janet, for making me feel welcome in the department.

Going back further, I extend my gratitude to teachers at different stages of my journey - my professors at the Indian Institute of Science, in particular, Diptiman Sen, Biplob Bhattacherjee, Vijay Shenoy, Subroto Mukerjee, Aninda Sinha, Rohini Godbole, Arindam Ghosh, and Anish Mokashi. In particular, I would like to thank Prof. Shasanka Roy for guiding me to the thrill of scientific discovery for the first time in my life, and to Subroto Mukerjee for teaching me how to think about research problems.

In my journey with physics, I have been lucky to cross paths with many co-travelers who have made the travel all the more worth undertaking. In grad school, I have enjoyed hitching rides with Andrew Guo, Yixu Wang, Gong Cheng, Michael Winer, Stefano Antonini, Yongchan Yoo, Tamoghna Barik, Ali Lavasani, Yi-Hua Lai, Naren Manjunath, Gautam Nambiar, Abu Patoary, and Navya Gupta, among many others. Along the way, I have been lucky to interact with many enterprising postdocs, who have taught me much of the tricks of the trade, and I would like to thank Chris Baldwin, Christopher White, Shenglong Xu, Shaokai Jian, and Gregory Bentsen. I am particularly grateful for the collaborations with Shenglong, who taught me all that I know

about tensor networks, and Greg, who lit up the dark days of pandemic-caused isolation with the joy of exploring a new research topic.

My time as a PhD student has been nourished by many friendships. The list would run too long, but I have to mention the friends I picked up in College Park: Prakhar, Anshuman, Xiaozhen, Tamoghna, Sohitri, Saurav, Arghya, Arushi, Aniruddha, Srishti, Amit, Spandan, Nikhil, Papia, Wade, Sergio, Landry, Abu, Amitava, Gautam, Batoul, Alireza, and many, many others. Some friends stuck with me from before. My friends from college, Sridevi, Naren, Shriya, Ananth, Alistair, Avishek, and Arpan, and from school, Anirban, Kaustuv, and Sougata, kept me sane during the last five years, and especially during the latter half, when their virtual presence took the sting out of physical isolation. I want to especially thank Naren, who has almost constantly been a few rooms away for over nine years, as a close friend from college, an office-mate at UMD, a housemate for five years, and also incidentally a co-author in a publication. I cherish our frienship and his counsel.

In College Park, and in the US in general, I have found community among colleagues at the university and outside through the 'Science for the People', and the 'Association for India's Development'. These connections have been important in keeping me grounded to the world during an often lonesome journey as a researcher in theoretical physics. I thank my friends in these organizations, especially Dr. Bhagat, Ravi, Aravinda, and Somnath, for helping me find meaning in community and in the fight for justice. I also thank the many strangers, trails, meadows, flora and fauna of College Park and the DC area who have made me feel welcome in these past five years. My journey in physics has been supported by fellowships and public education systems in India and the US, and I am grateful to the people of these countries for continuing to support public education and the fundamental sciences.

I would not have come to physics unless it was for the three of my grandparents and my mother, who as science teachers in school and college ensured that I was never too far from a physics book, and for my father, who kept his popular science books and love for geometrical puzzles handy. Growing up, it felt exhilarating to be able to pursue a career in discovery of the phenomena I was reading about. My parents, Kathika and Debatosh, were co-conspirators in that dream, letting me do my thing without imposing their will or interest, while always providing their unquestioned moral support. This thesis belongs as much to them, as it does to me.

Finally, this dissertation is in no small measure a reflection of the love of my partner, Sridevi. She has been a rock of support through the darkest and the brightest days, and a constant inspiration to become a better person. It has been a joy to be a part of each other's journey in science and life, even as we navigated much of it from a distance. I am grateful for having found her in my life, and I can't wait to walk together into newer adventures, with laughter and joy.

Table of Contents

List of Tables

List of Figures

Citations to previously published work

Much of this dissertation has appeared in print elsewhere and details for particular chapters are given below (*indicates equal contribution in publication).

- Chapter 1 is based on "Scrambling dynamics across a thermalization-localization quantum phase transition" by Subhayan Sahu, Shenglong Xu, and Brian Swingle (Phys. Rev. Lett. 123, 165902 (2019)) [2]

- Chapter 2 is based on "Information scrambling at finite temperature in local quantum systems" by Subhayan Sahu and Brian Swingle (Phys. Rev. B 99, 165131 (2019)) [3]

- Chapter 3 is based on "Measurement-induced purification in large-N hybrid Brownian circuits" by Gregory Bentsen*, Subhayan Sahu*, and Brian Swingle (Phys. Rev. B 104, 094304 (2021)) [4]

- Chapter 4 is based on "Entanglement Phases in large-N hybrid Brownian circuits with long-range couplings" by Subhayan Sahu*, Shao-Kai Jian*, Gregory Bentsen, and Brian Swingle (ArXiv:2109.00013) [5]

- Chapter 5 is based on "Efficient tensor network simulation of quantum many-body physics on sparse graphs" by Subhayan Sahu and Brian Swingle (ArXiv:2206.04701) [6]

Chapter 0: Introduction

Sometimes it's good to head out with no idea where you're going.

- Big Panda and Tiny Dragon, James Norbury.

0.1 Setting the stage and unveiling the actors

More is different

In the celebrated essay "More is different", physicist P.W. Anderson persuades the reader that the physics of a collection of objects can have emergent collective behavior which is not captured by the properties of the individual objects in isolation [7]. The idea of emergence also underlies the modern perspective that our knowledge of the natural world itself, when seen through the lens of renormalization group and emergence, is possible because of distinct collective behavior at different scales. The laws at any scale can be derived from an underlying UV description if we try very hard, but they are describable regardless by a theory of degrees of freedom only at that scale. A flock of birds can be described as a collective entity with its own dynamics, which is distinct from the description of the biological processes of an individual bird, which itself is distinct from the laws underlying the behavior of the quantum fields whose excitations determine the chemical composition of the molecules working in tandem in the bird's brain guiding it to flock with other birds.

Phases and phase transition

The laws of collective behavior of objects lead naturally to the concept of phases, which can be abstractly understood to be the universality classes of collective behavior of the physics at a particular scale. The simplest example is that of water and ice - these are distinct collective behaviors composed of individual water molecules, with vastly different physical properties. We often think of phases of matter in terms to the nature of the phase transition between them - water and ice are connected by the process of melting. Often phase transitions are laboratories of exploring the concept of emergence, because they are governed by scale-free physics which is described by an emergent universal physics unencumbered with the microscopic details of the actual system under study.

We typically think of phases of matter in equilibrium. However dynamical 'phases' and transitions between them occur in dynamics as well: consider, for example, the flow of a viscous liquid. For a Reynold's number below a critical value, the flow is laminar, which turns turbulent when the critical value is breached. There are also typical instances of 'driven' phase transitions, for example, a kicked classical rotor, which enters a chaotic phase when the 'kicking' strength is larger than a critical value.

Enter quantum

Physical objects obeying quantum mechanics show a richer diversity of collective phenomena and equilibrium and non-equilibrium phases. In this thesis we will explore these phenomena using the language of quantum information, which has been shown recently to reveal deep connections between physical phenomena at different scales, as well as provide an understanding of the emergence of thermalization and statistical mechanics.

A quantum state $|\psi\rangle$ can have correlations beyond what is possible classically, which can

be quantified by its entanglement. Consider the state $|\psi\rangle = (|00\rangle + |11\rangle)/\sqrt{2}$ on 2 qubits. When we just look at one of them, the reduced density matrix is the identity matrix, i.e. if measured in the computational basis, the state of one qubit will be $|0\rangle$ or $|1\rangle$ with equal probability. However, once one of the qubits is measured, the state of the other qubit is deterministic. This correlation is only possible because of the underlying principles of quantum mechanics, and can be expressed in terms of the entanglement. For concreteness, given a quantum state on a bipartite system $|\psi_{AB}\rangle$, the entanglement of subsystem A is given by the entropy of the reduced density matrix on A, $S_A = -\text{Tr}\rho_A \log \rho_A$, where $\rho_A = \text{Tr}_B |\psi\rangle \langle\psi|$. The notion of entanglement codifies the sentiment of Anderson's claim that 'more is different': there are more exotic (by which I mean more entangled) states in a composite Hilbert space $\mathcal{H}_{AB}$ than just product of states defined on subspaces $\mathcal{H}_A$ and $\mathcal{H}_B$. Quantum entanglement has already emerged as an organizing principle to study the behavior of ground states of quantum many-body systems, be it in the study of topologically ordered states [8], or in theoretically understanding the behavior of correlation functions in gapped phases of matter [9].

Entanglement dynamics and thermalization

Quantum systems undergoing time evolution $|\psi(t)\rangle = e^{-iHt}|\psi\rangle$ with its own Hamiltonian H generically evolve into states of higher complexity, with entanglement being generated between different parts of the system. This observation already provides a remarkably simple justification of thermodynamics and statistical mechanics [10].

Equilibrium statistical mechanics posits that time-averaged physical quantities behave as ensemble-averaged quantities on average. However the state of a system under quantum (or even classical) dynamics remains a well defined state in the corresponding Hilbert (or generalized configuration space). Classically, the emergence of a description based on statistical mechanics is

motivated by invoking either a separate bath or a coarse-grained knowledge of the evolution in phase space, which requires a subjective lack of knowledge of the time evolution of the classical system. However, quantum systems have this feature built in: due to entanglement being generated between different parts of the system under time evolution, any subsystem is not fully specified by the information of the degrees of freedom in the subsystem itself; rather they develop correlations with the rest of system. In other words, in isolated quantum systems subsystems can appear to be thermalized with time because the rest of the system acts as its bath.

To be more precise, consider a system Q and a subsystem $A \subset Q$ which undergoes a quantum time evolution under a Hamiltonian, $H = H_A + H_{Q\setminus A} + H_{\partial A}$, which has support on the subsystem A, the rest of the system $Q \setminus A$, and the boundary ∂A. Let us assume that the boundary term $H_{\partial A}$ is small compared to the bulk term in the Hamiltonian H_A. Now, an initial product state evolves into a state whose reduced density matrix is approximately the thermal state at late times, $\lim_{t\to\infty} \rho_A(t) \approx \rho_\beta = e^{-\beta H_A}/\mathrm{Tr} e^{-\beta H_A}$. The inverse temperature β corresponds to the temperature of the initial state, defined via the equation, $\mathrm{Tr}\left[\rho_\beta H_A\right] = e|A|$, e being the energy density.

Quantum information scrambling

A complimentary way of understanding the effect of quantum many-body dynamics on the quantum state is through the propagation of quantum information. This is most conveniently understood in the Heisenberg picture in terms of evolution of quantum operators. Consider a qubit system, where we start with an initial operator localized on one site. This encodes local information on that site. Under quantum time evolution, this information spreads to other sites of the system. If the dynamics is sufficiently complex, the information may not be accessible to any local probes, for example, by measuring any 1-body operator. This is the phenomenon of

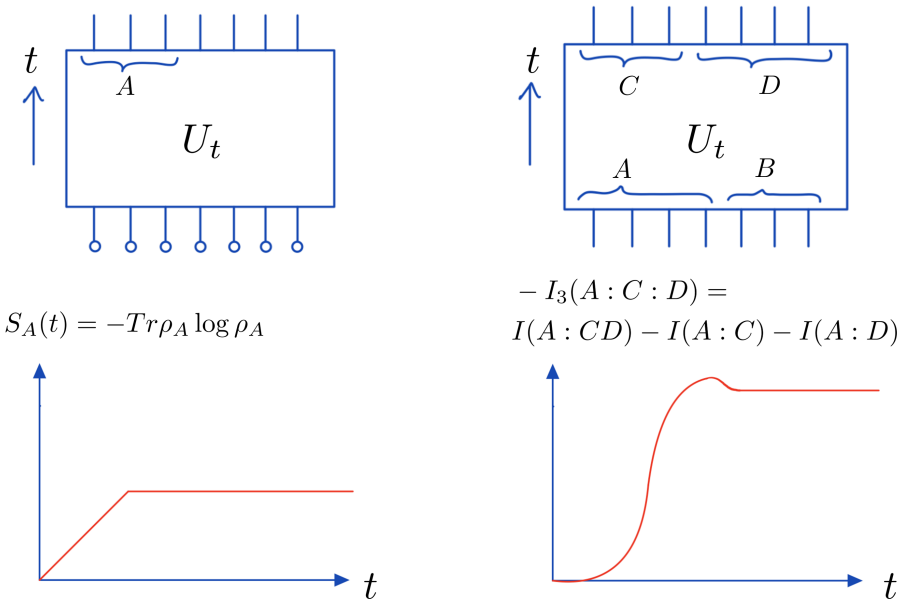

Figure 0.1: **Entanglement and scrambling dynamics** On the left panel I show the circuit corresponding to a generic many-body unitary evolution acting on an initially simple product state, and the evolution of the entanglement entropy of a subregion A, which increases with time before typically saturating. On the right panel I consider the partitioning of the initial and final states of a system undergoing time evolution. Scrambling is captured by the negative of the tripartite mutual information, which increases with time and typically approaches a maximal value corresponding to maximal scrambling under generic scrambling unitaries.

quantum information scrambling.

A conceptually simple way of quantifying scrambling in dynamics is through the tripartitie mutual information [11]. Consider a unitary evolution U_t acting on a system. We bipartition the initial state into two parts: A and B, and the final state into two parts C and D (see right panel in Fig. 0.1). By the channel-state duality one can view U_t as a state, and consider the mutual information between different parts of the initial and final partitions. Scrambling refers to how localized information in the initial state, say A, will not be recoverable from individual parts of the final state, C or D, but only from the whole system CD. Hence we consider the following quantity, the negative of the tripartite mutual information,

$$\begin{aligned} -I_3(A:C:D) &= I(A:CD) - I(A:C) - I(A:D) \\ &= S_{AC} + S_{AD} + S_{CD} - S_{ACD} - S_A - S_C - S_D. \end{aligned}$$

If this quantity is large and negative, this implies that U_t has successfully scrambled the system.

OTOCs

The tripartite mutual information is a conceptually simple probe of scrambling, but it is a complicated quantity to compute, or probe by experiments. Scrambling can also be quantified by using some conveniently defined correlation functions, called out-of-time-ordered-correlators or commutators (OTOCs) [12]. Consider an initial operator on site i, W_i, which under time evolution U becomes $W_i(t) = U^\dagger W_i U$. One can diagnose the spread of quantum information by considering its commutator with another operator V_j on a site j, $[W_i(t), V_j]$. The commutator starts out as $\delta_{i,j}$, but spreads out and becomes non-trivial at late times. A convenient measure of its complexity is the squared operator, often evaluated on the identity density matrix, $\mathrm{Tr}[W_i(t), V_j]^\dagger [W_i(t), V_j]$,

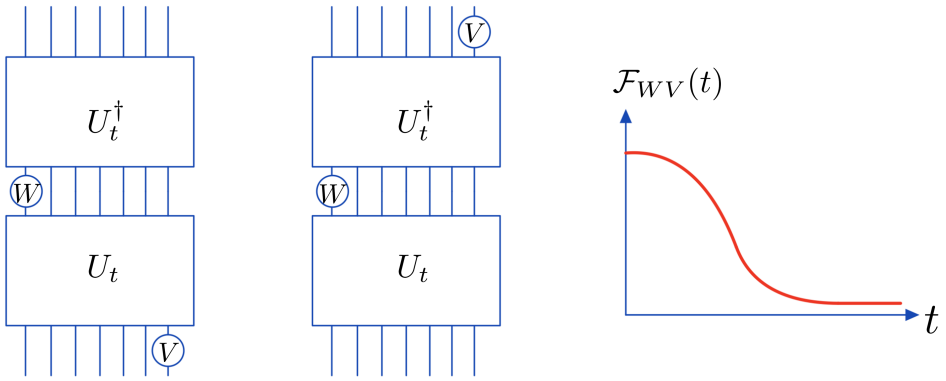

Figure 0.2: **OTOC and scrambling** The OTOC $\mathcal{F}_{WV}$ captures the overlap between states generated by two different quantum channels shown in the first two panels. Due to the spreading of the operator W the states evolve differently, leading to a decay in $\mathcal{F}_{WV}$. The last panel shows a typical evolution of $\mathcal{F}_{WV}$ under a scrambling unitary.

called the squared commutator, $C_{W_iV_j}(t)$.

If we consider the operators W and V to be unitary, then the squared commutator can be expanded,

$$C_{W_iV_j}(t) = 2\mathrm{Tr}\left[\mathbf{1}\right] - 2\mathrm{ReTr}\left[W_i^\dagger V_j^\dagger W_i V_j\right],$$

and the second term is called the out-of-time-ordered correlator, OTOC, $\mathcal{F}_{W_iV_j}(t)$. Scrambling is associated with the growth of $C_{W_iV_j}(t)$, or equivalently, the decay of $\mathcal{F}_{W_iV_j}(t)$. Note that although we have defined the squared commutator and the OTOC with respect to the maximally mixed state or the Identity matrix, they can be easily defined as correlation functions for a particular quantum state ρ, for example, $\mathrm{Tr}\left[\rho[W_i(t), V_j]^\dagger[W_i(t), V_j]\right]$.

The OTOC $\mathcal{F}_{W_iV_j}$ codifies a notion of chaos in quantum dynamics. The OTOC $\mathcal{F}_{W_iV_j}$ captures how local perturbations in the past can lead to vastly different operators at late times. $\mathcal{F}_{W_iV_j}$ can be expressed as the overlap of two quantum states, with slightly different quantum

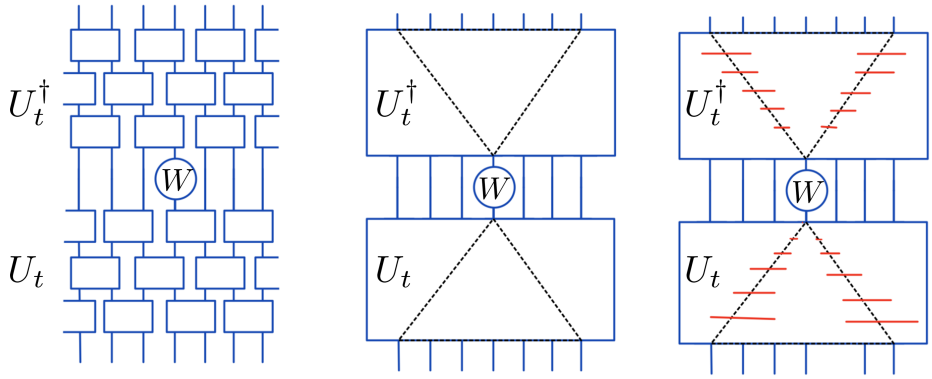

Figure 0.3: **Quantum information scrambling in local systems.** I show a schematic of the structure of a unitary evolution generated by local physics (Trotterized Hamiltonian evolution or local quantum circuits). A local operator evolves with an effective light-cone structure specified by a velocity, dubbed the 'butterfly velocity' (middle panel). The light-cone also generically broadens with time (last panel).

channels with and without a perturbation with an operator. As a quantum version of the butterfly effect, this perturbation can affect the subsequent time evolution, leading to vastly different states at later times, and hence small overlaps (see Fig. 0.2). In fact in certain semi-classical systems, it has been shown that [12],

$$\mathcal{F}_{W_i V_j}(t) \sim \mathrm{Tr}\left[\mathbf{1}\right]\left(1 - \#e^{\lambda_L t} + ...\right),$$

at early times, mimicking the exponential divergence in classical chaos. The quantity λ_L is the Lyapunov exponent associated with quantum information scrambling.

Locality and scrambling

Locality is a feature of much of the physics we observe around us. In the study of solid-state crystalline materials and lattice regulations of quantum field theory, considering a local Hamiltonian on the underlying lattice is often the starting point of the analysis. How does scrambling occur when the unitary evolution is generated by a geometrically local Hamiltonian?

We find that the geometric local circuits (which may arise either as the Trotterized unitary generated by a short-ranged Hamiltonian or as geometrically local quantum circuits) result in an effective light-cone structure (see Fig. 0.3) and a velocity dubbed the 'butterfly velocity' [13]. This is related to the Lieb-Robinson velocity which is the emergent speed limit in non-relativistic geometrically local systems [14]. However, while Lieb-Robinson velocity is a state-independent velocity defined for the Hamiltonian under consideration, the 'butterfly velocity' v_B is defined with respect to the OTOCs or the squared commutator, which are two-time correlation functions defined for a given state, and can be a state-dependent probe of the speed of the propagation of local information.

A feature of the light-cone of scrambling under local dynamics which has been discovered more recently is the phenomenon of the broadening of the operator wavefront with time (see the third panel in Fig. 0.3) [15, 16]. This was first appreciated in the context of random quantum circuits, but has been also demonstrated in Hamiltonian dynamics in quantum spin chains.

Questions addressed in this thesis

With this introduction it is now natural to pose some broad questions which I will address in some specific contexts throughout this dissertation.

First, what are the patterns of scrambling in generic strongly interacting quantum systems? How does scrambling depend on the temperature of the state, and the properties of the underlying equilibrium phases at low temperatures? I address this question by identifying features of OTOCs in local gapped quantum spin systems at low temperatures.

Second, can there be distinct dynamical phases of quantum systems, diagnosed by distinct patterns of entanglement and scrambling? In the introduction, it has already been pointed out that under generic quantum dynamics, systems are expected to thermalize, and typically at high

temperatures this leads to a generic thermal state with few distinguishing features apart from the long-lived hydrodynamic modes corresponding to the conserved charges of the dynamics. However, I will explore in this thesis how disorder and quantum measurements can lead to distinct dynamical phases, which do not follow this dictum.

Third, how do the patterns of entanglement in dynamically generated quantum states change when we consider systems without geometric locality? I explore this by considering quantum circuit evolutions generated by all-to-all and long-range interacting terms in the underlying Hamiltonian, in our study of measurement-induced entanglement phases.

These explorations in turn lead us to questions such as, what are the properties of quantum states associated with Hamiltonians which are not necessarily defined on an underlying Euclidean manifolds, but generic graphs? Utilizing properties of the underlying graph, I will explore how the entanglement patterns of these states may allow us to computationally simulate and probe the equilibrium and non-equilibrium phases of such systems efficiently.

0.2 The main act in five scenes

In this section, I motivate and briefly summarize the subsequent chapters.

0.2.1 Disorder and scrambling

In this chapter we consider the question, can generic quantum evolution generated by a class of Hamiltonians fail to thermalize? For non-interacting quantum models it was known for a long time that disorder can completely arrest quantum motion in low dimensions: a phenomenon known as Anderson localization [17]. This would suggest that generic states in disordered sys-

tems will remain localized for indefinite times without the propagation of any quantum information, leading to athermal behavior. More concretely, for a non-interacting quantum model in $d < 2$, any amount of disorder leads to all eigenstates being exponentially localized, while for higher dimensions, there is a 'mobility edge' i.e. an energy level below which all states are localized. Whether this phenomenon survives many-body interactions is a long-standing question. Recently the phenomenon of many-body localization (MBL) has garnered a lot of attention, and it has been claimed that for high enough disorders, the many-body eigenstates at the middle of the spectrum are localized, and hence athermal [18]. The situation is different from the non-interacting case, in the sense that the interaction terms lead to an inevitable spreading of quantum information, which however remains exponentially slower than the typical thermal behavior.

More recently, doubts have been cast on these assertions [19], primarily because of the limited sizes (generically with ≈ 20 qubits) for which the numerical experiments can be done for the many-body interacting systems. Even if the phenomenon of MBL as a genuine 'phase', for which it was claimed that the athermal behavior persists till 'infinite' times in the thermodynamic limit (exponential in the system sizes for finite systems), does not hold true, it has been definitively shown that high disorder does lead to very slow propagation of local information, at least as a transient behavior.

In this chapter we study the behavior of quantum information scrambling in a disordered interacting quantum spin chain. Using tensor network representation of the evolving operator, we find that the early time behavior of OTOCs can be computed very efficiently classically for very large systems (≈ 200 spins, for long times ($t \sim 100 J^{-1}$)). It turns out that this early time behavior is already enough to find features of localization and slow information scrambling when the disorder is tuned higher. From the numerical data, we find that the speed of scrambling,

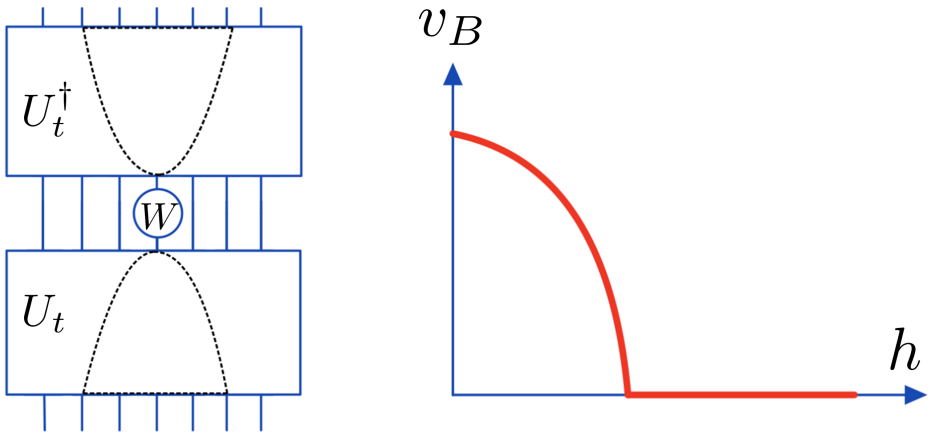

Figure 0.4: **Scrambling and disorder** We show the averaged sub-linear power-law lightcone that arises due to random disorders in a local interacting Hamiltonian. We further show a schematic on the right panel with the vanishing of v_B at a finite disorder h, which summarizes our findings from Chapter 1.

or the 'butterfly velocity' (v_B) actually goes to zero sharply at a finite disorder strength (see Fig. 0.4). For disorders below this finite 'critical' value, there is an effective linear light-cone for the evolving operator characterized by a positive v_B. At higher disorders, the light cone becomes a sub-linear power-law, which at even higher disorders becomes indistinguishable from the purported logarithmic lightcone for a genuine MBL phase (we are not able to resolve the presence or absence of such an MBL transition from our data). However, the linear to sublinear transition shows that even without proper MBL, the speed of the propagation of quantum information is severely restricted by the presence of disorder. We further find evidence that 'rare-regions' (small pockets of locally higher disordera) drive this transition, which occurs at much smaller disorders than the putative MBL transition.

0.2.2 OTOCs at finite temperatures

We found in our definition of the OTOCs and squared commutators that they are state-dependent measures of scrambling. In particular, it is interesting to consider these quantities with respect to the thermal density matrix, $\rho_\beta \propto e^{-\beta H}$, to study the effect of temperature on scrambling.

One straightforward finite temperature generalization of the squared commutator is the following,

$$C = \mathrm{Tr}\left[\rho_\beta [W_i(t), V_j]^\dagger [W_i(t), V_j]\right], \tag{0.1}$$

with the corresponding OTOC,

$$\mathcal{F} = \mathrm{Tr}\left[\rho_\beta W_i^\dagger(t) V_j^\dagger W_i(t) V_j\right]. \tag{0.2}$$

However in computations of scrambling in field theories, this quantity is formally infinite because of the fields being on the same space-time location on the corresponding Keldysh contour. Instead, the computation is typically done with respect to the OTOC defined symmetrically around the thermal circle,

$$\mathcal{F}_{\text{sym}} = \mathrm{Tr}\left[\rho_\beta^{1/4} W_i^\dagger(t) \rho_\beta^{1/4} V_j^\dagger \rho_\beta^{1/4} W_i(t) \rho_\beta^{1/4} V_j\right]. \tag{0.3}$$

This quantity can be obtained by analytic continuation of the regulated squared commuta-

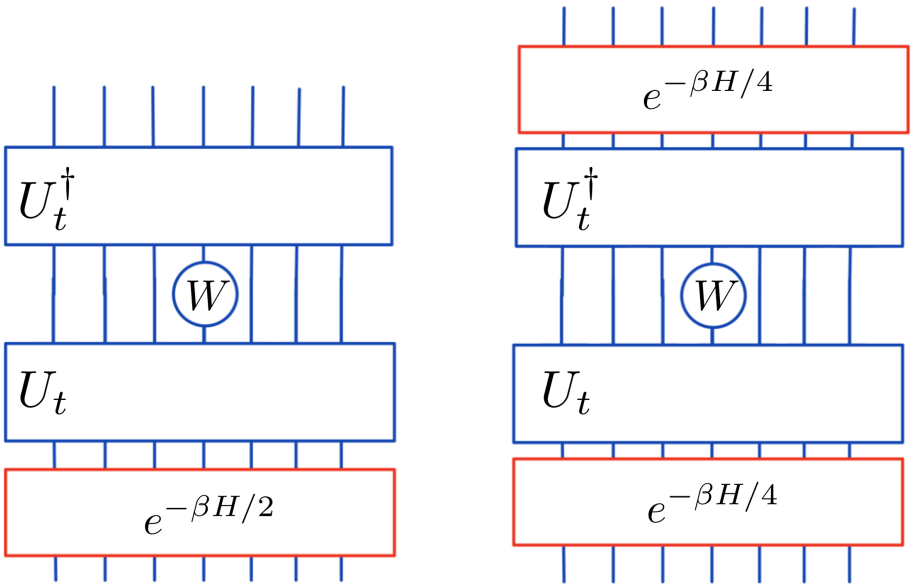

Figure 0.5: **Thermal OTOCs** corresponding to the unregulated (left panel) and symmetrically regulated OTOC (right panel) involves operator evolution with distinct patterns of thermal damping.

tor,

$$C_{\text{reg}} = \text{Tr}\left[\rho_\beta^{1/2}[W_i(t), V_j]^\dagger \rho_\beta^{1/2}[W_i(t), V_j]\right]. \tag{0.4}$$

The distinction between the OTOCs in Eq. 0.2 and Eq. 0.3 is shown in Fig. 0.5. In a seminal work, it was shown that the Lyapunov exponent associated with scrambling is bounded by the temperature [20],

$$\lambda_L^{\text{sym}} = \partial_t \log C_{sym} \leq 2\pi/\beta, \tag{0.5}$$

the so-called bound on chaos. Crucially, the Lyapunov exponent considered in the proof was obtained from the symmetrically regulated squared commutator as defined using the OTOC in Eq. 0.3. However, although it may be expected that the same bound holds true for Lyapunov

exponents obtained from other thermal squared commutators, such as the regulated or the unregulated squared commutator defined in Eq. 0.4 and Eq. 0.1 respectively, there are apriori no reasons why the theorem should apply to these quantities.

In this work I explore the issue of regulator-dependence by simulating the regulated and unregulated squared commutators at low temperature (of the order of the gap) for a gapped quantum spin chain in the paramagnetic phase. Using the same tensor network technology as in the first chapter, we can perform this computation for large spin chains of size ~ 100. We find that the numerically obtained Lyapunov exponents from the regulated and unregulated squared commutators violate the bound on chaos. This demonstrates that the bound on chaos applies exclusively to OTOCs with the symmetric regulator dependence (for which the bound was proven), and does not extend to other similarly defined physical quantities.

The second question I explore is that of the temperature dependence of the butterfly velocity. We find from the numerical data that the unregulated squared commutator is not at all affected by the lowering of temperature. On the other hand, the butterfly velocity obtained from the regulated squared commutator slows down as a power-law with the lowering of temperature, asymptotically approaching the scaling, $v_B \sim \beta^{-1/2}$. This suggests that in the unregulated case, high energy modes enter the computation even at low temperatures, which leads to an effectively temperature independent behavior consistent with the $\beta = 0$ high temperature scrambling. On the other hand, the regulated case is actually sensitive to the physics of the low-temperature modes.

Can we analytically understand the low temperature scaling of the butterfly velocity obtained from the regulated commutator? To address this, I perform a field theoretic computation of scrambling in the paramagnetic phase of an $O(N)$ model in 2+1D. In this phase, we find that the butterfly velocity has the same scaling as the speed of sound at low temperatures, $v_B \sim \beta^{-1/2}$.

However, the field theory computation does not capture the regulator dependence that we observed from the numerical spin chain computations.

0.2.3 Measurement induced entanglement transition

Under a unitary evolution generated by generic interacting Hamiltonians, a quantum state evolves to produce volume-law entanglement for contiguous subregions. As we discussed in the introduction, this is also associated with the thermalization by quantum dynamics, where subregions appear as thermal density matrices which are mixed states with thermal entropy.

Are there classes of many-body quantum dynamics where this does not hold true? In particular, are there generic dynamically generated 'phases' which do not appear thermal? We saw in a previous section that disordered systems lead to a slow scrambling phase which appears athermal for arbitrarily long times. More recently, yet another mechanism has been identified to give rise to restricted and tunable scrambling - repeated local measurements.

Quantum measurements involve collapsing the quantum state onto an eigenstate of the measurement operator. If the eigenstate has area-law entanglement, then the state post-measurement would have lost its long-range entanglement structure. In particular, measuring on-site operator would destroy all entanglement between the site and the rest of the system.

Consider a quantum circuit where the unitary gates are interspersed by single body measurement gates. We consider a parameter p which is the probability of measuring a particular qubit at any time. In a circuit of depth D on N qubits, we therefore have pDN measurements on average. It has been shown recently that tuning p leads to a dramatic change in the pattern of entanglement in the generated state [21, 22]. In particular, for generic systems it has been observed,

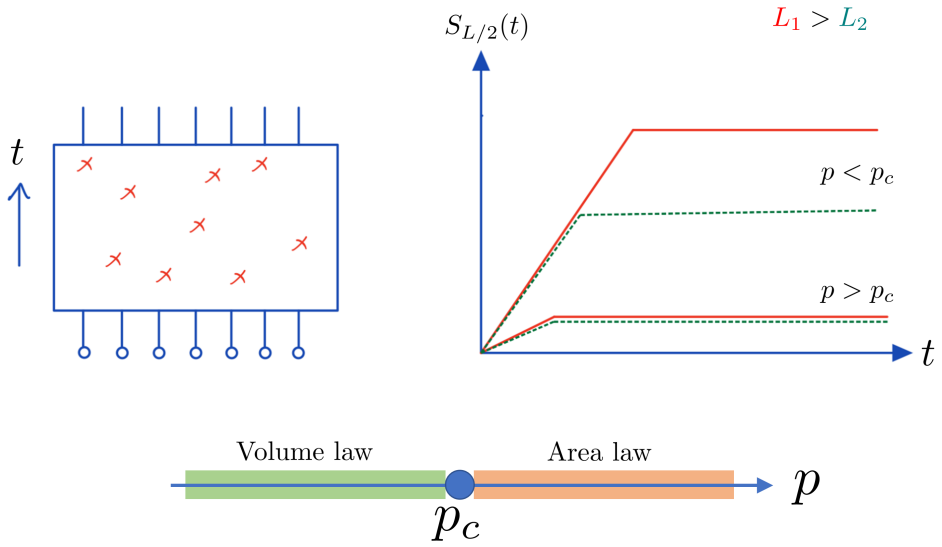

Figure 0.6: **Measurement induced entanglement transition in quantum circuits.** In the left panel we consider a unitary circuit (blue rectangle) insterspersed by local on-site projective measurements (red crosses). The circuit generates a steady state which has area law entanglement for half of the system if the rate of measurement is high $p > p_c$ and volume law entanglement if the rate of measurement is low $p < p_c$. p_c is the critical rate of measurement.

primarily using numerical tools, that for $p > p_c$ the obtained states have area law entanglement, while for $p < p_c$ the states have volume law entanglement (see Fig. 0.8). Here p_c is the critical rate of measurement associated with phase transition.

Measurement induced phase transition (MIPT) has been largely a numerical observation, and only recently attempts have been made to understand it analytically. Analytical understanding is important to justify the presence of the phase transition (and identify its universality class) for certain toy models, which builds more confidence in the numerical observations.

0.2.3.1 Purification transition in an all-to-all circuit

In Chapter 3, we make analytical progress towards the understanding of MIPT by constructing a toy model of hybrid dynamics (which refers to unitaries and measurement) for which

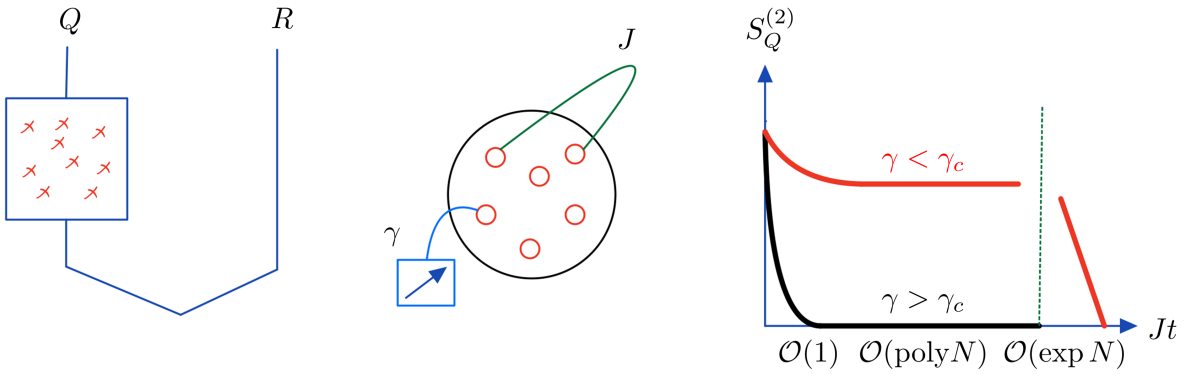

Figure 0.7: **Measurement induced purification transition in all-to-all connected quantum circuits.** The purification circuit is shown on the left panel, with the system qubits Q and the reference qubits R. In the middle panel I show the toy model we consider - a cluster of qubits, evolving with a random unitary generated by two qubit interaction of strength J and on-site weak measurement of strength γ. The evolution of the Rényi-2 entropy of the system as a function of time, for different strengths of measurement are shown in the right panel.

one can study the entanglement patterns of the final state using field theoretic computations. The phenomenon we study is the measurement-induced purification transition [23], which is closely related to the entanglement transition. In this setup, we start with a system and a reference, with the system being maximally entangled with the reference. The system is now subjected to the hybrid dynamics. If at the end of the dynamics the reference remains mixed, then we call it a mixed phase, while if the reference is purified then it is called the pure phase. This phase transition is again driven by the rate of measurements in the hybrid dynamics p.

In this chapter we consider a cluster of qubits undergoing all-to-all connected time dependent random Hamiltonian dynamics, interspersed with weak on-site measurements. Here weak measurement refers to the system being coupled to an auxiliary system, on which a projective measurement is performed. The strength of the measurement refers to the magnitude of the coupling of the system with the auxiliary system. In this setup we can compute the Rényi-2 entropy of the system and subsets of the system averaged over the randomness, by using replica field

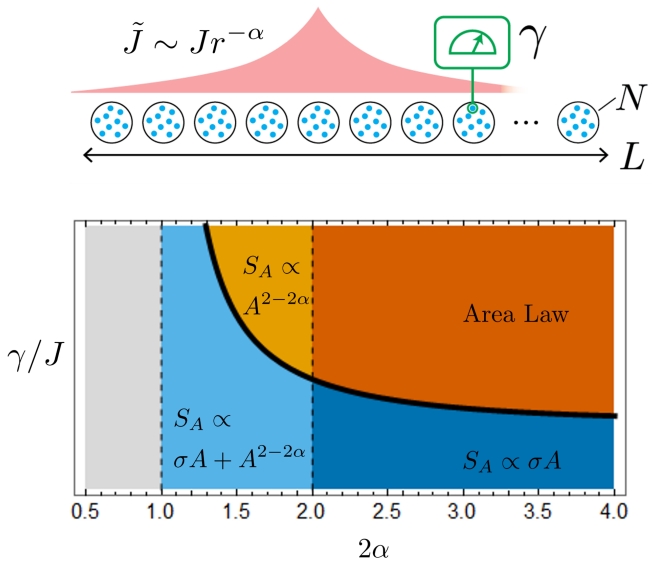

Figure 0.8: **Measurement induced purification transition in long-range interacting quantum circuits.** We consider a lattice of large-N clusters of qubits, which undergo hybrid dynamics with unitaries generated by long-range coupling terms decaying with distance as $r^{-\alpha}$, and on-site weak measurement with strength γ. The entanglement phase diagram as a function of γ and α is shown below.

theory at large-N, where N is the number of qubits in the cluster. We find that if the strength of the measurement is tuned to be higher than an analytically obtained critical strength, the system is purified in constant time-scale. On the other hand, if the measurement strength is low, then the system remains mixed until exponentially long timescales (see Fig. 0.6). We are also able to identify the critical field theory of the transition of the Rényi-2 entropy, which helps us to identify critical exponents of the transition analytically.

0.2.3.2 Measurement and long-range unitary induced entanglement phases

What distinct patterns of entanglement are possible as the fixed points of such hybrid dynamics? Can we design the hybrid dynamics such that we get a richer phase diagram than just the volume law to area law transition? In Chapter 4 we address this question by investigating the

effect of long-range interactions in the unitary on the obtained entanglement pattern.

Building on the previous all-to-all connected model, we now consider a lattice of such large-N clusters, with inter-cluster interactions. Furthermore, the inter-cluster interactions are considered to follow a power-law form with the distance between the clusters, falling off as $r^{-\alpha}$. In this setup, we again compute the Rényi-2 entropy of a contiguous collection of the clusters. We find that distinct entanglement phases emerge as a function of the measurement strength and the power-law exponent α, including fractional entangled phases where $S \sim A^{2-2\alpha}$, and volume law phases with power-law corrections, such as $S \sim A + A^{2-2\alpha}$, where A is the size of the contiguous sub-system (see Fig. 0.7).

0.2.4 Many-body physics beyond lattices

We often study quantum many-body physics on regular d-dimensional lattices, motivated by naturally occurring crystalline solid state materials and lattice regularizations of quantum field theories. However, there are interesting quantum phenomena beyond those feasible on lattices.

From a quantum information viewpoint, many-body sparse graphical models typically possess the feature of fast quantum information scrambling. The phenomena of fast scrambling was demonstrated first in all-to-all connected graphical models such as the Sachdev-Ye-Kitaev (SYK) model [12, 24], which are holographically dual to a quantum theory of gravity in one higher dimension [12, 24, 25]. In an SYK-like model on N sites, any local quantum information spreads across the whole system in a short scrambling time, $t_* \sim \log N$ [26, 27]. On the other hand, in generic local models on d-dimensional lattices, typical scrambling times are long $t_* \sim N^{1/d}$.

However, having a complete (i.e. all-to-all connected) graph is not necessary for getting

fast scrambling - generic sparse graphs can also scramble information quickly [28, 29]. Sparse graphical models are also attractive platforms to be simulated on a quantum processor, since the sparse connectivity of the graph can lead to efficient quantum simulation. In this context, reliable classical algorithms to simulate quantum many-body models on sparse graphs are highly desirable.

In Chapter 5, we take the first steps towards the study of quantum many-body physics on sparse graphs using tensor networks. Sparse graphs are 'expander' graphs with a high probability; furthermore, they are locally tree-like. Using these two features, we show that tensor network contraction, which is a difficult task on graphs with loops, can be approximately done using the belief propagation (BP) algorithm for locally tree-like graphs [30, 31]. In this chapter we use the BP algorithm and tensor networks to variationally access the ground state energies of quantum spin models defined on 'expander' graphs. This paves the way for future exploration of equilibrium and non-equilibrium quantum phenomena on sparse 'expander' graphs.

Chapter 1: Scrambling dynamics in disordered quantum spin systems

"What are you doing?" asked Tiny Dragon.

"I've no idea," said Big Panda, "but it's great fun."

- Big Panda and Tiny Dragon, James Norbury.

1.1 Introduction

It has long been known that disorder can slow or arrest quantum motion [17], leading to a localized state. Recently it was understood that localization can survive even strong interactions, a phenomenon dubbed many-body localization (MBL) [32, 33, 34]. More precisely, there is a quantum phase transition in interacting systems from a thermalizing phase to a localized phase with increasing disorder. The phase and phase transition have been intensely studied (e.g., [35, 36, 37, 38, 39, 40, 41, 42, 43, 44, 45, 46, 47, 48, 49, 50]), and there is a proof, given plausible assumptions, of the existence of MBL in one-dimensional spin chains with local interactions [51, 52].

In this work we are particularly concerned with the quantum phase transition (or transitions) that take a one-dimensional disordered system from a thermalizing phase to a localized phase [39, 42, 53, 54, 55, 56, 57, 58, 59]. It is natural to study this phase transition via dynamics [36, 37, 38, 40], because eigenstate based numerics are difficult to scale to large system sizes and

because dynamical properties are accessible in experiments [60, 61, 62]. We study a dynamical quantity related to quantum information scrambling, the squared commutator [11, 63, 64, 65].

Consider two local operators, W and V, in a one-dimensional spin chain, separated by a distance x. The squared commutator probes the extent to which V fails to commute with the time evolved Heisenberg operator $W(t) = e^{iHt}We^{-iHt}$. It is defined as the expectation value of the absolute value squared of the commutator of the $W(t)$ and V,

$$C(x,t) = \langle [W(t),V]^\dagger [W(t),V] \rangle. \tag{1.1}$$

It is closely related to the out of time ordered correlator (OTOC), $F(t) = \langle W^\dagger(t)VW^\dagger(t)V\rangle$. OTOCs are currently receiving attention as a diagnostic of quantum chaos [12, 20, 63, 66], including experimental proposals [67, 68, 69, 70] and early experiments measuring OTOCs [71, 72, 73, 74, 75, 76, 77, 78, 79, 80, 81, 82, 83, 84, 85, 86, 87]. In fact, [74] measured OTOCs to detect localization in NMR spin systems.

The squared commutator starts at zero for initially separated W and V, and then grows as the operator $W(t)$ spreads and overlaps with the location of V. In the absence of disorder, $C(x,t)$ typically grows ballistically, leading to an emergent linear light cone with butterfly velocity v_B. On the other hand, disorder can severely arrest the growth of $C(x,t)$, a manifestation of localization. It has been argued that MBL is characterized by an extensive number of local integrals of motion [41, 42, 43, 44], leading to an emergent logarithmic light cone [88]. Similarly, it was recently shown that the disorder averaged $C(x,t)$ exhibits a logarithmic light cone with $v_B = 0$ in the MBL phase [89, 90, 91, 92, 93, 94, 95].

In this chapter we study operator dynamics across the entire thermal-to-MBL phase dia-

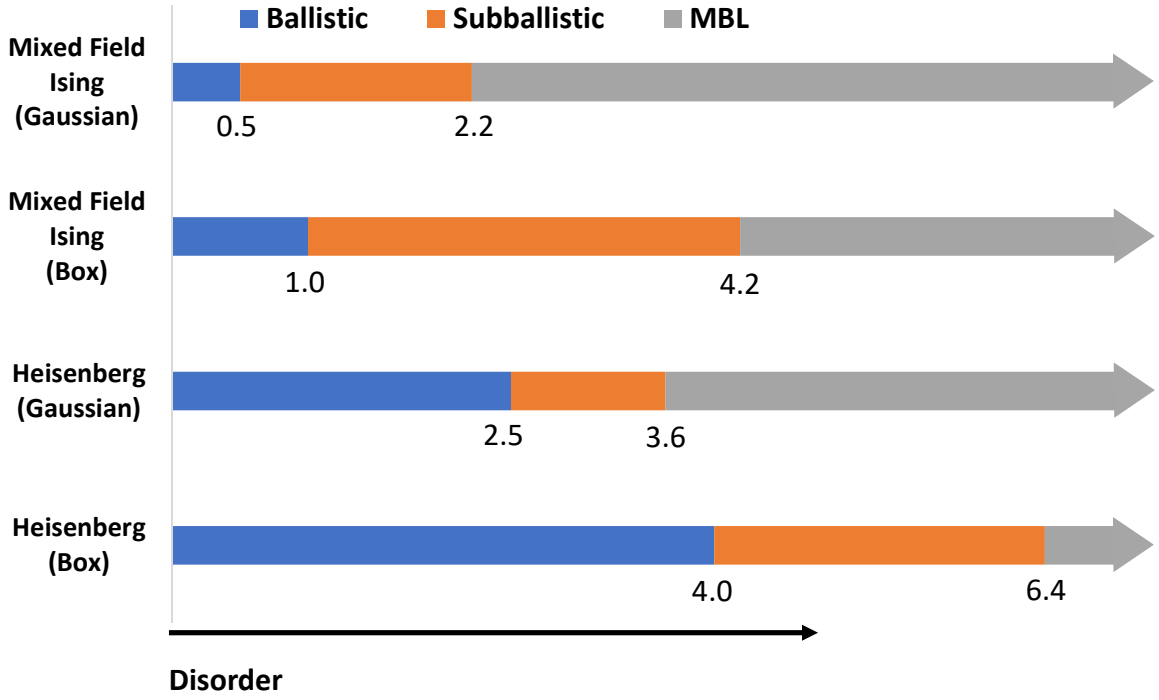

Figure 1.1: Phase diagram of operator spreading in disordered interacting spin systems with different disorder models. The Heisenberg Hamiltonian is defined using Pauli operators instead of spin-1/2 operators, so the W normalization is twice as large relative to the spin-1/2 convention.

gram, with a particular focus on the thermal side of the MBL eigenstate transition. This regime has attracted interest in the context of rare region effects which can slow down transport well before the MBL transition [45, 46, 96, 97]. One interesting question is whether the butterfly velocity survives arbitrarily weak disorder [98, 99]. It is challenging, since, for example, strong disorder RG [95] applies only in the MBL phase and state-of-the-art exact diagonalization is still limited to small sizes [98]. We use a recent t-DMRG based matrix product operator method to calculate dynamics of local Heisenberg operators [100] (see also [101, 102]) for larger system sizes (≈ 200 spins) and longer times than previously possible.

1.1.1 Summary of results

First, we observe a weak disorder phase with ballistic operator spreading ($v_B \neq 0$) as well as a sharp transition to a sub-ballistic phase ($v_B = 0$), at a disorder strength well below the putative MBL transition (see Fig. 1.1). This transition is characterized by a continuous vanishing of v_B and an apparent divergence of the wavefront broadening. Second, we study the variability of operator growth from one disorder realization to another, which also characterize the ballistic to sub-ballistic transition independent of the fitting procedure. This is also a clear numerical demonstration of rare regions which is only possible because of the large system size. Observations from the variability of the scrambling data motivate a simple phenomenological model of rare regions, from which we analytically substantiate the presence of the ballistic phase. Together these numerical observations reveal a rich dynamical phase diagram for disordered spin models (Fig. 1.1). Comparing to previous studies, we find that the loss of ballistic operator spreading occurs at a larger disorder strength than the diffusive to sub-diffusive transition in spin transport, indicating at least four non-trivial dynamical regimes [45, 46, 96, 97, 99, 103].

1.2 Model

For concreteness, we consider two one-dimensional spin chain models:

1. Mixed field Ising model with σ^z disorder

$$H = -J \sum_{r=1}^{L-1} Z_r Z_{r+1} - h_x \sum_{r=1}^{L} X_r - \sum_{r=1}^{L} h_{z,r} Z_r \tag{1.2}$$

2. Heisenberg model with σ^z disorder,

$$H = -J \sum_{r=1}^{L-1} (X_r X_{r+1} + Y_r Y_{r+1} + Z_r Z_{r+1}) - \sum_{r=1}^{L} h_{z,r} Z_r. \tag{1.3}$$

Here X_r, Y_r, Z_r are the local Pauli operators. For the mixed field Ising model, we choose the parameters $J = 1$, $h_x = 1.05$ and $\overline{h_{z,r}} = 0.5$. For the Heisenberg model, we choose the parameters $J = 1$ and $\overline{h_{z,r}} = 0$. For each spin chain we consider two different disorder probability distributions, box and Gaussian. For the box disorder, we draw the $h_{z,r}$ fields uniformly at random from the interval $[-W, W]$, with W being the disorder strength. For Gaussian disorder, the $h_{z,r}$ fields are Gaussian random variables with standard deviation (SD) W. The parameters for the mixed field Ising model have been chosen so that the $W = 0$ limit is strongly chaotic [100]. The Heisenberg model with box disorder has been extensively studied for chains with $L \lesssim 30$ spins, and it has been shown that the thermal-MBL transition occurs at $W \gtrsim 7$ [47]. We consider all these models to elucidate the robustness of the intermediate regime, and also to understand the role of disorder distribution on rare region effects.

1.3 Numerical method

Our technique is a real-time tensor network method for operator dynamics [100]. Studying real-time quantum dynamics using tensor network methods, such as state-based TEBD or t-DMRG methods [37, 38, 104, 105, 106, 107], is typically limited to early times, because the entanglement of the state is upper-bounded by $\log(\chi)$, where χ is the bond dimension of the matrix product state (MPS) [37]. However, in a recent paper [100], some of us have shown that

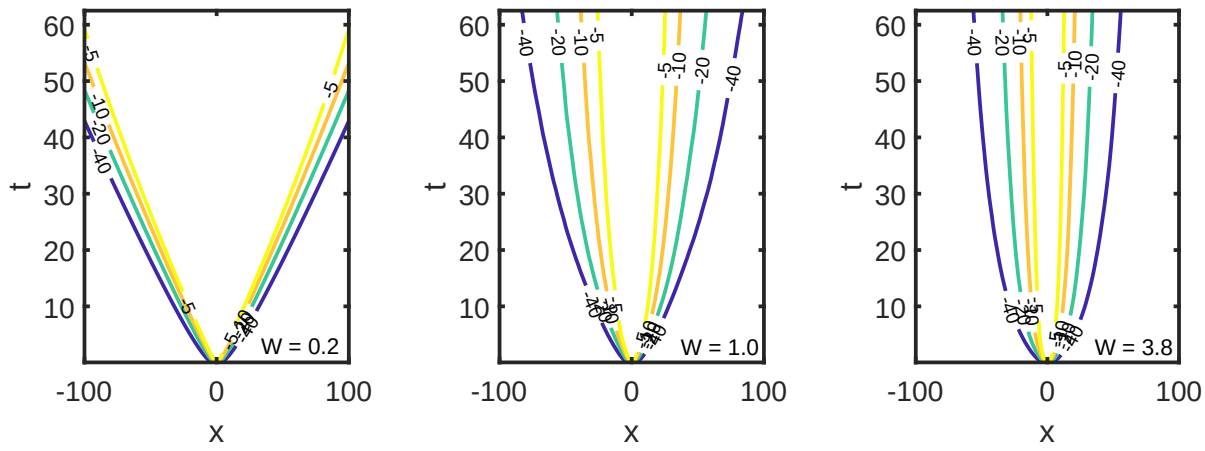

Figure 1.2: Plot of the contours of the averaged $\log(C)$, for the Mixed Field Ising model with Gaussian disorder. (averaged over $\sim$ 200 disorder realizations, for three disorders, $W = 0.2$ (ballistic), $W = 1.0$ (intermediate) and $W = 3.8$ (logarithmic). Bond dimension is 32. Convergence with bond dimension is discussed in a later section. Fluctuations away from the disorder averaging are discussed in Fig. 1.4 and in the corresponding section.)

by going to the Heisenberg picture, one can reliably access a much wider space-time region using dynamics of matrix product operators (MPO) because of the entanglement structure of the Heisenberg operator. The complexity of the operator only builds up within the lightcone and is not essential for studying the dynamical property of the wavefront. As a result, the butterfly velocity and the broadening of the wavefront can be accurately extracted from TEBD simulation on Heisenberg operators in the matrix product form with modest bond dimension.

We simulated the squared commutator in the infinite temperature Gibbs ensemble,

$$C(r - r', t) = \frac{1}{2^L} \mathrm{Tr}\left[(\right] [X_r(t), X_{r'}]^\dagger [X_r(t), X_{r'}]) \tag{1.4}$$

for spin chains of length $L = 201$ with maximal time of order $50-100$, in the units of $J^{-1} = 1$. A small Trotter step of $\delta t = 0.0025$ is used to obtain high numerical precision. For each disorder, we consider around $200-500$ disorder realizations and average $\log(C)$ over the different realizations.

This ensures that rare disorder realizations which could localize the operator growth are not overwhelmed by the ballistic samples during the averaging process. Fig. 1.2 shows light cone obtained from averaging $C(x,t)$ for different disorders, representing each phase in Fig. 1.1. We discuss convergence of the numerical procedure in a later section.

We detect the transition by extracting the butterfly velocity and the wavefront broadening from the averaged squared commutator. We use the universal form for the squared commutator ahead of the wavefront (where $C(x,t) << 1$), conjectured in [16, 100, 102],

$$C(x,t) \sim \exp\left(-\lambda_p \left(x - v_B t\right)^{1+p} / t^p\right) \tag{1.5}$$

Here, v_B is the butterfly velocity, and p is the wavefront broadening coefficient, which is known to be $p = 1$ for random unitary circuit models [15, 108], $p = 0$ for large-N holographic models and $p = \frac{1}{2}$ for non-interacting systems. The above form does not hold in the localized regime, which has a logarithmic lightcone [89, 90, 91, 92, 93, 94, 95]. Additionally, the shape of lightcone becomes power-law like before the MBL transition due to rare region effects [98, 99]. A general form that captures all the scenarios is,

$$C(x,t) \sim \exp\left(-\lambda_p \left(x - v_B t\right)^{1+p} / t^p + a \log(t)\right) \tag{1.6}$$

This form captures the cases where the lightcone is linear ($v_B \neq 0$, $a = 0$), power-law ($v_B = 0$, $p \neq 0$, $a = 0$) or logarithmic ($p = 0$, $v_B = 0$, $a \neq 0$), as the disorder strength increases.

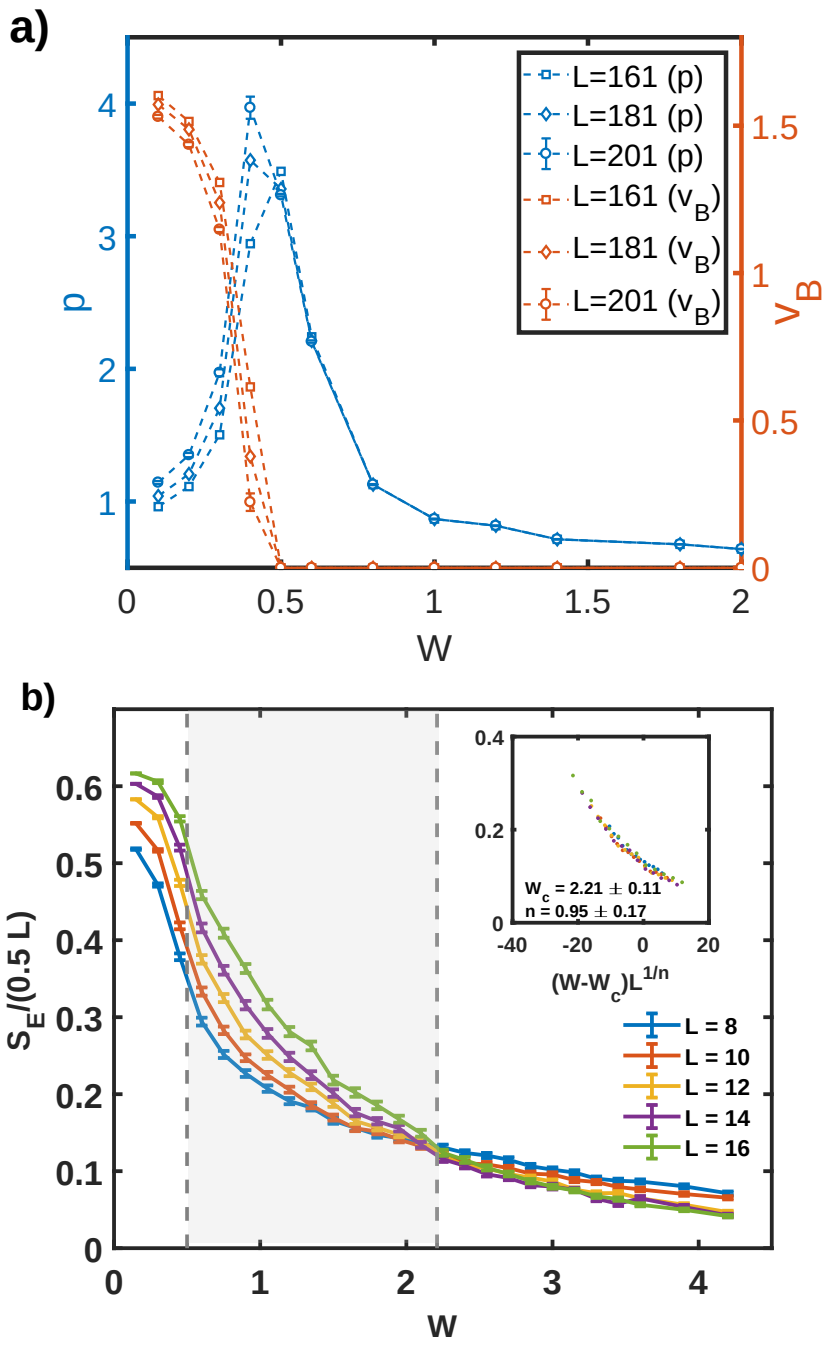

Figure 1.3: **a)** The extracted broadening coefficient p and butterfly velocity v_B are plotted for different sized systems, versus disorder. Note, v_B goes to zero and p has a peak at around disorder $W \sim 0.5$ with small finite-size effect. Errorbars obtained from the 95% confidence interval of fitting, are shown for the largest system size. **b)** Finite-size scaling on half-chain entanglement entropy estimates that the localization transition occurs at $W_c \sim 2.21$. The data collapse to the degree 3 polynomial ansatz $g[(W - W_c)L^{1/n}]$ with $n \sim 0.95$ is shown in the inset. The shaded region is the intermediate region.

1.4 Numerical results

1.4.1 Mixed-field Ising model with Gaussian disorder

Here we use the mixed-field Ising model with Gaussian disorder as an example to demonstrate the transitions in Fig. 1.1. The other three cases can be found in later parts of this section. In Fig. 1.3, we plot the extracted v_B and p versus disorder, for different lengths of the spin chain by fitting the data to the growth form (1.5). The fitting procedure and the goodness of fit are discussed in later parts.

The butterfly velocity decreases as the disorder strength increases and becomes zero at $W \sim 0.5$. On the other hand, p increases as W approaches the critical disorder, and decreases when W passes beyond that. This disorder is below the MBL transition disorder extracted from exact diagonalization study on the entanglement entropy scaling (Fig. 1.3(b)). The fact that v_B goes to zero and p peaks at the same disorder strength indicates a sharp transition before the true MBL transition, consistent with the weak-link model describing the rare region effects in disordered systems, studied recently [99].

Below the transition, the system is characterized by a finite v_B and p, indicating a linear lightcone with broadening front. Above the transition, the velocity becomes zero and the shape of the lightcone becomes powerlaw like, $x \sim t^{p/(p+1)}$. Our method captures the logarithmic lightcone in the strong disorder limit (Fig.1.2 (c)), but it is difficult to ascertain the transition to the logarithmic light cone from fitting the finite space-time data. This is discussed in S.M., Sec. II, where we also provide more evidence of logarithmic light cones at high disorder strength beyond the MBL transition. The transition identified here is different from the diffusive-subdiffusive

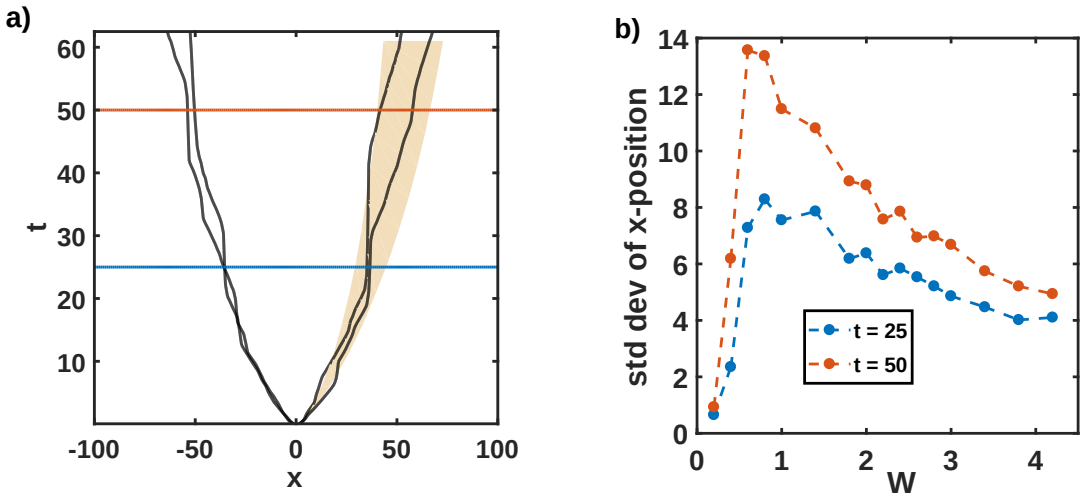

Figure 1.4: **a)** The bold black lines are *single realizations* of -15 contour lines of $\log(C)$ at disorder $W = 0.8$ for the mixed field Ising model with Gaussian disorder. Note the colored patch is given by the SD of the x positions for 180 realizations at a given time. Note that the two disorder realizations have distinct behaviors after $t = 25$, with one being significantly slower because of a local bottleneck of large disorder. **b)** SD of x-cuts at times $t = 25$ and $t = 50$, for 180 realizations for different disorders are plotted, which peaks at $W \sim 0.5$ and coincides with the critical disorder where v_B vanishes.

transition for dynamics of conserved quantities [96, 103]. In particular, we observe that in the Heisenberg model with box disorder, the $v_B = 0$ transition occurs at a higher disorder, $W \sim 4$ than the spin transport diffusive-subdiffusive transition disorder, $W \sim 1.1$ (from [96], in our Pauli matrix convention). This implies a separation of information propagation and spin transport.

1.4.2 Shot to shot variability

We also study the variability of the contours of $\log(C)$ from one disorder realization to another. In Fig. 1.4(a) a particular contour line of $\log(C)$ is plotted for two different disorder realizations with $W = 0.8$, which differ significantly. To characterize the shot to shot fluctuations, in Fig. 1.4(b), we plot the SD of x positions, and observe that at long time, the variability peaks at the same disorder ($W \sim 0.5$) where v_B vanishes. The divergence of fluctuations, obtained

without any numerical fitting, is remarkably consistent with the divergence of p in Fig. 1.3(a). This substantiates the transition at $W \sim 0.5$. Fig. 1.4(a) also demonstrates the microscopic mechanism for vanishing v_B before the MBL eigenstate transition. The contours for two different realizations have bottlenecks at certain space regions, where scrambling is arrested. This is a visualization of rare region effects - local stronger disorders in certain regions affecting average dynamical properties.

1.4.3 Convergence with bond dimension

In this section we demonstrate convergence with bond dimension for the squared commutator data. In Ref. [100], it was rigorously proven that if $C(x,t)$ is sufficiently small for all $x > x_0$, then the operator Renyi entropy with entanglement cut at x_0 is also small. This result implies that the MPO representation with a fixed finite bond dimension is faithful for operators of physical importance. There is still a possibility that errors could build up after repeated truncations, but it was also argued that these errors cannot propagate outside the emergent light cone.

In a many-body localized system, the light cone grows logarithmically instead of linearly with time, and thus one hopes to access an even wider region of the space-time with this method. In that sense, MBL is easier than chaos, as the spatial spread is less. In the chaotic case, the linear light cone ensures that errors within the light cone are contained within, but in the logarithmic case, the error containment is not so straight forward. Due to these two opposing factors, we need to numerically study the convergence of the light-cones with increasing bond dimension. We consider an $L = 201$ spin chain, and look at the overlap of $X_{r=101}(t)$ with X_r as a function of t. In Figs 1.5 and 1.6, we show convergence of both the single realization and the averaged data

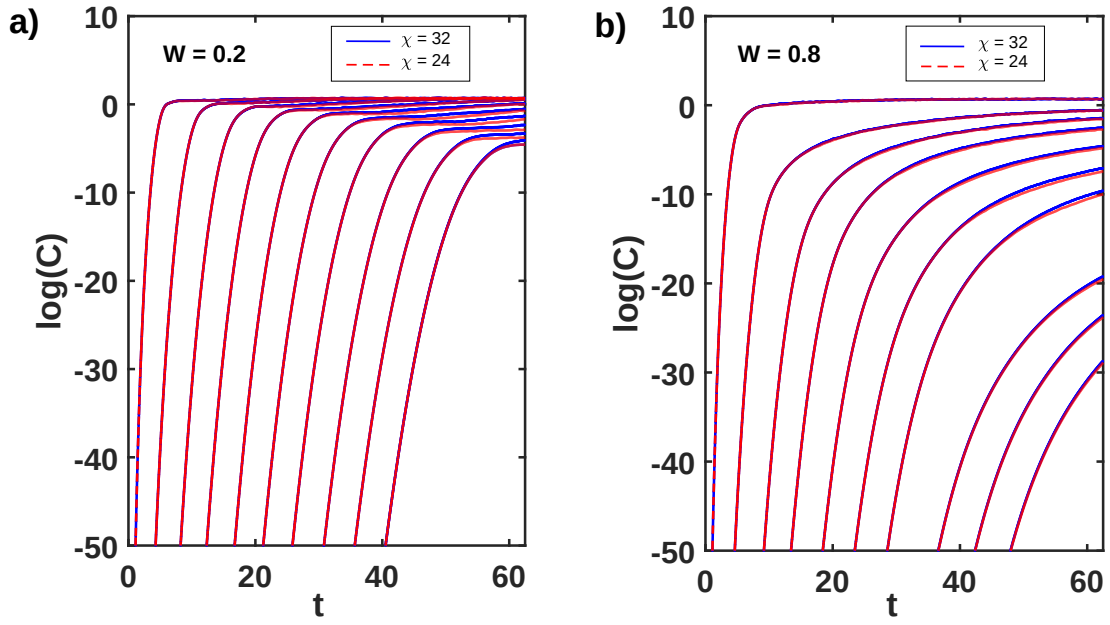

Figure 1.5: The logarithm of the squared commutator, $\log(C)$, for single realization with **a)** $W = 0.2$ and **a)** $W = 0.8$. The plots are for two bond dimensions, $\chi = 32$ (continuous blue line), and $\chi = 24$ (dotted red line). They are essentially indistinguishable.

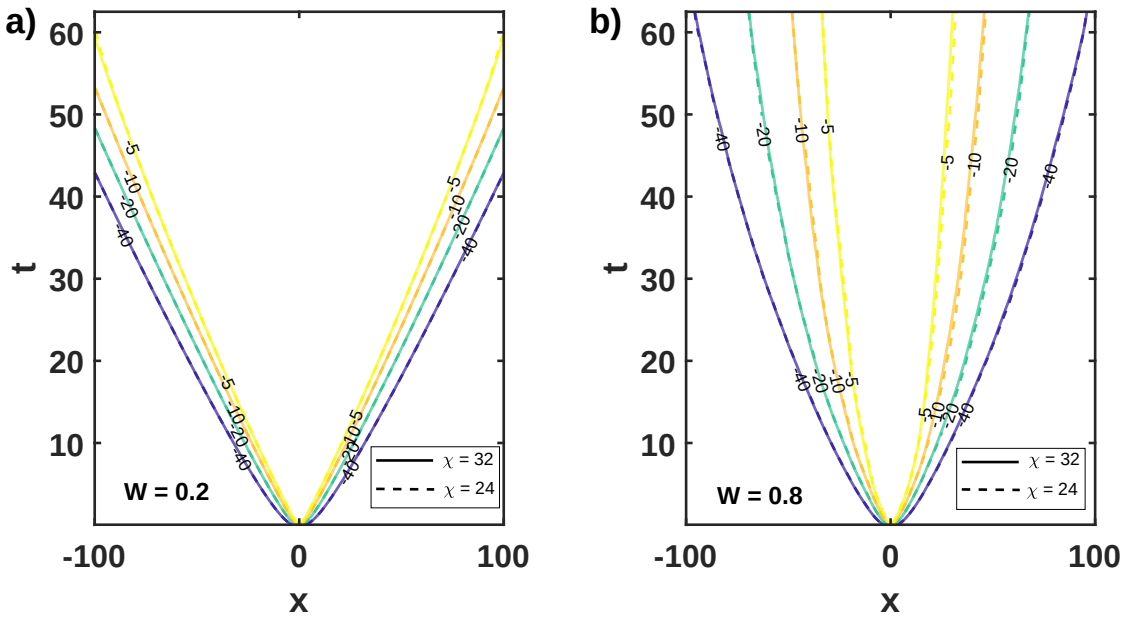

Figure 1.6: The contours of averaged $\log(C)$ (averaged over 500 disorder realizations) for two different disorders **a)** $W = 0.2$ and **b)** $W = 0.8$ for the mixed field Ising model with Gaussian disorder are plotted. The continuous lines are for $\chi = 32$, while the dotted lines are for $\chi = 24$.

of $\log(C)$ with increasing bond dimension ($\chi = 24$ and $\chi = 32$) respectively. The data shown here corresponds to the mixed field Ising model with Gaussian disorder, which was considered in the main letter. Since the obtained data converges well (for system sizes and times considered) the rest of the numerical results shown in this paper have been obtained from MPOs with bond dimension $\chi = 32$.

1.4.4 Extracting butterfly velocity and the logarithmic lightcone

To extract the physically relevant quantities from our numerical data, we employ a fitting procedure, in which we fit the disorder averaged $\log(C(x,t))$ to the fitting ansatz,

$$\log(C(x,t)) \sim a(x - v_B t - x_0)^{1+p}/t^p + c\log(t)$$

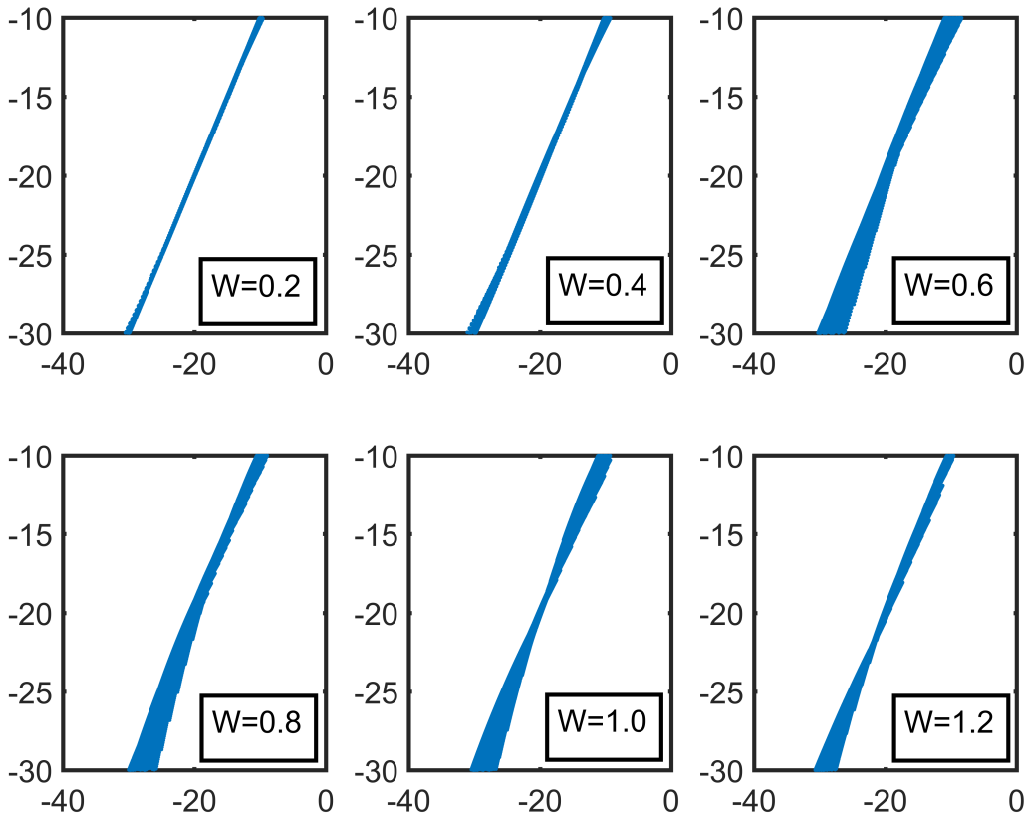

Figure 1.7: The averaged $\log(C)$ is plotted against the fitting ansatz $(x - v_B t - x_0)^{1+p}/t^p + c/a \log(t)$ for different disorders $W = 0.2, 0.4, ..., 1.2$, for the mixed field Ising model with Gaussian disorder. The fitted parameters for the figure are given in Table 1.1.

W	v_B	p	a	c	x_0
0.2	1.4357	1.3501	-1.1903	0.0452	0.1075
0.4	0.2227	3.9690	-0.0278	0.0000	-0.1005
0.6	0.0000	2.2058	-0.0867	0.0000	-0.1461
0.8	0.0000	1.1273	-0.2530	0.0000	0.3807
1.0	0.0000	0.8676	-0.3445	0.0000	1.8693
1.2	0.0000	0.8174	-0.3882	0.0000	1.8854

Table 1.1: Fitted parameters for Fig. 1.7

Note, the free parameters are a,c, the offset x_0, butterfly velocity v_B and the wavefront broadening coefficient p. We fit the averaged data over a large domain, $-30 < \log(C) < -10$, for which we are certain that the numerical procedure converges, to this ansatz, with the physical constraints $v_B \geq 0$ and $p \geq 0$. The collapse of the data to this fitting form is demonstrated in Fig. 1.7. The fitted parameters for the figure are given in Table 1.1.

The fitting ansatz that we employ has the merit of capturing various possible scenarios of operator growth. From the chaotic growth considered in [100] and [16] we expect $v_B > 0$ and some finite p for the situation without disorder. In the presence of weak disorder, there could be multiple possible options, one is that any weak disorder is enough to take v_B to zero (as was indicated in [98]), or, there could be a phase in the ergodic side which could have $v_B > 0$, as was argued in [99]. Furthermore, the behavior of the wavefront broadening in the presence of disorder is also not well understood. From the result of our numerical fitting procedure, we definitely see evidence of a ballistic phase in the presence of weak disorder, and furthermore, in the ergodic phase preceding the MBL transition, we observe a sharp transition at which v_B goes to zero and the broadening coefficient p seemingly diverges. The result doesn't change even if we remove the $\log$ term from the fitting ansatz, as its coefficient in the ergodic side has been observed to be vanishingly small.

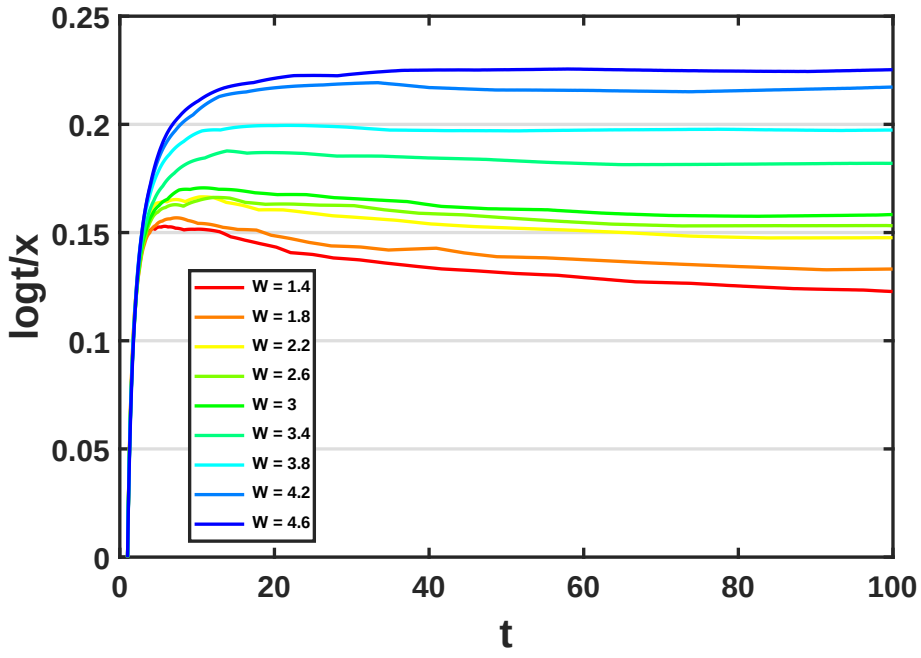

Figure 1.8: The -10 contour of the averaged $\log(C)$ for 201 sized chain is extracted at different disorders, and t and x coordinates are obtained. $\log(t)/x$ is plotted against t, for different disorders for the mixed field Ising model with Gaussian disorder. At strong disorders, $W \gtrsim 3.4$, the asymptotically flat plots provide evidence of a logarithmic light cone.

The fitting ansatz could also potentially capture the logarithmic lightcone in the MBL side. One possible way in which that can be achieved in the fitting ansatz is where $v_B = 0$, $p = 0$ and the coefficient of the $\log$ term is non zero. However we don't observe a sharp transition for the domain of disorders that we consider, possibly because the transition of a soft power law to logarithm is a invisible to the numerical fitting procedure given the finite domain.

In Fig. 1.8, we show evidence of the logarithmic lightcone without using any numerical fitting procedure. We consider a particular contour (-10 contour of $\log C$), and extract its x and t coordinates, and plot $\log(t)/x$ versus t for different disorders. If the contour is logarithmic, the plot should approach a fixed value monotonically from below, and shouldn't decrease at late times. On the other hand, if the contour has a power law behavior, the plot will decrease with

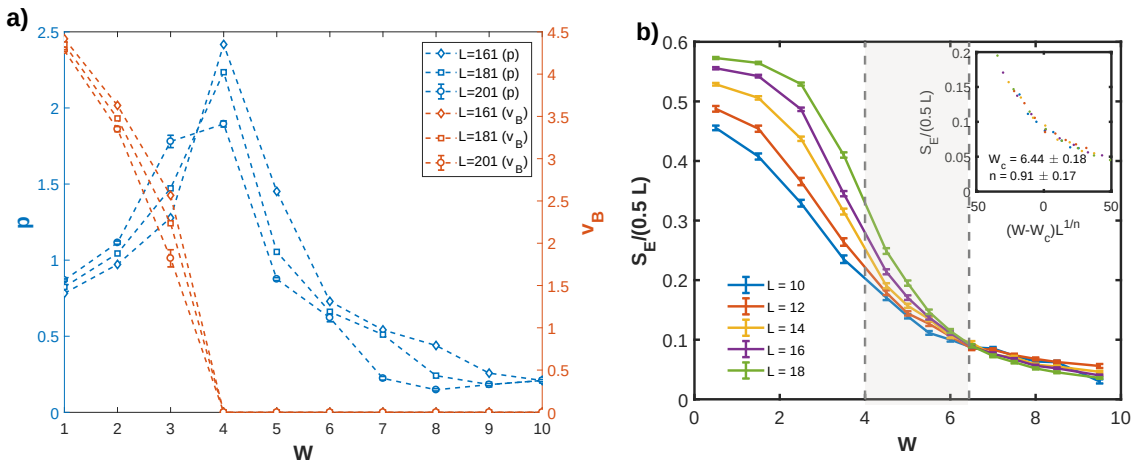

Figure 1.9: **a)** The extracted butterfly velocity v_B and broadening coefficient p are plotted for different sized systems of the disordered Heisenberg model (box), versus disorder. Note, v_B goes to zero and p has a peak at around disorder $W \sim 4$. Errorbars corresponding to the 95% confidence interval of fitting are shown for the largest system size.**b)** The MBL transition disorder is shown to be $W_c \gtrsim 6.44$, which implies the shaded intermediate region which has powerlaw lightcones.

time. In Fig 1.8, we indeed see that for high disorders ($W \gtrapprox 3.4$) the plot is aympotically flat (note the long times considered, $t = 100$). This provides evidence that at those disorders, the light cone is indeed logarithmic.

1.4.5 Heisenberg model and relation to diffusion

We consider the Heisenberg model with box disorder. The fitted v_B and p are shown in Fig 1.9. This also shows v_B going to zero and p diverging at a disorder $W \sim 4$, which is lower than the MBL transition disorder, which has been extensively studied, and is known to be $\gtrsim 7$ [47].

A related but distinct question is to study the dynamics of conserved quantities in the thermal regime in the presence of disorder. In [96], a transition between diffusive and subdiffusive transport was observed numerically in the Heisenberg chain, in the thermal phase. Corrected for the conventions used in the Hamiltonian we are considering, that transition occurs at $W \approx 1.1$,

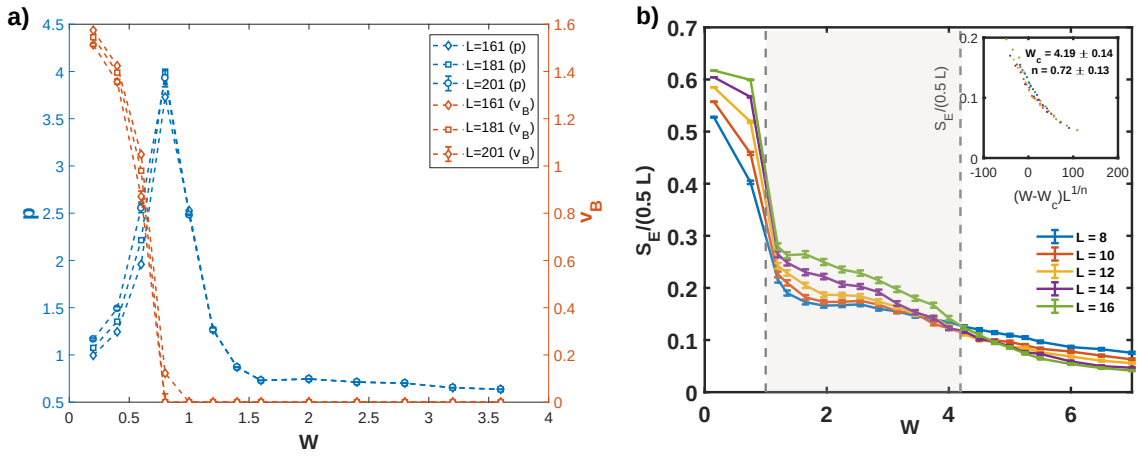

Figure 1.10: Results for the Mixed Field Ising model with box disorder. **a)** Extracted Butterfly velocity and broadening coefficient. Errorbars corresponding to the 95% confidence interval of fitting are shown for the largest system size. **b)** MBL transition ascertained by small system exact diagonalization.

which is not where we get the v_B to go to zero. So this observation implies that there are two distinct transitions in the thermal side of the disordered phases, one for diffusive to sub-diffusive transport (which happens at smaller disorder), and the other between the ballistic and sub-ballistic operator spreading.

1.4.6 Comparison between box and Gaussian disorder

In this section we show the results of our analysis for the other two disorder models that we considered, which complete the phase diagram in our main paper.

These results (Figs. 1.10, 1.11) demonstrate the versatility of the numerical procedure employed, and also indicates how rare regions affect the thermalization-localization transition. Gaussian disorders allow for rare fluctuations more occasionally than box disorders, which results in onset of sub-ballistic transport and localization at lower disorders for the Gaussian case than the case with box disorder.

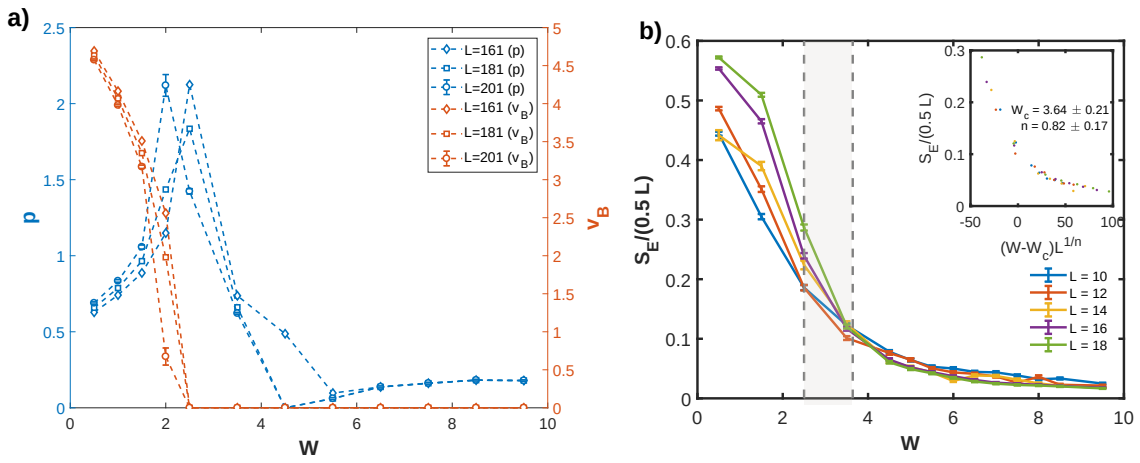

Figure 1.11: Results for the Heisenberg model with Gaussian disorder. **a)** Extracted Butterfly velocity and broadening coefficient.Errorbars corresponding to the 95% confidence interval of fitting are shown for the largest system size. **b)** MBL transition ascertained by small system exact diagonalization.

1.5 Rare region model

Motivated by above numerical results, we construct a simple model of rare regions which explains the emergence of power law, broadening behavior, and the existence of a ballistic phase at weak disorders. In a L sized spin chain with Gaussian random disorders $\mathcal{N}(0, \sigma^2)$, the SD of local disorder, might be different from σ. It might also exceed the MBL critical disorder ϵ_c, even when $\sigma < \epsilon_c$. Let ϵ be the disorder beyond which the operator growth has a logarithmic light cone. Consider a continuous stretch of $\alpha \log(L)$ spins, whose SD exceeds ϵ. The balance between the exponentially slow transport and logarithmic size of such region leads to overall subballistic information transport. Specifically, the time it takes for the information to propagate across the chain with one such rare region is $t \sim L/v_B + e^{\zeta\alpha \log L}$, where ζ is treated as the averaged inverse length scale associated with the logarithmic cone for the current purpose (It is defined carefully in S.M. Sec. V). In the limit $L \to \infty$, the average velocity L/t goes to zero for $\zeta\alpha > 1$,

indicating the subballistic scenario. This corresponds to the case where the rare region is long enough that it dominates the time, $t \sim L^{\zeta\alpha}$. As the ballistic transition is approached, we have $\zeta\alpha \to 1^+$. Comparing to the power-law lightcone $x \sim t^{p/(p+1)}$ indicates that $p \to \infty$, consistent with the apparent divergence of p at the ballistic-subballistic transition in our numerical result. A related but distinct approach was considered in [99], where the rare region effects on operator spreading were quantified using a coarse grained quantity related to the entanglement spreading across weak-links. Our model is directly in terms of the bare disorder and gives rise to consistent predictions.

The existence of a ballistic phase in the low disorder limit is also borne out of the simple model. Consider the probability of having *no* rare region of length $\alpha \log L$ with SD larger than ϵ in a disordered spin chain of length L with global SD σ, denoted as $q(\alpha; \sigma, \epsilon)$. In general, q decreases with σ and increases with α. Based on the above discussion, any α larger than $1/\zeta$ leads to subballistic slowing down of the information propagation. Therefore, a sufficient condition for ballistic propagation is that no such disruptive rare regions occur, i.e., $q(1/\zeta; \sigma, \epsilon) = 1$.

The sample variance of normal random variables $\mathcal{N}(0, \sigma^2)$ satisfy the Chi-squared distribution. Hence for n normal random samples we have

$$(n-1)\frac{s_n^2}{\sigma^2} \sim \chi_{n-1}^2 \tag{1.7}$$

where χ_{n-1}^2 is the Chi-squared distribution of $(n-1)$-th order and the sample variance is defined as,

$$s_n^2 = \sum_{i=1}^{n} \frac{(x_i - \bar{x})^2}{n-1} \tag{1.8}$$

We are interested in finding the probability that a n-sized region has locally larger variance than the putative critical disorder. Hence, the probability of a sample of size n (in our picture, a continuous region of n spins) having variance exceeding the subballistic-logarithmic critical transition strength ϵ^2 is obtained from the cumulative distribution function of the Chi-squared distribution,

$$\begin{aligned} p(n;\sigma,\epsilon) &= \text{Prob}(\sigma_n^2 \geq \epsilon^2) \\ &= 1 - \chi^2_{(n-1)|CDF}\left(\frac{n\epsilon^2}{\sigma^2}\right) \\ &= 1 - \frac{\gamma(\frac{n-1}{2}, \frac{n\epsilon^2}{2\sigma^2})}{\Gamma(\frac{n-1}{2})} \end{aligned} \tag{1.9}$$

Here, $\Gamma(s) = \int_0^\infty t^{s-1}e^{-t}dt$, is the Gamma function and $\gamma(s,x) = \int_0^x t^{s-1}e^{-t}dt$ is the incomplete Gamma function. For the 'bad bubbles' considered in the paper, we have

$$\begin{aligned} p(\alpha\log(L);\sigma,\epsilon) &= 1 - \frac{\gamma\left(\frac{\alpha\log(L)-1}{2}, \frac{\alpha\log(L)\epsilon^2}{2\sigma^2}\right)}{\Gamma\left(\frac{\alpha\log(L)-1}{2}\right)} \\ &\approx 1 - \frac{\gamma\left(\frac{\alpha\log(L)}{2}, \frac{\alpha\log(L)\epsilon^2}{2\sigma^2}\right)}{\Gamma\left(\frac{\alpha\log(L)}{2}\right)} \end{aligned} \tag{1.10}$$

Using the Chernoff bound we can bound this probability as

$$p(\alpha\log(L);\sigma,\epsilon) \leq \beta^{\alpha\log(L)}, \tag{1.11}$$

where $\beta = \left(\frac{\epsilon^2}{\sigma^2}e^{1-\frac{\epsilon^2}{\sigma^2}}\right)^{1/2}$. Hence, the probability $q(\alpha;\sigma,\epsilon)$ that there is no 'bad bubble' in a

length L chain satisfies,

$$\begin{aligned} q(\alpha;\sigma,\epsilon) &\geq \lim_{L\to\infty} \left(1-\beta^{\alpha\log(L)}\right)^{\frac{L}{\alpha\log(L)}} \\ \log q(\alpha;\sigma,\epsilon) &\geq \lim_{L\to\infty} \frac{L}{\alpha\log(L)} \log\left(1-\beta^{\alpha\log(L)}\right) \end{aligned} \tag{1.12}$$

We have thus proven the following inequality for the probability q of ballistic information transport (no 'bad bubble'),

$$q(1/\zeta;\sigma,\epsilon) \geq \left(1-\beta^{\log(L)/\zeta}\right)^{\frac{\zeta L}{\log(L)}} \tag{1.13}$$

where $\beta = \left(\frac{\epsilon^2}{\sigma^2} e^{1-\frac{\epsilon^2}{\sigma^2}}\right)^{1/2}$, with the specific choice $\alpha = 1/\zeta$. Since q is a probability, $\log(q) \in (-\infty, 0]$. The above bound is thus tight when the right hand side is 0. The prefactor $L/\alpha\log(L) \to \infty$ in the limit, so the right hand side can be zero only when $(L/\alpha\log(L))\log\left(1-\beta^{\alpha\log(L)}\right) \to 0$. Expanding the logarithm (which is justified as $\beta < 1$ for $\epsilon > \sigma$), we obtain

$$1 + \alpha\log(\beta) < 0 \tag{1.14}$$

i.e., $\beta < e^{-\frac{1}{\alpha}}$.

We now explain the meaning of ζ in our discussion of the rare region model. In the discussion so far, $q(\alpha;\sigma,\epsilon)$ is the probability of having no $\alpha\log(L)$ sized rare regions in our spin chain. From the definition of rare region (any region whose local disorder exceeds ϵ), it is clear that q is a cumulative probability, $q = \int_\epsilon^\infty d\epsilon' f(\alpha;\sigma,\epsilon')$, where $f(\alpha;\sigma,\epsilon')d\epsilon'$ is the probability that there exist no $\alpha\log(L)$ sized regions whose local disorder is exactly ϵ'. Corresponding to ϵ', there will be a logarithmic light cone, with an inverse length scale $\zeta'(\epsilon')$. The averaged time for information

propagation across a chain with one rare region then, is given by,

$$\begin{aligned} t &\sim (L - \alpha \log(L))/v_B + \int_{\epsilon}^{\infty} d\epsilon' f(\alpha; \sigma, \epsilon') e^{\zeta' \alpha \log(L)} \\ &\sim (L - \alpha \log(L))/v_B + e^{\zeta \alpha \log(L)} \end{aligned} \tag{1.15}$$

where we have defined ζ as an averaged length scale associated with a rare region. In the paper we have argued that $\zeta\alpha < 1$ corresponds to a ballistic phase, which, along with the earlier condition with respect to α, gives,

$$\frac{\epsilon^2}{\sigma^2} e^{1-\frac{\epsilon^2}{\sigma^2}} < e^{-2\zeta}. \tag{1.16}$$

Since ζ is finite, there exists a finite σ^*, below which all σ satisfy the sufficient condition for ballistic transport Eq. 1.16, leading to a finite window of a ballistic phase.

It is worth noting that the model only shows the existence of a ballistic phase for $\sigma < \sigma^*$. The inequality is a sufficient, but not a necessary condition for ballistic transport; hence σ^* should not be mistaken with the critical ballistic-subballistic transition. Furthermore, in our numerics, we can't resolve ϵ, where sub-ballistic becomes logarithmic (in a finite system data, a soft power law is difficult to resolve from a logarithm), or ζ which will be a complicated averaged scale. Hence we can't quantitatively verify Eq. 1.16. A more careful study of the difference between the average time $\bar{t}$ and the typical time $\exp(\overline{\log t})$ should be considered to further characterize the ballistic to sub-ballistic transition.

1.6 Conclusions

We studied the ballistic to sub-ballistic crossover in operator spreading for large interacting disordered spin systems using MPO dynamics, for different spin Hamiltonians and error models. Our numerical results establish the existence of a ballistic phase and a sharp transition to a subballistic phase. The numerical observation of fluctuations of the wavefront motivate a simple model of rare regions which explains aspects of this transition. Natural extensions of the rare region model would be to incorporate the effects of wavefront broadening into the analysis. Also our work demonstrates a separation between information propagation and spin transport [96, 103], which could be an interesting direction of future study.

Chapter 2: Information scrambling at finite temperature in local gapped quantum systems

"There is beauty everywhere," said Big Panda, "but sometimes it's difficult to see."

- Big Panda and Tiny Dragon, James Norbury.

2.1 Introduction

Quantum information scrambling has emerged as an important dynamical feature of interacting quantum systems ranging from tabletop atomic systems to toy models of black holes [11, 63, 64, 65, 109, 110, 111]. Scrambling refers to the way a closed chaotic quantum system delocalizes initially simple information such that it becomes inaccessible to all local measurements. Scrambling can be identified as a quantum analogue of the classical butterfly effect, as first discussed in a condensed matter context [66], and more recently explored in the context of holographic field theories and many-body systems such as the SYK model [12, 24, 112, 113]. Scrambling can be studied for generic quantum systems by calculating out-of-time-ordered correlation (OTOC) functions, which, for geometrically local systems, gives rise to a state dependent velocity of information propagation—the butterfly velocity [13, 100, 114]. OTOC functions can be measured for engineered quantum many body systems in the lab, with many proposals [79, 115, 116,

117, 118, 119, 120, 121, 122] and subsequent experiments [123, 124, 125, 126, 127, 128, 129].

For quantum systems at the semiclassical limit, the deviation of an OTOC function from its initial value grows exponentially with time, with an exponent that can be viewed as a quantum analogue of the classical Lyapunov exponent λ_L [12], although the connection to classical chaos is subtle [130, 131]. Deforming the contour along which path integrals are evaluated is a general technique one can use to regulate quantities in field theory and it leads to different choices of OTOCs at finite temperature, based on the contour on the thermal circle used to define it. One particular choice of contour leads to a well-behaved version of the OTOC that obeys a bound [20], $\lambda_L \leq 2\pi/\beta$, where β is the inverse temperature. This bound was later understood in the more general context of the growth of operator complexity and thermalization [132, 133]. However, exponents arising from other versions of OTOCs can have a strong dependence on the choice of contour [134, 135].

In this chapter, we systematically study the temperature and contour dependence of OTOCs in generic quantum systems with spatial locality and a mass gap. Our motivation for this study comes from two directions. First, we want to understand possible contour dependence of OTOCs in a non-perturbative calculation. Second, we want to understand the temperature dependence of various characteristics of scrambling as a system is cooled below its mass gap. At high temperature, we indeed find contour dependence of the OTOC. At low temperature, where our expectation is that the physics is that of a weakly interacting dilute gas of quasiparticle excitations, we find that the rate of growth of scrambling is exponentially suppressed while the butterfly velocity is of order the sound speed. Technically, these results are obtained by studying a gapped spin chain at large size numerically and a field theory model analytically. The remainder of the introduction provides neccessary background material for our study.

2.1.1 Squared commutators

Consider a local quantum system, where the dynamical degrees of freedom are operators supported on local subsystems labelled by their positions in real space, $\mathbf{x}$. An operator $W_{\mathbf{0}}$ originally localized at position $\mathbf{0}$ can spread in real space under a Heisenberg time evolution that generates $W_{\mathbf{0}}(t)$. The extent of its physical spreading can be diagnosed by taking its commutator with another local operator $V_{\mathbf{x}}$, i.e. $[W_{\mathbf{0}}(t), V_{\mathbf{x}}]$. The squared commutator, evaluated on a particular choice of initial state, can quantify the extent of operator growth, as it is a valid norm of the commutator.

However, in a quantum system at a finite temperature, T, this norm can be evaluated in several ways. Let us denote $\rho = e^{-\beta H}/Tr(e^{-\beta H})$ as the thermal density matrix ($\beta = 1/T$ is the inverse temperature). For any $0 \leq \alpha \leq 1$,

$$\mathcal{C}_{(\alpha)}(t, \mathbf{x}) = Tr\left(\rho^{\alpha}[W_{\mathbf{0}}(t), V_{\mathbf{x}}]^{\dagger}\rho^{(1-\alpha)}[W_{\mathbf{0}}(t), V_{\mathbf{x}}]\right), \tag{2.1}$$

is a Frobenius norm of the thermally smeared commutator $\rho^{(1-\alpha)/2}[W_{\mathbf{0}}(t), V_{\mathbf{x}}]\rho^{\alpha/2}$, which encodes a notion of the size of operator spreading.

Two choices of the squared commutator which have been studied in the literature, are the 'regulated' squared commutator, $C_r(t, \mathbf{x}) = \mathcal{C}_{1/2}(t, \mathbf{x})$, and the 'unregulated' squared commutator, $C_u(t, \mathbf{x}) = \mathcal{C}_1(t, \mathbf{x})$. When the expressions of the regulated and unregulated squared commutators are expanded, they contain terms which are thermally smeared versions of out of time ordered four point correlators of the form $W_{\mathbf{0}}(t)V_{\mathbf{x}}W_{\mathbf{0}}(t)V_{\mathbf{x}}$, evaluated on two distinct thermal contours, as shown in Fig. 2.1 a and b. In this work, we study these two squared commutators,

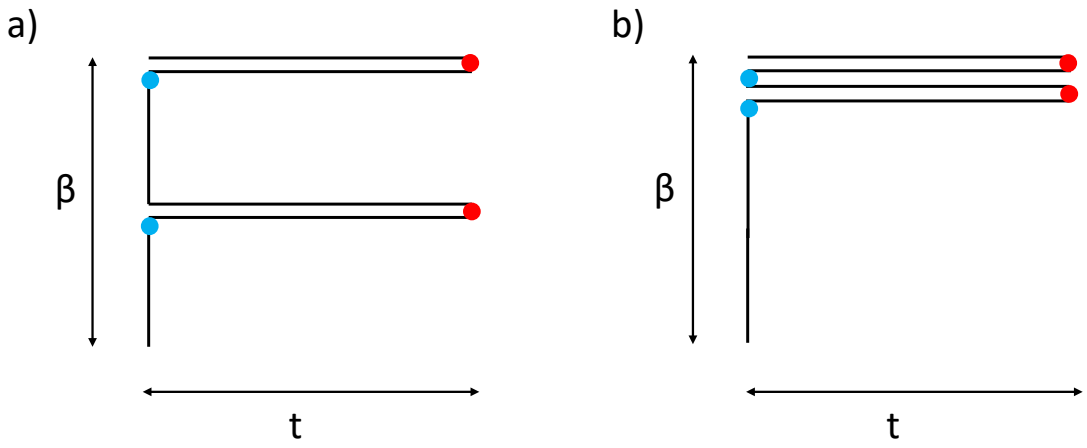

Figure 2.1: Contour for the (a) regulated and (b) unregulated out of time ordered correlators. The red points refer to the time evolved operators $W_{\mathbf{0}}(t)$, and the blue points refer to the probe operators $V_{\mathbf{x}}$. The regulated and the unregulated correlators are distributed in distinct ways along the thermal circle.

and explore the difference in the physics that they capture [134, 135].

2.1.2 Lyapunov exponent, butterfly velocity, and wavefront broadening

The squared commutator in holographic models, or in quantum systems with a semiclassical limit, grows exponentially at early times with a 'Lyapunov exponent' λ_L, $\mathcal{C}(t) \sim e^{\lambda_L t}$. In spatially local systems, the time argument can be replaced by the appropriate $t \to t - x/v_B$, where v_B is a velocity determining the speed of information scrambling, called the 'Butterfly velocity' [13, 114, 136, 137]. The butterfly velocity is state dependent analogue of the microscopic Lieb Robinson velocity [14].

However, interacting local quantum systems which are not in a semi-classical limit (that is, the number of local degrees of freedom is finite, and not large as in the case for systems with a semi-classical limit), show a qualitatively different behavior. As studies of random unitary circuits [15, 108], stochastic local Hamiltonian spin models [138], and numerical studies on

deterministic quantum spin models [2, 100, 139, 140] have shown, the near wave-front behavior of the squared commutator is,

$$\mathcal{C}(t, \mathbf{x}) \sim \exp\left(-\lambda \frac{(x/v_B - t)^{1+p}}{t^p}\right), \text{ for } x \gtrsim v_B t. \tag{2.2}$$

This behavior satisfies a ballistically growing and a broadening operator wavefront, $x \sim v_B t + \#t^{p/(1+p)}$, where v_B is the Butterfly velocity and p is the broadening coefficient. For $p = 1$, the broadening is diffusive, which is observed in the case of random unitary circuits [15, 108]. This ballistic-diffusive form doesn't exhibit an exponential 'chaotic' behavior. Until now, most studies of broadening were done at infinite temperature. However, unlike the 'Lieb Robinson velocity' of local quantum systems, the 'Butterfly velocity' is a state dependent information spreading velocity. The Lieb Robinson bound is formulated in terms of the matrix norm of the commutator, while the squared commutator is evaluated for a particular state. Since we can choose the state to be a Gibbs state at a particular temperature, the butterfly velocity derived from the squared commutator has a natural temperature dependence. Furthermore the Lyapunov exponent and butterfly velocity could depend non-trivially on the choice of the contour. In this paper we explore these questions through a combination of numerical studies on quantum spin systems and analytical studies of tractable semi-classical field theory models.

2.1.3 Summary of the results

In this chapter we use a combination of numerical and analytical techniques to study the temperature and contour dependence of squared commutator in strongly interacting, gapped, local quantum systems. We do this firstly using a novel numerical technique based on matrix

product operator (MPO) representation of Heisenberg operators to study scrambling in 1D quantum spin chains. We can access both the regulated and unregulated squared commutators in the early growth regime for a gapped, local Hamiltonian for large spin chains of ≈ 200 spins up to long times $t \sim 100J^{-1}$, where J^{-1} is the interaction scale of the Hamiltonian. Next, we study the low temperature behavior of the squared commutator in the paramagnetic phase of the $2+1D$ non-linear $O(N)$ model using perturbative calculation of the ladder-sum for the OTOC functions. We first list out the important results and the structure of the paper,

1. In Sec. 2.2, we introduce the MPO numerical technique and apply it to calculate both the regulated and unregulated squared commutators in 1D mixed field Ising Hamiltonian. We observe a broadening of the expanding operator wave-front at all temperatures. This broadening behavior had been previously observed for the infinite T ensemble [15, 100, 108, 139]; but here we confirm the persistence of the broadening behavior even at low temperatures.

For the regulated squared commutator we notice a strong temperature dependence of the broadening coefficient and butterfly velocity. We observe that at temperatures lower than the gap, $\beta > m^{-1}$, the butterfly velocity is consistent with a power-law ($(\beta m)^{-a}$ with $a > 0$) behavior.

For the unregulated squared commutator, on the other hand, we observe that the butterfly velocity and the broadening coefficient have no observable temperature dependence, and in fact remain constant even as the temperature is tuned from $\beta = 0$ to $\beta > m^{-1}$. This confirms a strong contour dependence of the OTOC [134, 135]. We also numerically study the contour dependence of $\partial_t C_{(\alpha)}(t, \mathbf{x})$ and make a comparison with the chaos bound to demonstrate that the bound doesn't apply to these squared commutators.

2. While the MPO technique can access temperatures below the gap, it is challenging to access very low temperatures. In order to calculate the temperature dependence at low tempera-

tures, in Sec. 2.3, we calculate the behavior of the regulated and unregulated squared commutator in the paramagnetic phase of the $2+1D$ non-linear $O(N)$ model. This is a gapped strongly interacting theory for which we can analytically calculate the scrambling behavior at large N using a diagrammatic ladder technique. We find that the Lyapunov exponent is $\lambda_L \sim e^{-\beta m}/\beta$, and the butterfly velocity is $v_B \sim (\beta m)^{-1/2}$ at low temperatures such that $\beta >> m^{-1}$. This shows that the butterfly velocity has the same scaling as the speed of sound of semiclassical massive particles. The field theory calculation can't, however, reproduce the broadening behavior or the contour dependence, indicating that finite N corrections need to be taken into account for those features.

3. In Sec. 3.5, we summarize our results and compare the numerical and analytical approaches. We discuss the relation between the temperature dependence of butterfly velocity obtained in this paper with a recently derived temperature dependent bound on butterfly velocity [140]. The bound is not sensitive to the contour dependence, and we show that it is consistent with temperature dependence of the butterfly velocities observed in Sec. 2.2 and 2.3.

2.2 Matrix product operator method for numerical calculation of scrambling

We now numerically study scrambling in a spatially local quantum system, consisting of tensor product of finite dimensional local Hilbert spaces, like spins on a lattice. The Hamiltonian is assumed to be a sum of geometrically local terms, and the lattice has a well defined position label.

Operators acting on vectors in a Hilbert space $\mathcal{H}$ can be viewed as vectors on a 'doubled' Hilbert space $\mathcal{H}_L \otimes \mathcal{H}_R$. Here the tensor product structure refers to the two copies - 'left' and

'right' - of the state Hilbert spaces. We introduce the notation $|..)$ to denote the operator as a vector. A local operator acting on the $\mathbf{0}$ position in the lattice, $|W_{\mathbf{0}})$, can be time evolved in the Heisenberg picture,

$$|W_{\mathbf{0}}(t)) = |U_t W_{\mathbf{0}} U_t^\dagger) = e^{it(H_L \otimes I - I \otimes H_R^*)} |W_{\mathbf{0}}). \tag{2.3}$$

One can now probe the evolved operator using a second local operator at a position $\mathbf{x}$ by constructing its commutator,

$$|O(\mathbf{x}, t)) = |[W_{\mathbf{0}}(t), V_{\mathbf{x}}]) = (1 \otimes V_{\mathbf{x}}^T - V_{\mathbf{x}} \otimes I)|W_{\mathbf{0}}(t)), \tag{2.4}$$

The squared commutator can be obtained by squaring this operator which measures the extent of quantum information scrambling in the system. The α dependent squared commutator defined in Eq. 2.1 can be expressed as a norm of an operator state, $\mathcal{C}_{(\alpha)} = (O_\alpha(\mathbf{x}, t, \beta)|O_\alpha(\mathbf{x}, t, \beta))$, where,

$$|O_\alpha(\mathbf{x}, t, \beta)) = |\rho^{(1-\alpha)/2} O(\mathbf{x}, t) \rho^{\alpha/2}). \tag{2.5}$$

2.2.1 Model and numerical method

We consider the mixed field quantum Ising model,

$$H = -\frac{1}{E_0} \left(J \sum_{i=1}^{L-1} Z_i Z_{i+1} + h_x \sum_{i=1}^{L} X_i + h_z \sum_{i=1}^{L} Z_i \right) \tag{2.6}$$

with $E_0 = \sqrt{4J^2 + 2h_x^2 + 2h_z^2}$, on a one dimensional lattice. The X and Z matrices are the usual Pauli matrices. The parameters chosen are, $J = 1, h_x = 1.05, h_z = 0.5$. Time is measured in the units of $J^{-1} = 1$. This is a gapped system, and the spectral gap between the ground state and the

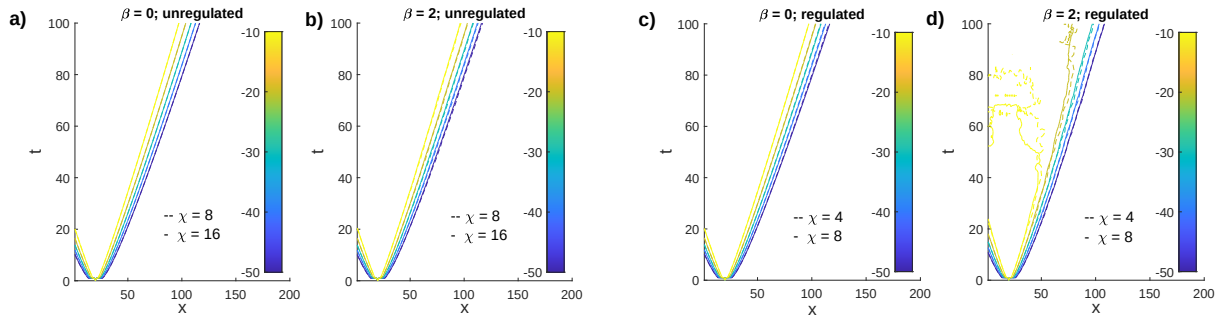

Figure 2.2: The contours of the logarithm of the regulated and unregulated squared commutator at different temperatures - a) $\beta = 0$ (unregulated), b) $\beta = 2$ (unregulated), c) $\beta = 0$ (regulated) and d) $\beta = 2$ (regulated) are shown. For the unregulated case bond dimensions, $\chi = 8$ and $\chi = 16$, and for the regulated case bond dimensions, $\chi = 4$ and $\chi = 8$ are considered. The data shows convergence even at low temperatures for low values of the squared commutator. We demonstrate in the Sec. 2.2.5, in Fig. 2.7, that the data has converged with bond dimension for $\log C_r < -30$, and for $\log C_u < -15$.

first excited state is ~ 1.13 as extracted from small size exact diagonalization.

We want to calculate $C_{u,r}(t, x)$ for large system sizes and upto long times, and we employ the Matrix product operators (MPO) based technique to time evolve operator states which extends the time dependent density matrix renormalization group (t-DMRG) technique [104, 105, 106, 107] to super-operators [100]. We first time evolve the local operator W by doing time evolution using super-operator $H \otimes I - I \otimes H^*$ on the operator state, following Eq. 2.3. We also obtain $|\rho)$ by evolving the identity $|I)$ operator state in imaginary time. Now, we can construct the operator state $|O_\alpha(t, \mathbf{x}, \beta))$ as defined in Eq. 2.5, for $\alpha = 1/2(1)$, and its norm squared is the required (un)regulated squared commutator.

In the MPO based method, at each Trotter step, we must truncate the MPO to a fixed bond dimension, thereby introducing errors. However, we will demonstrate that our numerical procedure converges (for small values of the squared commutator) at large system sizes ($L \sim 200$) and upto long times $t \sim 100$, even at low temperatures, which makes it a powerful method to study the temperature and contour dependence of quantum information scrambling.

We consider a $L = 200$ spin chain with the mixed field Ising Hamiltonian as in Eq. 2.6. We start with an operator X_{20}, a Pauli X operator localized at the site 20, and construct the squared commutator with Z operators at all sites of the chain. We perform the MPO-TEBD method with Trotter steps, $\delta t = 0.005$ for time evolution (to generate $X(t)$) and $\delta\beta = 0.05$ for imaginary time evolution (to generate ρ), for bond dimensions $\chi = 4, 8$ (regulated) and $\chi = 8, 16$ (unregulated). To calculate the regulated and unregulated squared commutators, we need to construct the MPOs $|O_{1/2}(t, x, \beta))$ and $|O_1(t, x, \beta))$, as defined in Eq. 2.5, respectively. For $|O_{1/2})$ we need to perform two MPO multiplications, $\rho^{1/4} \to [X_{20}(t), Z_x]\rho^{1/4} \to \rho^{1/4}[X_{20}(t), Z_x]\rho^{1/4}$, while for $|O_1)$, we need to perform one MPO multiplication, $\rho^{1/2} \to [X_{20}(t), Z_x]\rho^{1/2}$. The details of the numerical implementation, which include a comparison to exact diagonalization, discussions on convergence with bond dimension, and the fitting procedure, are provided in a later section, 2.2.5.

A heuristic justification of why the MPO approximation works is as follows - it was shown in [100] that the commutator $[X(t), Z_x]$ has a small operator entanglement outside the light-cone. It is also well understood that the thermal density matrix ρ satisfies an area law in mutual information [141], and hence is expected to be reliably approximated by a low bond dimension matrix product operator. These two arguments imply that the operator $|O_\alpha(t, \mathbf{x}, \beta))$ as defined in Eq. 2.5, which is an MPO multiplication of powers of ρ and the commutator $[X(t), Z_x]$, should have a small operator entanglement outside the light-cone (i.e. when the squared commutator is small), and hence can be well approximated by a low bond dimension MPO.

As has been pointed out previously, in [2, 100, 142], the MPO-TEBD method can capture the qualitative features of scrambling only if the scrambling data has converged with bond dimension. We ensure that all our further analysis is done on scrambling data only in the spatio-temporal domain where it has converged with bond dimension. We plot the contours of the

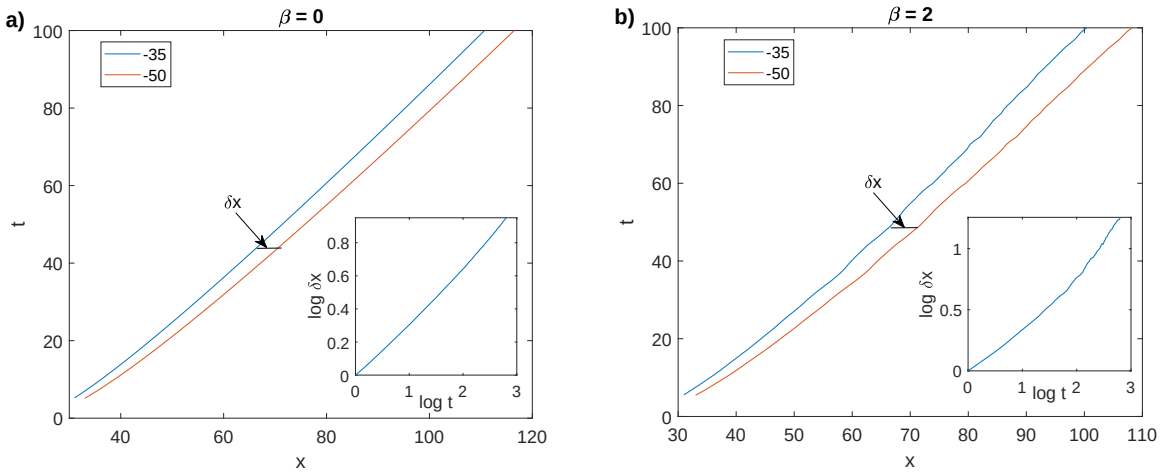

Figure 2.3: We extract the contours of $\log C_r = -35$ and -50 at different temperatures, for the data with $\chi = 8$. From the contours we extract δx, which is the spatial distance between the two contours. The time dependence of δx is shown in the inset; the fact that it is increasing with time demonstrates a broadening of the wavefront. The broadening persists even at a) high temperature $\beta = 0$ and b) low temperature $\beta = 2$.

squared commutator in Fig. 2.2, and demonstrate that the contours converge very well for small values of the squared commutator. The shape of the contours, where the data has converged, show that the wavefront propagates ballistically with a velocity.

2.2.2 Broadening of the wavefront

Without any numerical fitting, we demonstrate the broadening behavior of the operator wavefront even at low temperatures in the Fig. 2.3. We extract the spatial separation δx between two chosen contours of the $\log C_r$, and plot its time dependence in the insets of Fig. 2.3. A positive (and an increasing) slope implies a broadening behavior. In Fig. 2.3, we show data for the regulated case, but a similar study for the unregulated squared commutator also demonstrates a broadening behavior. Thus, the Figs. 2.2 and 2.3 together show that the early time (before the light-cone is reached) behavior of the squared commutator has a ballistic growth and a broadening wavefront.

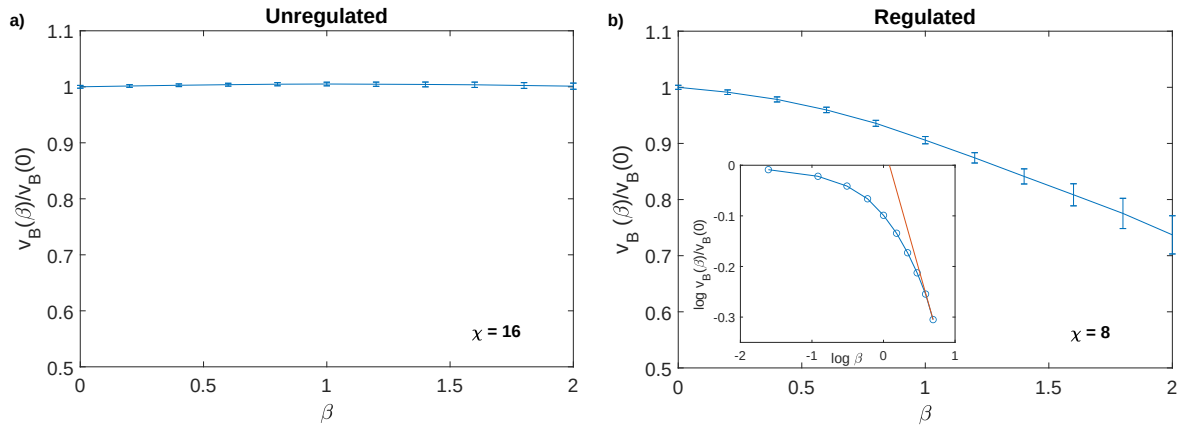

Figure 2.4: **a)** We plot the extracted $v_B(\beta)/v_B(0)$ for the unregulated case, as a function of β. The data is for $\chi = 16$ bond dimension. The butterfly velocity is practically constant at all temperatures. **b)** For the regulated case, we plot the normalized v_B, (i.e. $v_B(\beta)/v_B(0)$), extracted from the $\chi = 8$ data, as a function of β. In the inset, in the log-log scale, we demonstrate that the low temperature behavior of v_B is consistent with $\beta^{-1/2}$ (which is the slope of the red line plotted.).

In [100, 102, 138], it was argued that the squared commutator, near the wavefront, when $C(x,t) << 1$, can be captured by the following ansatz,

$$C(x,t) \sim exp\left(-\lambda_p \frac{((x-x_0)/v_B - t)^{1+p}}{t^p}\right). \tag{2.7}$$

One can identify the broadening coefficient p as,

$$\frac{\delta \log \delta x}{\delta t} \sim \frac{p}{p+1}. \tag{2.8}$$

We now fit our data to the ansatz in Eq. 2.7 to extract the Lyapunov exponent, butterfly velocity and broadening coefficient.

2.2.3 Temperature dependence of butterfly velocity

We extract the butterfly velocity, velocity dependent Lyapunov exponent and the broadening coefficient from the obtained numerical data by fitting them to the near wave-front ansatz in Eq. 2.7. In Fig. 2.4a, we plot fitted $v_B(\beta)/v_B(0)$ as a function of β for the unregulated case, and see that the fitted butterfly velocity has almost no discernible temperature dependence. In Fig. 2.4b, we plot the same for the regulated case, and notice a strong temperature dependence. The low temperature behavior is consistent with a power law decrease in the butterfly velocity as a function of β, as is shown in the inset of Fig. 2.4b. In Sec. 2.3, we show that at the low temperature limit of an analytically tractable field theory model with a mass gap m, the butterfly velocity has a temperature scaling which is the same as the equipartition behavior - $\sqrt{1/\beta m}$. The asymptotic low temperature behavior in the MPO calculation (even though the temperatures we access here are not very low compared to the spectral gap) is close to the $\sqrt{1/\beta m}$ behavior, as is demonstrated in Fig. 2.4b.

In a later section, 2.2.5, we also study the temperature dependence of the broadening coefficient p. In Fig. 2.9, we show that p for the unregulated case has a very weak dependence on temperature and remains practically constant as the temperature is lowered. The regulated case, however, has an increasing trend for p with decreasing temperature.

2.2.4 Contour dependence and chaos bound

For a symmetrically defined out of time ordered correlation function, there exists the Maldacena-Shenker-Stanford (MSS) chaos bound $\lambda_L \leq 2\pi/\beta$ [20]. The symmetric OTOC is

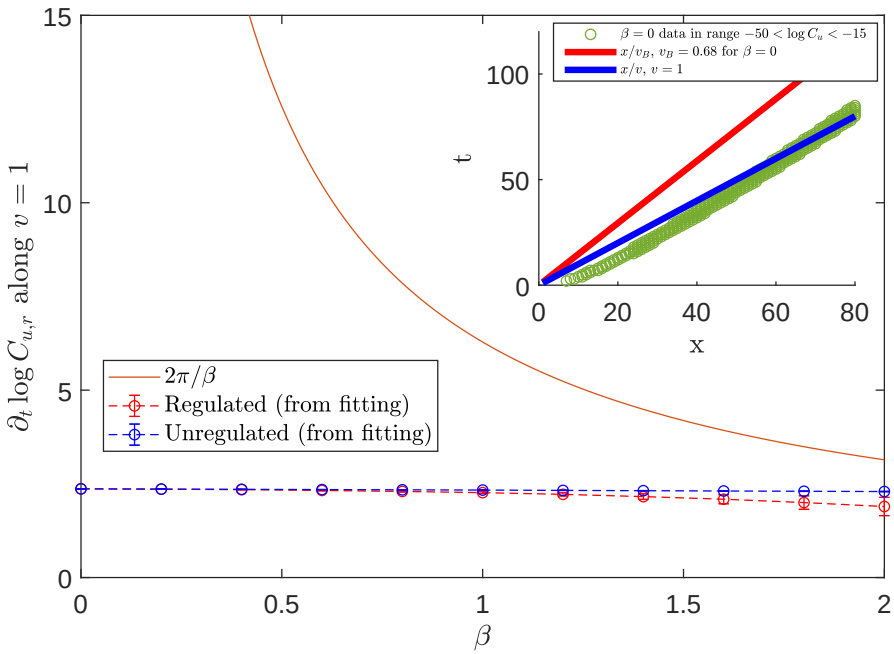

Figure 2.5: From the fitting of the obtained data of the regulated and unregulated squared commutators, we obtain the $\partial_t C_{u,r}$ from the near wavefront ansatz, along a 'ray' $x = t$ and compare it against the 'bound on chaos' $2\pi/\beta$. In the inset, we show the 'ray' $x = vt$ at $v = 1$, and compare that to the butterfly velocity $v_B = 0.68$ at $\beta = 0$ for C_u.

defined as,

$$F(t, \mathbf{x}) = Tr\left(\rho^{1/4} V_{\mathbf{x}} \rho^{1/4} W_0(t) \rho^{1/4} V_{\mathbf{x}} \rho^{1/4} W_0(t)\right). \tag{2.9}$$

This is related to the regulated squared commutator, as the $C_r(t, \mathbf{x})$, when expanded,

$$C_r(t, \mathbf{x}) = 2\left(Tr\left(\rho^{1/2} V_{\mathbf{x}} W_0(t) \rho^{1/2} W_0(t) V_{\mathbf{x}}\right) - ReF(t + i\beta/4, \mathbf{x})\right). \tag{2.10}$$

Let's introduce a related quantity $F_d(t, \mathbf{x}) = Tr\left(\rho^{1/2} V_{\mathbf{x}} \rho^{1/2} V_{\mathbf{x}}\right) Tr\left(\rho^{1/2} W_0(t \rho^{1/2} W_0(t)\right)$. In [20], it was proven that the following bound exists,

$$\frac{\partial \log\left(F_d(t, \mathbf{x}) - F(t, \mathbf{x})\right)}{\partial t} \leq \frac{2\pi}{\beta}. \tag{2.11}$$

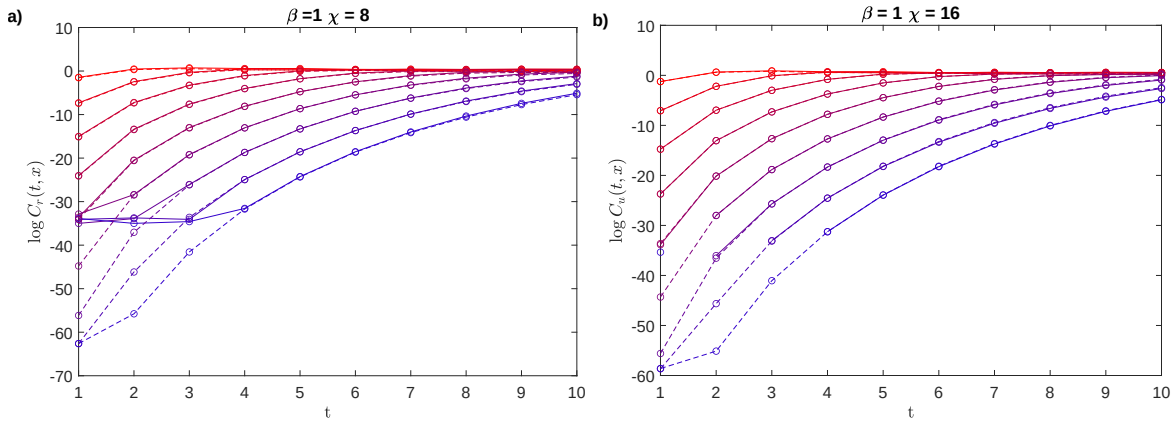

Figure 2.6: We demonstrate the convergence of our numerical method with exact diagonalization for small systems. a) For the regulated case, the $\chi = 8$ result has excellent agreement with exact diagonalization for $L = 10$ spin chain at $\beta = 1$. b) For the unregulated case, the same agreement is demonstrated for $\chi = 16$ result at $\beta = 1$.

Given this result, one might conjecture that the related quantity $\partial_t \log C_r(t, \mathbf{x})$ also satisfies the same bound. To study this, we can calculate $\partial_t \log C_r(t, \mathbf{x})$ along different 'rays' $x = vt$ [139]; if the near wavefront scrambling ansatz (Eq. 2.7) is satisfied, then $\partial_t \log C_{u,r}$ along a ray of velocity v is given by $\lambda_p(v/v_B - 1)^p(1 + pv/v_B)$. At sufficiently large v, this will violate the chaos bound. In Fig. 2.5, we plot the $\partial_t \log C_{r,u}(t, \mathbf{x})$, for a fixed 'ray' $x = t$, obtained from fitting of the unregulated and regulated cases to the ansatz, as a function of β and notice that the unregulated case is practically constant, and can violate the bound at lower temperatures. We confirm this without numerical fitting, in Sec. 2.2.5.1, Fig. 2.10. In Sec. 2.2.5.1 we also study $\partial_t \log C_{r,u}(t, x = vt)$, as a function of 'ray' velocity v. We find that at high ray velocities v, both $\partial_t \log C_r(t, vt)$ and $\partial_t \log C_u(t, vt)$ violate the bound. This shows that the MSS bound doesn't hold for the squared commutators we considered.

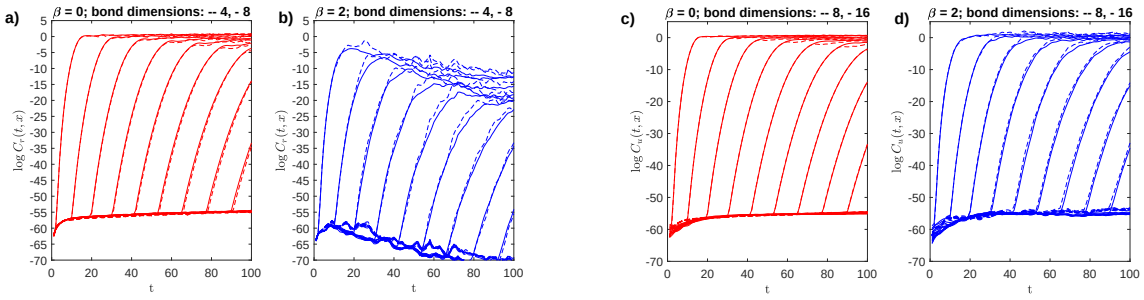

Figure 2.7: **a, b)** The log of the regulated squared commutator is plotted as a function of time, for the case of an operator $X_{20}(t)$ and Z_r, with $r = 30, 40, .., 200$, for bond dimensions $\chi = 4$ (dotted) and $\chi = 8$. The left and the right figures correspond to $\beta = 0$ (a) and $\beta = 2$ (b) respectively. Even at the low temperature, the data is seen to be converged for the range $-50 < \log C_r < -35$. Note we are able to access such small values accurately because we have expressed the regulated squared commutator as a square of a norm, and the norm can be estimated upto the numerical precision of MATLAB which is $\sim e^{-36}$, allowing us to push to around e^{-60} in precision. **c, d)** The log of the unregulated squared commutator is plotted as a function of time, for the case of an operator $X_{20}(t)$ and Z_r, with $r = 30, 40, .., 200$, for bond dimensions $\chi = 8$ (dotted) and $\chi = 16$. The left and the right figures correspond to $\beta = 0$ (c) and $\beta = 2$ (d) respectively. Even at the low temperature, the data is seen to be converged for the range $-50 < \log C_u < -15$.

2.2.5 Details of MPO numerics

In this section we provide some details of the numerical results shown in the previous sections. We first check the MPO TEBD numerical technique against exact diagonalization. In Fig. 2.6, we show the comparison of the MPO method to the results of exact diagonalization for a $L = 10$ sized spin chain. The machine precision of MATLAB being $\sim e^{-36}$, accuracy of $\log C$ from exact diagonalization is ~ -30. However, in our MPO numerical method, we express the squared commutator as the square of a norm, hence the precision is squared, with reliable numerical data of C down to $\sim e^{-60}$.

In order to demonstrate the convergence of the obtained squared commutator with bond dimension, we plot the log of the regulated and unregulated squared commutators as a function

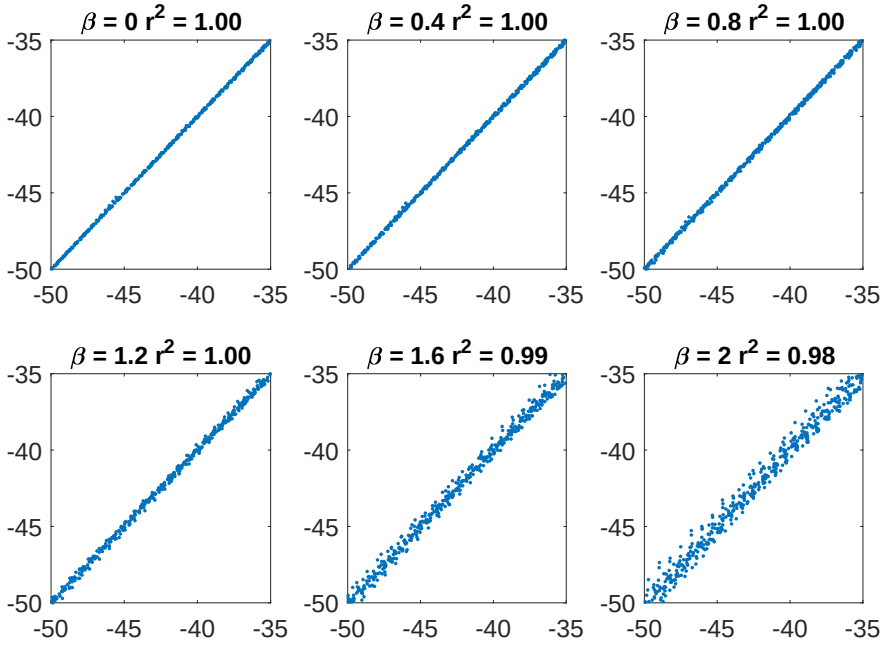

Figure 2.8: The collapse of the obtained regulated squared commutator for the data range $-50 < \log C_r < -35$, $20 < x < 200$ and $20 < t < 100$, to the near wave-front ansatz by least squared method. We have chosen this data range as we have confirmed the convergence of our numerical procedure in this range.

of time for different spatial differences in Fig. 2.7. Even without numerical fitting, it is clear from Fig. 2.7 that the regulated squared commutator has a strong temperature dependence, while the unregulated squared commutator is much less sensitive to temperature even when the temperature is tuned from $\beta = 0$ to $\beta = 2 > m^{-1}$, where the mass is the spectral gap ~ 1.13.

It is also seen that the early time data converges well with bond dimension. As has been noted before in [142], the qualitative lightcone behavior of the unconverged data obtained from the MPO method can be qualitatively different; hence for all our analysis and fitting we only use numerical data which are shown to converge.

We fit the converged data using least squared error method to the near wave-front ansatz of Eq. 2.7. The goodness of fit is studied in Fig. 2.8, where the data collapse to the fitted model is

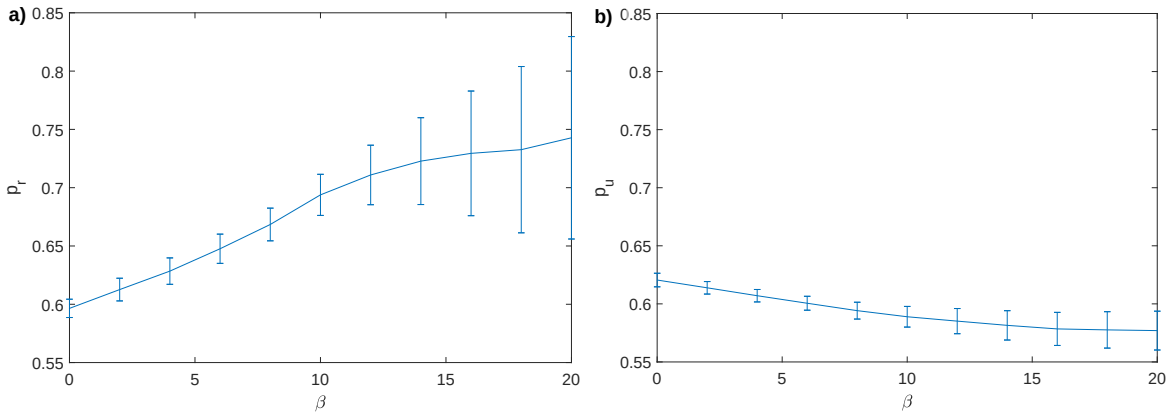

Figure 2.9: **a)** Broadening coefficient p obtained from the numerical fitting of regulated squared commutator is plotted as a function of β. **b)** p from fitting of the unregulated squared commutator is plotted as a function of β. The errorbars are from the 95% confidence intervals of the fit. To compare the regulated and the unregulated cases we have fixed the y-axis scales to be the same in the two plots.

shown at different temperatures.

The unregulated squared commutator was studied using a similar numerical technique in [140]. Our results indicate that the butterfly velocity obtained from the unregulated squared commutator is constant as function of temperature, even at temperatures lower than the gap, in contradiction with the indicated result from [140]. We checked the case for the $[Z(t), Z]$ type squared commutators as well, and our results are the same for both cases. In [140], the fitting was done for a much smaller spatio-temporal region $20 < x < 45$ and $1 < t < 5$ (in our units), and for a much smaller range $\log C_u > -22$, as compared to the situation considered here.

We also study the temperature dependence of the broadening coefficient obtained from the fitting in Fig. 2.9**a** (regulated) and Fig. 2.9**b**(unregulated). For the unregulated case, we see a fairly constant p which is insensitive to decreasing temperature. The regulated case shows an increasing trend with decreasing temperature.

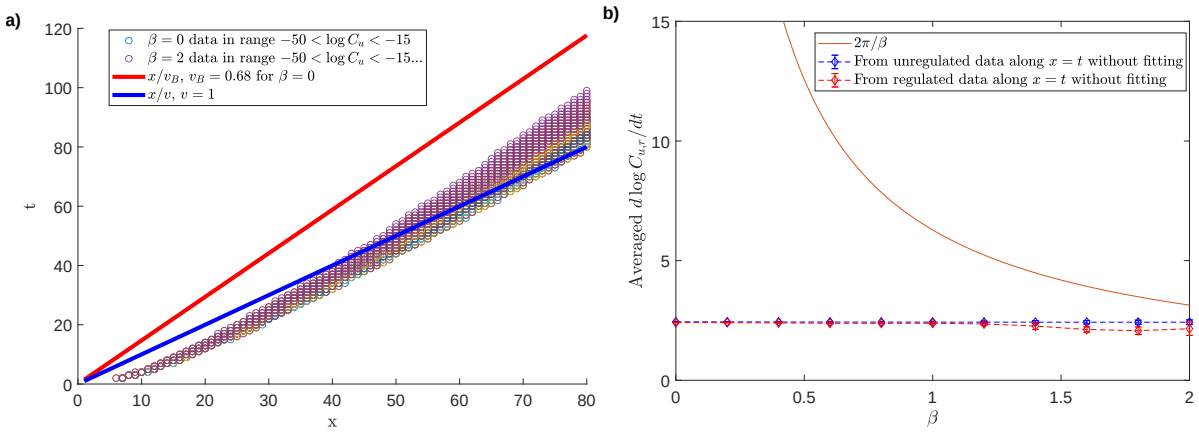

Figure 2.10: **a)** The data of the unregulated squared commutator for the data range $-50 < \log C_u < -15$, is picked out along the 'ray' $x = t$. $\partial_t C_u$ is evaluated in this domain, and the averaged $\partial_t C_u$ along $x = t$ is plotted as a function of β in b). Similarly data for the unregulated case can be picked up. **b)** The averaged $\partial_t C_{u,r}$ along $x = t$ is plotted as a function of β.

2.2.5.1 Contour dependence and chaos bound

We analyse in detail the contour dependence of $\partial_t C_{u,r}$, as was done in Sec. 2.2.4. In Fig. 2.10, we sketch how $\partial_t C_{u,r}$ is found without numerical fitting. We first pick out data along a 'ray' $x = t$, wherever the squared commutator has converged, and study $\partial_t C_{u,r}$ numerically. In Fig. 2.10b the averaged $\partial_t \log C_{u,r}$ along this ray is plotted as a function of β, and compared against the bound on chaos. The result is similar to Fig. 2.5, which was obtained by fitting to the near wavefront ansatz. Given the constancy of the unregulated case, the chaos bound could be violated at lower temperatures. These results are for a particular ray $x = t$, and as a function of β. We can also study $\partial_t \log C_{u,r}$ as function of the ray velocity v, where $x = vt$, for a particular β. If the near wavefront scrambling ansatz (Eq. 2.7) is satisfied, then $\partial_t \log C_{u,r}$ along a ray of velocity v is given by $\lambda_p(v/v_B - 1)^p(1 + pv/v_B)$. As v is increased beyond the v_B, the near wavefront ansatz predicts that the chaos bound can be violated. We test this numerically in Fig. 2.11, and we see that indeed $\partial_t \log C_{u,r}(t, vt)$ deviates from its near ansatz prediction at higher v.

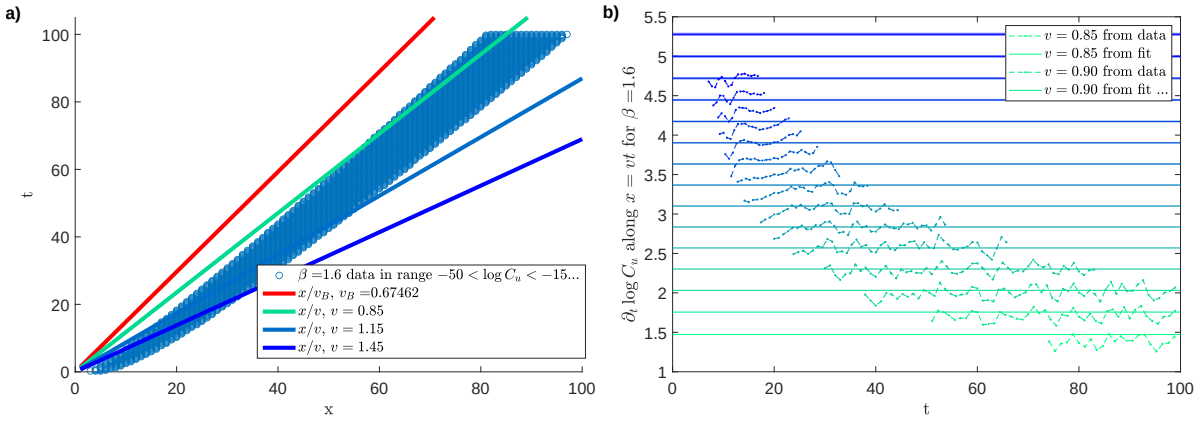

Figure 2.11: **a)** The data of the unregulated squared commutator for the data range $-50 < \log C_u < -15$, is picked up along different'rays' $x = vt$. This procedure can be repeated for the regulated case. **b)** For different v-s, $\partial_t \log C_u$ is plotted as a function of t (dots), and compared against the prediction from the near wavefront ansatz (constant lines whose thickness signify the confidence interval from the fitting to the ansatz). For lower v (i.e.) closer to the butterfly velocity v_B, the near wavefront behavior and the numerical result are the same, but they deviate for high ray velocities. The constancy of $\partial_t \log C_u$ along rays allow us to study their time averages as a function of β.

We also compare $\partial_t \log C_{u,r}(t, vt)$ against the chaos bound as a function of ray velocity v in Fig. 2.12, and see that for high ray velocities, the bound is violated for both the regulated and unregulated cases. Note however that the analysis on the data is done only on the domain where the data has converged and also lies along the rays - severely restricting the domain on which numerical differentiation can be reliably done to obtain $\partial_t \log C_{u,r}(t, vt)$.

2.2.6 Summary of findings from the MPO numerics

By studying squared commutators for large-sized, gapped spin chain which is spatially local, and has finite dimensional local Hilbert spaces, we got three distinctive features. First, the spatial locality leads to a ballistic wavefront propagating at the butterfly velocity, which has distinct temperature scaling for the regulated and unregulated cases. In the unregulated case the velocity is constant, while for the regulated case, the velocity decreases with temperature.

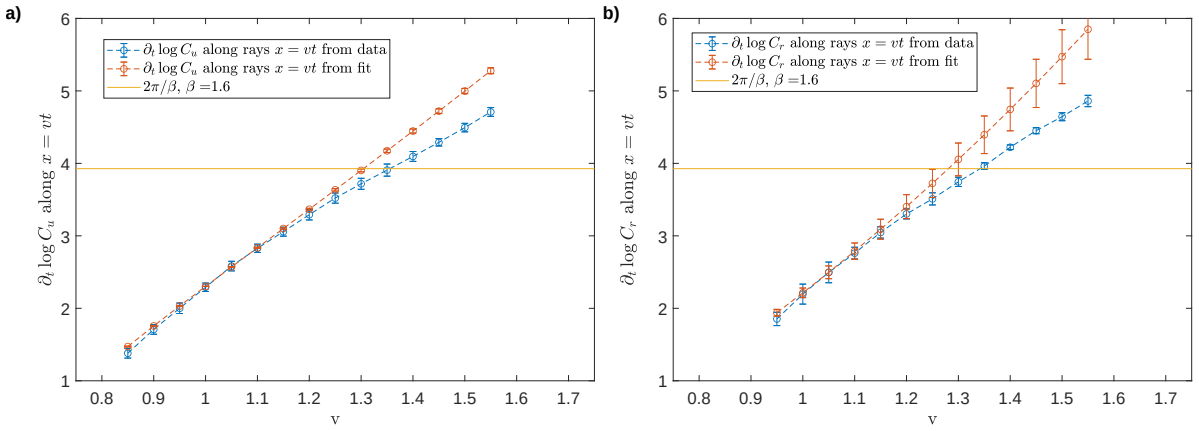

Figure 2.12: **a)** Time average of $\partial_t \log C_u(t, vt)$ is plotted for $\beta = 1.6$ as a function of ray velocity v (blue dots), and compared against the prediction from the near wavefront ansatz (red dots). **b)** Same analysis is done for the regulated case. The yellow line in both case refer to the chaos bound at $\beta = 1.6$.

Second, the wavefront broadens with time for both contours, and thus the squared commutator doesn't have pure exponential growth. Third, there are numerical indications that the chaos bound is not satisfied for these squared commutators.

In our numerical study we are limited by computational constraints and can't hope to access the true asymptotic scrambling behavior exactly. However, by restricting the analysis to only converged data, we have sufficient reasons to believe that the qualitative lessons hold true even asymptotically. As an example, the insets in Fig. 2.3 show that there is a drift in the broadening coefficient at longer times. But crucially, the drift is towards higher p, thus providing evidence that the phenomenon of broadening of wavefront persists even at the largest scales. Similarly, the qualitative evidences of temperature independence of scrambling for the unregulated case and the distinct temperature dependence for the regulated case are not dependent on the details of the numerical data, but are visible in Fig. 2.2 (see Fig.2.7 for another clarifying evidence).

Can we explain these behaviors using an analytically tractable model? In particular, can we understand the low temperature limit which is not accessible in the spin chain numerics? We

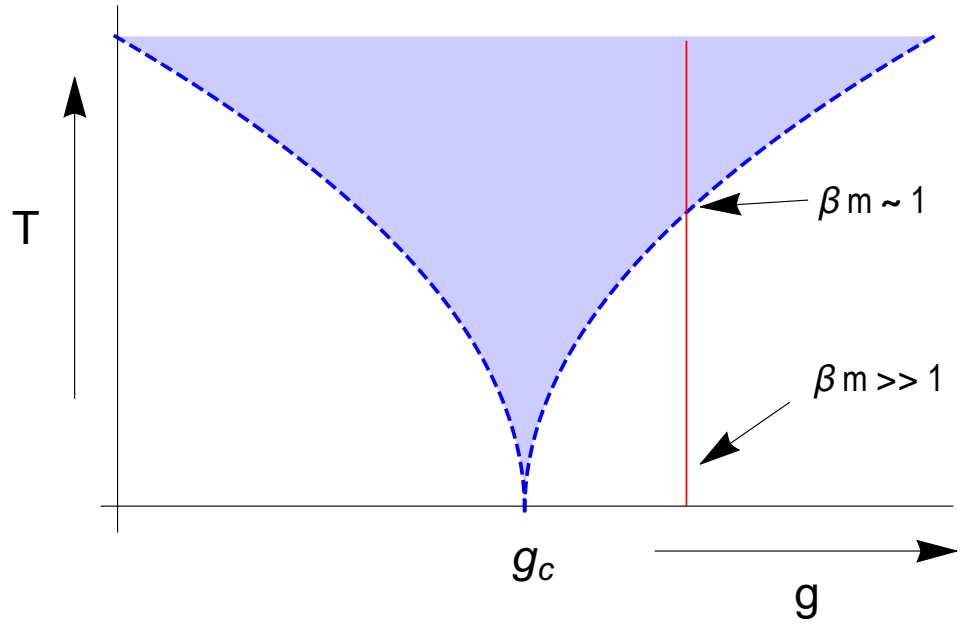

Figure 2.13: This is the critical phase diagram of the non-linear $O(N)$ model. The blue shaded region is controlled by the critical theory around the quantum critical point at $T = 0$ and $g = g_c$, while the dashed lines indicate a cross-over to the phases controlled by the symmetry of the zero temperature phases away from the critical point. We focus on the low temperature behavior of the symmetry unbroken paramagnetic phase $g > g_c$.

explore that in the next section, where we consider a non-linear $O(N)$ model in $2 + 1D$, which is spatially local, and solvable at large N. We study the scrambling behavior at low temperatures for the gapped phase of the model, and find that the butterfly velocity indeed varies as $\sqrt{T/m}$ at low temperatures. However, we will find that the field theory calculation doesn't show contour dependence or wavefront broadening.

2.3 Scrambling in the paramagnetic phase of the non-linear $O(N)$ model

The non-linear $O(N)$ model is a spatially local field theory of an $O(N)$ symmetric vector field ϕ_a, with $a = 1, .., N$. The theory is solvable at large N, and in this limit this model differs

from the spin chain in the fact that the local Hilbert space is not finite. Furthermore, to avoid complications in the field theory at $1+1D$ due to scattering, we study this model at $2+1D$, and we expect that dimensionality will not affect qualitative features of the temperature and contour dependence. The critical phase diagram [143] of this model is shown in Fig. 2.13. We analyse this model using Ladder sum techniques developed in [114, 144] (see also [145, 146, 147, 148]), and study both the temperature and contour dependence of the squared commutators.

The real time lagrangian for this theory is given by,

$$\mathcal{L} = \frac{1}{2}\left[\sum_a (\partial\phi_a)^2 - \frac{v}{2N}\left(\phi_a^2 - \frac{N}{g}\right)^2\right] \tag{2.12}$$

The action is given by $\int_x \mathcal{L}$, where the space-time integration $\int_x$ is over $2+1D$. We have set the speed of light c and $\hbar$ to 1. The parameter g (which determines the bare mass) can be tuned across a quantum critical point that occurs at $g = g_c$, and v is the self-interaction coupling constant. We consider the strong coupling (large v) and large-N limit. In [114], scrambling behavior was studied at the critical point g_c, by evaluating the regulated squared commutator using a perturbative ladder sum calculation with $1/N$ as the small parameter [114, 144]. Following the diagrammatic techniques used in these studies, we study scrambling on the paramagnetic phase of the model at $g > g_c$, where there are quasiparticle-like excitations with finite bare mass m. We study the temperature dependence of the scrambling in the low temperature limit $\beta m >> 1$.

The main goal of this section is to analytically obtain temperature dependence of the butterfly velocity at low temperatures. We didn't have access to very low temperatures in Sec. 2.2, and we intend to explore the regime $\beta m >> 1$ using this field theory model.

The generalized squared commutator in different contours given in Fig. 2.1 is given by,

$$C_\alpha(t,\mathbf{x}) = -\frac{1}{N^2}\sum_{ab} Tr\left(\rho^\alpha[\phi_a(t,\mathbf{0}),\phi_b(0,\mathbf{x})]\rho^{1-\alpha}[\phi_a(t,\mathbf{0}),\phi_b(0,\mathbf{x})]\right). \tag{2.13}$$

The regulated and the unregulated squared commutators are given by $C_r = C_{1/2}$, and $C_u = C_1$, respectively.

We summarize the results of this section before showing the explicit calculations. Using the ladder-sum calculation, we find that both the regulated and unregulated squared commutators have the following early time behavior,

$$C_{r,u}(t,\mathbf{x}) \sim \frac{1}{N} e^{\lambda_0\left(t-\frac{x^2}{v_B t}\right)}, \tag{2.14}$$

where the 'Lyapunov' exponent, $\lambda_0 \sim e^{-\beta m}/\beta N$, and the butterfly velocity, $v_B \sim (\beta m)^{-1/2}$. This implies that at low temperatures, the butterfly velocity has the same temperature scaling as the speed of sound (which also scales as $(\beta m)^{-1/2}$) of the semi-classical gas of dilute quasiparticle excitations of the paramagnetic phase of the $O(N)$ model at low temperature.

2.3.1 Basic diagrammatics and low temperature relaxation rate

In this section we set up the basic computation of the squared commutator in the language of field theory. Much of the details have been moved to Appendix A for brevity.

We introduce auxiliary Hubbard Stratonovich (HS) field λ to solve the interacting problem.

The Euclidean Lagrangian we consider is

$$\mathcal{L}_E = \frac{1}{2}\left[\sum_a (\partial\phi_a)^2 - \frac{\lambda}{\sqrt{N}}\left(\sum_a \phi_a^2 - \frac{N}{g}\right) - \frac{\lambda^2}{4v}\right] \tag{2.15}$$

The HS field λ is chosen so that it generates a zero temperature mass, m, such that, $\frac{-\langle\lambda\rangle}{\sqrt{N}} = m^2$. The HS field also acts as a Lagrange multiplier, fixing (at large N), $\langle\sum \phi_a^2\rangle = \frac{N}{g}$. At finite temperature T, the constraint imposed by the HS field is

$$NT\sum_{i\omega_n}\int_{\mathbf{k}}^{\Lambda} \frac{1}{\omega_n^2 + \epsilon_{\mathbf{k}}^2} = \frac{N}{g}, \text{ where } \epsilon_{\mathbf{k}} = \sqrt{\mathbf{k}^2 + m^2}. \tag{2.16}$$

Here, and in the rest of the paper, $\int_{\mathbf{p}}$ stands for $\int \frac{d^2\mathbf{p}}{(2\pi)^2}$. At $\beta = \frac{1}{T} = \infty$, this fixes g in terms of m and Λ,

$$\frac{1}{4\pi}(\Lambda - m) = \frac{1}{g} \tag{2.17}$$

At finite temperature, the mass will be modified, as a function $m(\beta)$. We restrict ourselves to low temperature, assuming the hierarchy of scales $\Lambda >> m >> \beta^{-1}$. This implies $m(\beta) \approx m$, i.e., the thermal mass is approximately the same as the bare mass.

The perturbative calculation of the squared commutator can be set up using the basic ingredients - the real time retarded and Wightman propagators of the fields ϕ_a and the HS field λ. The retarded propagators are identified as horizontal lines, while the Wightman propagators are denoted as the vertical lines in the diagrams (in momentum space).

For the ϕ field, bare Euclidean propagator in imaginary time τ is $\mathcal{G}(\tau, \mathbf{x}) = Tr\left(\rho\phi_a(\tau, \mathbf{x})\phi_b(0, \mathbf{0})\right)$, where, ρ is the thermal density matrix, $\rho = e^{-\beta H}/(Z = Tr(e^{-\beta H}))$. The retarded propagator is defined as $\mathcal{G}_R(t, \mathbf{x})\delta_{ab} = -iTr\left(\rho[\phi_a(t, \mathbf{x}), \phi_b(0, \mathbf{0})]\right)\theta(t)$. In the Fourier space, they are related

by analytic continuation of the Matsubara frequencies, $\mathcal{G}_R(\omega, \mathbf{k}) = -\mathcal{G}(i\omega_n \to \omega, \mathbf{k})$. We can calculate and denote the retarded bare propagator as,

$$\text{————} \quad := \quad \mathcal{G}_R^{(0)}(\omega, \mathbf{k}) = \frac{1}{(\omega + i0^+)^2 - \epsilon_{\mathbf{k}}^2}. \tag{2.18}$$

The spectral function is defined as $A(\omega, \mathbf{k}) = -2Im[\mathcal{G}_R(\omega, \mathbf{k})]$. The bare ϕ spectral function is given by,

$$A^{(0)}(\omega, \mathbf{k}) = \frac{\pi}{\epsilon_{\mathbf{k}}}[\delta(\omega - \epsilon_{\mathbf{k}}) - \delta(\omega + \epsilon_{\mathbf{k}})]. \tag{2.19}$$

The generalized Wightman function is defined as,

$$\mathcal{G}_W^{(\alpha)}(t, \mathbf{x})\delta_{ab} := Tr\left(\rho^{\alpha}\phi_a(t, \mathbf{x})\rho^{1-\alpha}\phi_b(0, \mathbf{0})\right). \tag{2.20}$$

By going to the spectral representation, we show in App. A.1,

$$\mathcal{G}_W^{(\alpha)}(\omega, \mathbf{k}) = \frac{A(\omega, \mathbf{k})}{2\sinh\frac{\beta\omega}{2}} e^{(\alpha - 1/2)\beta\omega}. \tag{2.21}$$

For the λ field, the bare Euclidean propagator is $\mathcal{G}_\lambda^{(0)}(i\omega_n, \mathbf{k}) = -4v$. At infinite v, one can dress the λ propagators as shown in Fig. 2.14. In that case,

$$\mathcal{G}_\lambda(i\omega_n, \mathbf{k}) = \frac{\mathcal{G}_\lambda^0}{1 - \Pi\mathcal{G}_\lambda^0} \underbrace{\longrightarrow}_{v\to\infty} -\frac{1}{\Pi(i\omega_n, \mathbf{k})}, \tag{2.22}$$

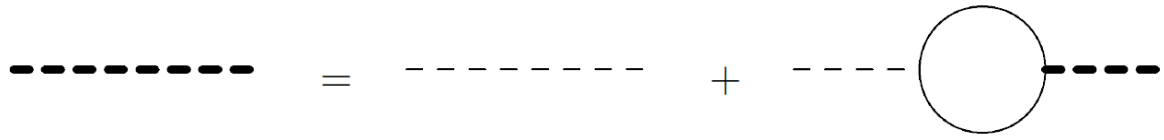

Figure 2.14: The resummed λ propagator

where Π is the one loop ϕ bubble,

$$\Pi(i\nu_n, \mathbf{k}) = \frac{T}{2} \sum_{i\omega_n} \int_{\mathbf{q}}^{\Lambda} \frac{1}{(\omega_n + \nu_n)^2 + \epsilon^2_{\mathbf{q}+\mathbf{k}}} \frac{1}{\omega_n^2 + \epsilon^2_{\mathbf{q}}}. \tag{2.23}$$

The retarded polarization bubble is given by analytic continuation, $\Pi_R(\omega, \mathbf{k}) = \Pi(i\omega_n \to \omega, \mathbf{k})$. The resummed retarded λ propagator is then denoted as,

$$:= \quad \mathcal{G}_{R,\lambda}(\omega, \mathbf{k}) = \frac{1}{\Pi_R(\omega, \mathbf{k})}. \tag{2.24}$$

From the λ spectral function, $A_\lambda(\omega, \mathbf{k}) = -2Im[\mathcal{G}_R(\omega, \mathbf{k})]$, we can define the generalized λ Wightman function,

$$\mathcal{G}^{(\alpha)}_{W,\lambda}(\omega, \mathbf{k}) = \frac{A_\lambda(\omega, \mathbf{k})}{2 \sinh \frac{\beta\omega}{2}} e^{(\alpha - 1/2)\beta\omega}. \tag{2.25}$$

We need to dress the bare ϕ propagator, for which we need to calculate the self energy as given in Fig. 2.15, from which one can obtain the retarded self energy by analytic continuation. The

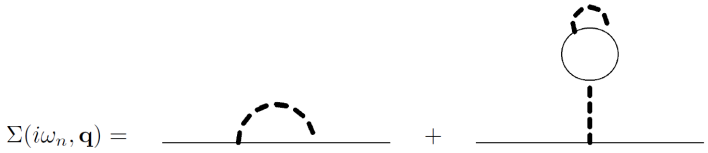

Figure 2.15: The ϕ self energy

resummed retarded propagator is denoted by a thick line,

$$\text{———} \quad := \quad \mathcal{G}_R(\omega, \mathbf{k}) = \frac{1}{(\omega + i0^+)^2 - \epsilon_{\mathbf{k}}^2 + \Sigma_R(\omega, \mathbf{k})}, \tag{2.26}$$

where Σ_R is the retarded self energy. In App. A.2 and App. A.3 we calculate the polarization bubble (Fig. 2.14) and the self energy (Fig. 2.15) respectively, in the low temperature regime, $\beta m >> 1$.

From the self energy, we can obtain the relaxation rate of ϕ quasiparticles at momentum $\mathbf{q}$, which is defined as,

$$\Gamma_{\mathbf{q}} = \frac{Im[\Sigma_R(\epsilon_{\mathbf{q}}, \mathbf{q})]}{2\epsilon_q}. \tag{2.27}$$

In App. A.3, we demonstrate that at $\mathbf{q} = 0$, the inverse lifetime $\tau_\phi^{-1} = \Gamma_{\mathbf{q}=\mathbf{0}}$ [149], can be evaluated at low temperature,

$$\Gamma_0 = \frac{1}{\tau_\phi} \approx \frac{2\pi}{N\beta} e^{-\beta m}. \tag{2.28}$$

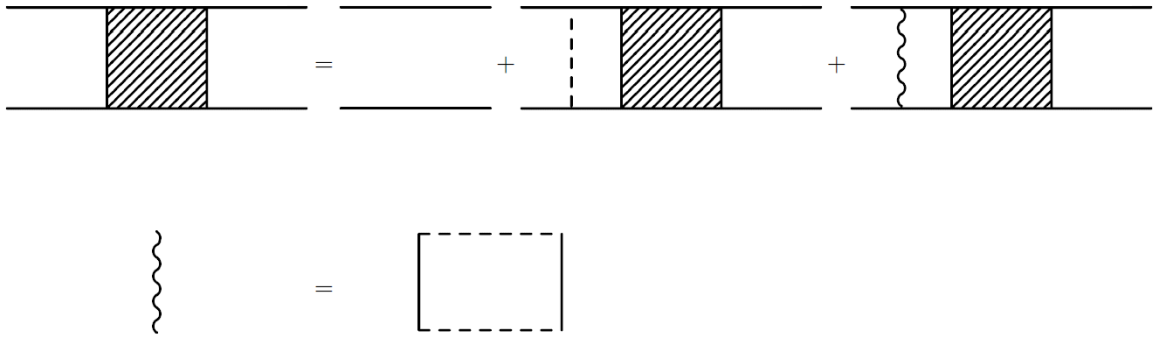

Figure 2.16: Bethe Saltpeter equation for the out of time ordered correlation function. In the diagram, all horizontal lines are retarded propagators, while the vertical lines are the Wightman propagators.

For general $\mathbf{q}$, we have,

$$\Gamma_{\mathbf{q}} \approx \frac{1}{2N} e^{\beta\epsilon_{\mathbf{q}}/2} \int_{\mathbf{k}} e^{-\beta\epsilon_{\mathbf{k}}/2} \mathcal{R}_{1+}^{(1/2)}(\mathbf{k}, \mathbf{q}), \tag{2.29}$$

where, $\mathcal{R}_{1+}^{(1/2)}(\mathbf{k}, \mathbf{q})$ is given in Eq. A.15 in App. A.3.

2.3.2 Ladder sum calculation

We finally calculate the regulated squared commutator, given in Eq. 2.13 perturbatively in $1/N$, using the ladder-sum rules described in [114], which we will extensively use. The calculation boils down to solving a Bethe Saltpeter equation in momentum space for the out of time ordered 4 point function, as shown in Fig. 2.16. There are two sides of the ladder, which are connected by 'rungs' - which are the Wightman functions. The first diagram on the RHS of Fig. 2.16 is the 'free' term $\frac{1}{N}[\mathcal{G}_R(t, \mathbf{x})]^2$, which doesn't have any exponential in time behavior, hence is not important for diagnosing chaos. There are two types of rungs - the Type I and Type II rungs

correspond to the second and third diagram on the RHS of the top line in Fig. 2.16 respectively. The expressions for the two rung contributions can be easily written down from the diagram; for example, the Type I rung can be expressed as,

$$C_{\alpha,\text{Type I}}(\nu,\mathbf{k}) = \frac{1}{N}\int\frac{d\omega}{2\pi}\int_{\mathbf{p}}\int\frac{d\omega'}{2\pi}\int_{\mathbf{p}'}\mathcal{G}_R(\nu-\omega,\mathbf{k}-\mathbf{p})\mathcal{G}_R(\omega,\mathbf{p}) \\ \mathcal{G}^{(\alpha)}_{W,\lambda}(\omega'-\omega,\mathbf{p}'-\mathbf{p})\mathcal{G}_R(\nu-\omega',\mathbf{k}-\mathbf{p}')\mathcal{G}_R(\omega,\mathbf{p}'). \tag{2.30}$$

The result for the Type II rung is very similar, with the replacement $\mathcal{G}^{(\alpha)}_{W,\lambda}(\omega'-\omega,\mathbf{p}'-\mathbf{p}) \to \mathcal{G}^{(\alpha)}_{\text{eff}}(\omega',\omega,\mathbf{p}',\mathbf{p})$, where,

$$\mathcal{G}^{(\alpha)}_{\text{eff}}(\omega',\omega,\mathbf{p}',\mathbf{p}) = \int\frac{d\omega''}{2\pi}\int_{\mathbf{p}''}\mathcal{G}^{(\alpha)}_{W}(\omega''-\omega,\mathbf{p}''-\mathbf{p})\mathcal{G}^{(\alpha)}_{W}(\omega'-\omega'',\mathbf{p}'-\mathbf{p}'') \\ \mathcal{G}_{R,\lambda}(\nu-\omega'',-\mathbf{p}'')\mathcal{G}_{R,\lambda}(\omega'',\mathbf{p}''). \tag{2.31}$$

We set up the Bethe Saltpeter equation by defining a function $f(\nu,\mathbf{k};\omega,\mathbf{p})$, such that,

$$C_{(\alpha)}(\nu,\mathbf{k}) = \frac{1}{N}\int\frac{d\omega}{2\pi}\int_{\mathbf{p}} f^{(\alpha)}(\nu,\mathbf{k};\omega,\mathbf{p}). \tag{2.32}$$

As was shown in [114], it is convenient to consider the "on-shell" ansatz for $f(\nu,\mathbf{k};\omega,\mathbf{p})$,

$$f^{(\alpha)}(\nu,\mathbf{k};\omega,\mathbf{p}) = \frac{f^{(\alpha)}_{+}(\nu,\mathbf{k};\mathbf{p})}{2\epsilon_{\mathbf{p}}}\delta(\omega-\epsilon_{\mathbf{p}}) + \frac{f^{(\alpha)}_{-}(\nu,\mathbf{k};\mathbf{p})}{2\epsilon_{\mathbf{p}}}\delta(\omega+\epsilon_{\mathbf{p}}). \tag{2.33}$$

We can approximate the product of the retarded Green functions by their most singular (in ν) terms (for small k, such that $\Gamma_{\mathbf{k-p}} \approx \Gamma_{\mathbf{p}}$),

$$G_R(\nu-\omega,\mathbf{k}-\mathbf{p})\mathcal{G}_R(\omega,\mathbf{p}) \to \frac{\pi i}{2\epsilon_{\mathbf{p}}\epsilon_{\mathbf{k-p}}}\left[\frac{\delta(\omega-\epsilon_{\mathbf{p}})}{\nu-(\epsilon_{\mathbf{p}}-\epsilon_{\mathbf{k-p}})+2i\Gamma_{\mathbf{p}}}+\frac{\delta(\omega+\epsilon_{\mathbf{p}})}{\nu+(\epsilon_{\mathbf{p}}-\epsilon_{\mathbf{k-p}})+2i\Gamma_{\mathbf{p}}}\right]. \tag{2.34}$$

Further, we have, $\epsilon_{\mathbf{p}}-\epsilon_{\mathbf{k-p}} \approx \mathbf{k}.\nabla_{\mathbf{p}}\epsilon_{\mathbf{p}}$, and for small $\mathbf{p}$, $\nabla_{\mathbf{p}}\epsilon_{\mathbf{p}} \approx \mathbf{p}/m$. The Bethe Saltpeter equation can now be written as [114],

$$(-i\nu \pm i\frac{\mathbf{k}.\mathbf{p}}{m})f^{(\alpha)}_{\pm}(\nu,\mathbf{k};\mathbf{p}) = \frac{1}{N}\int_{\mathbf{p}'}\hat{\mathcal{K}^{(\alpha)}}(\mathbf{p}',\mathbf{p})f^{(\alpha)}_{\pm}(\nu,\mathbf{k};\mathbf{p}'), \tag{2.35}$$

where,

$$\begin{aligned}
&\hat{\mathcal{K}^{(\alpha)}}(\mathbf{p}',\mathbf{p}) = \mathcal{R}^{(\alpha)}_1(\mathbf{p}',\mathbf{p}) + \mathcal{R}^{(\alpha)}_2(-\mathbf{p}',\mathbf{p}) - 2N\Gamma_{\mathbf{p}}(2\pi)^2\delta^{(2)}(\mathbf{p}'-\mathbf{p}), \text{ and,}\\
&\mathcal{R}^{(\alpha)}_{1,2}(\mathbf{p}',\mathbf{p}) := \mathcal{R}^{(\alpha)}_{1,2+}(\mathbf{p}',\mathbf{p}) + \mathcal{R}^{(\alpha)}_{1,2-}(\mathbf{p}',\mathbf{p}), \text{ where,}\\
&\mathcal{R}^{(\alpha)}_{1\pm}(\mathbf{p}',\mathbf{p}) := \frac{1}{4\epsilon_{\mathbf{p}'}\epsilon_{\mathbf{p}}}\mathcal{G}^{(\alpha)}_{W,\lambda}(\pm\epsilon_{\mathbf{p}'}-\epsilon_{\mathbf{p}},\mathbf{p}'-\mathbf{p}) \text{ and } \mathcal{R}^{(\alpha)}_{2\pm}(\mathbf{p}',\mathbf{p}) := \frac{1}{4\epsilon_{\mathbf{p}'}\epsilon_{\mathbf{p}}}\mathcal{G}^{(\alpha)}_{\text{eff}}(\pm\epsilon_{\mathbf{p}'},\epsilon_{\mathbf{p}},\mathbf{p}',\mathbf{p}).
\end{aligned} \tag{2.36}$$

The inverse life-time $\Gamma_{\mathbf{p}}$ was defined in Eq. 2.29. Recall $\alpha = 1/2$ refers to the regulated case, while, $\alpha = 1$ refers to the unregulated case. Because of the spectral relation in Eq. 2.21, we have, $\mathcal{G}^{(1)}_W(\omega) = e^{\beta\omega/2}\mathcal{G}^{(1/2)}_W(\omega)$. Thus, the kernel functions are also related simply as, $\mathcal{R}^{(1)}_{1,2}(\mathbf{p}',\mathbf{p}) = e^{\beta\left(\epsilon_{\mathbf{p}'}-\epsilon_{\mathbf{p}}\right)/2}\mathcal{R}^{(1/2)}_{1,2}(\mathbf{p}',\mathbf{p})$. We calculate the kernel functions from the Type I and Type II rungs, $\mathcal{R}^{(1/2)}_{1,2\pm}$, at low temperature, in App. A.5.

2.3.2.1 Kernel functions at low temperature

From the expressions for the kernel functions $\mathcal{R}_{1,2}^{(1/2)}(\mathbf{p}', \mathbf{p})$, obtained in Eqs. A.15, A.22, A.26 and A.27 in App. A.5, it becomes clear that the kernel functions are exponentially suppressed as $\exp\left(-\beta(\epsilon_{\mathbf{p}'} - \epsilon_{\mathbf{p}})/2\right)$. Expanding in terms of the small parameter $|\mathbf{p}' - \mathbf{p}|$ in the kernel functions, we get the following low temperature approximation,

$$\mathcal{R}_1^{(1/2)}(\mathbf{p}', \mathbf{p}) = \mathcal{R}_2^{(1/2)}(\mathbf{p}', \mathbf{p}) = e^{-\beta m} \frac{8\pi\sqrt{2\pi}}{\sqrt{\beta m}|\mathbf{p}' - \mathbf{p}|m^2} e^{-\beta(|\mathbf{p}'-\mathbf{p}|^2/8m)}. \tag{2.37}$$

We can extract the temperature scaling of the kernel integration, by rescaling $\mathbf{p}, \mathbf{p}' \to \mathbf{p}\sqrt{m}/\sqrt{\beta}, \mathbf{p}'\sqrt{m}/\sqrt{\beta}$. Furthermore, to solve the Bethe Saltpeter equation numerically, we need to create a discrete 2D grid of momenta, with momentum spacing Δp. We can thus replace the integral in Eq. 2.35 with a discrete sum,

$$(-i\nu \pm \frac{i\mathbf{k}.\mathbf{p}}{\sqrt{\beta m}}) f_{\pm}^{(\alpha)}(\nu, \mathbf{k}; \mathbf{p}) = \frac{(\Delta p)^2}{4\pi^2 N} \frac{e^{-\beta m}}{\beta} \sum_{\mathbf{p}'} \hat{K}_{\mathbf{p}'\mathbf{p}}^{(\alpha)} f_{\pm}^{(\alpha)}(\nu, \mathbf{k}; \mathbf{p}'), \tag{2.38}$$

with the kernel matrix defined as,

$$\begin{aligned} &\hat{K}_{\mathbf{p}'\mathbf{p}}^{(\alpha)} = \left[\hat{R}_1^{(\alpha)}\right]_{\mathbf{p}'\mathbf{p}} + \left[\hat{R}_2^{(\alpha)}\right]_{\mathbf{p}'\mathbf{p}} - 2\hat{\Gamma}_{\mathbf{p}}\delta_{\mathbf{p}'\mathbf{p}} \text{ and, } \hat{\Gamma}_{\mathbf{p}} = \frac{1}{2} e^{\left(\mathbf{p}^2 - \mathbf{p}'^2\right)/4} (\Delta p)^2 \left[\hat{R}_1^{(1/2)}\right]_{\mathbf{p}'\mathbf{p}} \text{ where,} \\ &\left[\hat{R}_1^{(\alpha)}\right]_{\mathbf{p}'\mathbf{p}} = \left[\hat{R}_2^{(\alpha)}\right]_{\mathbf{p}'\mathbf{p}} = \frac{8\pi\sqrt{2\pi}}{|\mathbf{p}' - \mathbf{p}|} e^{-(|\mathbf{p}'-\mathbf{p}|^2/8)} e^{(\alpha-1/2)\left(\mathbf{p}'^2 - \mathbf{p}^2\right)/2}. \end{aligned} \tag{2.39}$$

We create a discrete 2D grid of rescaled non-dimensionalized momenta, with a hard cutoff of $\Lambda = 1$. This is justified as the kernel matrix is exponentially suppressed in $|\mathbf{p}' - \mathbf{p}|^2$.

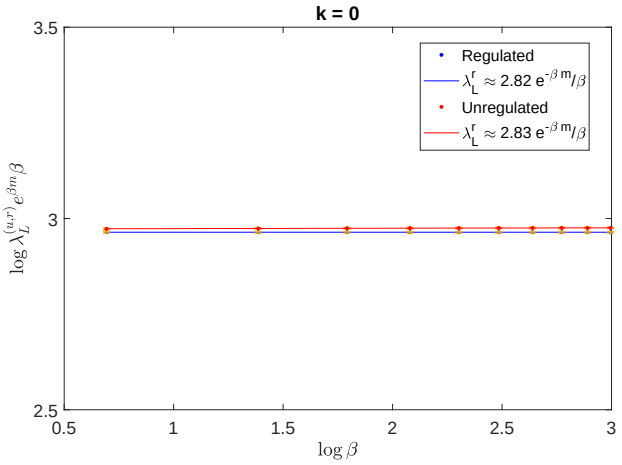

Figure 2.17: Scaled maximal eigenvalue of the Eq. 2.38 at $\mathbf{k} = 0$, $\lambda_L(k = 0)e^{\beta m}\beta N$, is plotted as a function of inverse temperature β in the log-log scale (we rescaled factors of N in the numerics , and N = 1 in the figure.). The errorbars are estimated from the uncertainty of extrapolating the eigenvalues to the continuous limit $dp \to 0$. The behaviour is constant with temperature, confirming $\lambda_L \sim e^{-\beta m}/\beta N$. Also, the result is same for both the regulated and unregulated cases showing that the ladder method is contour-independent.

We want to find the temporal behavior of $C_{r,u}(t, \mathbf{x})$. We can thus replace $-i\nu \to \partial_t$ in Eq. 2.38 and solve the matrix equation for its eigenvalues. If there are real positive eigenvalues, we can infer that there is an exponential growth in the regulated squared commutator. We denote the leading eigenvalue as $\lambda_L^{r,u}(\mathbf{k})$.

2.3.2.2 Temperature scaling of the butterfly velocity

First, let us restrict to $k = 0$. From Eq. 2.38, we have, $\lambda_L^{r,u}(k = 0) \sim e^{-\beta m}/\beta N$. By numerically finding the largest eigenvalue of the matrix equation we assert that the leading eigenvalue is always real and positive, leading to an exponential growth in the squared commutator. The details of the numerical computation are given in Appendix A.6, and the results for both the regulated and the unregulated cases are demonstrated in Fig. 2.17. Furthermore, the relevant inverse time-scale is also given by $\Gamma_0 = e^{-\beta m}/\beta N$, (Eq. 2.28). Hence, we can rescale the Bethe Saltpeter equation by this scale, and introduce a rescaled external momentum, $\mathbf{u} = \mathbf{k}/\left(\sqrt{\beta m \Gamma_0}\right)$, and a

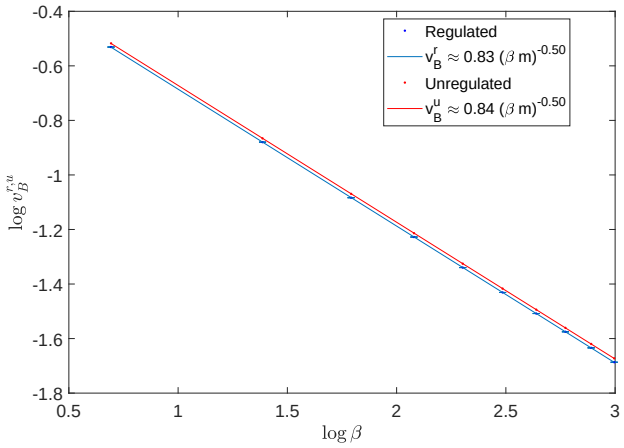

Figure 2.18: Using the fitted λ_0, λ_2 and λ_i, the butterfly velocity v_B is calculated from Eq. 2.45, and plotted against β in a log-log scale. The low temperature behavior of v_B is $v_B \approx \frac{0.83}{\sqrt{\beta m}}$ - for both the regulated and the unregulated cases.

rescaled time $\tilde{t} = \Gamma_0 t$.

The matrix equation can be now recast as,

$$(\partial_{\tilde{t}} \pm i\mathbf{u}.\mathbf{p})\, f_{\pm}^{(\alpha)}(\nu, \mathbf{k}; \mathbf{p}) \sim \sum_{\mathbf{p}'} \hat{K}_{\mathbf{p}'\mathbf{p}} f_{\pm}^{(\alpha)}(\nu, \mathbf{k}; \mathbf{p}'). \tag{2.40}$$

For small u, the eigenvalues of this matrix equation can be approximated by

$$\tilde{\lambda}_L(u) \approx \tilde{\lambda}_0 - \tilde{\lambda}_2 u^2 \pm i\tilde{\lambda}_i u, \tag{2.41}$$

because of the spherical symmetry of the leading eigenvector at $\mathbf{k} = 0$. Here, $\tilde{\lambda}_{0,2,i} \sim \mathcal{O}(1)$, and by rescaling back, $\lambda_{0,2,i} \sim e^{-\beta m}/\beta N$. The quadratic form of the real part and the linear form for the imaginary part have been verified numerically in Fig. A.2 in App. A.6. Now, the regulated

and unregulated squared commutator can be evaluated as,

$$\begin{aligned} C_{r,u}(t,\mathbf{x}) &= \frac{1}{N}\int_{\nu}\int_{\mathbf{k}}\int_{\mathbf{p}} e^{i\mathbf{k}.\mathbf{x}-i\nu t}\left(\frac{f_{+}^{r,u}(\nu,\mathbf{k};\mathbf{p})}{2\epsilon_{\mathbf{p}}}+\frac{f_{-}^{r,u}(\nu,\mathbf{k};\mathbf{p})}{2\epsilon_{\mathbf{p}}}\right) \\ &= \frac{1}{N}\int_{\mathbf{k}} e^{i\mathbf{k}.\mathbf{x}+\lambda_0 t-\lambda_2 u^2 t}\left(e^{i\lambda_i u t}\chi_{\mathbf{k}}^{r,u,+}+e^{-i\lambda_i u t}\chi_{\mathbf{k}}^{r,u,-}\right), \end{aligned} \tag{2.42}$$

where, $\chi_{\mathbf{k}}^{r,u,\pm}$ is the eigenvector of the matrix eigenvalue in Eq. 2.38. If there are no singularities in $\chi_{\mathbf{k}}^{r,u,\pm}$, we can assume the two terms in the integral depends only on the saddle points of the exponents. Recalling $u = k/\left(\sqrt{\beta m}\Gamma_0\right)$, the two saddle points are given by,

$$\mathbf{k}_{\pm}^{*} = (\beta m\Gamma_o^2)\frac{i\left(\mathbf{x}\pm\frac{\lambda_i t}{\sqrt{\beta m}\Gamma_0}\right)}{2\lambda_2 t}. \tag{2.43}$$

When $C_{r,u}(t,\mathbf{x})$ is evaluated, one of the terms will be exponentially suppressed in x compared to the other. Keeping only the leading term, we get,

$$C_{r,u}(t,\mathbf{x}) \sim \frac{1}{N}\exp\left[\lambda_0 t-\frac{\beta m\Gamma_0^2\left(x-\frac{\lambda_i t}{\sqrt{\beta m}\Gamma_0}\right)^2}{4\lambda_2 t}\right]. \tag{2.44}$$

The first term comes from the pure exponential growth that was present for the $u = 0$ case, and the second term is reminiscent of the broadening form of the squared commutator in Eq. 2.7. By finding the level sets of the exponential for the ballistic condition $x \sim v_B t$, we have the following expression for the butterfly velocity v_B,

$$v_B^{r,u} = \sqrt{\frac{4\lambda_0\lambda_2}{\beta m\Gamma_0^2}}+\frac{\lambda_i}{\sqrt{\beta m\Gamma_0^2}}. \tag{2.45}$$

Since $\lambda_{0,2,i} \sim \Gamma_0$, we get the following temperature dependence of the butterfly velocity,

$$v_B^{r,u} \sim \sqrt{\frac{1}{\beta m}}. \tag{2.46}$$

Note that this is the same scale as the speed of sound of the ideal classical gas at finite temperature. Hence the butterfly velocity from the regulated squared commutator of this essentially classical gas has the same temperature scaling as the speed of sound. Furthermore, the particular temperature scaling $\sqrt{1/\beta m}$ of the butterfly velocity arises because the thermal scale is the appropriate scale to non-dimensionalize the momenta, and doesn't depend on the exact form of $\tilde{\lambda}_L(u)$.

From the numerically obtained eigenvalues, we can see from Fig. 2.18, that the butterfly velocity from regulated and unregulated squared commutators are the same at low temperatures,

$$v_B \approx \frac{0.83}{\sqrt{\beta m}}. \tag{2.47}$$

This shows that the ladder calculation is insensitive to contour dependence.

At fixed t, for a fixed difference of $C_{r,u}(t, \mathbf{x})$, one finds from Eq. 2.44 that the spread $\epsilon = x - v_B t \sim$ constant. This implies that this form of the squared commutator doesn't have a broadening behavior. A similar exercise for the spin chain result in Eq. 2.7, would show a time dependent spread, $\epsilon \sim t^{p/(p+1)}$, implying broadening.

In deriving these results, we assumed that the integral expression of the squared commutator in Eq. 2.42 is dominated by the saddle point contribution. In [148], it was noted that OTOCs obtained from ladder sum calculations generically have a pole in momentum space wherever

$\lambda_L(k) = 2\pi/\beta$,

$$C(t, \mathbf{x}) \sim \frac{1}{N} \int_{\mathbf{k}} \frac{e^{i\mathbf{k}.\mathbf{x}+\lambda_L(k)t}}{\cos \frac{\lambda_L(k)\beta}{4}}. \tag{2.48}$$

However, in the $O(N)$ theory, the chaos exponent $\lambda_L(k) \sim 1/N$ is N suppressed, hence these poles occur at parametrically large values of the momentum. Provided that x/t is N-independent, the saddle point momentum is always closer to the real axis than the pole and hence controls the integral. For example, as we have seen from the k dependence of $\lambda_L(k)$ in Fig. A.1 in Appendix. A.6, if $\lambda_L(k = i|k|) \sim \lambda_0 \beta |k|^2/m$ at large imaginary k, then the closest pole in the upper half plane would be at $|k| \sim \sqrt{\frac{m}{\beta} \frac{N\lambda_{\text{max}}}{\lambda_0}}$. This momentum is very large due to large N and the large ratio $\lambda_{\text{max}}/\lambda_0$.

2.3.3 Summary of findings from the field theory calculation

In this section, we studied the temperature and contour dependence of squared commutator in a solvable large N local model using the ladder technique. We find that our analysis can describe the temperature scaling of the butterfly velocity. However, it is insensitive to the contour of thermal ordering. This is not unexpected, as the ladder method is not expected to exhibit contour dependence [150]. It also doesn't capture the broadening behavior that was observed in Sec. 2.2.

The field theory model differs from the spin chain numerics in two ways - the number of spatial dimensions, and in the fact that the spin chain has finite local Hilbert space unlike the field theory model, which is solvable at large N - an effectively classical description. It is thus likely that the broadening and the contour dependence are sourced by quantum fluctuations due to the finiteness of the local Hilbert space [138], which is not captured in this calculation.

2.4 Bounds on temperature dependence of butterfly velocity

Locality in gapped quantum spin chains can lead to microcausality and short ranged correlation [9]. Can we use similar techniques to bound the behavior of butterfly velocity?

In this section we discuss state dependent bounds on butterfly velocity in local gapped systems which were introduced in [140]. The general definition of squared commutator in Eq. 2.1 can be rewritten as $\mathcal{C}_\alpha(t, \mathbf{x}, \rho) = -Tr\left(\rho^\alpha O \rho^{1-\alpha} O\right)$, where, $O = i\left[W_{\mathbf{0}}(t), V_{\mathbf{x}}\right]$. By restricting to $x = vt$, one can define the velocity dependent Lyapunov exponents,

$$\lambda(v, \rho) = \lim_{t\to\infty} \frac{1}{t} \ln C(vt, t, \rho). \tag{2.49}$$

The butterfly velocity can be defined as the largest velocity for which the Lyapunov exponent is positive,

$$v_B(\rho) = \sup\left\{v : \lambda(v, \rho) \geq 0\right\}. \tag{2.50}$$

We define the support of the commutator, O as a region S of diameter $2R(v, t)$, around a point $\mathbf{0}$. The scrambling velocity is defined as the rate of increase of this support,

$$v_S(\rho) = \lim_{t\to\infty} \frac{R(v, t)}{t}. \tag{2.51}$$

We consider the Hamiltonian H to be defined on a lattice, composed of geometrically local terms, and such that it has a finite gap. We introduce the shifted zero expectation-value Hamiltonian, $\tilde{H} = H - Tr(\rho H)$. We can divide the shifted Hamiltonian into terms supported

inside and outside S,

$$\tilde{H} = \sum_{i \in S} \tilde{h}_i + \sum_{j \in \Lambda - S} \tilde{h}_j. \tag{2.52}$$

Let us consider the near wavefront ansatz,

$$\lambda(v, \rho) = -\lambda \left(\frac{v}{v_B} - 1 \right)^{1+p}. \tag{2.53}$$

In [140], it was shown that for the unregulated squared commutator, the rate of change of butterfly velocity with temperature, $\partial_\beta v_B$ can be bounded,

$$\lambda (\Delta v)^p (\Delta v + 1) |\partial_\beta \ln v_B| \leq 2h \left(v_S(\rho) - \xi \lambda(v, \rho) \right), \tag{2.54}$$

where $\Delta v = v/v_B - 1$, $\xi > 0$ is the finite correlation length, and h is given by,

$$h = \sup_i \frac{\left| Tr \left(\sqrt{\rho} \tilde{h}_i \sqrt{\rho} OO \right) \right|}{Tr \left(\rho OO \right)}. \tag{2.55}$$

At low temperature, $\beta \to \infty$, $\rho \sim |0\rangle\langle 0|$. From Eq. 2.55, $h \propto \langle 0 | \tilde{h}_i | 0 \rangle$, and hence 0, which implies,

$$\partial_\beta \ln v_B \to 0 \text{ as } \beta \to \infty. \tag{2.56}$$

We first review the proof for the unregulated case due to [140] and then also extend the bound to the butterfly velocity obtained from the regulated squared commutator, and show that the same low temperature behavior as in Eq. 2.56 holds in that case as well. However, we note that the bound can't differentiate between a power-law vanishing butterfly velocity at low temperature and a constant butterfly velocity. Low temperature behaviors of both the regulated and unregulated

cases which were obtained in Sec. 2.2, i.e., $v_B \sim \beta^{-1/2}$ and $v_B \sim$ constant respectively, are consistent with Eq. 2.56.

We first discuss the bound on butterfly velocity obtained from the unregulated squared commutator as given in [140]. We differentiate C_u with respect to the inverse temperature β to obtain,

$$\partial_\beta C_u = -Tr\left(\tilde{H}\rho OO)\right). \tag{2.57}$$

We want to upper bound $|\partial_\beta C_u|$. By separating out the contributing terms to two parts - inside and outside a ball of radius $R+\delta$ around the point x_0 (a region we call S'), we have,

$$|\partial_\beta C_u| \leq \sum_{i\in S'} \left|Tr\left(\rho OO\tilde{h}_i\right)\right| + \sum_{j\in \Lambda - S'} \left|Tr\left(\rho OO\tilde{h}_j\right)\right|. \tag{2.58}$$

For the terms outside the ball S', we invoke the Exponential Clustering Theorem, which states, for two operators W_1 and W_2 supported on non-overlapping regions A and B on a lattice system with a gapped Hamiltonian, there exist, ξ and $\mathcal{N}$, such that,

$$|Tr\left(\rho W_1 W_2\right) - Tr\left(\rho W_1\right) Tr\left(\rho W_2\right)| \leq \mathcal{N} min\{|\partial A|, |\partial B|\}\|W_1\|\|W_2\| e^{-|A-B|/\xi}, \tag{2.59}$$

where, $|A-B|$ is the minimum distance between the regions A and B. Here, ξ is the correlation length, which is finite because of the presence of the gap. The Exponential Clustering Theorem can be proved using Lieb Robinson bound techniques [9]. Now, $Tr\left(\rho\tilde{h}_i\right) = 0$. Thus the sum of

'outside' terms in the RHS of Eq. 2.58, can bounded in the following way -

$$\begin{aligned}\sum_j ... &\leq 2\mathcal{N} min\{|\partial A|, |\partial B|\}\|O\|^2 \sum_{j=\delta}^{\infty} e^{-j/\xi} \\ &= \mathcal{M}\int_{\delta}^{\infty} dx e^{-x/\xi} \text{ where } \mathcal{M} \text{ is suitably defined,} \\ &= \mathcal{M}\xi e^{-\delta/\xi}.\end{aligned} \tag{2.60}$$

The 'inside' terms in the RHS of Eq. 2.58, can be bounded in the following way,

$$\begin{aligned}\sum_i ... &\leq h \sum_{i\in S'} |Tr\left(\rho O O\right)| \\ &= V_{R+\delta} C_u(t, vt, \rho),\end{aligned} \tag{2.61}$$

where, h is a maximum over the different terms of the shifted Hamiltonian, and V_r is the size of the region of radius r, i.e., $V_r = 2r + 1$. Two convenient choices of h are,

$$h = 2 \sup_i \|h_i\| \text{ or,} \tag{2.62}$$

$$h = \sup_i \frac{\left|Tr\left(\sqrt{\rho}\tilde{h}_i\sqrt{\rho}OO\right)\right|}{Tr\left(\rho OO\right)}. \tag{2.63}$$

Combining both the contributions, we get,

$$|\partial_\beta C_u| \leq V_{R+\delta} h C_u(t, vt, \rho) + \mathcal{M}\xi e^{-\delta/\xi} \tag{2.64}$$

Usually at late times, $C(t \to \infty) = e^{\lambda(v,\rho)t}$. For $v > v_B$, $\lambda(v, \rho) < 0$. We can choose $\delta = (-\xi\lambda(v, \rho) + \epsilon)t$ for some positive ϵ, which makes the second term in Eq. 2.64 subleading compared to the first term, and hence can be dropped. Essentially, the contribution to the bound

from sufficiently outside the support of the operator O can be dropped.

Now, using the ansatz $C_u = e^{\lambda(v,\rho)t}$, we obtain the following bound for the rate of change of the Lyapunov exponent,

$$\begin{aligned}
|\partial_\beta \lambda| &\leq h \lim_{t\to\infty} \frac{V_{R-\xi\lambda(v,\rho)t}}{t} \\
&= 2h \left(\lim_{t\to\infty} \frac{R}{t} - \xi\lambda(v,\rho) \right) \\
&= 2h \left(v_S(\rho) - \xi\lambda(v,\rho) \right) \text{ from the definition of the scrambling velocity from Eq. 2.51.}
\end{aligned} \tag{2.65}$$

We can further analyze this scrambling bound by using the near wavefront ansatz,

$$\lambda(v,\rho) = -\lambda \left(\frac{v}{v_B} - 1 \right)^{1+p}. \tag{2.66}$$

Let's introduce the short hand $\Delta v = v/v_B - 1$. For this ansatz, we have,

$$\partial_\beta \lambda(v,\rho) = \lambda(\Delta v)^{1+p} \left[\partial_\beta \ln \lambda + \ln(\Delta v)\partial_\beta p - (1+p)\frac{v/v_B}{\Delta v}\partial_\beta \ln v_B \right] \tag{2.67}$$

Close to the Butterfly velocity, i.e., when $v \gtrsim v_B$, the last term is the leading term. Thus for $\Delta v = 0^+$, we have the bound on rate of change of butterfly velocity,

$$\lambda(\Delta v)^p(\Delta v + 1)|\partial_\beta \ln v_B| \leq 2h \left(v_S(\rho) - \xi\lambda(v,\rho) \right) \tag{2.68}$$

Now, say $\beta \to \infty$. For the gapped system, $\rho = |0\rangle\langle 0|$. We can estimate h using the definition, in

Eq. 2.55. For this ρ, $h \propto \langle 0|\tilde{h}_i|0\rangle$, and hence 0, which implies,

$$\partial_\beta \ln v_B \to 0 \text{ as } \beta \to \infty \tag{2.69}$$

Note, however, unlike the assertion in [140], this doesn't imply a freezing out of the Butterfly Velocity at temperatures below the gap. In fact, even power-law ansatz, $v_B \sim \beta^{-a}$ for $a > 0$, satisfies the above bound, and our observation $v_B \sim \beta^{-1/2}$ is certainly admissable.

2.5 Scrambling bounds for regulated squared commutator

We can extend the bounds to the butterfly velocity from regulated squared commutator, $C_r = -Tr\left(\sqrt{\rho}O\sqrt{\rho}O\right)$, as well. Differentiating with β, we obtain,

$$\begin{aligned} \partial_\beta C_r &= -Tr\left(\tilde{H}\sqrt{\rho}O\sqrt{\rho}O\right) \\ &= -Tr\left(\tilde{H}\rho O\rho^{1/2}O\rho^{-1/2}\right). \end{aligned} \tag{2.70}$$

Now, we invoke the Araki bound [151], which states, in 1 dimensional quantum lattice systems with a gap, for any finitely supported operator A with support R, the operator $\rho^s A\rho^{-s}$ is also supported, upto exponential correction, on a ball of support $R + l(\beta s)$, where $l(x)$ is an entire function not larger than exponential in x. Thus, the support of $\rho^{1/2}O\rho^{-1/2}$, and hence of $O\rho^{1/2}O\rho^{-1/2}$ has radius $\sim R + \mathcal{A}e^{\mathcal{B}\beta}$, for appropriately defined numbers $\mathcal{A}, \mathcal{B}$. Hence, the entire argument of the previous section follows by replacing $R \to R + l(\beta/2)$, and we can bound the rate of change of Lyapunov exponent and Butterfly velocity obtained from the regulated squared commutator as well. In particular, in deriving these bounds, the effect of this thermal broadening

can be ignored, since, $l(\beta)/t \to 0$, as $t \to \infty$. Hence, all the scrambling bounds derived for the unregulated case also follow naturally for the regulated case.

2.6 Discussions

In this paper we have studied the temperature and contour dependence of quantum information scrambling for local gapped interacting systems in two different models and for a wide range of temperatures.

We first introduced a tensor network based technique to calculate both regulated and unregulated squared commutators in quantum spin chains at temperatures ranging across the spectral gap. For the regulated case, the butterfly velocity decreases with lowering temperature, and is consistent with a power law $v_B \sim \beta^{-a}$ for $a > 0$ at intermediate-to-large β. We also observe a strong contour dependence, and point out that the butterfly velocity obtained from the unregulated squared commutator remains insensitive to the temperature variation. In fact, a careful study of $\partial_t C(t, \mathbf{x})$ shows that the chaos bound cannot be generalized away from the special contour ordering used to prove it.

To get an analytical handle on local gapped systems at temperatures lower than what can be accessed in the spin chain numerics, we use a perturbative field theoretic ladder sum technique, and calculate the temperature dependence of the squared commutator in the paramagnetic phase of the $O(N)$ model. There we confirmed that the characteristic speed of information scrambling at low temperature is proportional to the speed of sound of a classical gas, i.e. $v_B \sim \beta^{-1/2}$, confirming the intuition that the low temperature state can be accurately modeled as a weakly interacting dilute gas of massive quasiparticles. However, the scrambling in this model is insen-

sitive to the contour, and also doesn't have the broadening feature.

The strong contour dependence we observe in our spin-chain numerics is in the spirit of the results from previous Schwinger-Keldysh calculations in [134, 135], which showed similar contour dependence. Our result for the strongly interacting quantum spin chain compliments their perturbative arguments. These results taken together suggest that the unregulated case accesses high energy modes even at low temperatures, thereby remaining insensitive to the effects of temperature. Although we did not find such behavior in the $O(N)$ model at leading order in $1/N$, we expect higher order corrections will modify this conclusion since there are multiple energy scales in the problem in addition to temperature.

The numerical study also reveals the existence of a wave-front broadening effect that persists even at low temperatures. This feature is not captured in the field theory calculations, and remains an interesting theoretical challenge for the future. As was suggested in [138], quantum fluctuations due to the finiteness of the local Hilbert spaces will play a significant role in the broadening behavior.

Using Lieb Robinson [14] bounds, it has recently been demonstrated [140] that locality and short ranged correlations imply temperature dependent bounds on the butterfly velocity defined from the unregulated squared commutator. In App. 2.4, we review the derivation of this bound and extend it to the regulated case. In particular, it can be shown that the butterfly velocity (obtained from either unregulated or regulated cases) obeys the bound,

$$\partial_\beta v_B \to 0, \text{ as } \beta \to \infty. \tag{2.71}$$

These bounds are consistent with a constant butterfly velocity at low temperatures $v_B \sim$ constant

(unregulated case from spin chain numerics) and with a butterfly velocity proportional to a power of temperature $v_B \sim \beta^{-a}$ for $a > 0$ (regulated case from the spin chain dynamics and field theory calculation, with $a = 1/2$). The existing bounds are contour independent and hence cannot constrain the contour dependence.

The strong contour dependence that we observe has non-trivial implications for temperature dependent scrambling studies in future experiments. Our work shows that the regulated and the unregulated cases capture different physics, thus enriching the large set of phenomena falling under the umbrella of scrambling.

Chapter 3: Measurement-induced purification in large-N hybrid Brownian circuits

"A new day and a new beginning," said Tiny Dragon.

"What shall we do with it?"

- Big Panda and Tiny Dragon, James Norbury.

3.1 Introduction

As a quantum many-body system evolves in time, its state vector follows a trajectory in Hilbert space guided by unitary dynamics and measurements. Unitary evolution is generated by a system's Hamiltonian, while measurements are generated by coupling the system to a macroscopic apparatus that records the value of some observable and simultaneously collapses the state vector. If a quantum system is composed of many parts and if the interactions and measurements involve only a few of these parts at a time, then the operator which updates the quantum state has the general structure of a network composed of many elementary pieces glued together. When the number of elementary pieces is large and the time is long, the evaluation of such a network is akin to evaluating the partition function of a generalized statistical mechanics problem, analogous to an Ising model where one allows more local degrees of freedom and all kinds

of few-body interactions with coupling parameters that may be complex or even random. This point of view has a long tradition in theoretical physics, with recently studied examples including [152, 153, 154, 155, 156, 157].

From this point of view, computing the dynamics of quantum many-body observables is part of a very general class of problems that also includes evaluating partition functions of classical statistical models and studying imaginary time evolution of local quantum systems. Given this overarching framework, one goal is to classify and understand all possible distinct classes of behaviors (phases) and the transitions between them (phase transitions). Many of these problems directly relate to experimentally realizable observables; even in cases where direct experimental access is challenging, a general understanding of the space of possible behaviors can shed indirect light on measurable observables.

In this chapter, we consider a recently discovered class of such phases and phase transitions which involve the interplay of unitary scrambling dynamics and single-body measurements [21, 22, 158]. The phenomena of interest arise from a competition between the unitary part, which tends to move the state away from a product form by generating entanglement, and the measurement part, which tends to move the state towards a product form by decreasing entanglement. We make progress towards an effective field theory description of this physics by defining and solving a mean-field-like model that exhibits a similar phase transition.

In more detail, the competition between scrambling dynamics and measurements in hybrid local quantum circuits composed of 2-body unitary scrambling gates interspersed with local projective measurements leads to a measurement-induced phase transition (MIPT) from a volume-law entangled phase to an area-law entangled phase above a critical measurement rate [21, 22, 158, 159, 160]. These phenomena are also related to dramatic phase transitions that can occur

in the entanglement structures of final states in noisy quantum computers [161]. The hybrid circuit discoveries were followed by a series of works studying related transitions in a variety of models, exploring the critical properties, and studying relations to quantum error correcting codes [162, 163, 164, 165, 166, 167, 168, 169, 170, 171, 172, 173]. More recently, some papers have considered all-to-all models and again found analogous phases and phase transitions [174, 175]. Similar transitions have also been observed recently in fermionic chains of coupled Sachdev-Ye-Kitaev (SYK) models with imaginary damping terms [176]. Related dynamics in free-fermion systems have also been studied [177, 178].

Distinct from but related to the entanglement transition in local systems, it was found that measurements in quantum circuits can also drive a purification transition, where an initial mixed state is dynamically purified in constant time by repeated measurements occurring above a critical rate, while remaining mixed until exponential times for measurement rates below this critical rate [23, 179]. From a quantum information processing point of view, the volume-law phase or the mixed phase can be identified as a randomly-generated quantum error correcting code [163, 164, 166, 173], where the scrambling dynamics effectively 'hides' the quantum information from local measurements.

The interplay between unitary dynamics and measurement in quantum mechanics is an old and rich subject [161, 180, 181, 182]. In particular, weak continuous measurements of the type studied here have a long history stemming largely from quantum optics and cold atoms [183, 184, 185, 186, 187, 188, 189, 190, 191, 192, 193, 194]. In fact the monitored dynamics we consider here – in which the quantum state evolution is conditioned upon obtaining particular measurement results – is most naturally described in terms of the *quantum trajectories* formalism, a standard tool in the analysis of open quantum systems [181]. Continuous weak measurements

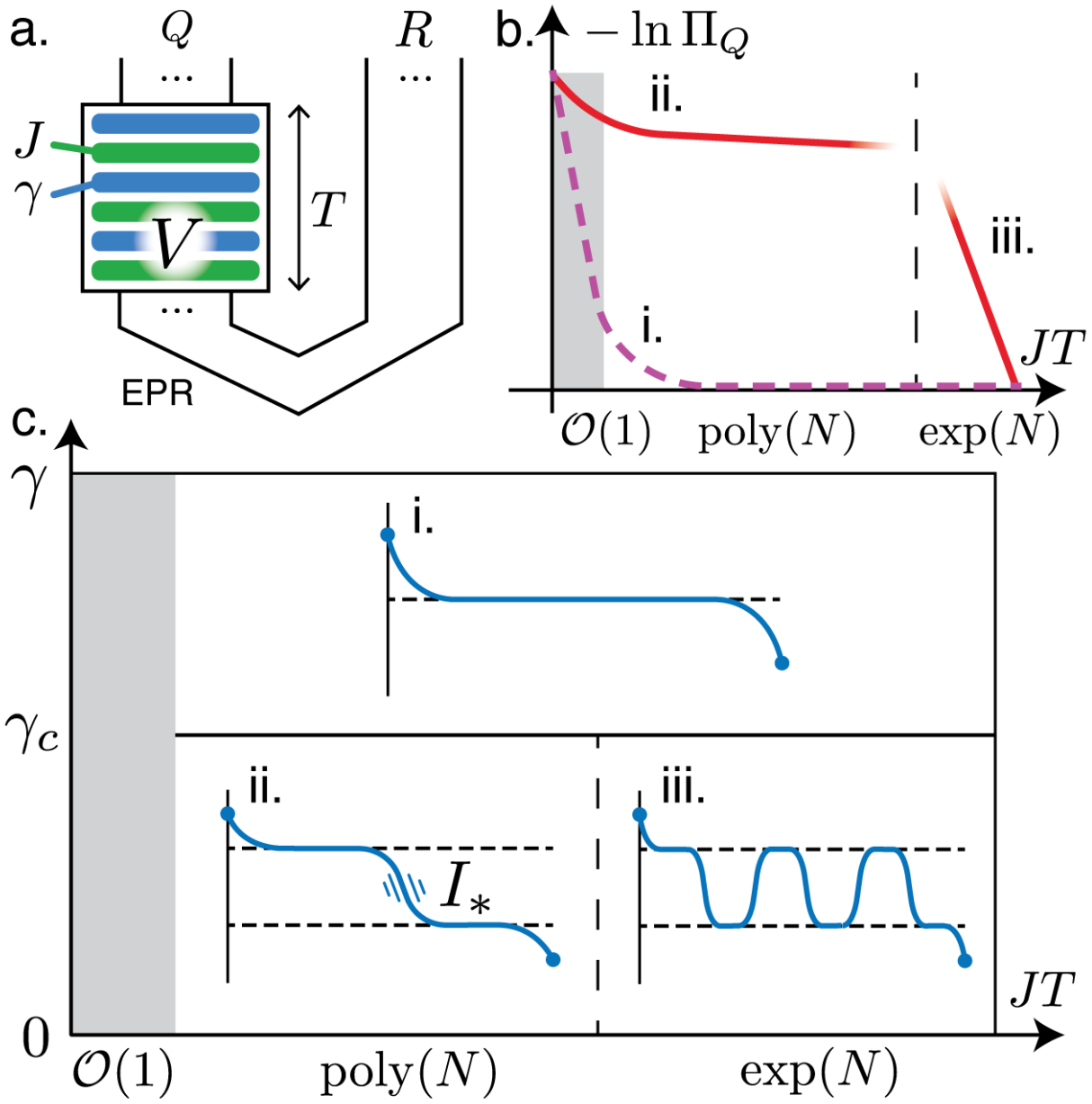

Figure 3.1: **Purification phase diagram for hybrid Brownian circuits.** (a) Hybrid Brownian circuits V composed of alternating layers of unitary Brownian dynamics of strength J (green) and non-unitary weak-measurement Brownian dynamics of strength γ (blue) exhibit a measurement-induced purification transition diagnosed by the purity Π_Q of qubits Q that are initially maximally entangled with a reference system R. (b-c) Above the critical point $\gamma > \gamma_c$ (i) bulk fields (solid blue) traverse through a single saddle point (dotted black), leading to a pure phase with purity $\Pi_Q \sim 1$ (b, dotted purple). Below the critical point $\gamma < \gamma_c$ (ii) the bulk fields tunnel between two symmetry-broken saddle points (dotted black) via a single-instanton configuration, leading to a mixed phase with $\Pi_Q \sim T \exp(-NI_*) \ll 1$ for polynomially-long times T (b, solid red). At exponentially long times the instantons proliferate and destroy the mixed phase (iii). Dynamics at early times (grey boxes) are also accessible in these models but are not the main focus of this work.

of this kind have recently been used in experiments to engineer quantum Zeno dynamics capable of producing metrologically useful entanglement [188, 190] as well as to drive phase transitions in ensembles of cold atoms [194].

The novelty of our current interest is in the interplay of these weak measurements with the many-body scrambling dynamics of a strongly-interacting system, where the competition between these two forces drives a phase transition in the structure of the many-body entangled state [23, 162, 174] that is underpinned by a dynamically-generated error-correcting code [163, 164, 166]. Whereas existing theoretical and experimental work on weak measurements, quantum feedback, and quantum control has focused largely on single- or few-body dynamics, the hybrid dynamics we consider here is strongly chaotic and many-body. In these many-body systems the quantum state follows an increasingly complex trajectory that can rapidly explore arbitrary regions of the exponentially-large Hilbert space. For this reason, new techniques and approaches are required to characterize and understand hybrid entanglement dynamics in the many-body context.

Due to the inherently many-body nature of these entanglement transitions, the earliest work on measurement-induced phase transitions was driven by numerical simulations of Clifford circuits, in which a restricted subgroup of quantum operations can be simulated efficiently on a classical computer. Subsequently, Refs. [162, 163] showed that Haar-random hybrid circuits in $1+1$d could be mapped exactly onto effective replica statistical mechanics problems in 2d. In these replica Potts models, the volume-law phase can be identified as the 'low-temperature' replica permutation symmetry-broken phase of the Potts model, while the area-law phase is associated with replica-symmetric 'paramagnetic' phase. Moreover, as we emphasize below, there are actually families of observables and phase transitions related to different kinds of averaging

procedures which translate to different kinds of replica limits. These and other mappings are general, but analytical progress has been hampered by the presence of non-positive weights in the generalized partition function; in certain cases the problem can be ameliorated by considering the limit of large local Hilbert space dimension or restricting to special classes of circuits. One also has to take a delicate replica limit to access entanglement observables averaged with respect to Born probabilities.

Throughout this body of work, a still outstanding goal is the construction of effective field theories which capture the universal physics of these various transitions. Here we make progress towards that goal by introducing new analytical tools for directly accessing measurement-induced entanglement transitions. In particular, we introduce a broad family of microscopic all-to-all hybrid Brownian circuit models exhibiting measurement-induced phase transition (MIPT) that also feature solvable large-N (mean-field) solutions. We focus on a particularly simple member of this family featuring Brownian 2-body unitary dynamics [27] and Brownian 1-body weak measurements [181, 192] and characterize the MIPT in this model in terms of the purification dynamics of a system of spins in a cluster Q that are initially maximally-entangled with a reference system R as shown in Fig. 3.1a. We write down and analyze a path integral representation for an average Π_Q of the purity $\mathrm{Tr}\left[\rho_Q^2\right]$ of the system which is controlled in the large-N limit. The technology can be readily generalized to higher moments $\mathrm{Tr}\left[\rho_Q^n\right]$ of the system density matrix as we show in Appendix B.2.

The path integral representation of the purity involves four replicas which are coupled by various collective fields and N copies of an auxiliary few-spin path integral that depends on the collective fields. We analyze this path integral using a saddle-point approach. At large N and time polynomial in N, the leading saddle point gives two distinct phases as a function of the

measurement-to-scrambling ratio γ/J as shown in Fig. 3.1b-c. Sufficiently strong measurements $\gamma > \gamma_c$ yield a paramagnetic (replica symmetry unbroken) phase with a single dominant saddle point (Fig. 3.1c.i) for all circuit depths $T \gg \mathcal{O}(1)$. As the measurement strength γ decreases through the critical point γ_c, this saddle point continuously splits into a pair of degenerate saddle points, leading to a spontaneous breaking of the replica symmetry (Fig. 3.1c.ii). Non-equal boundary conditions at times $t = 0, T$ promote the formation of *instanton* configurations in the bulk with action I_* that traverse between the two saddle points. At exponentially long times $T \sim \exp(NI_*)$, we must include subleading approximate saddles involving multi-instanton configurations. The instantons proliferate at long time and the replica symmetry is restored (Fig. 3.1c.iii).

These hybrid Brownian circuit models are motivated from several points of view. First, we wanted to consider continuous-time models for the more direct access they provide to path-integral and field-theory representations of the physics. Second, we wanted to consider models with all-to-all interactions which typically have simpler statistical properties, and we do observe that various distinct methods of averaging the purity are nearly identical for experimentally-accessible systems of modest size. Third, we wanted to analytically study the entanglement of subsystems to reveal how information about the reference is hidden from small subsystems, a key property of quantum codes. Fourth, we wanted to study models in which higher-body unitary dynamics and higher-body measurements could be seamlessly incorporated. Finally, while mean-field scrambling dynamics is also analytically accessible in random all-to-all fermion models, here we wanted to study models consisting of spins which are more directly related to potential near-term experimental realizations in cold-atom platforms. In the following we discuss each of these motivations in more detail and survey some of the main results.

First, the continuous-time path integral representation of our hybrid Brownian circuits makes it particularly easy to derive a field-theory representation of the purification phase transition. In particular, at low measurement rates close to but below the critical rate γ_c, we find in section 3.3.3 that the system entropy has critical exponent $3/2$, i.e., $-\ln \Pi_Q \sim N(\gamma_c - \gamma)^{\zeta}$, with $\zeta = 3/2$. The corresponding field theory is particularly simple, an effective $0+1$d Ising field theory, which hosts a phase transition in the limit of infinite N for finite T. Moreover, by including subleading saddles at finite N, we show in section 3.3.5 that instantons destabilize the mixed (symmetry broken) phase leading to asymptotic purification of the system at exponentially long time.

Second, a crucial aspect of the MIPT phenomena is that they are visible only in entanglement-sensitive observables like the purity that are non-linear in the density matrix. Since measurement outcomes are fundamentally random in quantum physics, one must carry out a large number of experimental trials (exponential in the number of measurements) to generate even a few copies of a particular state associated to a fixed set of measurement outcomes, which would be necessary to estimate these observables. These include so-called 'forced' transitions where one post-selects on a particular measurement outcome and the quantum state evolves according to a fixed non-unitary transformation [174, 195, 196, 197, 198] (our measurement setup is of this kind). It is also interesting to attempt to circumvent the experimental overheard by considering special hybrid circuits [199, 200].

Given this exponential post-selection cost, we are justified in considering MIPTs in families of observables with comparable experimental accessibility, no harder than simulating the Born averaged observable. The above phase diagram applies to a simple kind of averaged purity in which we average the unnormalized purity and probability separately and then divide. This cir-

cumvents the theoretical difficulty associated with averaging the purity with respect to the Born probability. We show in section 3.2.2 and in Appendix B.1 that this analytically-tractable averaging procedure actually corresponds to an experimentally-accessible observable which requires comparable experimental effort to the Born-averaged quantity. Moreover, we offer evidence from exact diagonalization that these two distinct averages are actually nearly identical in the mixed phase at modest system size.

Third, we can also directly access the purity Π_A of subsystems $A \subset Q$ in our path integral representation by modifying the boundary conditions on the path integral. In particular, this allows us to make contact between our path integral representation and the dynamically-generated quantum error correcting codes generated in the mixed phase. We show in section 3.4 that the subsystem purities are consistent with this code property and identify a critical subsystem fraction k_c above which the subsystems of Q with more than $k_c N$ qubits are entangled with the reference R for any time T polynomial in N. Within our model, we can also access the critical exponent of k_c analytically, and we find $k_c - 1/2 \sim (\gamma_c - \gamma)^\mu$, with $\mu = 1$.

Fourth, while we focus most of our attention in this work on a single model, we emphasize that the tools we develop in sections 3.2 and 3.3 are quite general. In particular, in Appendix B.2 we provide explicit path integral representations for a family of models indexed by (p, q) featuring p-body unitary interactions and q-body weak measurements. Such models could be relevant for studying measurement-only transitions [201, 202, 203, 204, 205, 206] and we conjecture they will have an even higher degree of self-averaging for larger p, q. Furthermore, these all-to-all clusters can readily be placed on different geometries, such as chains and trees, and also with various kinds of experimentally-realizable long-range interactions. We reserve detailed study of these more general models to future work.

Finally, we emphasize that hybrid Brownian dynamics similar to the type we study here could in principle be probed in experiments with optically-trapped cold neutral atoms coupled to a single-mode cavity. All-to-all interactions between atomic qubits mediated by photons in the optical cavity mode can be engineered to generate strong scrambling dynamics [207, 208, 209]. Single-site measurements in principle could be performed using state-of-the-art single-site resolution imaging techniques [210, 211]. Alternatively, weak continuous measurements of collective spin observables could be performed by monitoring photons escaping from the rear port of the cavity [188, 212] (see Appendix B.7). To probe the purity Π_Q one could prepare two identical copies of the state within a pair of atomic subensembles and interfere them [213]. To guarantee identical measurement results in the two copies one would need to perform an exponentially large number of experimental trials and post-select on matching measurement records as noted above [179]. While we acknowledge that these are daunting experimental challenges, in principle the analytical results we derive here provide precise predictions for the outcomes of real experiments that could be performed in the laboratory.

In the rest of the introduction we provide an outline for the rest of the paper. Section 3.2 introduces the hybrid Brownian circuit models and describes how they may be converted into a large-N path integral description. In section 3.2.1 we introduce the minimal $(2, 1)$ hybrid Brownian circuit model, followed by a description the averaged purity Π_Q that serves as our order parameter in section 3.2.2. We also explain the experimental interpretation of the averaged quantity in this section. In section 3.2.3 we derive the path integral representation for the purity Π_Q and derive a simplification for spin-1/2 systems in section 3.2.4. We discuss the discrete replica permutation symmetry group and its representation in path integral language in section 3.2.5.

In section 3.3 we study the purification transition in the $(2,1)$ hybrid Brownian model via large-N methods and obtain the phase diagram shown in Fig. 3.1. In section 3.3.1.1 we consider time-independent saddle-point solutions of the path integral and show that the MIPT transition is driven by a spontaneously-broken $\mathbb{Z}_2$ symmetry in the bulk. In section 3.3.1.2 we consider the role of non-uniform boundary conditions and show that these drive instanton transitions between the two degenerate saddle points. In section 3.3.2 we show that these ingredients lead to the three phases shown in Fig. 3.1b-c and compute analytical estimates for the purity Π_Q in each of these phases. In section 3.3.3 we derive a field theory for the model near criticality and show that the critical exponent for the entropy $-\ln \Pi_Q$ is $\zeta = 3/2$. We also study the path integral numerically using gradient descent methods and find a critical exponent $\zeta = 1.44 \pm 0.07$ consistent with the analytical prediction. In section 3.3.4, we show that the saddle-point approach can also capture the time-dependence of the purity at early times, and compare these predictions with results from numerical exact diagonalization in small systems. In section 3.3.5 we study the disintegration of the phase at exponentially long times due to the proliferation of instantons.

In section 3.4 we consider the purity Π_A of subsystems $A \subset Q$ as a function of subsystem fraction $k = |A| / |Q|$. In section 3.4.1 we show that measuring the purity of subsystems is equivalent to a straightforward modification of the boundary conditions in the path integral. In section 3.4.2 we use our field theory for the transition to find a critical exponent for subsystem fraction $\mu = 1$. In section 3.4.3 we interpret these results in terms of a dynamically-generated quantum error correcting code in the mixed phase. In section 3.5 we review our results and discuss directions for future work.

3.2 Hybrid Brownian circuits

In this section we define the microscopic model, a hybrid Brownian circuit combining time-dependent all-to-all 2-spin interactions and post-selected local weak measurements, and show how to express the purity Π_Q as a path integral expression with a large-N limit. This model can be generalized to allow for p-spin interactions and post-selected weak measurements of q-spin operators as described in Appendix B.2, but in the main text we focus on the simplest case with $p = 2$, $q = 1$. The system Q consists of N spins initialized in a maximally-entangled state with N additional reference spins R. The system Q is then evolved with the hybrid Brownian circuit V while the reference R is left untouched as shown in Fig. 3.1a.

In the large-N limit, we expect this model to exhibit at least two hybrid dynamical phases and a measurement-induced phase transition between them as a function of the effective measurement rate. As discussed in the introduction, the physics of these phases is only visible in non-linear functions of the quantum state. We therefore construct path integral representations of the squared probability P^2 to obtain the post-selected state and of the unnormalized purity Z_2 of the system qubits. These are the simplest observables that both access the measurement-induced phase transition and are analytically calculable. Both integrals P^2, Z_2 can be analyzed in the large-N limit by saddle-point analysis, yielding a mean-field description of the measurement-induced phase transition. In section 3.3 we analyze the physics of the $(p, q) = (2, 1)$ model at large N and demonstrate the phase structure illustrated in Fig. 3.1.

3.2.1 Model

Consider a system of N spin-S SU(2) degrees of freedom S_i^α, $i = 1, \ldots, N$, $\alpha = x, y, z$ subject to an alternating sequence of unitary and non-unitary Brownian dynamics as illustrated in Fig. 3.1a. For the moment we leave the spin length S unspecified, but we specialize to $S = 1/2$ in section 3.2.2.

On even timesteps $t = m\Delta t$, with m an integer, the spins evolve under a Brownian unitary matrix $U(t) = \exp\left[-iH(t)\Delta t/2\right]$ with Hamiltonian

$$H(t) = \sum_{\substack{i<j \\ \alpha,\beta}} J_{ij}^{\alpha\beta}(t) S_i^\alpha S_j^\beta \tag{3.1}$$

with time-dependent all-to-all couplings $\mathbf{J} = J_{ij}^{\alpha\beta}(t)$ [27]. These couplings are independent white-noise-correlated Gaussian random variables with zero mean and covariance

$$\begin{aligned} &\left\langle J_{ij}^{\alpha\beta}(t) J_{i'j'}^{\alpha'\beta'}(t') \right\rangle_{\mathbf{J}} \\ &\qquad = \frac{J}{N(S+1)^4} \frac{\delta_{tt'}}{\Delta t/2} \delta_{ii'} \delta_{jj'} \delta^{\alpha\alpha'} \delta^{\beta\beta'}. \end{aligned} \tag{3.2}$$

The scale of the fluctuations of the coupling is set by the coupling parameter $J \geq 0$. The normalization $1/N(S+1)^4$ ensures that the Hamiltonian (4.1) is extensive in N and intensive in S, and the factor $\delta_{tt'}(\Delta t/2)^{-1}$ is a regularization of the Dirac delta function $\delta(t - t')$ for white-noise random variables.

On odd timesteps $t = (2m+1)\Delta t/2$ the spins are subjected to single-site weak measurements along random spin directions. To perform each measurement we introduce an auxiliary

qubit initialized in $|\psi\rangle_{\text{aux}} = |0\rangle_{\text{aux}}$ and couple it to the system via a unitary interaction,

$$\exp\left[-i\frac{\Delta t}{2}\mathcal{O}(t)\sigma^x_{\text{aux}}\right]|\Psi\rangle\,|0\rangle_{\text{aux}}\,, \tag{3.3}$$

where $|\Psi\rangle$ is the state of the many-body system prior to the weak measurement, σ^x_{aux} is the Pauli-x operator acting on the auxiliary qubit, and $\mathcal{O}(t) = \sum_{i,\alpha} n_i^\alpha(t) S_i^\alpha$ is the random spin operator to be measured. We then perform a projective measurement of the auxiliary qubit in the σ^y_{aux} eigenbasis and post-select for $+1$ results. The many-body state $|\Psi\rangle$ is thereby transformed to

$$\begin{aligned}|\Psi\rangle &\to M(t)\,|\Psi\rangle \\ &= \left(1 - \frac{1}{2}\mathcal{O}\Delta t - \frac{1}{8}\mathcal{O}^2\Delta t^2 + \cdots\right)|\Psi\rangle\end{aligned} \tag{3.4}$$

to lowest order in $\Delta t/2$ (note that $M(t) \neq \exp\left[-\mathcal{O}(t)\Delta t/2\right]$). Note that under this measurement setup, the state evolves non-unitarily, and also deterministically, without any inherent measurement randomness. Similar to the unitary Brownian dynamics above, we take the coefficients $\mathbf{n} = n_i^\alpha(t)$ to be independent white-noise-correlated Gaussian random variables with zero mean and covariance

$$\left\langle n_i^\alpha(t) n_{i'}^{\alpha'}(t')\right\rangle_{\mathbf{n}} = \frac{\gamma}{(S+1)^2}\frac{\delta_{tt'}}{\Delta t/2}\delta_{ii'}\delta^{\alpha\alpha'}. \tag{3.5}$$

The fluctuations in $\mathbf{n}$ are controlled by the parameter $\gamma \geq 0$. Due to the post-selection step the operator $M(t)$ does not conserve probabilities, and the resulting state $M(t)\,|\Psi\rangle$ is not normalized.

The full time evolution of the system is constructed by stacking alternating layers of $U(t)$

and $M(t)$ gates

$$V \equiv \prod_{t=0}^{T} M(t)U(t) \tag{3.6}$$

as shown in Fig. 3.1a. Given an initial state ρ_0 and a fixed disorder realization $\mathbf{J}, \mathbf{n}$ this hybrid circuit produces the unnormalized output state $\tilde{\rho}(V) = V\rho_0 V^\dagger$ with probability $P = \mathrm{Tr}\left[\tilde{\rho}(V)\right] \leq 1$. The relative strength of measurement and scrambling in this circuit is controlled by the dimensionless ratio γ/J.

3.2.2 Phase structure and observables

When $\gamma = 0$ the weak measurement layers have no effect and we recover a unitary Brownian circuit that strongly scrambles quantum information [27]. For a system Q maximally entangled with a reference R at time $t = 0$ (Fig. 3.1a), the purely unitary dynamics obtained at $\gamma = 0$ preserves the entanglement between Q, R for all time. Specifically, if we measure the 2nd Rényi entropy of the system as a function of a time, it will remain at its maximal value $S_Q^{(2)} = N \ln 2$ for all time. This is analogous to a 'volume-law' phase for the Rényi entropy of the system. We can also equivalently consider the purity $\Pi_Q = \exp\left(-S_Q^{(2)}\right)$.

Once we consider a non-zero rate γ of weak measurements, the purely unitary dynamics is modified to include processes that degrade entanglement. In particular, for sufficiently large γ the measurements will dominate and all the entanglement between the system and the reference will be destroyed, thus *purifying* the system. In this case, $S_Q^{(2)} = 0$ and $\Pi_Q = 1$ (Fig. 3.1b, dotted purple) [23].

The Rényi entropy $S_Q^{(2)}$ or the purity Π_Q therefore serve as order parameters for the *purification transition*. Our goal in the remainder of this section is to derive a path integral expression

for the purity Π_Q, computed for a particular analytically-tractable disorder average. We begin by specifying in more detail the quantity of interest.

Consider a single realization of the circuit $V = V(\mathbf{J}, \mathbf{n})$ which produces a pure unnormalized quantum state $\tilde{\rho}(V)$ of the system and reference. To calculate the purity $\mathrm{Tr}\left[\tilde{\rho}_Q^2(V)\right]$ of the system's reduced density matrix $\tilde{\rho}_Q(V) = \mathrm{Tr}_R\left[\tilde{\rho}(V)\right]$ for this trajectory, we introduce a second identical copy $\tilde{\rho}'(V) = \tilde{\rho}(V)$ of the system and reference with the same post-selected measurement results and identical dynamics and compute the expectation value of the $\mathrm{SWAP}_{QQ'}$ operator [213, 214, 215, 216],

$$Z_2(V) \equiv \mathrm{Tr}\left[\tilde{\rho}_Q^2(V)\right] = \mathrm{Tr}\left[(\tilde{\rho} \otimes \tilde{\rho}')\mathrm{SWAP}_{QQ'}\right], \tag{3.7}$$

which gives the purity of the unnormalized state $\tilde{\rho}_Q(V)$. The purity $\Pi_Q = \mathrm{Tr}\left[\rho_Q^2\right] = Z_2/P^2$ of the normalized state $\rho_Q = \tilde{\rho}_Q/\mathrm{Tr}\left[\tilde{\rho}_Q\right]$ is obtained simply by dividing Z_2 by the squared probability for this trajectory,

$$P^2(V) \equiv \mathrm{Tr}\left[\tilde{\rho}_Q(V)\right]^2 = \mathrm{Tr}\left[\tilde{\rho} \otimes \tilde{\rho}'\right]. \tag{3.8}$$

From Eqs. (3.7) and (3.8) it is clear that the quantity Z_2 differs from P^2 only in the presence of the $\mathrm{SWAP}_{QQ'}$ operator. As we shall see, this SWAP operator modifies the initial and final boundary conditions of the system, leading to fundamentally different physics in Z_2 and P^2.

The normalized purity $\Pi_Q = Z_2/P^2$ is in principle an experimentally-accessible observable and can be measured in the following way, which we discuss in more detail in Appendix B.1. The experimentalist first fixes the parameters $\mathbf{J}, \mathbf{n}$ and then applies the Brownian circuit dynamics $V(\mathbf{J}, \mathbf{n})$, repeatedly performing the necessary projective measurements until the desired

measurement record is obtained (i.e. $+1$ for all σ^y_{aux} measurements). If the σ^y_{aux} outcomes are close to equally likely, this will require a number of experimental runs scaling like $2^{N_{\text{aux}}}$, where N_{aux} is the total number of auxiliary measurement qubits used over the whole circuit. Each successful run is stored as a quantum state $\tilde{\rho}(V)$, and then once enough copies of the state have been obtained, the experimentalist can perform SWAP tests to estimate the value of the purity $\Pi_Q(V) = Z_2(V)/P^2(V)$ for this circuit realization V. If the purity is expected to be small, this estimate will require many samples to gather sufficient statistics. The total number of experiments required in this brute force approach is thus no more than 2^{aNt+bN}, where the 2^{aNt} piece represents the $2^{N_{\text{aux}}}$ experimental runs required for post-selection and the 2^{bN} piece represents extra copies needed to estimate the purity from SWAP tests.

Next, we can consider sampling the normalized purity $\Pi_Q(V)$ over different circuit realizations $V = V(\mathbf{J}, \mathbf{n})$. The average of these samples then defines the circuit-averaged purity $\overline{\Pi_Q}$. The circuit-averaged purity can be estimated experimentally by simply repeating the above procedure for each sample $\mathbf{J}, \mathbf{n}$, yielding

$$\overline{\Pi_Q} = \sum_V \pi(V) \frac{Z_2(V)}{P^2(V)}, \tag{3.9}$$

where $\pi(V) = \pi(V(\mathbf{J}, \mathbf{n}))$ is the probability for a particular circuit realization $\mathbf{J}, \mathbf{n}$. While the experimental protocol for computing this disorder-averaged quantity is clear, this kind of average is difficult to calculate with, since the random variables $\mathbf{J}, \mathbf{n}$ appear in numerator and denominator of Eq. (3.9).

In this work we make analytical progress by sampling trajectories differently. A particularly

convenient choice is to consider

$$\langle \Pi_Q \rangle = \frac{\langle Z_2 \rangle}{\langle P^2 \rangle}, \tag{3.10}$$

where both $\langle Z_2 \rangle = \sum_V \pi(V) Z_2(V)$ and $\langle P^2 \rangle = \sum_V \pi(V) P^2(V)$ are individually averaged over circuit realizations $V = V(\mathbf{J}, \mathbf{n})$. While one might reasonably protest that the disorder-averaged quantity $\langle \Pi_Q \rangle$ is not as physical as the quantity $\overline{\Pi_Q}$, we show in Appendix B.1 that measuring $\langle \Pi_Q \rangle$ just corresponds to sampling the purity $\Pi_Q(V)$ over trajectories with a different probability distribution $\pi'(V)$ from the usual circuit probability distribution $\pi(V)$. Moreover, we demonstrate that the disorder-averaged quantity $\langle \Pi_Q \rangle$ requires only classical post-processing and no more quantum resources than simulating $\overline{\Pi_Q}$.

In the rest of the paper, we consider the deterministic weak measurement setup for qubits $S = 1/2$, and suppress the $\langle \ldots \rangle$ notation for Π_Q, Z_2 and P^2, always referring to the particular averaged quantity whenever Π_Q, Z_2 and P^2 are considered. Also, we will make statements about the Rényi-2 entropy-like quantity $-\ln \langle \Pi_Q \rangle$ derived from the averaged purity $\langle \Pi_Q \rangle$. This is obviously not the same as the averaged Rényi-2 entropy of the system, since we are averaging the purity and then taking the logarithm. In the rest of the paper, when referring to the entropy of the system we always refer to the quantity $-\ln \langle \Pi_Q \rangle$, which is what we can access analytically.

3.2.3 Path integral representation

We have expressed the unnormalized purity Z_2 and squared probability P^2 in Eqs. (3.7) and (3.8) using two identical copies $\tilde{\rho}' = \tilde{\rho}$ of the unnormalized state. To express these quantities in path-integral language, we first use the Choi-Jamiołkowski isomorphism to convert the mixed-state dynamics on two copies of the system into pure-state dynamics on four copies [217, 218]. In

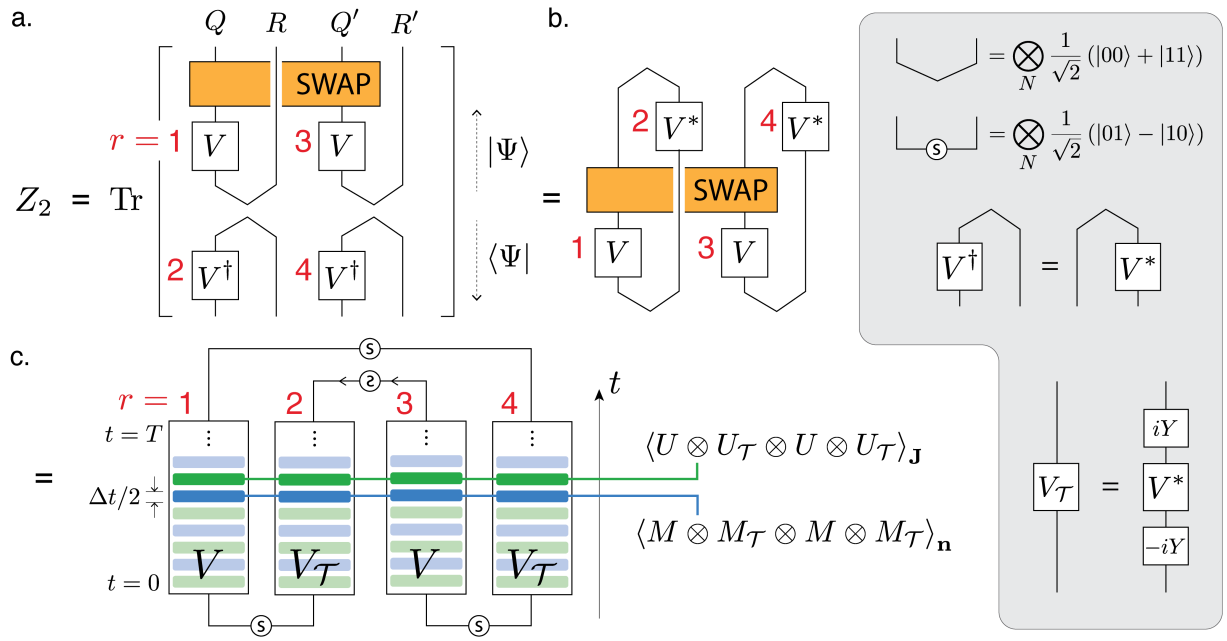

Figure 3.2: **Unnormalized purity for the hybrid Brownian circuit.** The purity $Z_2 = \mathrm{Tr}\left[\tilde{\rho}_Q^2\right]$ of the unnormalized state $\tilde{\rho}_Q$ is equivalent to the expectation value of the $\mathrm{SWAP}_{QQ'}$ operator evaluated on two identical copies $\tilde{\rho}, \tilde{\rho}'$ of the system. Straightforward rearrangement of the circuit yields pure-state dynamics on four replicas $r = 1, 2, 3, 4$ with nontrivial boundary conditions at $t = 0, T$. Because the Brownian coefficients $\mathbf{J}, \mathbf{n}$ are uncorrelated in time, the disorder averages $\langle \cdot \rangle_{\mathbf{J},\mathbf{n}}$ at each circuit layer (solid green, solid blue) can be computed independently. Arrows on the $t = T$ boundary condition indicate a 'reversed' singlet state $|(32)\rangle = -|(23)\rangle$. The corresponding circuit for the squared probability P^2 is identical except for the SWAP-ed boundary condition at $t = T$.

its simplest form, this isomorphism just maps the two-copy density matrix $|\psi\rangle\langle\psi| \otimes |\psi'\rangle\langle\psi'|$ to the four-replica pure state $|\psi\rangle|\psi\rangle|\psi'\rangle|\psi'\rangle$. More generally, this isomorphism provides a mapping between quantum operators $\mathcal{O}$ acting on a Hilbert space $\mathcal{H}$ and pure quantum states $|\mathcal{O}\rangle$ living in a doubled Hilbert space $\mathcal{H} \otimes \mathcal{H}$.

In our calculation this conversion from mixed-state dynamics to doubled pure-state dynamics is easiest to see when the quantities Z_2, P^2 are represented graphically using a tensor-network representation as shown in Fig. 3.2a, where downward-facing external legs represent bras $\langle\psi|$ and upward-facing legs represent kets $|\psi\rangle$. The two copies of the system Q, Q' are initially maximally entangled with their respective reference systems R, R' via EPR pairs $|\mathrm{EPR}\rangle = \bigotimes_N (|00\rangle + |11\rangle)/\sqrt{2}$. Hybrid Brownian dynamics V are then applied to the system qubits Q, Q', and the $\mathrm{SWAP}_{QQ'}$ operator (orange) exchanges qubits in the two systems to yield the purity Z_2. Each instance of the time-evolution matrix V has been labeled by a *replica index* $r = 1, 2, 3, 4$.

Evaluating the trace and using the identity

$$\langle \mathrm{EPR}| (V^\dagger \otimes \mathbb{I}) = \langle \mathrm{EPR}| (\mathbb{I} \otimes V^*) \tag{3.11}$$

we can bring the purity into the form shown in Fig. 3.2b. In this form the dynamics may be interpreted as pure-state dynamics on four replicas of the system, where replicas $r = 1, 3$ are subject to time-evolution V while replicas $r = 2, 4$ are subject to complex-conjugated time-evolution V^*. The EPR pairs and $\mathrm{SWAP}_{QQ'}$ operator yield nontrivial boundary conditions on the initial and final quantum states as shown in Fig. 3.2c. These boundary conditions are analogous to those imposed at the input and output states of Haar-random tensor network models exhibiting

a MIPT [166].

Complex conjugation V^* is naturally related to time-reversal symmetry in quantum mechanics [219]. For spin-1/2 degrees of freedom, the conventional definition of time reversal also includes conjugation by $i\sigma^y$, since complex conjugation alone only reverses the y component of spin,

$$(\sigma^x, \sigma^y, \sigma^z)^* = (\sigma^x, -\sigma^y, \sigma^z). \tag{3.12}$$

In replicas $r = 2, 4$ we therefore reflect all spin components in the σ^x, σ^z spin plane via the operator $iY = i\prod_i \sigma_i^y$, such that

$$\begin{aligned} V^* &= (-iY)(iY)V^*(-iY)(iY) \\ &= (-iY)V_{\mathcal{T}}(iY) \end{aligned} \tag{3.13}$$

where $V_{\mathcal{T}} = (iY)V^*(-iY)$ is the properly time-reversed version of the time evolution operator V [219]. With this additional coordinate change the spin-1/2 Pauli matrices transform correctly as $\vec{\sigma} \to \vec{\sigma}_{\mathcal{T}} = -\vec{\sigma}$ as required for angular momentum vectors under time-reversal $\mathcal{T}$. We regard this additional rotation as a convenient parameterization that makes the $\mathrm{SU}(2)$ invariance of the problem manifest in the resulting path integral.

The remaining factors of $\pm iY$ introduced into the four-replica circuit by this change of

coordinates serve to convert the initial and final EPR pairs into spin singlets:

$$\mp\frac{1}{\sqrt{2}}\left(\mathbb{I}\otimes i\sigma_y\right)\left(|00\rangle+|11\rangle\right)_{rs}=\pm\frac{1}{\sqrt{2}}\left(|01\rangle-|10\rangle\right)$$
$$=\pm|(rs)\rangle \tag{3.14}$$

where $|(rs)\rangle$ denotes a spin-singlet state between replicas r, s. The spin-singlet is antisymmetric under replica exchange $|(rs)\rangle = -|(sr)\rangle$, but because the four-replica circuit features pairs of identical singlet states at $t = 0, T$ these overall negative signs cancel such that Z_2, P^2 are always positive. The unnormalized purity Z_2 is initialized with spin-singlet pairs $|(12)(34)\rangle$ entangling replicas 1-2 and 3-4 as shown in Fig. 3.2c, while the final state $|(14)(32)\rangle$ has spin singlets entangling replicas 1-4 and 3-2 due to the $\mathrm{SWAP}_{QQ'}$ operator. These non-equal boundary conditions in Z_2 lead to most of the interesting physical consequences explored in this work. By contrast, without the $\mathrm{SWAP}_{QQ'}$ operator the squared probability P^2 has identical singlet-pair states $|(12)(34)\rangle$ at both initial and final times.

With the unnormalized purity Z_2 and squared probability P^2 expressed in terms of pure-state dynamics on four replicas $r = 1, 2, 3, 4$, we now perform the disorder average over the Brownian coefficients $\mathbf{J}, \mathbf{n}$ and show that this leads to path-integral expressions for Z_2, P^2. Because the disorder $\mathbf{J}, \mathbf{n}$ is uncorrelated in time due to the delta function $\delta_{tt'}$, we may compute the disorder average for each circuit layer $U(t), M(t)$ separately as shown in Fig. 3.2c. Expanding each $U(t) = \exp\left[-iH(t)\Delta t/2\right]$ to lowest order in Δt, the disorder average over a single unitary

layer yields

$$\begin{aligned}\langle U\otimes U_{\mathcal{T}}\otimes U\otimes U_{\mathcal{T}}\rangle_{\mathbf{J}} &= 1-\frac{\Delta t^2}{4}\sum_{r<s}(-1)^{r+s}\langle H^r H^s\rangle_{\mathbf{J}}-\frac{1}{2}\frac{\Delta t^2}{4}\sum_r\langle H^r H^r\rangle_{\mathbf{J}}+\mathcal{O}(\Delta t^4)\\ \langle H^r H^s\rangle_{\mathbf{J}} &= \frac{J}{\Delta t}\frac{N}{(S+1)^4}\left(\frac{1}{N}\sum_i \mathbf{S}_i^r\cdot\mathbf{S}_i^s\right)^2. \end{aligned}\tag{3.15}$$

where terms linear in Δt vanish because $\mathbf{J}$ has zero mean and where $\mathbf{S}_i^r\cdot\mathbf{S}_i^s\equiv\sum_\alpha S_i^{\alpha,r}S_i^{\alpha,s}$ is the standard dot product. The second line holds as an operator equation, where $H^{r,s}$ denote copies of the Hamiltonian (4.1) acting on replicas $r,s=1,2,3,4$. The factor of Δt in the denominator comes from the regularization of the white-noise random variables Eq. (3.2), while the overall factor of N comes from the sum $\sum_i$ over spins and is ultimately responsible for large-N control. The replica-dependent factor $(-1)^{r+s}$ is a consequence of the time-reversed dynamics in replicas $r=2,4$, and is a crucial feature of the field theory governing the MIPT.

We can therefore express each disorder-averaged unitary circuit layer as a propagator $I_J[\mathbf{S}_i^r]$ over $4N$ spins $\mathbf{S}_i^r$:

$$\begin{aligned}\langle U\otimes U_{\mathcal{T}}\otimes U\otimes U_{\mathcal{T}}\rangle_{\mathbf{J}} &= e^{-NI_J[\mathbf{S}_i^r]\Delta t},\\ I_J[\mathbf{S}_i^r] &\equiv \frac{J}{4(S+1)^4}\sum_{r<s}(-1)^{r+s}\left(\frac{1}{N}\sum_i\mathbf{S}_i^r\cdot\mathbf{S}_i^s\right)^2\\ &\quad+\frac{JS^2}{2(S+1)^2}\end{aligned}\tag{3.16}$$

which holds as an operator equation to lowest order in Δt. Similar manipulations for the non-

unitary circuit layers yield a propagator $I_\gamma[\mathbf{S}_i^r]$

$$\begin{aligned}\langle M \otimes M_{\mathcal{T}} \otimes M \otimes M_{\mathcal{T}} \rangle_{\mathbf{n}} &= e^{-NI_\gamma[\mathbf{S}_i^r]\Delta t}, \\ I_\gamma[\mathbf{S}_i^r] &\equiv \frac{-\gamma}{2(S+1)^2} \sum_{r<s} (-1)^{r+s} \left(\frac{1}{N} \sum_i \mathbf{S}_i^r \cdot \mathbf{S}_i^s \right) \\ &+ \frac{\gamma S}{(S+1)}\end{aligned} \tag{3.17}$$

where there is a relative minus sign in the first term compared to Eq. (3.16). In terms of the propagators I_J, I_γ, the disorder-averaged unnormalized purity Z_2 (or squared probability P^2) is given by a stack of alternating unitary and non-unitary propagators with appropriate boundary conditions, i.e.

$$\begin{aligned}&\left\langle Z_2 \text{ or } P^2 \right\rangle_{\mathbf{J},\mathbf{n}} \\ &= \langle \psi_T | \prod_t e^{-NI_\gamma \Delta t} e^{-NI_J \Delta t} | \psi_0 \rangle\end{aligned} \tag{3.18}$$

where the initial and final states

$$|\psi_0\rangle, |\psi_T\rangle = \{|(12)(34)\rangle, |(14)(32)\rangle\} \tag{3.19}$$

are the singlet-pair states enforcing the non-uniform boundary conditions that distinguish Z_2 from P^2. Notice that both the unitary and non-unitary propagators in Eq. (3.18) are preceded by a factor N which allows for analytical control over fluctuations in the thermodynamic limit.

In performing the disorder average we have exchanged inter-site couplings $S_i^\alpha S_j^\beta$ in the original Hamiltonian (4.1) for inter-replica couplings $\mathbf{S}_i^r \cdot \mathbf{S}_i^s$ in the propagator (3.18). As a

consequence, the propagators I_J, I_γ are functions only of the mean-field variables

$$G_{rs} = \left(\frac{1}{N} \sum_i \mathbf{S}_i^r \cdot \mathbf{S}_i^s \right) / (S+1)^2 \tag{3.20}$$

with $r < s$, which mediate all spin-spin interactions. Because these mean fields consist of a large number of independent and identical degrees of freedom, their dynamics is highly classical with fluctuations controlled by the system size N. These simplifying features are typical of disorder-average calculations performed in the context of mean-field spin glass theory [220, 221] and the SYK model [12, 25, 222], where the high amount of connectivity between degrees of freedom naturally leads to mean-field behavior. Because our Brownian interactions are all-to-all, a similar phenomenon occurs in our hybrid model and the physics can be captured by the mean fields G_{rs}.

Formally, we convert the propagator (3.18) to a path integral by introducing an over-complete basis of coherent spin states $|\mathbf{\Omega}\rangle_i^r$ parameterized by $\mathrm{SO}(3)$ unit vectors $\mathbf{\Omega}$ and satisfying the eigenvalue equation $\mathbf{\Omega} \cdot \mathbf{S}_i^r |\mathbf{\Omega}\rangle_i^r = S |\mathbf{\Omega}\rangle_i^r$ for each spin $\mathbf{S}_i^r$ [223, 224]. Using this basis we insert resolutions of the identity

$$\mathbb{I} = \int \frac{2S+1}{4\pi} d^2\mathbf{\Omega}_i^r \, |\mathbf{\Omega}_i^r\rangle \langle \mathbf{\Omega}_i^r| \tag{3.21}$$

at each timestep Δt following the usual rules of path integration. This effectively converts the spin operators in the propagators I_J, I_γ into classical $\mathrm{SO}(3)$ vectors $\mathbf{S}_i^r \to (S+1)\mathbf{\Omega}_i^r$. The standard path integral derivation also generates 'kinetic' or Berry phase terms $\sim \Omega \partial_t \Omega$ in the path integral coming from overlaps $\langle \mathbf{\Omega}_i^r(t) | \mathbf{\Omega}_i^r(t+\Delta t) \rangle$ of the coherent spin states at consecutive time steps [224] (see Appendix B.2.0.3 for more details).

Next, to enforce the identification (3.20) we introduce six time-dependent mean fields $G_{rs}(t)$ and six Lagrange multiplier fields $F_{rs}(t)$ into the path integral via the identity

$$1 = \int \prod_{r<s} \mathcal{D}F_{rs}\mathcal{D}G_{rs} \exp\left[\int dt \sum_{r<s} iF_{rs}\left(G_{rs} - \frac{1}{N}\sum_i \mathbf{\Omega}_i^r \cdot \mathbf{\Omega}_i^s\right)\right] \tag{3.22}$$

With this delta-function constraint now explicit in the path integral, we may simply substitute the mean fields G_{rs} for any mean-field Heisenberg terms $\sum_i \mathbf{\Omega}_i^r \cdot \mathbf{\Omega}_i^s/N$ that appear in the propagators I_J, I_γ. In particular, the unitary part I_J of the path integral Eq. (3.16) contributes quadratic terms $\propto JG_{rs}^2$ while the non-unitary part I_γ Eq. (3.17) contributes linear terms $\propto \gamma G_{rs}$. After making this replacement the only spins $\mathbf{\Omega}_i^r$ explicitly remaining in the path integral are those coupled to the Lagrange multiplier fields iF_{rs} coming from the delta-function constraint Eq. (3.22).

Thus in the limit $\Delta t \to 0$ at fixed T we finally arrive at

$$\begin{aligned}
Z_2 \text{ or } P^2 &= \int \left(\prod_{r<s} \mathcal{D}F_{rs}\mathcal{D}G_{rs}\right) \exp\left[-NI\left[F_{rs}, G_{rs}\right]\right] \\
I[F_{rs}, G_{rs}] &= \int_0^T dt \left[\frac{J}{4}\sum_{r<s}(-1)^{r+s}G_{rs}^2 - \frac{\gamma}{2}\sum_{r<s}(-1)^{r+s}G_{rs} - i\sum_{r<s}F_{rs}G_{rs}\right] - \ln K[F_{rs}, \psi_0, \psi_T] \\
K[F_{rs}, \psi_0, \psi_T] &= \langle\psi_T| \exp\left[-\int_0^T dt \sum_{r<s} iF_{rs}\frac{\mathbf{S}^r \cdot \mathbf{S}^s}{(S+1)^2}\right] |\psi_0\rangle \,.
\end{aligned} \tag{3.23}$$

where we have expressed the path integral over spins $\mathbf{S}^r$ as a time-ordered exponential propagator $K[F_{rs}, \psi_0, \psi_T]$ and the choice of boundary states $|\psi_0\rangle, |\psi_T\rangle$ determines whether the expression corresponds to Z_2 or P^2. The path integral expression (3.23) is the main technical result of this section. Here the quadratic terms in the action $\propto JG_{rs}^2$ correspond to the unitary part of the dy-

namics while the linear terms $\propto \gamma G_{rs}$ correspond to the non-Hermitian weak measurement part. The competition between these two terms as a function of γ/J is what drives the measurement-induced phase transition in this model.

Due to the overall factor of N preceding the action $I[F_{rs}, G_{rs}]$ in Eq. (3.23), we can evaluate the path integral via steepest-descent when N is large. In this limit, the action I may be viewed as a classical Lagrangian where the first two terms describe effective potential energies for the mean fields G_{rs} and the third term is a coupling between the G_{rs} and the Lagrange multipliers F_{rs}. The propagator K evolves an initial state $|\psi_0\rangle$ of four spin-1/2 degrees of freedom $\mathbf{S}^r$ to a final state $|\psi_T\rangle$ under the influence of time-dependent external fields $iF_{rs}(t)$. We perform this steepest-descent analysis for time-independent fields F_{rs}, G_{rs} in section 3.3.1.1, and consider time-dependent fields leading to instanton transitions in section 3.3.1.2. This large-N analysis yields an analytically tractable description of the system over a large portion of the phase diagram shown in Fig. 3.1.

Although our focus in this work is on the simplest mean-field model (3.23) featuring bilinear spin interactions ($p = 2$), single-spin weak measurements ($q = 1$), and probed by the purity $\mathrm{Tr}\left[\tilde{\rho}_Q^n\right]$ with $n = 2$, we show in Appendix B.2 how this $(2, 1)$ model can be easily generalized to arbitrary (p, q) hybrid Brownian models featuring higher-order interaction and measurement terms and probed by nth-order moments $\mathrm{Tr}\left[\tilde{\rho}_Q^n\right]$ of the density matrix. From this more general derivation we find that the choice of p, q only affects the G_{rs}-dependent part of the action I, while the propagator K is unaffected by the order of the unitary interactions or weak measurements. By contrast, the parameter n changes the number of replicas r, s but otherwise leaves the path integral (3.23) unchanged. We reserve the study of these more general models for future work.

3.2.4 Simplification of spin-1/2 propagator K

Before performing a saddle-point analysis of the action (3.23) at large-N, however, it is convenient to first simplify the four-replica propagator $K[F_{rs}, \psi_0, \psi_T]$ for the special case $S = 1/2$. This case is particularly easy to calculate because the Heisenberg coupling terms $\mathbf{S}^r \cdot \mathbf{S}^s$ in the propagator as well as the initial and final singlet-pair states are all manifestly $\mathrm{SU}(2)$ invariant. In fact, because the initial and final states $|(12)(34)\rangle$, $|(14)(32)\rangle$ are pairs of $\mathrm{SU}(2)$ spin singlets, the four-replica system is constrained at all times to live in the subspace of total spin $\mathbf{S}^{\mathrm{Tot}} = 0$, in which the total spin operators $\mathbf{S}^{\mathrm{Tot}} = \sum_r \mathbf{S}^r$, summed over all four replicas, act trivially and the Casimir operator $\mathbf{S}^{\mathrm{Tot}} \cdot \mathbf{S}^{\mathrm{Tot}} = \mathcal{S}(\mathcal{S}+1)$ has eigenvalue $\mathcal{S} = 0$. For four spin-1/2 degrees of freedom $\mathbf{S}^r$ with $r = 1, 2, 3, 4$ this subspace is two-dimensional and is spanned by the basis vectors

$$\begin{aligned} |\uparrow\rangle &= \frac{1}{2\sqrt{3}} \left(2\,|1010\rangle + 2\,|0101\rangle - |0011\rangle - |1100\rangle \right. \\ &\qquad\qquad \left. - |1001\rangle - |0110\rangle\right) \\ |\downarrow\rangle &= \frac{1}{2} \left(|0011\rangle + |1100\rangle - |1001\rangle - |0110\rangle\right) \end{aligned} \tag{3.24}$$

which transform trivially under global $\mathrm{SU}(2)$ rotations generated by the total spin operators $\mathbf{S}^{\mathrm{Tot}}$. We view this two-dimensional subspace of the replica space as encoding an effective two-level system $|\psi(t)\rangle = \psi_\uparrow(t)\,|\uparrow\rangle + \psi_\downarrow(t)\,|\downarrow\rangle$ which we refer to as a *replica-bit* or *r-bit*. The instantaneous state of the r-bit may be drawn on a Bloch sphere as shown in Fig. 3.3.

In the two-dimensional basis $|\uparrow\rangle, |\downarrow\rangle$ the initial and final boundary conditions may be sim-

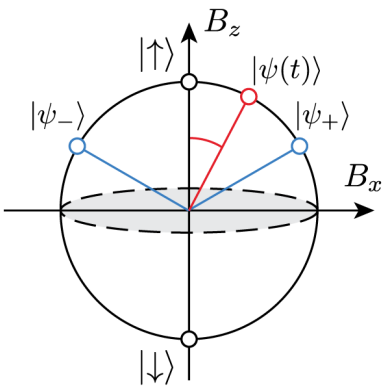

Figure 3.3: **Bulk two-level r-bit subspace** $|\uparrow\rangle, |\downarrow\rangle$. For $S = 1/2$, the $\mathrm{SU}(2)$ symmetry of the problem kinematically constrains the dynamics to a single effective qubit or *r-bit* $|\psi(t)\rangle$ (red) living in the $\mathbf{S}^{\mathrm{Tot}} = 0$ subspace spanned by $|\uparrow\rangle, |\downarrow\rangle$. The r-bit's trajectory $|\psi(t)\rangle$ must begin on the singlet-pair state $|\psi_+\rangle = |(12)(34)\rangle$, and end on the same singlet-pair state for P^2 or on the SWAP-ed singlet-pair state $|\psi_-\rangle = |(14)(32)\rangle$ for Z_2.

ply written in terms of the states

$$|\psi_\pm\rangle = \frac{\sqrt{3}}{2}|\uparrow\rangle \pm \frac{1}{2}|\downarrow\rangle, \tag{3.25}$$

where the initial and final states $|\psi_0\rangle, |\psi_T\rangle$ take the values:

	$t = 0$	$t = T$
Z_2	$\|\psi_+\rangle$	$\|\psi_-\rangle$
P^2	$\|\psi_+\rangle$	$\|\psi_+\rangle$

(3.26)

such that Z_2, P^2 differ only in the final boundary conditions at $t = T$. The difference between the non-uniform boundary conditions for Z_2 compared to the uniform boundary conditions for P^2 will be crucial in distinguishing between the mixed and purified phases.

The propagator in the two-dimensional r-bit subspace simplifies to

$$K[\vec{B}, \psi_0, \psi_T] = \\ \langle \psi_T | \exp\left[\frac{1}{2}\int_0^T dt\ \vec{B}(t)\cdot\vec{\sigma}\right] |\psi_0\rangle\, e^{B_0 T/2} \tag{3.27}$$

where $\vec{\sigma}$ are the 2×2 Pauli matrices acting on the r-bit $|\uparrow\rangle, |\downarrow\rangle$ subspace and $\vec{B}(t)$ is a time-dependent 'magnetic field' with components

$$\begin{aligned} B_x &= \frac{2}{3\sqrt{3}}\left(iF_{12} + iF_{34} - iF_{14} - iF_{23}\right) \\ B_y &= 0 \\ B_z &= \frac{2}{9}\sum_{r<s} iF_{rs} - \frac{2}{3}\left(iF_{13} + iF_{24}\right) \end{aligned} \tag{3.28}$$

and where terms proportional to the identity within the r-bit subspace have been collected into the term

$$B_0 = \frac{2}{9}\sum_{r<s} iF_{rs}. \tag{3.29}$$

The time-dependent bulk fields $B_x(t), B_z(t)$ encode the relevant mean-field dynamics of the r-bit $\psi(t)$, and in general must execute nontrivial motions in the bulk in order to satisfy the non-equal boundary conditions $|\psi_0\rangle, |\psi_T\rangle$. By contrast, the remaining fields in the action I appear simply as quadratic Gaussian fields and may therefore be trivially integrated out of the path integral,

leading to the effective action

$$
\begin{aligned}
Z_2 \text{ or } P^2 &= \int \mathcal{D}B_x \mathcal{D}B_z \exp\left[-NI[\vec{B}]\right] \\
I[\vec{B}] &= \int_0^T dt \left[\frac{27B_x^2}{4J} - \frac{81B_z^2}{4J} + B_z(1+18\gamma) - \frac{J}{72} - \frac{4\gamma^2}{J} - \frac{\gamma}{2}\right] - \ln K[\vec{B}, \psi_0, \psi_T] \\
K[\vec{B}, \psi_0, \psi_T] &= \langle \psi_T | \exp\left[\frac{1}{2}\int_0^T dt \left(B_x\sigma_x + B_z\sigma_z\right)\right] |\psi_0\rangle \,. \qquad (3.30)
\end{aligned}
$$

which is a simplification of the general path integral (3.23) for the special case $S = 1/2$.

In this form, one can view the magnetic field variables $\vec{B}(t)$ as 'guiding fields' for the bulk r-bit, in the sense that the propagator $-\ln K$ in (C.47) is minimized when the r-bit $|\psi(t)\rangle$ is in the instantaneous ground state of the effective 'magnetic-field' Hamiltonian $H(\vec{B}) = -\vec{B}(t)\cdot\vec{\sigma}/2$ appearing in the propagator K. As a result of this coupling between the magnetic field variables $\vec{B}(t)$ and the bulk r-bit $|\psi(t)\rangle$, we expect the fields $\vec{B}(t)$ to be strongly time-dependent near $t = 0, T$ in order to guide the r-bit $|\psi(t)\rangle$ to its appropriate boundary conditions $|\psi_{0,T}\rangle$. We see these expectations borne out in gradient-descent numerics in section 3.3.

A crucial ingredient in the path integral representation of Z_2 or P^2 in Eq. (C.47) is the contour of integration of the B_x and B_z fields. Due to the minus sign preceding the B_z^2 term in Eq. (C.47) we conclude that for the path integral to be well defined, B_x must be integrated along the real axis, while B_z must be integrated along the imaginary axis. We shall discuss this issue of contour integration more fully in section 3.3.1.1. Note also that until now we have not made any assumptions about the time-dependence of the fields $\vec{B}(t)$. The simplified expression (C.47) for the path integral over the fields B_x, B_z follows solely from the $\mathrm{SU}(2)$ symmetry of the four-replica propagator K and the fact that the boundary states $|\psi_0\rangle\,, |\psi_T\rangle$ belong to a particular

spin sector.

For the rest of the paper we will focus on the properties of the path integral (C.47), which we shall discuss in terms of classical field configurations $\vec{B}(t)$. But it should always be borne in mind that this is only a particular example of the more general path integral expression (3.23) and further higher-body generalizations.

3.2.5 Replica symmetry

The pure-state dynamics on four replicas shown in Fig. 3.2c possesses a number of discrete symmetries. The microscopic bulk dynamics $\mathbb{V} = V^{(1)} \otimes V_{\mathcal{T}}^{(2)} \otimes V^{(3)} \otimes V_{\mathcal{T}}^{(4)}$ on replicas $r = 1, 2, 3, 4$ is manifestly invariant under the replica symmetry group

$$G = (S_2 \times S_2) \rtimes \mathbb{Z}_2, \tag{3.31}$$

where the inner $S_2 \cong \mathbb{Z}_2$ denote symmetric groups permuting the time-reversed or non-time-reversed replicas amongst themselves with generators $\sigma : 1 \leftrightarrow 3$ and $\sigma' : 2 \leftrightarrow 4$ [174]. The outer $\mathbb{Z}_2$ in the semidirect product is generated by an operation τ corresponding to time-reversal $\mathcal{T}$ on all four replicas followed by exchange of even and odd replicas $1 \leftrightarrow 2$, $3 \leftrightarrow 4$, where $\sigma' = \tau\sigma\tau$. Crucially, the generator τ is antiunitary; as we discuss in Appendix B.3, this fact constrains the spectrum of $\mathbb{V}$ to be real or for for its eigenvalues to come in complex-conjugate pairs. This is the same mechanism that guarantees the reality of the spectrum in non-Hermitian PT-symmetric quantum mechanics [225, 226, 227, 228].

To be explicit we can express the symmetry generators σ, τ directly in terms of their effects on the path integral expressions (3.23) and (C.47). In Eq. (3.23) the generator σ simply exchanges

spins $\mathbf{S}_i^1 \leftrightarrow \mathbf{S}_i^3$ in the propagator K, while the generator τ exchanges even and odd replicas and flips the sign of all spins $\mathbf{S}_i^1 \leftrightarrow -\mathbf{S}_i^2$, $\mathbf{S}_i^3 \leftrightarrow -\mathbf{S}_i^4$. If we ignore the boundary conditions $|\psi_{0,T}\rangle$, each of these transformations can be undone by an appropriate redefinition of the fields F_{rs}, G_{rs}, leaving the bulk action I invariant. In the reduced spin-1/2 action Eq. (C.47), σ generates a reflection about σ^z in the r-bit subspace:

$$\sigma : \vec{\sigma} \to \sigma^z \vec{\sigma} \sigma^z \tag{3.32}$$

Ignoring the boundary conditions, this transformation can be undone by a redefinition of the x-component of the magnetic field $B_x \to -B_x$, which leaves (C.47) invariant. The action is trivially invariant under τ as this generator acts trivially in the r-bit space $|\uparrow\rangle, |\downarrow\rangle$.

The boundary conditions $|\psi_\pm\rangle = |(12)(34)\rangle, |(14)(32)\rangle$ break the replica symmetry group down to a subgroup $H \subset G$ generated by the mutually-commuting generators τ, c, where

$$c \equiv \sigma\tau\sigma \tag{3.33}$$

corresponds to performing time-reversal $\mathcal{T}$ on all four replicas followed by a 'reflection' in replica space $1234 \leftrightarrow 4321$. The generators τ, c leave the boundary states $|(12)(34)\rangle, |(14)(32)\rangle$ invariant, while the generator σ transforms these two states into one another:

$$\sigma\,|(12)(34)\rangle = |(14)(32)\rangle \tag{3.34}$$

The generator σ therefore represents a $\mathbb{Z}_2$ symmetry generator of the bulk symmetry group G that is explicitly broken by the boundary states.

We shall find in the next section that this same $\mathbb{Z}_2$ symmetry is also spontaneously broken in the bulk of the four-replica system below the critical point $\gamma < \gamma_c$, leading to two ordered phases that transform into one another via the generator σ. By imposing non-equal boundary conditions $|(12)(34)\rangle, |(13)(24)\rangle$ at times $t = 0, T$ that explicitly break the σ-symmetry, we force the system in the ordered phase to transition somewhere in the bulk between the two symmetry-broken ordered phases via a domain wall or 'kink'. This is entirely analogous to imposing non-equal boundary conditions on either end of a conventional Ising chain (in dimension $d > 1$) in thermal equilibrium [162]. In both cases, the bulk systems undergo spontaneous $\mathbb{Z}_2$ symmetry breaking transitions as a function of measurement rate or temperature, respectively, with an ordered phase below the critical point. In the ordered phase, the non-equal boundary conditions force the creation of domain walls or 'kinks' in the bulk where the system rapidly transitions from one symmetry-broken phase to the other in order to satisfy the boundary conditions. We shall see this picture emerge explicitly for the hybrid Brownian model in the next section, where we study the path integral Eq. (C.47) in the large-N limit.

3.3 Measurement-induced purification at large N in the $(2, 1)$ hybrid Brownian circuit

The path integral (3.23), along with its simplification (C.47) for spin-1/2 degrees of freedom, expresses the disorder-averaged purity Z_2 for hybrid Brownian dynamics in terms of mean-field variables F_{rs}, G_{rs} (or $\vec{B}$) whose fluctuations are controlled by the large parameter N. In the thermodynamic limit $N \to \infty$, the factor of N preceding the action I in the path integral (3.23),(C.47) allows for analysis via steepest-descent methods (also known as saddle-point or

stationary phase methods [229]). At infinite N, the leading contribution to the path integral comes from the dominant saddle point (or saddle point manifold). This section primarily focuses on this regime of the path integral, meaning large N at fixed T. We will also focus on the regime where $T > J^{-1}, \gamma^{-1}$ is larger than the various microscopic time-scales in the problem, which is a quasi-steady-state regime in which early time transients have died away.

At finite N, there are two kinds of corrections to the leading saddle point answer, fluctuations around the saddle point, which are perturbative in $1/N$, and additional subleading saddles, which are non-perturbative in $1/N$, e.g. $e^{-N} = e^{-1/(1/N)}$. We leave the study of perturbative corrections from fluctuations to future work. We do, however, consider contributions from subleading saddles in section 3.3.5. These give rise to important new effects in the long-time limit at fixed N, leading to the disintegration of the mixed phase.

Our main purpose in this section is to analyze the path integrals for Z_2 and P^2 in the saddle-point approximation using a combination of analytical and numerical tools. We will show that the model exhibits two phases separated by a continuous phase transition as a function of the measurement strength γ. The boundary conditions at $t = 0, T$ deserve special attention as they are a departure from typical large-N or saddle-point analyses. Typically, such calculations are concerned with the equilibrium physics of a Hamiltonian H at inverse temperature β with the path integral constructed to compute the partition function $Z = \mathrm{Tr}\left[e^{-\beta H} \ldots\right]$. Because of the trace, such a path integral naturally has time-translation symmetry, and the relevant saddle points may usually be taken to be time independent. In our case, however, the propagator $K[\vec{B}, \psi_0, \psi_T]$ explicitly breaks time translation invariance, and we are forced to consider time-dependent saddle points in the analysis. Nevertheless, when T is large compared to microscopic scales, the relevant saddle-point configurations will be approximately time-independent for a majority of the time

domain.

The plan for the remainder of this section is as follows. In sections 3.3.1.1 and 3.3.1.2 we outline the different components that are used to construct saddle-point solutions. These components include 'bulk' configurations which are time-independent, instanton-like configurations that are localized in time, and boundary effects which are concentrated near the boundaries $t = 0, T$. In section 3.3.2 we use these components to show the existence of and analyze two distinct phases in the purity. In section 3.3.3 we consider the critical point between these two phases and analyze the resulting effective field theory of the transition. In section 3.3.4 we consider the dynamics of the purity at early times from the perspective of numerical gradient descent and exact diagonalization. Finally, in section 3.3.5 we comment on late times at fixed N, which we analyze by summing over subleading saddles with multi-instanton configurations.

3.3.1 Components of saddle-point configurations

3.3.1.1 Bulk (time-independent) configurations

While we expect general field configurations $\vec{B}(t)$ to be time-dependent, especially near the boundaries $t = 0, T$, we first consider the physics of the path integral (C.47) deep in the bulk, i.e. dynamics occurring at times $1/J \ll t \ll T$ very far from either the initial or final boundary. Because the propagator K is local in time, fields $\vec{B}(t)$ deep in the bulk are largely unaffected by the faraway $t = 0, T$ boundary conditions. Moreover, time-dependent variations $|\partial_t \vec{B}| > 0$ are penalized in the action (C.47) via kinetic-energy terms in the propagator K. We therefore expect fields deep within the bulk to be time-independent.

For a time-independent magnetic field $\vec{B}(t) = \vec{B}$, the propagator (C.47) is easy to evaluate

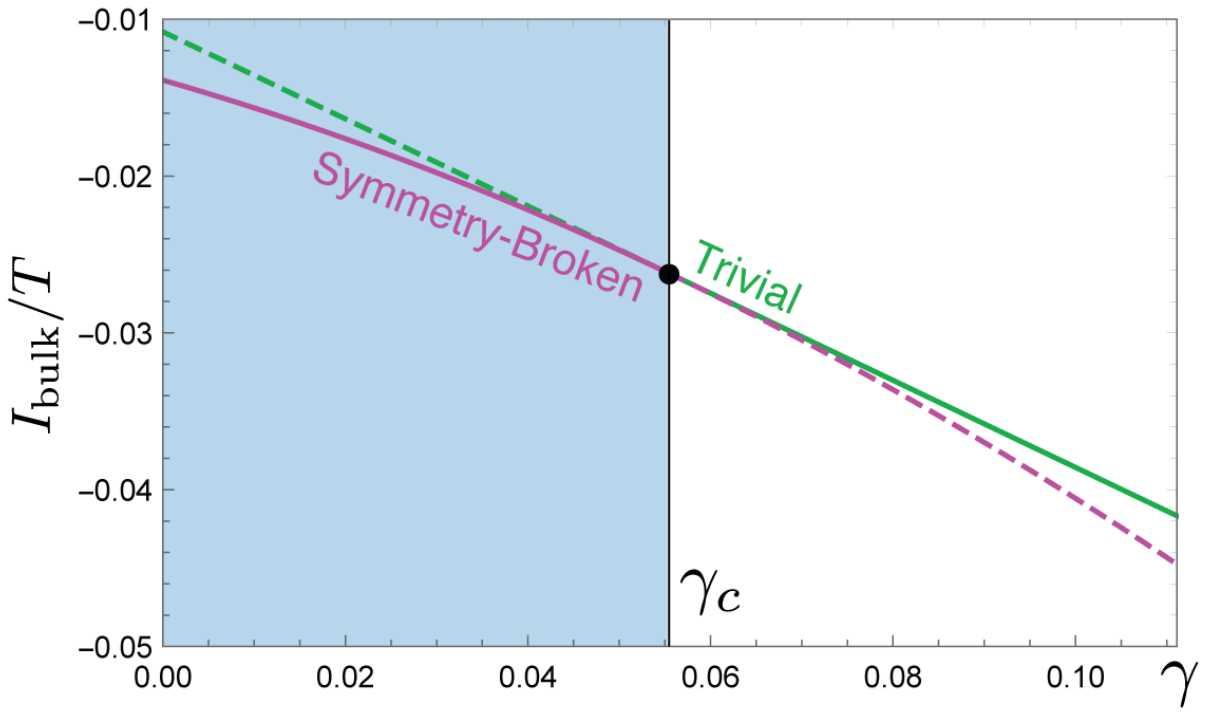

Figure 3.4: **Classical bulk action for the trivial and symmetry-broken saddles.** For all values of γ the bulk action I_{bulk} for the symmetry-broken saddles (purple) is always smaller than the trivial saddle (green), but above the critical point $\gamma > \gamma_c$ the symmetry-broken saddle points (dotted purple) are imaginary and do not contribute to the path integral (see Fig. 3.5). The symmetry-broken saddle points (solid purple) therefore dominate below the critical point $\gamma < \gamma_c$ while the trivial saddle point (solid green) dominates above $\gamma > \gamma_c$. This smooth exchange of saddle-point dominance at $\gamma = \gamma_c$ is responsible for the second-order measurement-induced purification transition in the $(2, 1)$ model.

and one obtains

$$K \approx \exp\left(\frac{TB}{2}\right) + \exp\left(-\frac{TB}{2}\right), \tag{3.35}$$

where $B \equiv \sqrt{B_x^2 + B_z^2}$ and where we have dropped the contributions from the boundary states $|\psi_0\rangle, |\psi_T\rangle$, which are subdominant in the limit of large T (and have not been treated properly by our assumption of time-independence anyway). Assuming real and positive B and large T, we may simply replace $\ln K \to BT/2$ in the action $I[\vec{B}]$ (C.47).

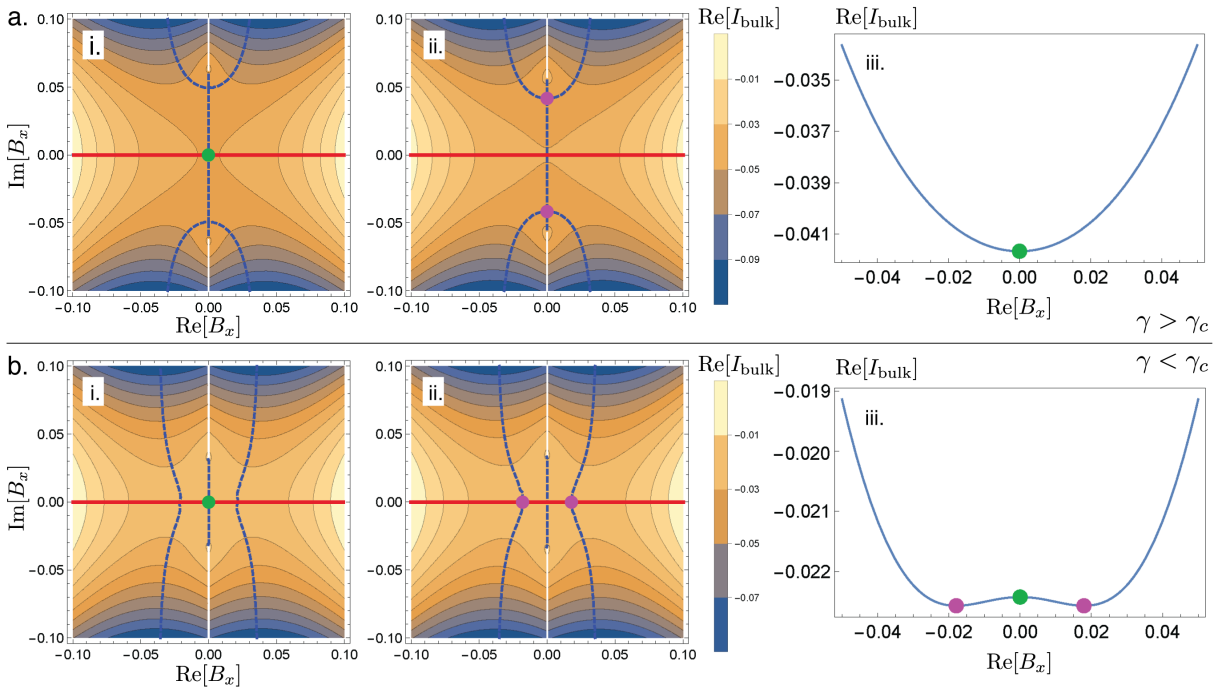

Figure 3.5: **Time-independent saddle-point analysis.** With B_z fixed to its saddle-point value, plots of $\mathrm{Re}[I_{\mathrm{bulk}}]$ in the complex B_x plane reveal the $\mathbb{Z}_2$ symmetry breaking in the bulk responsible for the purification transition. Dotted blue and solid red lines show contours of steepest descent. (a) Above the critical point $\gamma > \gamma_c$, the trivial (i., green) and symmetry-broken (ii., purple) saddle-points lie on the imaginary-B_x axis. Because the integration contour for B_x in the path integral lies along the real axis (solid red), only the trivial saddle point contributes to the effective bulk action I_{bulk} (iii). (b) Below the critical point $\gamma < \gamma_c$, all three saddle points lie on the real-B_x axis (i,ii) and therefore all three contribute to the bulk action (iii), where the symmetry-broken saddle-points (purple) minimize the effective bulk action I_{bulk}.

With this replacement, one can now easily determine the time-independent saddle points of the action $I[\vec{B}]$ (C.47) in the large-N limit by solving the Euler-Lagrange equations $\partial_{B_x} I = \partial_{B_z} I = 0$. We find one symmetric saddle point,

$$\begin{aligned} B_x &= 0 \\ B_z &= \frac{4}{9}\left(\gamma + \frac{1}{2}\gamma_c\right), \end{aligned} \tag{3.36}$$

and a pair of degenerate symmetry-broken saddle points

$$\begin{aligned} B_x &= \pm\frac{1}{3}\sqrt{(\gamma_c - \gamma)\,(\gamma + 3\gamma_c)} \\ B_z &= \frac{1}{3}(\gamma + \gamma_c), \end{aligned} \tag{3.37}$$

where $\gamma_c \equiv J/18$ is the critical point where all three saddle-point solutions coincide. The symmetric saddle is invariant under the replica permutation symmetry $B_x \to -B_x$, while the second pair of saddle points explicitly break this replica symmetry.

The bulk action I_{bulk} for these saddle points are plotted in Fig. 3.4 as a function of the measurement rate γ. Note that the symmetry-broken saddle points (purple) always have lower action than the trivial saddle point (green); the dominant saddle point, however, depends on the direction of the integration contour. In the region $\gamma < \gamma_c$, the symmetry-broken saddles are indeed dominant, but for $\gamma > \gamma_c$, the trivial saddle controls the path integral. We now explain these points.

In Fig. 3.5, we plot the contours of the real part of the action in Eq. (C.47) in the complex plane of B_x with B_z set to its saddle-point value. The original contour of integration is along the

real B_x axis. For $\gamma < \gamma_c$ the replica symmetry broken saddles (Fig. 3.5b, purple dots) lie along the contour of integration, and are the minimum-action saddles as confirmed in Fig. 3.5b(iii). However, for $\gamma > \gamma_c$, the corresponding symmetry broken saddles lie along the imaginary axis (Fig. 3.5a). The contour of integration cannot be deformed to pass through these saddles while maintaining a valid estimate of the integral using only the saddle point value.

In order for the saddle-point value to make the only important contribution to the integral, the contour of integration must pass though the saddle point in such a way that the saddle is a local minimum. However, for $\gamma > \gamma_c$, the desired integration contour hits a branch cut that leads off to infinity in a direction for which the value of the integrand diverges. This means that the symmetric saddle (Fig. 3.5a(iii), green dot) is actually the relevant saddle to estimate the integral when $\gamma > \gamma_c$. Hence, there is a bulk phase transition at $\gamma = \gamma_c$ across which the replica permutation symmetry is spontaneously broken.

This symmetry breaking appears explicitly in the problem if we plot the real part of the action I as a function of B_x above and below the transition point (Fig. 3.5a,b(iii)), which reveals a straightforward double-well potential with spontaneously-broken $\mathbb{Z}_2$ symmetry $B_x \leftrightarrow -B_x$ below the transition $\gamma < \gamma_c$.

3.3.1.2 Time-dependent configurations

The time-independent analysis of the previous section revealed the key $\mathbb{Z}_2$ symmetry-breaking physics that is responsible for the purification transition in the $(2, 1)$ hybrid model. But the time-independent bulk solutions alone cannot be the whole story: indeed, as the bulk action I is identical for Z_2 and P^2, the time-independent bulk solutions alone appear to predict

a purity $Z_2/P^2 = 1$ for all γ, which is clearly incorrect. Neglected in this time-independent analysis are the non-equal boundary conditions at times $t = 0, T$ which explicitly break time translation symmetry in the problem.

To correctly evaluate the path integral expressions (C.47) in the large-N limit (or (3.23) and its generalizations in Appendix B.2), we must expand the action I around 'classical' time-dependent configurations of the fields $\vec{B}(t)$ $(G_{rs}(t), F_{rs}(t))$ that properly account for boundary effects at $t = 0, T$. Quantum fluctuations around these classical configurations are controlled by the factor of N preceding the action I, analogous to the role played by $1/\hbar$ in semiclassical (WKB) expansions [229]. By definition the classical field configurations $\vec{B}(t)$ obey the time-dependent Euler-Lagrange equations that extremize the action I, including time-derivatives terms $\partial_t B_{x,z}$ coming from the path-integral expansion of the propagator K as well as boundary terms associated with the boundary states $t = 0, T$.

These full time-dependent Euler-Lagrange equations can be solved numerically in the general case, and analytically in some special cases, including with time-independent configurations and near the critical point. In the discussion below, we focus on the regime where T is much larger than any microscopic scale, so we are not considering transients associated with times of order γ^{-1} or J^{-1}. We will return to consider dynamics on these short timescales in section 3.3.4.

There are two kinds of time-dependent configurations that will be important. The first are edge configurations in which, under the influence of the boundary states $|\psi_0\rangle, |\psi_T\rangle$ in the propagator K, the $\vec{B}(t)$ fields near $t = 0, T$ are deformed away from their time-independent values deep in the bulk. These boundary contributions are relevant for any value of γ. The second are instanton-like configurations in which the $\vec{B}(t)$ fields traverse from one symmetry-broken saddle to another. These are only relevant for $\gamma < \gamma_c$.

We first discuss the edge configurations, focusing on the regime $\gamma > \gamma_c$ as illustrated in Fig. 3.6a. These configurations are found using a numerical gradient descent algorithm which takes the action (C.47), discretizes the time direction to approximate the kernel K, and then searches through classical configuration space $\vec{B}(t)$ to find the time-dependent fields $B_x(t)$ and $B_z(t)$ that extremize the action; for further details of the gradient-descent numerics, see Appendix B.5. Deep in the bulk the fields $B_x(t), B_x(t)$ take their trivial saddle-point values $B_x = 0, B_z = 2\gamma_c/3$ as expected (Fig. 3.6a). Near the boundaries, however, the fields $B_x(t), B_z(t)$ differ considerably from their bulk value due to the influence of the boundary states in the definition of K. Crucially, since the initial and final states $|\psi_0\rangle, |\psi_T\rangle$ are symmetric about the $B_x = 0$ saddle-point, the action evaluated on the time-dependent configurations are identical for P^2 and Z_2 up to corrections that are exponentially small in T. As a result, these contributions cancel in the ratio $\Pi_Q = Z_2/P^2$, yielding $\Pi_Q \approx 1$.

Similar edge configurations are also relevant for $\gamma < \gamma_c$, but instanton configurations now also play a role. For $\gamma < \gamma_c$, there are two symmetry-broken bulk saddle configurations $B_x^{\pm}$ (dotted black in Fig. 3.6b). An important new ingredient is that the bulk saddles are distinguished by the boundary conditions. The boundary state at $t = 0$ in the definition of P^2 and Z^2 favors the B_x^+ saddle (upper dashed black line), while the boundary state at $t = T$ in the definition of Z_2 favors the B_x^- saddle (lower dashed black line). The identical boundary conditions in P^2 favor a configuration shown in the left panel of Fig. 3.6b in which the bulk saddle is B_x^+ and there are identical edge configurations near $t = 0$ and $t = T$. By contrast the non-equal boundary conditions in Z_2 favor a configuration that traverses from B_x^+ to B_x^- over a localized time window. This single-instanton configuration is shown in the right panel of Fig. 3.6b. Due to the reflection symmetry $B_x \leftrightarrow -B_x$ of the propagator K under the generator σ, the overlap between $|\psi_0\rangle$

and the ground state of the B_x^+ saddle Hamiltonian is equal to the overlap between $|\psi_T\rangle$ and the ground state of the B_x^- saddle Hamiltonian. As a result, the edge contributions to the action are approximately the same in the left and right panels of Fig. 3.6b, and these contributions therefore cancel from the ratio $\Pi_Q = Z_2/P^2$.

The time-translation symmetry of the bulk implies that the instanton is approximately free to move in time, giving rise to a zero mode in the path integral as is typical for instanton physics. This means that for $\gamma < \gamma_c$, we do not have just an isolated saddle point but a continuous family of nearly-degenerate saddle points. For this reason, the instanton contributes an additional 'entropic' factor $\propto (T - T_0)$ to the purity Z_2 with T_0 some short-time regulator that arises because the instanton cannot get too close to the $t = 0, T$ boundaries without changing its action.

We note that there are other possible time-dependent configurations that could be relevant for Z_2. In particular, one might try to avoid the action cost of the instanton by considering a configuration that adheres closely to the B_x^+ saddle until times of order T. Then around $t = T$, the $\vec{B}(t)$ fields could bend towards the B_x^- saddle to some degree. Such a configuration might be viewed as a partial instanton 'bound' to the $t = T$ boundary. One can find approximate solutions of roughly this form, but at least when T is large, the unbound instanton configuration always has lower action than such a bound configuration in every calculation we have done.

3.3.2 Phases of the path integral

With the above ingredients in hand, we can now obtain the structure of the purity Π_Q as a function of γ. The bulk phase transition at $\gamma = \gamma_c$ drives the transition in Π_Q, but to correctly compute this quantity we must include edge and instanton effects as discussed above.

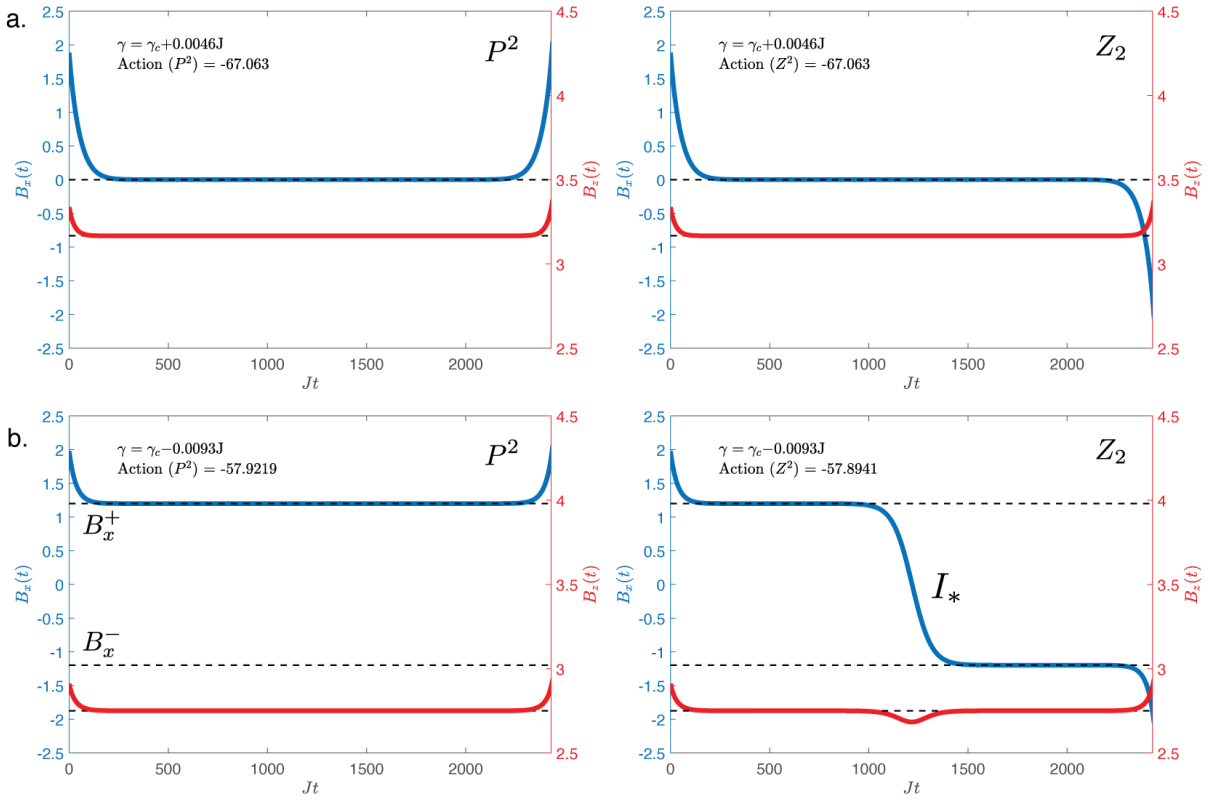

Figure 3.6: **Time-dependent classical field configurations $\vec{B}(t)$ from numerical gradient descent.** Optimal classical field configurations $B_x(t)$ (blue), and $B_z(t)$ (red) as obtained by numerical gradient descent over $\mathrm{Re}\, I[\vec{B}]$ of the 'magnetic-field' action Eq. (C.47). Gradient descent is performed by taking $J\delta t = 0.05$, until the threshold $\delta I = 10^{-7}$ is reached for the action difference, requiring $\sim 10^4$ iterations for the parameters considered here. (a) Above the critical point $\gamma > \gamma_c$ the configurations are dominated by a single trivial time-independent saddle point (dotted black), where the different boundary conditions in Z_2, P^2 lead to nontrivial boundary dynamics in the field $B_x(t)$ near $t = 0, T$. (b) Below the critical point $\gamma < \gamma_c$, the optimal configurations are dominated by a pair of symmetry-broken saddle points (dotted black). The non-uniform boundary conditions in Z_2 promote the formation of an instanton with action I_* somewhere in the bulk that traverses between the two saddle points.

For $\gamma > \gamma_c$, there is only a single symmetric bulk saddle and the edge contributions to the action are identical for Z_2 and P^2 (Fig. 3.6a). Again, this follows from the important fact that the boundary states at $t = 0$ and $t = T$ as well as the trivial bulk saddle are symmetric with respect to the reflection symmetry $B_x \leftrightarrow -B_x$. For this reason, the classical actions for Z_2 and P^2 are identical, up to corrections that decay exponentially with T and we therefore expect $Z_2/P^2 \approx 1$. Moreover, although we do not explicitly consider $1/N$ fluctuations in this work, we note that it seems plausible that the $1/N$ corrections are also equal order-by-order in Z_2 and P^2 up to corrections that decay exponentially with T.

For $\gamma < \gamma_c$, there are two symmetry-broken bulk saddles (Fig. 3.6b), and the instanton configuration with action I_* and 'entropy' $\propto (T - T_0)$ controls the Z_2 path integral. Once again, due to the symmetry under $B_x \leftrightarrow -B_x$ we expect the edge contributions to the action for P^2 and Z_2 to be identical and the only difference arises from the extra instanton in Z_2.

Combining these results together, we find that at large N and fixed $T > J^{-1}, \gamma^{-1}$ (with T large compared to microscopic scales), the purity exhibits two phases,

$$\Pi_Q = \frac{Z_2}{P^2} = \begin{cases} \frac{T-T_0}{a(T)} \exp\left(-N I_*(\gamma)\right) & \gamma < \gamma_c \\ 1 & \gamma \geq \gamma_c, \end{cases} \tag{3.38}$$

where $(T - T_0)/a(T)$ is the ratio of the functional determinants entering Z_2 and P^2 (and we are only really interested in the explicit T dependence, although $a(T)$ may have some weak T dependece as well). Note that for $\gamma > \gamma_c$ we expect the Z_2 and P^2 functional determinants to be approximately equal (it would be good to check this expectation explicitly). Finally, we remind the reader that this result concerns large N and fixed T; we discuss late-time dynamics at fixed

N in section 3.3.5.

3.3.3 Phase transition

From the above analysis, which yields the large-N estimate (3.38) for the purity Π_Q, we find that the value of the purity in the mixed phase $\gamma < \gamma_c$ is governed almost entirely by the instanton action I_*. For $\gamma \ll \gamma_c$, this depends on the details of the spin propagator K. However, in the vicinity of the critical point $\gamma = \gamma_c$, it is possible to analytically determine the instanton action as a function of γ. In this section, we outline the effective field theory of the transition and compute the instanton action. This allows us to determine various critical exponents which have an expected mean-field character arising from the large-N limit.

Near the critical point, the symmetry breaking field B_x has magnitude $B_x \propto \sqrt{J(\gamma_c - \gamma)}$ which vanishes at the critical point, while the field B_z remains finite and of the order of J by Eqs. (3.36) and (3.37). Thus, near the critical point, one can find the time-dependence of the instanton configuration analytically by expanding the action in terms of the small field B_x. For the instanton configurations, the B_z field in the action can be set to be a constant value set by the bulk saddle point, in agreement with our observations from gradient descent numerics (Fig. 3.6). Keeping in mind that the σ_x, σ_z terms in the 'magnetic-field' Hamiltonian $H(\vec{B}) = -\vec{B}(t) \cdot \vec{\sigma}/2$ in the propagator $K[\vec{B}, \psi_0, \psi_T]$ (Eq. (C.47)) do not commute at different times t, one can expand the term $-\ln K$ in orders of $B_x \propto \sqrt{J(\gamma_c - \gamma)}$ which is the small parameter, while keeping the time-dependence explicit. Keeping terms up to second order in $B_x(t)$ (and dropping constant

terms) the action in Eq. (C.47) can be rewritten as

$$I[\vec{B}] \approx \int dt \frac{27}{4J} B_x^2(t) - \frac{1}{8J} \int dt_1 dt_2 B_x(t_1) B_x(t_2) f(t_1, t_2) + \mathcal{O}(B_x^4)$$
$$\text{with the kernel } f(t_1, t_2) = \frac{\cosh \alpha(T - 2|t_1 - t_2|)}{\cosh \alpha T},\ \alpha = \frac{\gamma + \gamma_c}{6J} \tag{3.39}$$

where we have fixed the field $B_z = (\gamma + \gamma_c)/3$ to its time-independent saddle-point value.

One can take $T \to \infty$ in the integration kernel safely, since most of the instantons occur far from the boundary, thereby simplifying the kernel to $f(t_1, t_2) = e^{-2\alpha|t_1 - t_2|}$. Since the kernel is tightly-peaked near $t_2 = t_1$, one can expand in t_2 near t_1 and obtain the time-dependence of the field $B_x(t)$. The lowest order of time dependence occurs at quadratic order B_x^2, and all higher orders of time-dependence are suppressed at least to quartic order B_x^4. Thus, keeping only the lowest order of time dependence, we can just consider the time-independent part of the B_x^4 term in the action. This can be easily obtained from the bulk saddle solutions Eq. (3.37) and expanding the time-independent action to order B_x^4, which gives a contribution $\int dt B_x^4/(128\alpha^3 J^3)$. Combining these results, and also extracting the time-independent part of the kernel in Eq. (3.39) for simplicity, the action $I[\vec{B}]$ can be approximated as,

$$I[\vec{B}] \approx \int dt\ B_x(t) \left(\frac{27}{4J} B_x(t) + \frac{1}{128\alpha^3 J^3} B_x^3(t) \right.$$
$$\left. - \frac{1}{8J} \int ds B_x(s) e^{-2\alpha|t-s|} \right), \tag{3.40}$$

where the first two terms correspond to the time-independent contributions and the final term captures the time dependence of $B_x(t)$.

One can easily check that there exist static solutions $B_x(t) = B_x$ satisfying the time-

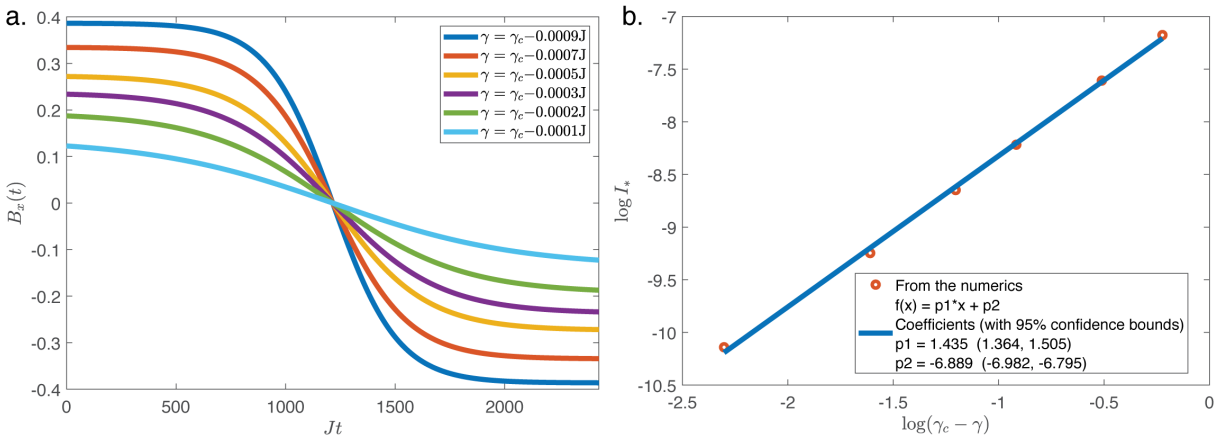

Figure 3.7: **Instanton configurations near criticality and critical exponent from gradient descent numerics.** (a) Bulk instanton configurations $\vec{B}(t)$ obtained from numerical gradient descent for measurement rates $\gamma = \gamma_c - \Delta\gamma$ just below the critical point. Gradient descent is performed by taking $J\delta t = 0.05$, until the threshold $\delta I = 10^{-7}$ is reached for the action difference. For the close-to-critical γ considered, the analytically obtained instanton configuration in Eq. (3.46) are fixed points of the gradient descent algorithm. (b) Critical scaling of the instanton action I_* shows a critical exponent $\zeta = 1.44 \pm 0.07$, which is consistent with the theoretical expectation, $\zeta = 3/2$.

independent equations of motion for the action (3.40). These time-independent equations of motion are

$$\frac{27B_x}{2J} + \frac{B_x^3}{32\alpha^3 J^3} - \frac{B_x}{4J}\int_{-\infty}^{+\infty} ds e^{-2\alpha|t-s|} = 0. \tag{3.41}$$

Evaluating the integral this simplifies to

$$B_x^3 = 32\alpha^3 J^3 \left(\frac{1}{4J\alpha} - \frac{27}{2J}\right) B_x = \delta B_x \tag{3.42}$$

which has static solutions

$$B_x = 0, \pm\sqrt{\delta} \tag{3.43}$$

where we have introduced the parameter $\delta \equiv 2(\gamma+\gamma_c)^2(\gamma_c-\gamma)/J$. Close to criticality, this static solution for B_x is consistent with the earlier time-independent results, approximately the same as

the Eq. (3.37), differing only at order $\mathcal{O}(\gamma_c - \gamma)^{3/2}$ for $\gamma \lesssim \gamma_c$.

One can also easily find time-dependent solutions $\vec{B}(t)$ to the action (3.40). Since the kernel $e^{-2\alpha|t-s|}$ is tightly peaked near $s = t$, we can Taylor-expand the field as $B_x(s) = B_x(t) + (s-t)B_x'(t) + (s-t)^2 B_x''(t)/2 + ...$ in the equation of motion. After some algebra we obtain the time-dependent equation of motion for the field $B_x(t)$ with a second-order time derivative,

$$B_x''(t) = -\delta B_x(t) + B_x^3(t). \tag{3.44}$$

Eq. (3.44) is exactly the equation of motion of a scalar field in a ϕ^4 potential with a mass set by δ, which vanishes at criticality, $\delta \to 0$. This is the correct theory near criticality, as any higher order time derivatives are suppressed either by factors of $1/\alpha$ or δ. The bulk field theory model close to criticality $\delta \to 0$ is thus given by,

$$\begin{aligned} I[\vec{B}] &= \int dt \left(\frac{1}{2}(\partial_t B_x)^2 + V(B_x) \right), \\ V(B_x) &= -\delta \frac{B_x^2}{2} + \frac{B_x^4}{4} \end{aligned} \tag{3.45}$$

which is just the action for a scalar ϕ^4 theory, where B_x is the scalar field and δ is the mass. The purification transition in the $(2,1)$ hybrid Brownian circuit model is therefore captured by the same universal physics as a 0+1d Ising model.

In the mixed phase $\delta > 0$, we expect time-dependent instanton transitions between the static solutions $B_x = \pm\sqrt{\delta}$ just as in section 3.3.2. The instanton configuration has a field profile that asymptotes from $B_x = \sqrt{\delta}$ in the far past to $B_x = -\sqrt{\delta}$ in the far future. The equation of

motion in Eq. (3.44) has instanton solutions of the required form, with

$$B_x^*(t) = -\sqrt{\delta} f_*(t),$$
$$f_*(t) = \tanh t\sqrt{\delta/2}. \tag{3.46}$$

We can plug this solution back into the action (3.40) to compute the action cost of the instanton I_*, relative to a background that stays in one saddle for all time. This calculation yields

$$I_* = \delta^{3/2} \int \frac{dy}{\sqrt{2}} \left((f_*')^2 - \frac{f_*^2}{2} + \frac{f_*^4}{4} + \frac{1}{4} \right). \tag{3.47}$$

The integral is just a numerical constant independent of δ, so the instanton action contribution goes like $I_* \sim \delta^{3/2}$.

We confirm that this instanton configuration is correct for the full action in Eq. (C.47) by feeding the instanton solution (3.46) into the action and checking if there are nearby configurations with smaller action. In Fig. 3.7, we find time-dependent configurations of the field $B_x(t)$ from numerical gradient descent that are indistinguishable from the analytically-obtained solution in Eq. (3.46) within the threshold for gradient descent. Furthermore, by numerically computing the action cost of these optimal configurations as a function of measurement rate γ we find a critical exponent $\zeta = 1.44 \pm 0.07$ consistent with the analytically-obtained $\zeta = 3/2$. Hence, as the purity undergoes a transition at $\gamma = \gamma_c$, the entropy $-\ln \Pi_Q$ has a scaling form

$$-\ln \Pi_Q \sim N(\gamma_c - \gamma)^\zeta. \tag{3.48}$$

with critical exponent $\zeta = 3/2$.

3.3.4 Time-dependence of purity

The statements made so far have been for the purity of the system at long times $T > J^{-1}, \gamma^{-1}$ after some initial early-time transients controlled by the microscopic parameters. In this section we study these early-time dynamics for times $T \sim J^{-1}, \gamma^{-1}$, accessing the purity on $O(1)$ time-scales using the saddle-point approach as well as exact diagonalization numerics. In Fig. 3.8a, we plot the Rényi-2 entropy $-\log_2 \Pi_Q$ or $S_Q^{(2)}(t)$, as a function of time for different γ, by finding minimal action configurations of the fields at different time intervals. To access this numerically, we perform gradient descent with the action in Eq. (C.47), and interpret the results using the formula, $S_Q^{(2)}/N \sim I_* - \ln(T)/N$, from Eq. (3.38). For $\gamma > \gamma_c$, we find that the instanton action I_* goes to zero (equivalently, the system is purified) at $O(1)$ timescales, preceded by an exponential decay. For $\gamma < \gamma_c$, I_* exponentially decays to a finite non-zero values (this is most clearly evident in the numerics for low γ, deep in the mixed phase). For the entropy, this plateau region ultimately gives in to a logarithmic decay with time (see Eq.(3.38)), which is not captured using gradient descent to estimate I_*. Directly using $S_Q^{(2)}/N \sim I_* - \ln(T)/N$, we can visualize the actual time dependence of the entropy, even for a modest choice $N = 6$ for γ deep in the mixed phase, in the inset of Fig. 3.8a. The $\ln T$ term becomes more and more important when we fix a finite N and increase T.

To access the dynamics at finite N, we resort to exact diagonalization using Krylov subspace methods [230, 231, 232]. The unitary layers (4.1) of the Brownian circuit are computed via the conventional Krylov subspace technique with subspace dimension $N_K = 8$ and timestep

$\delta t = 0.01$ in dimensionless units where $J = 1$. The non-unitary measurement layers (C.13) are computed by using the identity

$$M(t) = \left(\frac{1}{2} - \frac{i}{2}\right) \exp\left[-i\mathcal{O}(t)\delta t/2\right] + \left(\frac{1}{2} + \frac{i}{2}\right) \exp\left[i\mathcal{O}(t)\delta t/2\right]. \tag{3.49}$$

In our numerical simulations we compute the exponentiations $\exp\left[\pm i\mathcal{O}(t)\delta t/2\right]|\Psi\rangle$ separately using the conventional Krylov subspace technique and sum the results with appropriate complex coefficients to give $M(t)|\Psi\rangle$. At each timestep $t = m\delta t$ we independently sample coefficients $J_{ij}^{\alpha\beta}(t), n_i^{\alpha}(t)$ from normal distributions with zero mean and variance given by Eqs (2),(5) respectively. Using this disorder realization we then construct the Brownian generators $H(t), \mathcal{O}(t)$, and compute the time-evolved unnormalized state $|\Psi(t+\delta t)\rangle = U(t)M(t)|\Psi(t)\rangle$. For each disorder realization we compute both the purity $\mathrm{Tr}\left[\tilde{\rho}_Q^2(t)\right]$ and squared probability $\mathrm{Tr}\left[\tilde{\rho}_Q(t)\right]^2$ of the reduced unnormalized state $\tilde{\rho}_Q(t) = \mathrm{Tr}_R\left[|\Psi(t)\rangle\langle\Psi(t)|\right]$ as a function of time.

These methods allow us to simulate hybrid Brownian dynamics for modest system sizes, $N = |Q| = |R| = 6$ and for times as long as $Jt = 200$. In Fig. 3.8b we plot the resulting Rényi entropy $-\log_2 \Pi_Q$ at different rates of measurement γ. We find that for $\gamma > \gamma_c$, the behavior is qualitatively similar to measurement only dynamics (without the unitary part of the circuit), for which the entropy exponentially decays to 0 (although very small values of the entropy are inaccessible in the exact diagonalization numerics). For $\gamma < \gamma_c$, it is difficult to distinguish the plateau region (since here $N \sim 1$), and the eventual decay due to the entropic factor $\ln T$. However, the plots here already show that the late time behavior qualitatively deviates from the exponential decay, instead showing a much slower decay at late times. We identify in the inset

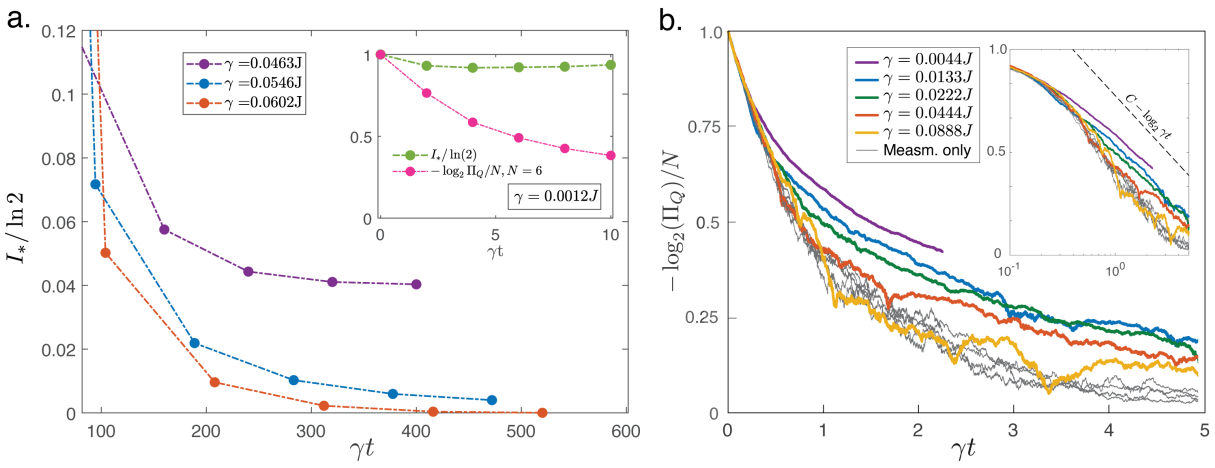

Figure 3.8: **Time dependence of Rényi-2 entropy, from saddle-point calculation and exact diagonalization.** (a) We plot the instanton action I_* as a function of time at different γ, obtained by performing gradient descent of the action in Eq. (C.47) for field configurations at different time intervals. Note, $\gamma_c = J/18 = 0.0556J$. For $\gamma > \gamma_c$ (red), I_* goes to zero, while for $\gamma < \gamma_c$ (blue, purple), it approaches a finite non-zero plateau at late times. Close to criticality (blue), this plateau value is small, approaching zero, $I_* \to 0$ as $\gamma \to \gamma_c$. This result is true for $N = \infty$, where the saddle-point solution is exact. Inset shows estimated Rényi-2 entropy of the system for $\gamma < \gamma_c$ deep in the mixed phase accounting only for the instanton action (green), and including the $-\ln T/N$ term for $N = 6$ (pink) to show the logarithmic decay in entropy at late times. Gradient descent is performed by taking $J\delta t = 0.1$, until the threshold $\delta I = 10^{-6}$ is reached for the action difference. (b) We probe the time dependence for finite N, for system size $|Q| = |R| = 6$, via exact diagonalization. We note that for $\gamma > \gamma_c$ (yellow), and for measurement-only dynamics (J = 0) (gray), the entropy largely follows an exponential decay to zero. However, for $\gamma < \gamma_c$, the time plots deviate from the exponential decay at later times. In the inset, we find at the latest times, there is a logarithmic decay in the entropy, $-\log_2 \Pi_Q \propto -\log T$. For exact diagonalization via Krylov method, averaging is done over 50 disorder realizations, with $J\delta t = 0.01$, $Jt = 200$ and $N_K = 8$ Krylov subspace dimension.

of Fig. 3.8b that this late time behavior is consistent with the factor of $\ln T$ in $-\ln \Pi_Q$, which comes from the entropic freedom of the instanton in Eq. (3.38). In the next section, we discuss the role of the entropic enhancement of the purity in the eventual late time disintegration of the mixed phase.

3.3.5 Phase disintegration at late times

Although the mixed phase $\gamma < \gamma_c$ is robust to repeated single-qubit measurements over extensive timescales $T \sim \text{poly}(N)$, at very long times T exponential in the system size, the measurements ultimately destroy entanglement between R, Q and the mixed phase disintegrates [23, 173]. In the path integral representation (C.47) this disintegration occurs due to the proliferation of instantons, which are heavily favored in the path integral at long times due to the 'entropic' factor $(T - T_0)/a(T)$ found in section 3.3.2. At large N these multi-instanton configurations are subleading saddle-point configurations in the path integral and therefore do not contribute to the result at strictly $N \to \infty$. For very large but finite N, however, we must sum over these additional subleading saddles in the path integral.

To see the breakdown of the mixed phase explicitly, first consider the contribution z_ℓ to the path integral (C.47) coming from a configuration $\vec{B}_\ell(t)$ consisting of ℓ instantons. Due to the boundary conditions, the full instanton contribution is a sum over all odd ℓ for Z_2 or over all even ℓ for P^2. For sufficiently large T, we may apply the dilute-gas approximation in which the ℓ instantons are assumed to be widely separated in time and non-interacting [233]. In this limit, each instanton independently contributes an action penalty e^{-NI_*} and an 'entropic' factor $\propto (T - T_0)/a(T)$ coming from integration over the zero-mode [233, 234]. In this approximation, and ignoring the contribution of the boundary conditions at $t = 0, T$ the ℓ-instanton configuration

has amplitude

$$z_\ell \equiv \int \mathcal{D}\eta \, \exp\left[-N \int_0^T dt \, I[\vec{B}_\ell(t) + \eta(t)]\right]$$
$$\approx \frac{1}{\ell!} e^{-\ell N I_*} \, (T/a)^\ell \, z_0 = \frac{1}{\ell!} \mathcal{R}^\ell z_0 \tag{3.50}$$

where $\mathcal{R} \equiv z_1/z_0 = e^{-NI_*}(T - T_0)/a(T)$, and the 'entropic' term $(T - T_0)/a(T)$ comes from the functional determinant capturing the quantum fluctuations $\eta(t)$ around the classical configuration $\vec{B}_\ell(t)$ as discussed in section 3.3.1.2 [233]. We have to divide by $\ell!$ because instantons must always precede anti-instantons. The numerical value of the $\mathcal{O}(1)$ constant $a(T)$ depends on the details of the action $I[\vec{B}]$ and can be found by computing a functional determinant in the path integral after removing the zero-mode fluctuations of the instanton [233, 234].

Summing over even (or odd) ℓ we find

$$\sum_{\ell \text{ even}} z_\ell = z_0 \cosh \mathcal{R}$$
$$\sum_{\ell \text{ odd}} z_\ell = z_0 \sinh \mathcal{R} \tag{3.51}$$

which gives a disorder-averaged purity

$$Z_2/P^2 = \tanh \mathcal{R}. \tag{3.52}$$

At intermediate times $T \sim \text{poly}(N)$ the exponential penalty e^{-NI_*} dominates and instantons are disfavored $\mathcal{R} \ll 1$ such that $Z_2/P^2 \approx \mathcal{R}$ as found in section 3.3.2. At exponentially long times $T \sim \exp(I_* N)$, however, instantons become much more attractive $\mathcal{R} \to 1$ due to the

'entropic' factor $(T - T_0)/a(T)$. We therefore find that instantons proliferate at late times with $Z_2/P^2 \to 1$ as $T \to \infty$, corresponding to purification of the state and the disappearance of the mixed phase. We note that the instanton action I_*, along with the functional determinant $(T - T_0)/a(T)$, determines the crossover point $T \sim \exp(I_* N)$. This late-time destruction of the phase is similar to that found in phenomonological studies of MIPTs in 1+1d using capillary-wave theory [173].

3.4 Purification dynamics for subsystems

In the previous section we considered the purity Π_Q of the full system consisting of all $|Q| = N$ qubits as an order parameter for the transition in the $(2, 1)$ model. It is also interesting to ask whether the transition can be probed using only a fraction $k = |A| / |Q|$ of the system's qubits, with $A \subset Q$ [179]. In section 3.4.1, we study the disorder-averaged purity Π_A for variable-size subsystems A and show that the purification transition is only visible for sufficiently large $k > k_c(\gamma) \geq 1/2$, leading to the phase diagram shown in Fig. 3.10. Using a modified version of the bulk field theory (3.45) we identify the critical point $k = k_c$ in this diagram as a second-order phase transition in section 3.4.2 and compute its critical exponent $\mu = 1$ using analytical and numerical methods. Finally, we show in section 3.4.3 that these results can be interpreted in the language of quantum error correcting codes.

3.4.1 Subsystem purity

Consider a modified circuit setup shown in Fig. 3.9a where we compute the purity $\Pi_A = \mathrm{Tr}\,[\rho_A^2]$ of a portion $|A| = kN$ of the system qubits using a $\mathrm{SWAP}_{AA'}$ operator while the re-

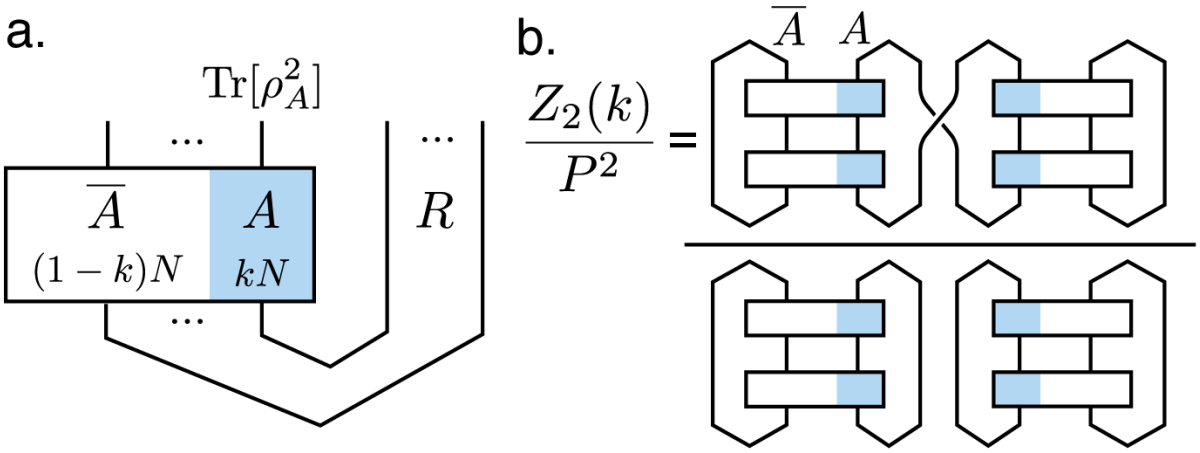

Figure 3.9: **Purification dynamics for subsystems** $A \subset Q$**.** (a) Subsets $A, \overline{A}$ of the system Q are both initially maximally entangled with the reference R, but only the purity Π_A of the subsystem A is computed, while the remaining qubits $\overline{A}$ are traced over. (b) The disorder-averaged purity $Z_2(k)/P^2$ represented as a quantum circuit, where in the numerator the $\mathrm{SWAP}_{AA'}$ operator has been applied only to qubits in subsystem A.

maining $\left|\overline{A}\right| = (1-k)N$ qubits are traced over. Similar to section 3.2 we compute the disorder-averaged purity $Z_2(k)$ and probability P^2 of the unnormalized state $\tilde{\rho}_A = \mathrm{Tr}_{R,\overline{A}}\left[\tilde{\rho}(V)\right]$ as shown in Fig. 3.9b, where the $\mathrm{SWAP}_{AA'}$ operator in this case leads to nontrivial boundary conditions only between the A, A' subsystems. Converting this to a path integral expression leads to an action identical to (C.47) except for the replacement

$$\begin{aligned} \ln K &\to k \ln K_A + (1-k) \ln K_{\overline{A}} \\ K_A &= K[\vec{B}, \psi_+, \psi_-] \\ K_{\overline{A}} &= K[\vec{B}, \psi_+, \psi_+] \end{aligned} \tag{3.53}$$

in the unnormalized purity $Z_2(k)$; the probability P^2 is left unchanged by the k-dependence. Here $K[\vec{B}, \psi_0, \psi_T]$ is the propagator from Eq. (C.47) and the boundary states $|\psi_\pm\rangle$ have been defined in Eq. (3.25). An analogous replacement can be made to compute subsystem purities

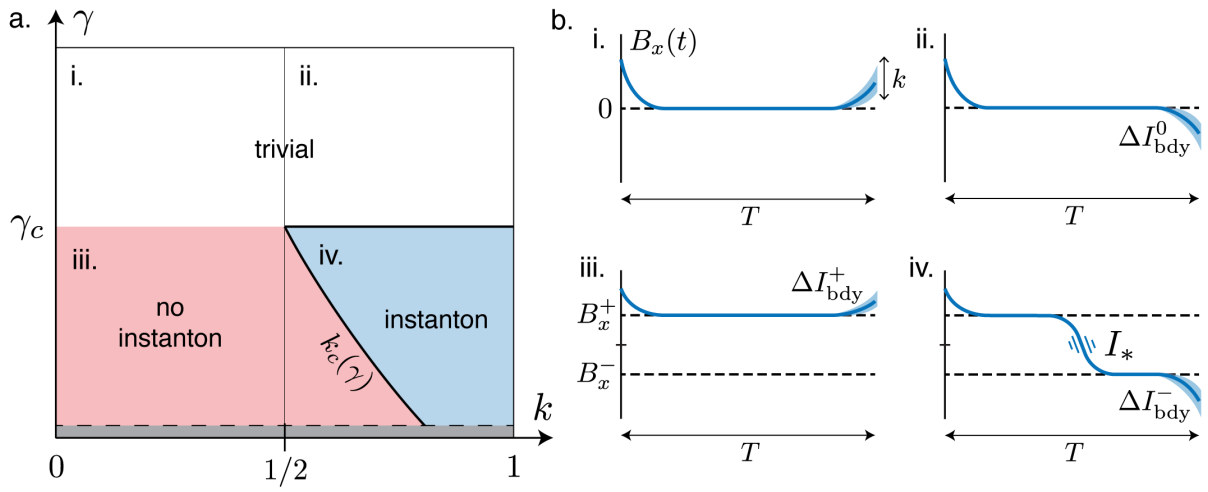

Figure 3.10: **Subsystem purity phase diagram.** (a) At times $T \sim \text{poly}(N)$, the subsystem purity Π_A exhibits three distinct phases as a function of γ, k which are governed by the corresponding classical field configurations $\vec{B}(t)$ (b). Above the critical point $\gamma > \gamma_c$ the bulk fields (solid blue) primarily occupy the trivial saddle point $B_x = 0$ (dotted black), leading to a trivial (purified) phase for all k (i-ii). Below the critical point $\gamma < \gamma_c$, the zero-instanton configuration (iii) dominates for small $k < k_c(\gamma)$ while the single-instanton configuration (iv) with action I_* is dominant for large $k > k_c(\gamma)$.

in the general path integral (3.23). For $k = 1$ these path-integral expressions reduce to their original forms (C.47),(3.23) as required. We therefore find that the bulk physics remains entirely unchanged by varying k and inherits the same set of time-independent saddle points as discussed in section 3.3.1.1. Dependence on the subsystem fraction k enters only through the boundary effects in the propagators $K_{A,\overline{A}}$.

The interplay of bulk physics and boundary effects in $Z_2(k), P^2$ leads to a nontrivial phase diagram as a function of γ, k as shown in Fig. 3.10a. We can argue through the major features of this phase diagram by comparing the action costs $I[\vec{B}(t)]$ of various time-dependent classical field configurations $\vec{B}(t)$, which dominate the path integral at large N. Eqs. (C.47) and (3.53) indicate that this action cost near the $t = 0$ boundary will be the same for $Z_2(k)$ and P^2 regardless of the value of k, and hence will cancel out in the purity $Z_2(k)/P^2$. It is the future boundary condition

at time $t = T$, generated by the $\mathrm{SWAP}_{AA'}$ operator acting on subsystems A, A', that distinguishes between the different phases.

Let us first discuss the relevant time-dependent configurations of the $\vec{B}(t)$ fields. In Fig. 3.10b, we consider classical configurations of the field $B_x(t)$ at different values of k and γ at intermediate times $T \sim \mathrm{poly}(N)$. As shown in Fig. 3.10b(i-ii), for $\gamma > \gamma_c$ the classical path (solid blue) begins in a configuration $B_x > 0, B_z < 0$ that is bent towards the $|\psi_+\rangle$ state, traverses through the single trivial saddle point $B_x = 0$ (dotted black) and either returns to $B_x > 0$ for $k < 1/2$ (Fig. 3.10b(i)) or continues on to $B_x < 0$ for $k > 1/2$ (Fig. 3.10b(ii)). The action cost associated with the future boundary deflection is identical for k and $1 - k$ because of the symmetry $B_x \to -B_x$ and $k \to 1 - k$.

For $\gamma < \gamma_c$, the situation is more complicated as shown in Fig. 3.10b(iii-iv) due to the presence of the two symmetry-broken saddle points $B_x^{\pm}$ (dotted black), which can host instanton transitions between them. For small $k < 1/2$ (Fig. 3.10b(iii)) the purity $Z_2(k)$ is dominated by the $|\psi_+\rangle$ future boundary condition, so B_x spends most of its time on the nearest bulk saddle point B_x^+ with the deflection at the future boundary similar to (but not identical to) that of the past boundary. As the fraction k increases, however, the $|\psi_-\rangle$ contribution begins to significantly affect the future boundary condition and B_x field is pulled towards $B_x < 0$ in order for the r-bit $|\psi(t)\rangle$ to have higher overlap with $|\psi_-\rangle$ at $t = T$. For sufficiently large $k > k_c$, the future boundary condition forces an instanton to appear somewhere in the bulk (Fig. 3.10b(iv)).

Because of the extra action cost $I_*(\gamma)$ of the instanton, the transition point between the zero- and single-instanton configurations Fig. 3.10b(iii-iv) in the mixed phase $\gamma < \gamma_c$ always occurs at a critical fraction $k = k_c(\gamma) > 1/2$ larger than half the system size. By the same reasoning, we also expect $k_c \to 1/2$ as $\gamma \to \gamma_c$ due to vanishing instanton cost $I_* \to 0$ as the

symmetry-broken saddle-points $B_x^{\pm}$ rejoin at the critical point. Together, these arguments allow us to map out the major features of the k, γ phase diagram Fig. 3.10 for subsystem purity at times $T \sim \text{poly}(N)$.

Similar to section 3.3.2, we can estimate the purity $Z_2(k)/P^2$ in each of these phases by computing the action cost $I[\vec{B}(t)]$ of the classical time-dependent field configurations $\vec{B}(t)$ discussed above. Above the critical point $\gamma > \gamma_c$, the action gets contributions from the trivial bulk saddle point $B_x = 0$ as well as the boundary contributions near $t = 0, T$ as illustrated in Fig 3.10b(i-ii). Similar to what we found in section 3.3.2, the bulk contribution and the $t = 0$ boundary contributions cancel in the ratio $Z_2(k)/P^2$, so the purity in this phase is controlled entirely by the difference of future boundary contributions $\Delta I^0_{\text{bdy}}(k, \gamma)$. Note that $\Delta I^0_{\text{bdy}}(1 - k, \gamma) = \Delta I^0_{\text{bdy}}(k, \gamma)$ from the $k \leftrightarrow 1 - k$ symmetry present for $\gamma > \gamma_c$.

Below the critical point $\gamma < \gamma_c$ and for small subsystems $k < k_c$, the zero-instanton configuration Fig. 3.10b(iii) dominates and we obtain nontrivial contributions $I_{0,T}$ to the action from the boundary dynamics near $t = 0, T$ and from the bulk saddle point B_x^+. As with $\gamma > \gamma_c$, the bulk contribution and the $t = 0$ boundary contribution I_0 are common to both $Z_2(k)$ and P^2, so the purity is controlled by the difference of the $t = T$ boundary contributions denoted $\Delta I^+_{\text{bdy}}(k, \gamma)$. For larger subsystems $k \geq k_c$ the single-instanton configuration Fig. 3.10b(iv) dominates and we obtain nontrivial contributions in the action from the boundary dynamics $I_{0,T}$, from the bulk saddle value, and from the bulk instanton with action I_*. Again, the bulk saddle contribution and $t = 0$ boundary contribution are common to $Z_2(k)$ and P^2, so the ratio is controlled by $I_* + \Delta I^-_{\text{bdy}}$ where ΔI^-_{bdy} denotes the difference of future boundary contributions in the presence of an instanton.

Combining these results, we find estimates for the subsystem purity $Z_2(k)/P^2$ in all three

regions of the phase diagram Fig. 3.10:

$$\frac{Z_2(k)}{P^2} = \begin{cases} \frac{T-T_0}{a'(T)} \exp\left[-N\left(I_*(\gamma) + \Delta I^-_{\text{bdy}}(k,\gamma)\right)\right] & \gamma < \gamma_c,\ k \geq k_c \\ \exp\left[-N\Delta I^+_{\text{bdy}}(k,\gamma)\right] & \gamma < \gamma_c,\ k < k_c \\ \exp\left[-N\Delta I^0_{\text{bdy}}(k,\gamma)\right] & \gamma \geq \gamma_c \end{cases} \tag{3.54}$$

where we have included the 'entropic' term $(T - T_0)/a'(T)$ (with a possibly different prefactor $a'(T)$) in the single-instanton configuration coming from the zero-mode motion of the instanton. These k-dependent purity estimates are a generalization of the $k = 1$ purity estimates in Eq. (3.38).

The expressions (3.54) are similar to those obtained using capillary-wave theory as a phenomenological description of measurement-induced transitions in $1 + 1$d systems [173]. In this picture, the bulk of the circuit is viewed as a two-dimensional statistical mechanics system supporting a collection of domains separated by domain walls. In the mixed phase, small subsystems A with nontrivial boundary conditions at the late-time boundary are unable to force most of the bulk to transition between phases and the system therefore has a domain wall pinned near the subsystem A. This is analogous to the case $\gamma < \gamma_c, k < k_c$ in Eq. (3.54), where the boundary action ΔI^+_{bdy} is analogous to the energy cost of the pinned domain wall.

Sufficiently large subsystems A at the late-time boundary, by contrast, can force the entire bulk to transition, leading to a 'domain-wall decoupling' effect where it is entropically favorable for the system to support two decoupled domain walls: one in the bulk that is free to move in time, and another that is pinned near the small subsystem $\overline{A}$. This situation is analogous to the case $\gamma < \gamma_c, k \geq k_c$ in Eq. (3.54) where the instanton action I_* corresponds to the energy cost

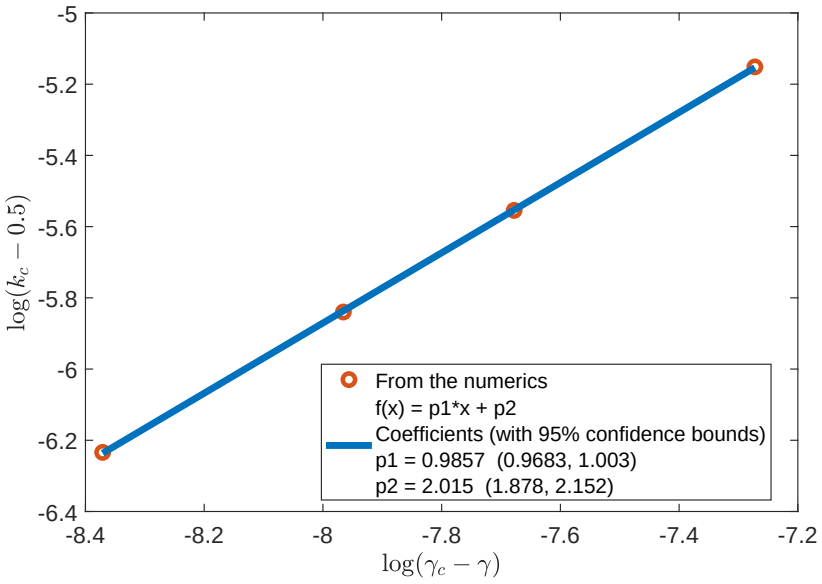

Figure 3.11: **Subsystem purity critical exponent μ from gradient descent numerics.** The critical subsystem fraction $k_c(\gamma)$ is identified for measurement rates $\gamma < \gamma_c$ just below the critical point by finding points in the k, γ plane (red) where the boundary action $\Delta I_{\rm bdy}$ is equal to the single-instanton action I_* (see Fig. B.4 of Appendix B.5). A linear fit (blue) gives an estimate $\mu = 0.99 \pm 0.01$, consistent with $\mu = 1$ from analytical arguments.

of the bulk domain wall and the boundary action $\Delta I^-_{\rm bdy}$ corresponds to the energy cost of the pinned domain wall. In particular, the entropic prefactor $(T - T_0)/a'(T)$ coming from the zero-mode motion of the instanton corresponds to the entropy of the decoupled domain wall in the bulk; in both cases, this additional entropy is the reason why the single-instanton (or decoupled domain-wall) configuration is favorable despite the additional cost I_* of creating the instanton (or domain wall) [173]. While the capillary-wave theory is phenomenological and specifically tailored for $1 + 1$d systems, in Eq. (3.54) we have obtained similar expressions for the same physical phenomena starting from an exactly-solvable all-to-all microscopic model.

3.4.2 Critical scaling of k_c near γ_c

We can also study the behavior of $k_c(\gamma)$ close to the bulk phase transition $\gamma = \gamma_c$, in the symmetry broken phase. For this, we can numerically compare the action penalty for the boundary $\Delta I_{\text{bdy}} \equiv \Delta I^+_{\text{bdy}} - \Delta I^-_{\text{bdy}}$ with the instanton action I_*. We perform an optimization of the fields with the initial configurations corresponding to the two cases in Fig. 3.10b(iii-iv), to locally minimize the action in Eq. (3.53) for $\gamma \lesssim \gamma_c$. We identify the critical fraction $k_c \gtrsim 1/2$ by interpolating to find the value of k above which $\Delta I_{\text{bdy}} > I_*$, such that the single-instanton configuration is dominant (see Appendix B.5 for more details). We find numerically in Fig. 3.11 that k_c scales with $\gamma_c - \gamma$ as

$$k_c - \frac{1}{2} \sim (\gamma_c - \gamma)^\mu, \text{ for } \gamma \text{ close to } \gamma_c. \tag{3.55}$$

A linear fit yields an estimate $\mu = 0.99 \pm 0.01$ for the critical exponent.

Close to the bulk critical point, we can also adopt the previously described critical field theory model, now embellished with a boundary term, to analytically argue that $\mu = 1$. We showed earlier that the bulk field theory close to criticality is given by the action (3.45). We now model the boundary effect at $t = T$ with a delta function pinning field with action

$$I[\vec{B}] \to I[\vec{B}] + \int dt\, h B_x \delta(t - T). \tag{3.56}$$

where h is an additional field controlling the strength of the pinning effect.

The delta function is regulated by setting $\delta(t-T) \to \delta(t-T+\epsilon)$ and taking $B_x(t) = B_{x,\text{bdy}}$

(a constant) for $t \in [T-\epsilon, T]$. The equation of motion then implies that $\partial_t B_x$ jumps across $t = T-\epsilon$, $-\partial_t B_x(T) + \partial_t B_x(T-\epsilon) + h = 0$. Since $\partial_t B_x(T) = 0$, we find that $\partial_t B_x(T-\epsilon) = -h$. In other words, $-h$ is the slope of the $B_x(t)$ configuration at $t = T^-$. Close to criticality, we expect the following scaling,

$$h \propto (k - 1/2). \tag{3.57}$$

This is because, for $k > 1/2$, the SWAP-ed boundary condition should dominate, and the B_x field at the future boundary should go lower than the $B_x \approx 0$ bulk saddle point, leading to $-h < 0$ i.e. $h > 0$. On the other hand, for $k < 1/2$, the trivial boundary condition should dominate, and the B_x field at the future boundary should go higher than the $B_x \approx 0$ bulk saddle point, leading to $h < 0$. Close to $k \sim 1/2$, the linear scaling of $h \propto (k - 1/2)$ can thus be justified and we expect our simplified model of the boundary condition to capture the universal physics.

The value of $B_{x,\mathrm{bdy}}$ is determined by appealing to a conservation law. For $t < T - \epsilon$, the quantity

$$\mathcal{H}[\vec{B}] = \frac{1}{2}(\partial_t B_x)^2 - V(B_x) \tag{3.58}$$

is conserved – in the language of classical mechanics this is the statement that the classical Hamiltonian $\mathcal{H}[\vec{B}]$ corresponding to the Lagrangian $I[\vec{B}]$ is conserved. If we consider solutions that asymptote to a saddle point in the far past, then we know that $\mathcal{H} = -V(\sqrt{\delta}) = \delta^2/4$. Now, we can consider the two different cases as before – firstly where the B_x field configuration asymptotes to $B_x^+ = \sqrt{\delta}$, and secondly to $B_x^- = -\sqrt{\delta}$, in the far past. Consider $B_{x,\mathrm{bdy}} = B_x(-\infty) + a$, where for the two cases, $B_x(-\infty) = \pm\sqrt{\delta}$. Because of the conservation law, we can solve for a close to criticality where $|a/\sqrt{\delta}| \ll 1$ and we obtain $a \propto -h/\sqrt{2\delta}$. Note, we have selected the correct sign of a consistent with the fact that higher h should lower the boundary field compared

to the bulk saddle.

Finally, we read off the excess boundary actions $\Delta I^{\pm}_{\text{bdy}}$ for both cases from Eq. (3.56). To leading order in a we find

$$\begin{aligned} \Delta I^{\pm}_{\text{bdy}} &= \pm h\sqrt{\delta} + h\,\mathcal{O}(a) \\ \implies \Delta I_{\text{bdy}} &= 2h\sqrt{\delta}. \end{aligned} \tag{3.59}$$

Recall that in section 3.3.3 we found that $I_* \propto \delta^{3/2}$. Thus the condition for the zero-instanton and single-instanton configurations exchanging dominance $\Delta I_{\text{bdy}} > I_*$ occurs when $h \propto \delta$. Combined with Eq. (3.57), we find that k_c scales as $(k_c - 1/2) \propto \delta$, and thus $\mu = 1$.

3.4.3 Mutual information and error-correction

We can also understand the mixed phase at low measurement rate in this model through the lens of quantum error correction. Consider $\gamma \lesssim \gamma_c$, and $k \gtrsim k_c(\gamma)$. For this case, the dominant saddle-point configuration for the field $B_x(t)$ will be the single-instanton configuration shown in Fig. 3.10b(iv). On the other hand, for a subsystem fraction $k' = (1-k)$, the dominant saddle point will be the zero-instanton configuration shown in Fig. 3.10b(iii). Since the boundary conditions are symmetric with respect to the saddle points (i.e. the overlap between $|\psi_+\rangle$ and the r-bit state favored by B_x^+ is equal to the overlap between $|\psi_-\rangle$ and the B_x^- state), we can deduce a strong relation between the purities for k and $(1-k)$.

In particular, this symmetry dictates that $\Delta I^{+}_{\text{bdy}}(1-k) = \Delta I^{-}_{\text{bdy}}(k)$. For the Rényi-2 en-

tropies at $\gamma \lesssim \gamma_c$ and $k \gtrsim k_c(\gamma)$, we therefore have

$$\begin{aligned} S_k^{(2)} &= \Delta I_{\text{bdy}}^{-}(k) + I_*, \\ S_{1-k}^{(2)} &= \Delta I_{\text{bdy}}^{+}(1-k), \\ S_1^{(2)} &= I_*. \end{aligned} \tag{3.60}$$

From these relations, and the identity relating the two boundary effects, we may deduce

$$S_k^{(2)} = S_{1-k}^{(2)} + S_1^{(2)} \tag{3.61}$$

at $\gamma \lesssim \gamma_c$ and $k \gtrsim k_c(\gamma)$.

Because we may interpret the $\text{SWAP}_{AA'}$ operator shown in Fig. 3.9 as acting either at the $t = 0$ boundary or at the $t = T$ boundary (this is equivalent to cyclically permuting the SWAP operator in the trace), the entropy $S_k^{(2)}$ can be identified as the Rényi-2 entropy of either a subsystem of fraction k of the system Q or of the reference R. As a result, Eq. (3.61) can be understood as the statement that for sufficiently large $k > k_c$, the mutual information between the $(1-k)N$ qubits in the subsystem $\overline{A}$ and the N qubits in the reference R vanishes identically, when measured by the disorder-averaged Rényi-2 entropy. That is,

$$\begin{aligned} &I^{(2)}\left(\overline{A} : R\right) \\ &\quad = S^{(2)}\left(\overline{A}\right) + S^{(2)}\left(R\right) - S^{(2)}\left(\overline{A}, R\right) \\ &\quad = S^{(2)}\left(\overline{A}\right) + S^{(2)}\left(R\right) - S^{(2)}\left(A\right) \\ &\quad = S_{1-k}^{(2)} + S_1^{(2)} - S_k^{(2)} = 0. \end{aligned} \tag{3.62}$$

where in the second line we have used the fact that $S^{(2)}(\overline{A}, R) = S^{(2)}(A)$ because the state $\tilde{\rho}(V)$ is pure.

This result is consistent with the system forming a quantum error correcting code. The physical interpretation of the result (3.62) is that small parts of the system $\overline{A}$ contain no information about the reference R, after some of the system-reference entanglement is destroyed by the measurements. To be explicit, consider using the entire remaining system purity to encode information. We have $S_1^{(2)}$ logical qubits encoded within N qubits and a reference entangled with those $S_1^{(2)}$ logical qubits. Eq. (3.62) states that any subsystem $\overline{A}$ of size less than $1 - k_c < 1/2$ has zero Rényi mutual information with the reference R. If these statements also held for the mutual information $I(\overline{A} : R)$ computed from the von Neumann entropies, then the existence of a recovery channel would be guaranteed which could undo the erasure of the subsystem $\overline{A}$.

Of course, these statements are only established here for the 2nd Rényi mutual information defined via a certain averaging procedure. More work is therefore needed to establish the existence of a recovery map since the mutual information can depend on the Rényi index n, and also on the averaging procedure. In order to make the connection to quantum error correction rigorous, we would also in principle need to include $1/N$ corrections and carefully work with approximate recovery maps. These are interesting topics to pursue in future work; here we content ourselves with describing the analogous phenomenon at the level of the 2nd Rényi entropy.

3.5 Discussion

In this work we introduced new tools for analyzing measurement-induced purification transitions in the large-N limit. Specifically, the $(2, 1)$ hybrid Brownian circuit introduced in section

3.2 exhibits a purification transition described by a relatively simple mean field theory that is analytically tractable at large N. We represented a particular disorder average over the purity as a path integral coupling four replicas, and derived the critical properties of the replica permutation breaking in the system, which is manifested as the purification transition for the system. Since the model is all-to-all, and the saddle-point point analysis depends on taking the large N limit, the resulting field theory can be viewed as a minimal mean field description for the purification transition. Furthermore, since the resulting theory is a simple Ising field theory in $0+1$ dimensions, the critical exponents can be analytically understood, and also sheds light on the late time purification in the mixed phase through the mechanism of instanton proliferation. We also derived an entropic relation between subsystem and the reference, which allows us to identify the mixed phase as being a dynamically generated quantum error correcting code.

This work adds to the growing paradigm of interpreting entanglement dynamics in quantum circuits through statistical mechanical models in the replica space in the context of hybrid circuits [157, 162, 163, 164, 166, 176, 228] and more broadly in random circuits [152, 153, 154, 155, 156]. However, this model differs from the earlier works in considering the large-N limit that allows us to make progress in interpreting entropy-like quantities as path integrals dominated by their saddle points. This is distinct from the large local Hilbert space dimension which is often necessary to make analytical progress in the random and hybrid circuits, and these two limits can lead to distinct physics. Our analysis here focused on contributions to lowest order in $1/N$. However, one can also study the subleading $1/N$ effects, which we reserve for future studies.

We emphasize that the $(p, q) = (2, 1)$ model studied here using the purity ($n = 2$) is only one example of a large family of hybrid Brownian circuit models with measurement-induced transitions. Straightforward generalizations of the Brownian circuit layers introduced in sec-

tion 3.2 can generate p-body unitary interaction terms and q-body non-unitary measurement terms. Further, by introducing additional copies of the state $\tilde{\rho}$ one can probe the phase transition using higher moments of the density matrix $n > 2$. We show in Appendix B.2 that each of these models leads to a distinct $(p, q)_n$ path integral representation with a large-N limit. In particular, for reasonably small $n = 3, 4, 5, \ldots$ we expect that the combination of $\mathrm{SU}(2)$ and replica symmetry will kinematically constrain the system to subspaces of small dimension similar to what we found in section 3.2.4 for $n = 2$, allowing for analytical access to the purification transition at large N for higher-order Rényi entropies $n > 2$. Furthermore, this setup can be extended to a combination of different q-body measurements, without the unitary part, allowing for exploration of measurement-only dynamics within the hybrid Brownian setup. Such measurement-only circuits have recently been shown to harbor symmetry-protected-measurement-only phases [201, 202, 203, 204, 205, 206] and phase transitions, which could be investigated in these Brownian setups as well.

Other straightforward generalizations include studying the (p, q) models at higher spin S or for more general degrees of freedom such as $\mathrm{SU}(Q)$ spins or fermions. We expect many of these models to also show measurement-induced transitions governed by boundary conditions and instanton effects similar to the story presented here for the $(2, 1)_2$ path integral, although of course the details will differ considerably depending on the specifics of the model. Another exciting direction is to consider chains or lattices of (p, q) models, with nearest-neighbor Brownian spin-spin interactions between individual clusters. This would allow for direct connection to measurement-induced phase transitions in $1 + 1$d models, including analytical estimates of the spatial critical exponent. We reserve study of these more general models for future work.

Chapter 4: Entanglement Phases in large-N hybrid Brownian circuits with long-range couplings

Sometimes, you just have to be silly.

- Big Panda and Tiny Dragon, James Norbury.

4.1 Introduction

Modern quantum technologies facilitate increasingly detailed access to quantum phases of matter with complex patterns of many-body entanglement [235]. In particular, long-range interactions decaying with distance as $r^{-\alpha}$, available in state-of-the-art experiments featuring Rydberg atoms, trapped ions, and neutral atoms in optical cavities, are capable of dramatically altering the dynamics of quantum information [236, 237, 238, 239, 240, 241, 242, 243] and rapidly generating complex many-body entanglement [244, 245, 246, 247, 248, 249, 250]. Our understanding of entanglement dynamics in generic strongly-interacting many-body systems is still under rapid development. A prime example is the recent discovery of robust phases of many-body entanglement which survive for exponentially long times in hybrid quantum circuits consisting of scrambling unitary evolution interspersed with repeated local measurements [4, 21, 22, 23, 158, 159, 160, 161, 162, 163, 164, 165, 166, 167, 168, 170, 171, 174, 175, 179, 197, 200, 201, 202,

203, 205, 206, 251, 252]. At low measurement rates initially local information is dynamically encoded in many-body entangled states which are robust to subsequent measurements, resulting in a volume-law-entangled phase stabilized by a dynamically-generated quantum error-correcting code (QECC) [162, 164, 166, 173, 253]. At higher measurement rates, the many-body entanglement is destroyed, leading to an area-law-entangled phase.

It is highly desirable to develop theoretical tools to easily estimate entanglement properties of many-body states generated by strongly-interacting quantum dynamics. In this work we develop exactly solvable models composed of large-N clusters of qubits or fermions in a 1D chain [Fig. 4.1(a)], for which entanglement properties can be computed using path-integral techniques. In particular, these methods provide simple pen-and-paper calculations for the dynamics of many-body entanglement that can be immediately applied to problems of experimental interest. We understand the entanglement phases in these models in terms of a replica-symmetry-breaking transition of a corresponding statistical mechanical system, and derive analytical expressions for entanglement entropies, code properties of the QECC phase, and critical properties of the phase transition. We summarize our primary findings in Figs. 4.1(b-d), including a phase diagram, critical properties at the phase transition, and the error-correcting properties as a function of the measurement rate and the long-range exponent α.

Our analysis of these large-N models leads to several new results and insights. First, our models go beyond the standard set of tools – Clifford circuits, matrix product states, and exact diagonalization – typically used to study entanglement dynamics, and are able to provide an analytical mean-field understanding of entanglement phases and measurement-induced phase transitions. Second, the analytical control afforded by our models allows us to derive new results, namely that long-range interactions generate novel sub-region entanglement structure, leading to

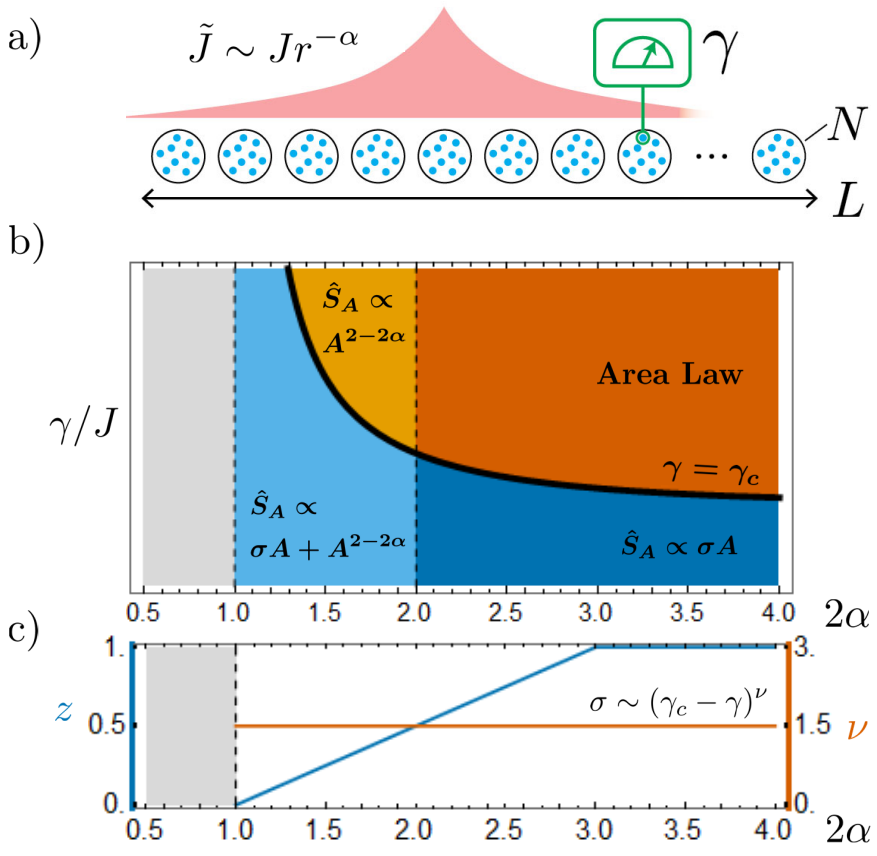

d)

Measurement Rate	Power-law Exponent	Code Rate	Code Distance
$\gamma < \gamma_c$	$2\alpha < 2$	σNL	$NL^{2-2\alpha}$
	$2\alpha > 2$	σNL	$\mathcal{O}(\log L)$

Figure 4.1: (a) Monitored large-N models with long-range interactions. (b) Entangled phases for Brownian spin and SYK_4 models as a function of measurement rate γ/J and long-range exponent α. $\hat{S}_A$ is the quasi-Rényi entropy of a contiguous subsystem of volume A. (c) Dynamical critical exponent z and domain wall tension critical exponent ν vs α. (d) Error-correcting properties of the measurement-induced phases at large L.

a non-trivial QECC phase with a tunable sub-extensive code distance $L^{2-2\alpha}$ for $\alpha < 1$, where L is the number of clusters in the chain. The entanglement phase diagram we find is thus even richer than previously known [254, 255, 256], and suggests a recipe for constructing QECCs with enhanced code distance. Third, the models we study are experimentally relevant as large-N clusters naturally occur in cold atom experiments, including ensembles of atomic spins coupled uniformly to optical cavities [257, 258, 259, 260] and ensembles of Rydberg atoms clustered within a single blockade radius [261, 262]. Fourth, our results highlight the crucial role played by interactions in stabilizing the volume-law phase. We demonstrate this point explicitly by studying a non-interacting circuit on fermions with long-range hopping and find two distinct fractal entangled phases [256], but no QECC phases. Lastly, although we focus here on the more easily computable Rényi entropies, we also expect similar calculations to allow for analytical calculations of von-Neumann entropies using an appropriate replica limit [263].

4.2 Setup

Here we consider a system Q of particles (qubits or fermions) arranged into a 1D chain of L clusters, each containing a large number N of particles as shown in Fig. 4.2. The particles are subjected to two competing dynamics: long-range Brownian unitary interactions $U(t)$ that rapidly generate entanglement leading to a volume-law phase, and continuous weak monitoring $M(t)$ that tends to destroy entanglement leading to an area-law phase. To probe the transition between these two phases, we maximally entangle the system Q with a reference S [Fig. 4.2(a)], and compute entanglement Renyi entropies $\hat{S}_A^{(n)}$ of system subregions $A \subset Q$. We shall show that these entropies can be readily computed using path-integral techniques, leading to straight-

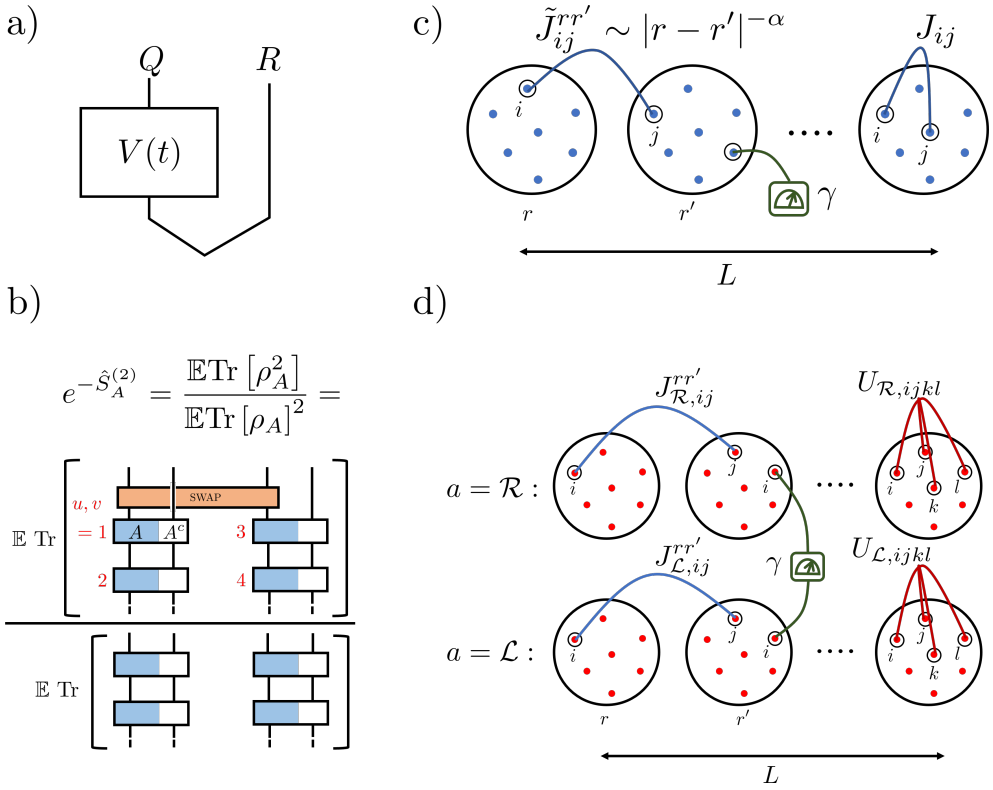

Figure 4.2: (a) System Q is maximally entangled with reference R and evolves under monitored dynamics $V(t)$. (b) Quasi Rényi-2 entropy represented as a quantum circuit. (c) Brownian qubit chain with L clusters, each composed of N qubits. (d) SYK_4 model with two independent chains of length L coupled by measurement.

forward pen-and-paper estimates for salient physical quantities including code properties and critical exponents.

For an analytical treatment, we focus on the quasi Rényi entropy [264] of the reduced density matrix ρ_A of a contiguous subsystem A of Q, $\hat{S}_A^{(n)} = -\log \frac{\mathbb{E}\mathrm{Tr}\left[\rho_A^n(t)\right]}{\mathbb{E}\mathrm{Tr}[\rho_A(t)]^n}$, where $\mathbb{E}$ is a disorder average over measurement outcomes and circuit realizations [1]. The denominator is necessary for normalizing the state generated by the non-unitary evolution, and the ratio of averages is considered for ease of calculation over the averaged Rényi entropy which involves averaging the ratio of two multi-replica quantities.

[1]The relation between Rényi entropy, quasi Rényi entropy and the von Neumann entropy is explained in Appendix C.1.

$\hat{S}_A^{(2)}$ involves tracing over two copies of density matrix $\mathrm{Tr}\left[\rho^2(t)\right]$ with $\rho(t) = V(t)\rho V^\dagger(t)$, which we can interpret in terms of time evolution $\mathbf{V}(t) = V^{(1)} \otimes V^{(2)*} \otimes V^{(3)} \otimes V^{(4)*}$ on four replicas $r = 1, 2, 3, 4$ [4, 265]. Here, $1, 2$ $(3, 4)$ denote the first (second) Rényi replica, and $1, 3$ $(2, 4)$ denote forward (backward) time-evolution. In the replicated Hilbert space, the quasi Rènyi entropy can be expressed as a ratio of propagators, $\exp\left(-\hat{S}_A^{(2)}\right) = \frac{\langle\langle \mathcal{S}_A|\mathbb{E}\mathbf{V}(t)|\mathcal{I}\rangle\rangle}{\langle\langle \mathcal{I}|\mathbb{E}\mathbf{V}(t)|\mathcal{I}\rangle\rangle}$, for appropriately defined initial and final states $|\mathcal{I}\rangle\rangle$, $|\mathcal{S}_A\rangle\rangle$ in the replicated Hilbert space (see Appendix C.1). The numerator has twisted boundary conditions $|\mathcal{S}_A\rangle\rangle$ which swap replicas $1, 3$ at the final time $t = T$ [Fig. 4.2(b)], reflecting the SWAP test in the trace $\mathrm{Tr}\left[\rho_A^2\right]$ [266].

We will construct analytically-tractable models for qubits and fermions for which the propagator $\mathbb{E}\mathbf{V}(t)$ can be expressed as a large-N path integral with classical action NI that is amenable to saddle point analysis. Consequently, the quasi Rényi entropy is simply proportional to the difference between the large-N saddle-point actions with and without the SWAP boundary condition [4, 265, 267], $\hat{S}_A^{(2)} \propto N\left(I_{\text{SWAP}} - I\right)$.

4.3 Hybrid Brownian circuit on qubits

We first consider a system of qubits $\mathcal{S}_{r,i,\alpha}$ residing in clusters r and labeled by an intra-cluster index i and spin component $\alpha = x, y, z$. During each time step Δt, the qubits evolve under a two-body scrambling unitary matrix $U(t) = \exp\left[-iH(t)\Delta t/2\right]$ for half the duration, and under one-body weak measurement for the rest of the time. The unitary is generated by

$$H(t) = \sum_{r,i<j,\alpha\beta} J_{ij\alpha\beta}(t)\mathcal{S}_{ri\alpha}\mathcal{S}_{rj\beta} + \sum_{r'\neq r,ij\alpha\beta} \tilde{J}^{rr'}_{ij\alpha\beta}(t)\mathcal{S}_{ri\alpha}\mathcal{S}_{r'j\beta}, \tag{4.1}$$

with intra-cluster coupling J_{ijuv}, and inter-cluster coupling $\tilde{J}^{rr'}_{ij\alpha\beta}$ between spins at site r with spins at r' [Fig. 4.2(c)]. For the weak measurement, a random one-body operator at the given time, $\mathcal{O}(t) = \sum_{i,\alpha} n_i^\alpha(t)\mathcal{S}_{i\alpha}$ is coupled to an auxiliary qubit, which is then projectively measured followed by post-selection (see Appendix C.2). This results in a deterministic evolution of the state with a non-unitary operator $M(t) \sim \left(1 - \frac{1}{2}\mathcal{O}\Delta t - \frac{1}{8}\mathcal{O}^2\Delta t^2 + \cdots\right)$. The system evolves under a circuit constructed by stacking alternating layers of $U(t)$ and $M(t)$ gates, $V(t) \equiv \prod_{t=0}^{T} M(t)U(t)$.

We consider Brownian Gaussian couplings and measurements with zero mean and variance, $\mathbb{E}\left[n(t)n(t')\right] \sim \delta_{tt'}/\Delta t$, $\mathbb{E}\left[J(t)J(t')\right] \sim \delta_{tt'}/(N\Delta t)$ and $\mathbb{E}\left[\tilde{J}(t)\tilde{J}(t')\right] \sim gJ|r_1 - r_2|^{-2\alpha}\delta_{tt'}/(N\Delta t)$ (Appendix C.2). Here we have suppressed the indices of $n, J, \tilde{J}$ which should be considered to be independent and random, and the factor of N is introduced for a meaningful large-N limit. We also take the continuum time limit $\Delta t \to 0$. This model allows us to make analytical progress in accessing the quasi-Rényi entropies.

We now introduce multiple replicas $u, v \in \{1, 2, 3, 4\}$ of the system, and use SWAP tests between the replicas to measure Rényi entropies [213, 216]. Averaging over the random couplings $J, \tilde{J}, n$ introduces inter-replica interaction, which in the large-N limit are mean-field couplings $G_r^{uv} \sim 1/N \sum_i \mathcal{S}_{ri}^u \cdot \mathcal{S}_{ri}^v$ between replicas u, v. We decouple the G fields by introducing Hubbard-Stratonovich replica-fields iF_r^{uv}. The averaged circuit $\mathbb{E}\mathbf{V}(t)$ can now be expressed as a path integral in these fields (Appendix C.2), $\mathbb{E}\mathbf{V}(t) = \int \mathcal{D}\left[iF_r^{uv}\right] \exp\left(-I\left[iF_r^{uv}\right]\right)$ with the action,

$$\frac{I[iF_r^{uv}]}{N} = \sum_r \Big[\sum_{u<v} \int_t \Big((-1)^{u+v+1} \sum_{r'} \mathcal{J}_{rr'} \left(iF_r^{uv}\right)\left(iF_{r'}^{uv}\right) - \Gamma\left(iF_r^{uv}\right) \Big) - \log \mathcal{K}_r \Big]. \tag{4.2}$$

$\mathcal{K}_r = \mathrm{Tr}\left[\exp\left(\int_t \sum_{u<v} \frac{-iF_r^{uv}}{(\mathcal{S}+1)^2}(\mathcal{S}_r^u \cdot \mathcal{S}_r^v)\right)\right]$ is the spin propagator which determines the bulk theory. The renormalized interaction between different sites is long-range, $\mathcal{J}_{rr'} \sim |r-r'|^{-2\alpha}$ (Appendix C.2), For specific matrix elements like $\langle\langle \mathcal{S}_A | \, \mathbb{E}\mathbf{V}(t) \, | \mathcal{I} \rangle\rangle$, the spin propagator $\mathcal{K}_r$ has to be evaluated with fixed boundary condition instead of the trace.

4.4 Replica permutation symmetry breaking

The action (4.2) is invariant under the replica symmetry group $G = (S_2 \times S_2) \rtimes \mathbb{Z}_2$, where the two inner $S_2 \cong \mathbb{Z}_2$ denote permutations of the forward and backward replicas $1 \leftrightarrow 3$ and $2 \leftrightarrow 4$ [4, 174]. The outer $\mathbb{Z}_2$ in the semidirect product is generated by time-reversal $\mathcal{T}$ on four replicas followed by exchange of even and odd replicas $1 \leftrightarrow 2$, $3 \leftrightarrow 4$. The boundary states for the entropy $\hat{S}_A^{(2)}$ explicitly break $1 \leftrightarrow 3$ (or equivalently $2 \leftrightarrow 4$) symmetry.

Saddle point analysis [4] of the bulk action in the mean field limit reveals a phase transition at $\gamma_c = \frac{J}{9}\left(1 + 2g\zeta(2\alpha)\right)$ with the Riemann Zeta function $\zeta(\alpha) \equiv \sum_{r=1}^{\infty} \frac{1}{r^\alpha}$, and an order parameter field $\phi \sim \frac{2}{3\sqrt{3}}\left(iF_{12} + iF_{34} - iF_{14} - iF_{23}\right)$. For $\gamma > \gamma_c$ the saddle point is $\phi = 0$, while for $\gamma < \gamma_c$, ϕ is non-zero and comes in a pair, $\phi \propto \pm\sqrt{\gamma_c - \gamma}$. The replica permutation $1 \leftrightarrow 3$ is equivalent to $\phi \leftrightarrow -\phi$ symmetry, which is spontaneously broken for $\gamma < \gamma_c$. The Landau-Ginzburg field theory is given by (see Appendix C.3)

$$\frac{I_{\text{eff}}}{N} = \int_{t,r}\left[-\phi\partial_t^2\phi - b\int_s' \frac{\phi_r\phi_s}{|r-s|^{2\alpha}} - \phi\partial_r^2\phi - \frac{\delta}{2}\phi^2 + \frac{\phi^4}{4}\right], \tag{4.3}$$

which for $2\alpha > 1$ has a phase transition effected by the mass term $\delta \propto \gamma_c - \gamma$, with $\delta > (<) 0$ being the symmetry-broken (symmetric) phase, and the $\mathbb{Z}_2$ phase transition occurring at $\delta \to 0$. The long-range term appears with a regulated integral: $\int_s'$ to be read as $\int_{\mathbb{R}\setminus(r-\varepsilon, r+\varepsilon)} ds$, with an

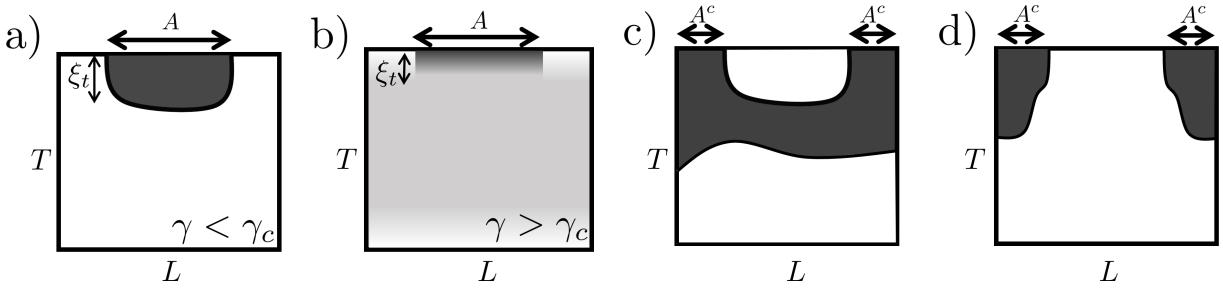

Figure 4.3: Domains and domain walls in the anisotropic Ising model corresponding to the quasi-entropy $\hat{S}_A^{(2)}$ of a small subregion A in the ferromagnetic phase (a, black $\phi > 0$ and white $\phi < 0$ are symmetry-broken domains separated by a domain wall), and the paramagnetic phase $\phi = 0$ (b, light gray). The entropy of the complement subregion A^c corresponds to one of two possible competing domain-wall configurations (c,d).

ultraviolet cut-off ε. For $b \neq 0$, this is the long wavelength theory of an anisotropic long range Ising model [268, 269, 270] in 2D, where the interaction is long-range along space and short-range along time. For $2\alpha < 1$ the power law contribution diverges, so J must be scaled with L to take the thermodynamic limit: the system behaves as a single all-to-all cluster with NL qubits without any volume to area-law transition. There is however a phase transition in the purification times for the system and its parts [4].

For $2\alpha > 3$ the long-range term is irrelevant and the transition is governed by the short-ranged fixed point. For $2\alpha < 3$, the underlying Ising model is anisotropic with a non-trivial dynamical critical exponent,

$$z = \begin{cases} 1 & 2\alpha > 3 \\ \frac{2\alpha-1}{2} & 1 < 2\alpha < 3. \end{cases} \tag{4.4}$$

In this regime we have two distinct correlation lengths $\xi_t \sim \delta^{-\frac{1}{2}}$ and $\xi_r \sim \delta^{-\frac{1}{2z}}$ corresponding to the time-like and space-like directions, respectively.

4.5 Entanglement phases

Using the effective action (4.3) we now calculate the quasi entropy of $\rho_A(t)$ for a contiguous region $A \subset Q$. The twisted boundary condition in I_{SWAP} corresponds to pinning $\phi > 0$ within the subregion A at the future time boundary $t = T$, and pinning $\phi < 0$ on all other boundaries [Fig. 4.3(a,b)]. In the symmetry-broken phase $\delta > 0$ the bulk organizes into domains separated by a domain wall [Fig. 4.3(a)] such that the bulk field is positive $\phi > 0$ (black) within a temporal correlation length ξ_t of the final time-boundary of the subregion A and negative $\phi < 0$ (white) throughout the remainder of the bulk. In the symmetric phase $\delta < 0$ only the trivial bulk saddle point $\phi = 0$ [Fig. 4.3(b), light gray] contributes, and therefore this pinning effect is only relevant very close to the final time boundary . For $A \ll L$ the excess energy $I_{\text{SWAP}} - I$ of this configuration compared to the configuration without the twisted boundary condition is simply given by the energy cost of the power-law interaction acting along a spatial slice of height ξ_t:

$$J\xi_t \int'_{r\in A, s\in A^c} dr ds \frac{1}{|r-s|^{2\alpha}} \sim J\xi_t A^{2-2\alpha} + \text{const.} \tag{4.5}$$

In the symmetry broken phase $\delta > 0$ (see Appendix C.4), the twisted boundary condition at $t = T$ supports a bulk domain wall with spatial extent A and time-like height ξ_t. The space-like part of the domain wall with spatial extent A has a domain wall tension $\sigma_r \sim \xi_t \left(\phi/\xi_t\right)^2 \propto \delta^{\frac{3}{2}}$. The time-like part of the domain wall also contributes an energetic term (sub-extensive in A)

arising from the power-law just like (4.5). Combining these results together we have [2],

$$\frac{\hat{S}_A^{(2)}}{N} \sim \begin{cases} cJ\xi_t A^{2-2\alpha} & \text{for } \gamma > \gamma_c \\ J\left(\sigma_r A + c\xi_t A^{2-2\alpha}\right) & \text{for } \gamma < \gamma_c. \end{cases} \tag{4.6}$$

We emphasize that the power-law correction to the entropy in the volume-law (symmetry-broken) phase is a novel result, which leads to enhanced error-correcting properties for long-range hybrid circuits.

4.6 Error correcting properties

$\hat{S}_R^{(2)}$ in the volume-law phase $\gamma < \gamma_c$ can be understood to be the 'rate' of the QECC, which refers to the amount of logical information of R that is encoded in Q and protected from 'errors' due to measurements with a Code Rate $\sim \hat{S}_R^{(2)} \sim \sigma N L$. The mutual information $\hat{I}^{(2)}(A:R) = \hat{S}_A^{(2)} + \hat{S}_R^{(2)} - \hat{S}_{A^c}^{(2)}$ between a subregion A and the reference R is related to the contiguous 'code distance', which refers to the size of the largest contiguous subsystem of Q whose deletion would not spoil the encoded information of R [173][3]. From (4.6) we have $\hat{S}_A^{(2)} \sim N\left(\sigma A + c\xi_t A^{\upsilon}\right) + \mathcal{O}(1)$ and $\hat{S}_R^{(2)} \sim N\sigma L + \mathcal{O}(1)$, where $\upsilon \equiv 2 - 2\alpha$. The quasi entropy $\hat{S}^{(2)}(A^c)$ is the minimum of two configurations in Fig. 4.3(c,d) [173, 253],

$$\hat{S}_{A^c}^{(2)} \sim \min\left\{\hat{S}_A^{(2)} + \hat{S}_R^{(2)}, N\left(\sigma(L-A) + c\xi_t(L-A)^{\upsilon}\right)\right\}.$$

[2] In the absence of power-law terms, we obtain $1/N$ logarithmic corrections to the entropy in the symmetry-broken phase for the local model, which arise from the fluctuations of the domain wall [173].

[3] This statement comes with two important caveats. First, the theorem proved in [173] rigorously applies only to Clifford circuits (stabilizer states), whereas here our Brownian circuit elements clearly take the quantum state outside the Clifford group. Second, to make meaningful information-theoretic arguments one must ultimately work with the disorder-averaged von Neumann entropy $-\mathbb{E}[\mathrm{Tr}\left[\rho_A \log \rho_A\right]]$

The cross-over between the two occurs for a critical subregion size $A^* \sim \frac{1}{2\sigma} L^v + \mathcal{O}(N^{-1})$. Thus, for $A < A^*$ we have $\hat{I}^{(2)}(A:R) \approx 0$, and NA^* can be identified as a power-law code distance,

$$\text{'Code Distance'} \sim NL^v \text{ for } \gamma < \gamma_c. \tag{4.7}$$

The distance can be tuned with the long-range exponent α, and is sub-linear but scales favorably with L for $2\alpha < 2$. For $2\alpha > 2$, the code distance is $1/N$ suppressed and scales as $\log L$ in our model (see Appendix C.5).

4.7 Monitored SYK chain

We now turn to the study of the effects of long-range couplings on the fermionic monitored Brownian Sachdev-Ye-Kitaev (SYK) chain circuit introduced in [265]. This allows us to separately consider the effects of the long-range coupling and the interactions, which highlight the role of interactions on the entanglement properties of the states generated by hybrid circuits. The setup contains a left ($\mathcal{L}$) and a right ($\mathcal{R}$) chain with L clusters of N Majorana fermions each [265, 271, 272] [Fig. 4.2(d)], with chain undergoing intermittent unitary evolution and monitoring. The unitary evolution is generated by inter-cluster long-range two-fermion of strength $J_{ij}^{rr'} \sim |r - r'|^{-\alpha}$ and on-site four-fermion interaction of strength U_{ijkl}^{r}, which are both independent Brownian variables for each chain. We study the free-fermion limit $U \to 0$ which allows us to consider the effects of long-range hopping and an on-site interaction separately. The $\mathcal{L}$ and $\mathcal{R}$ chains are coupled by a inter-chain parity measurement for each site, described by Kraus operators, $\{M_1^{r,i}, M_2^{r,i}\} = \{\pi_{r,i}^- + \sqrt{1-s^2}\pi_{r,i}^+, s\pi_{r,i}^+\}$, where $\pi_{x,i}^{\pm} = \frac{1}{2}(1 \mp i2\psi_{r,L,i}\psi_{r,R,i})$. s denotes the measurement strength, chosen as [273] $s = \sqrt{\gamma \Delta t}$, with $\Delta t \to 1$ keeping γ fixed. It is

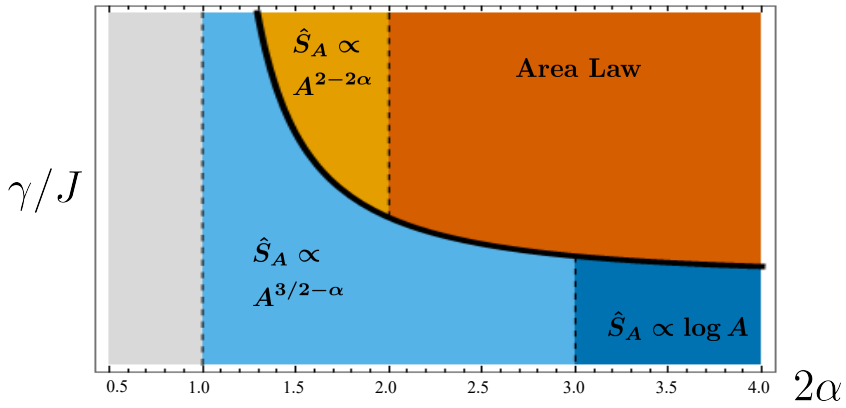

Figure 4.4: Phases of long-range monitored SYK_2 model.

convenient to define $\hat{J} = J\zeta(2\alpha)$ and $\tilde{\gamma} = \gamma/\hat{J}$ and $\tilde{U} = U/\hat{J}$.

4.8 Landau-Ginzburg theory

The theory for quasi-Rényi entropy for the free-fermionic case ($U = 0$) is invariant under the replica symmetry group $(O(2)\times O(2))\rtimes\mathbb{Z}_2$ (see Appendix C.5), where the two $O(2)$ transformations rotate the $1,3$ and $2,4$ contours, respectively. This continuous symmetry (in contrast to the discrete symmetry for the qubits) is spontaneously broken for $\gamma < \hat{J}$, resulting in a Goldstone mode θ_r [274] corresponding to the relative $O(2)$ rotation angle at site r. The effective theory of the Goldstone mode can be derived,

$$\frac{I_{\text{eff}}}{N} = \frac{\rho}{2}\sum_k \int_\Omega \left(\frac{\Omega^2}{\gamma^2} + (1-\epsilon_k)\right)|\theta_k(\Omega)|^2, \tag{4.8}$$

where $\theta_k = \frac{1}{\sqrt{L}}\sum_r \theta_r e^{-ikr}$ and $\epsilon_k \equiv \frac{1}{\zeta(2\alpha)}\sum_{r=1}^{\infty}\frac{\cos kr}{r^{2\alpha}}$ results from the power-law hopping, similar to [267], and the stiffness $\rho = \hat{J}(1-\tilde{\gamma}^2)$ vanishes at $\tilde{\gamma} = 1$, indicating a phase transition at $\gamma = \hat{J}$. The long-range couplings lead to a nontrivial dynamical exponent as before (4.4).

In the symmetry-broken phase ($\gamma/\hat{J} < 1$), the boundary condition pins the angle $\theta = \pi/2$

in subsystem A, and $\theta = 0$ in A^c [267], equivalent to creating half-vortices at the left and right boundaries of A. $\hat{S}_A^{(2)}/N$ can be mapped to the correlation function of a vortex creation operator and scales as $\log A$ for $\alpha > 3/2$ (long-range coupling is irrelevant and we get logarithmic free energy for vertices), and as $A^{3/2-\alpha}$ for $1/2 < \alpha < 3/2$ (Appendix C.5). In the symmetric phase same analysis as (4.5) leads to a distinct fractal phase when $\alpha < 1$ [Fig. 4.4]. The free energy of vortices is proportional to the stiffness and its critical exponent is simply $\nu = 1$ for all $\alpha > 1/2$. When we turn on interactions $U > 0$, the replica symmetry is reduced to a discrete group $(C_4 \times C_4) \rtimes \mathbb{Z}_2$. There is consequently a Z_4 symmetry-breaking transition which reproduces the same entanglement and error-correcting phase diagram as the spin model as shown in Fig. 4.1(b).

4.9 Concluding remarks

The phase diagram in Fig. 4.1 can be readily generalized to Brownian chains in higher dimensions, and demonstrates an entanglement transition for all $2\alpha > d$, with non-trivial dynamical exponent $z = (2\alpha - d)/2$ for $d < 2\alpha < d+2$. The subextensive correction arising from (4.5) is $A^{2d-2\alpha}$. It will be interesting for future studies to study the Rényi entropy for general n and the entanglement entropy at $n \to 1$, and quantify the $1/N$ effects on the phase diagram.

Chapter 5: Efficient tensor network simulation of quantum many-body physics on sparse graphs

"You don't do much," said Tiny Dragon.

"I'm full of potential," said Big Panda with a yawn.

- Big Panda and Tiny Dragon, James Norbury.

5.1 Introduction

Quantum many-body physics is generally studied on regular d-dimensional lattices since the underlying graph is motivated by naturally occurring crystalline solid state materials and lattice regularizations of quantum field theories. However, there are interesting quantum phenomena beyond those feasible on lattices. On one hand, properties of most topological phases of matter do not depend on the exact triangulation of the underlying manifold. In the other extreme, one can study interacting quantum many-body systems on underlying graphs which do not have any smooth manifold structure. The corresponding classical problem was first studied by Bethe [275] in the context of alloys, and since then in the context of spin glasses on random graphs [276]. Previous studies of quantum many-body systems focusing on Bethe lattices and generic sparse graphs have identified several interesting phenomena including approximate solv-

ability leading to mean-field numerical methods [277], quantum spin glass states [278], and the absence of Goldstone bosons on 'expander' graphs [279].

From a modern quantum information perspective, many-body sparse graphical models typically possess the feature of fast quantum information scrambling, which was demonstrated first in all-to-all connected graphical models such as the Sachdev-Ye-Kitaev (SYK) model [12, 24]. These models are holographically dual to a quantum theory of gravity in one higher dimension [12, 24, 25]. In a SYK-like model on N sites, any local quantum information spreads across the whole system in a short scrambling time, $t_* \sim \log N$ [26, 27]. On the other hand, in generic local models on d-dimensional lattices, typical scrambling times are long $t_* \sim N^{1/d}$. In fact, having a complete (i.e. all-to-all connected) graph is not necessary for getting fast scrambling - generic sparse graphs can also scramble information quickly while retaining the feature of approximate solvability [28, 29]. Sparse graaphical models are also attractive platforms to be simulated on a quantum processor, since the sparse connectivity of the graph can lead to efficient quantum simulation. There have already been efforts to realize non-trivial graphs as the platform for many-body physics in quantum simulation architectures [280]. In this context, reliable classical algorithms to simulate quantum many-body models on sparse graphs are highly desirable.

Tensor network states are useful classical ansätze for representing and manipulating entangled quantum states [281, 282]. They have been used to study quantum many-body systems, most successfully in 1 spatial dimension, where tensor networks are routinely used to study ground state properties of gapped Hamiltonians [283, 284], and simulate short-time quantum time evolution [285].

Tensor network states, more specifically matrix product states, can be readily generalized to

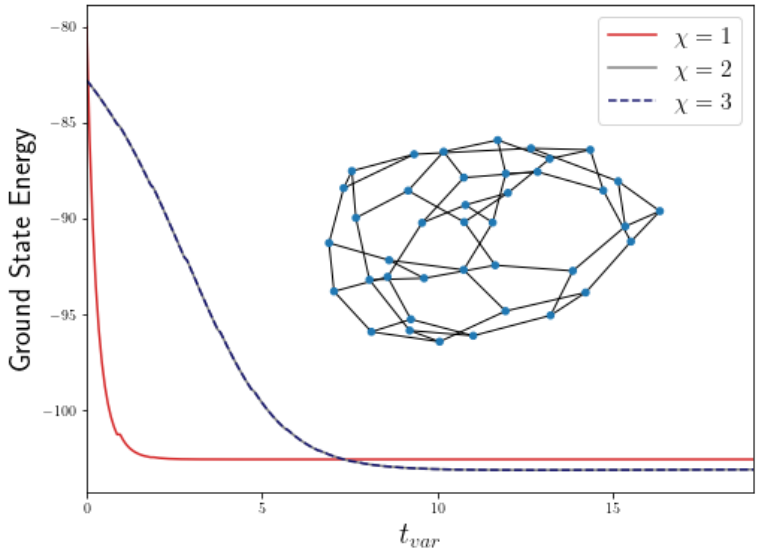

Figure 5.1: **Approximate ground state preparation** for a mixed-field Ising model defined on a random regular graph on 40 vertices [inset]. The parameters of the Hamiltonian for the local terms coupling the quantum spins on nearest neighbors on the graph are $J_{zz} = -1$, and on-site terms $h_x = -2, h_z = -0.5$. The variational algorithm is described in Sec. 5.5. Here we show that the ground state energy has converged by increasing the bond dimension χ from $1 - 3$.

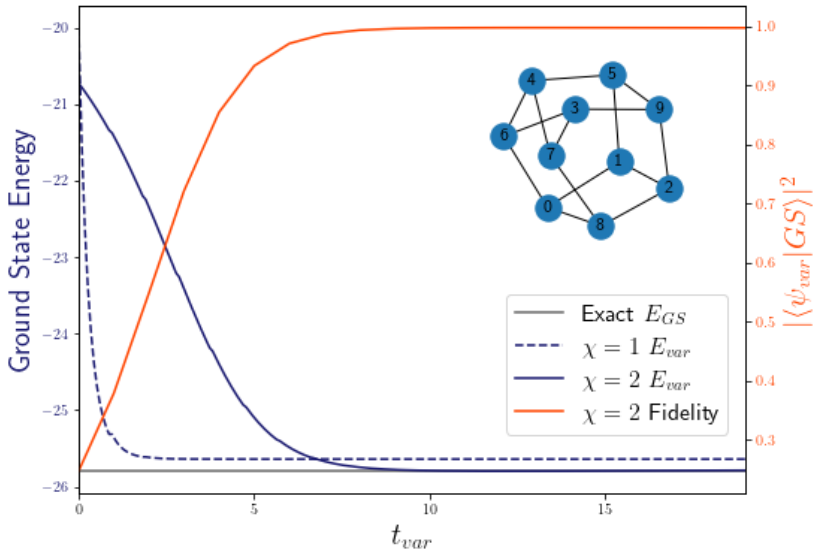

Figure 5.2: **Approximate ground state preparation** for a mixed-field Ising model defined on a random regular graph on 10 vertices [inset]. The parameters of the Hamiltonian are same as Fig. 5.1. Here we show that the ground state energy of the variational ground state $\chi = 2$ has converged to the exact ground state energy value, which is accessed by exact diagonalization. We also estimate the overlap of the variationally prepared state with the exact ground state obtained from exact diagonalization, $|\langle\psi_{var}|GS\rangle|^2$, which goes to 1 after a few steps of the variational algorithm.

higher dimensions [286]. In higher dimensions the representation of such states is still efficient, i.e. the numerical resources required to represent the state scales polynomially with the number of sites of the underlying graph. However the computation of expectation values of local operators is prohibitively hard; one dimension is special because there exists an efficient way to contract tensor networks that fails in higher dimensions. In fact, contraction of generic tensor network states in a 2-d lattice or Projected Entangled Pair States (PEPS) is $\#P$ complete [287], so any NP hard problem can be encoded in such tensor networks. However, approximate methods of contracting classes of 2-d tensor networks (for example, [286, 288, 289]) or efficient manipulation methods for a restricted class of 2-d tensor networks (for example, [290, 291]) are still very useful.

In this work, we demonstrate that approximate local properties of certain class of tensor network states defined on sparse graphs can be efficiently computed using message passing or Belief Propagation (BP) algorithms [292]. Efficient classical simulation of generic sparse graphical models are severely restricted by the presence of cycles or loops in the graph. However, we show in this work that the locally tree-like property of generic sparse graphs allows us to efficiently study the properties of quantum states on such graphs using tensor network contraction by belief propagation. Before describing the details, we first demonstrate the usefulness of such a method. In Fig. 5.1, we variationally access the ground state properties of strongly interacting mixed-field quantum Ising model defined on a sparse random regular graph with 40 vertices. These system sizes are inaccessible to exact diagonalization, and traditional tensor network methods also do not work well for such graphs, as tensor network contraction is severely affected by the presence of cycles in the graph. However, we show in this work that the BP algorithm can efficiently compute local energy functionals for tensor network states defined on such graphs, which allows us to systematically access the ground state energy in a standard laptop in a few

minutes. In Fig. 5.2 we show by comparison to an exact computation in a graph with 10 vertices that the prepared tensor network state is indeed the ground state of the Hamiltonian considered. In later sections we will describe the method and demonstrate careful numerical benchmarks.

A typical class of problems where BP can be employed is in extracting marginal distributions from Gibbs distribution of classical spin models. Consider a classical spin model defined on a graph G, with the Hamiltonian $H = -\sum_{a,b\in\mathcal{N}_a} h_{ab}(s_a, s_b)$ where $\mathcal{N}_a$ refers to the graph neighborhood of the site a, and h_{ab} refers to the local energy on an edge ab. The Gibbs distribution $P(\{s_i\}) \propto e^{-\beta H(\{s_i\})}$ is efficiently represented by specifying the edge energy functionals h_{ab} for all edge $ab \in G$ that connect the vertices a and b. However, accessing marginal probability distributions of one (or few spins) requires one to contract the Gibbs distribution over the graph G, which can be hard, and BP algorithms can provide an approximate solution to this problem. A generic theory for the success of BP is still an area of active research, however, it has been shown that the results obtained from BP algorithms are equivalent to the Bethe Peierls approximation (where the underlying graph is assumed to be an infinite tree Bethe lattice) [293]. On a tree graph (which by definition lacks cycles), the BP algorithm is exact, while on a graph with cycles there is no guarantee that the algorithm will converge or provide the correct answer. However, these algorithms are routinely used even for graphs with cycles, and empirically provide correct answers when the underlying graph is locally tree-like [31, 294]. In fact, BP has been instrumental in decoding classical low-density parity-check (LDPC) error correcting codes [31].

Tensor network states can be mapped to the graphical models described above [295], where the amplitude corresponding to the tensor network state is analogous to the Gibbs distribution over a classical graphical model, and accessing the local reduced density matrices is analogous to marginalizing the Gibbs distribution. Based on this understanding, it was shown by Leifer and

Poulin that tensor network contraction can be done using BP [30]. More recently, Alkabetz and Arad [296] showed that BP algorithms can be used to access local observables in PEPS defined over 2-d lattices, and provide the same answer as other widely used approximate PEPS contraction methods [289]. Led by the intuition of BP being more successful when the underlying graph is locally tree-like, we employ BP to study tensor network states on sparse locally tree-like graphs, and develop variational methods to prepare tensor network states that are approximate ground states of local Hamiltonians defined on such graphs. This also allows us to study interesting physics questions such as the phase diagram of a transverse field Ising model across the symmetry-breaking quantum phase transition.

Local properties of thermal states of sparse graphical Hamiltonians have been previously studied using the quantum cavity and quantum belief propagation methods [297, 298, 299, 300, 301], which are quantum formulations of the BP-inspired classical cavity algorithms [302]. The idea in those works is to represent the quantum partition function as a classical probability distribution and find its marginals using belief propagation. Our work builds a bridge between those methods and the problem of tensor network contraction on generic graphs, which can lead to future cross fertilization of these fields.

Let us briefly comment on the layout of the rest of the paper. We first introduce notation and brief definitions for graphs and sparse graph tensor network states in Sec. 5.2. In Sec. 5.3 we describe the BP algorithm for contracting tensors and explain the intuition why the method is expected to work for accessing local expectation values for sparse tensor network states. In Sec. 5.4 we demonstrate the viability of this method by computing local operator expectation values for a variety of graph-like quantum states on random regular graphs. Finally, in Sec. 5.5 we use the BP contraction method to variationally prepare ground states of local Hamiltonians

defined on sparse graphs. This allows us to study the phase diagram of a transverse field Ising model on a random regular graph across the usual $\mathbb{Z}_2$ symmetry-breaking transition. We end by commenting on the prospects of the BP contraction methods in tensor networks, and studying many-body physics on sparse graphs.

5.2 Tensor networks on graphs

A graph $G(V, E)$ is specified by its set of vertices V, and the set of edges E connecting any two vertices. G is $r-$regular if the degree, or the number of neighbors of each site, is constant and equals to r. If any subgraph of G forms a closed chain, we call that a cycle; tree graphs are graphs which have no cycle. A complete graph on N vertices is one where every vertex has an edge connecting it to every other vertex, i.e. it is the unique $(N-1)$-regular graph on N vertices.

Given an underlying graph G, we can define a class of tensor network states, by assigning a set of tensors located on each vertex, where the virtual bonds correspond to the edges connecting that site (see Fig. 5.3a-f). A tensor network state with uniform bond dimension (i.e. the dimension of the virtual space) χ and physical dimension d on r-regular graph is specified by a set of $r+1$ rank tensors with $d\chi^r$ entries.

Matrix product states form a class of these general tensor network states when the underlying graph is a 1-dimensional lattice (Fig. 5.3b). Accessing local operators on such 1-d tensor network states is efficient because there is an efficient algorithm to contract it, which depends on the fact that any connected subgraph can be separated from the lattice by cutting only 1 or 2 edges; hence any matrix manipulation during the contraction procedure scales linearly with the number of vertices N of the graph. This feature works not just for 1-d, but for any tree-like geom-

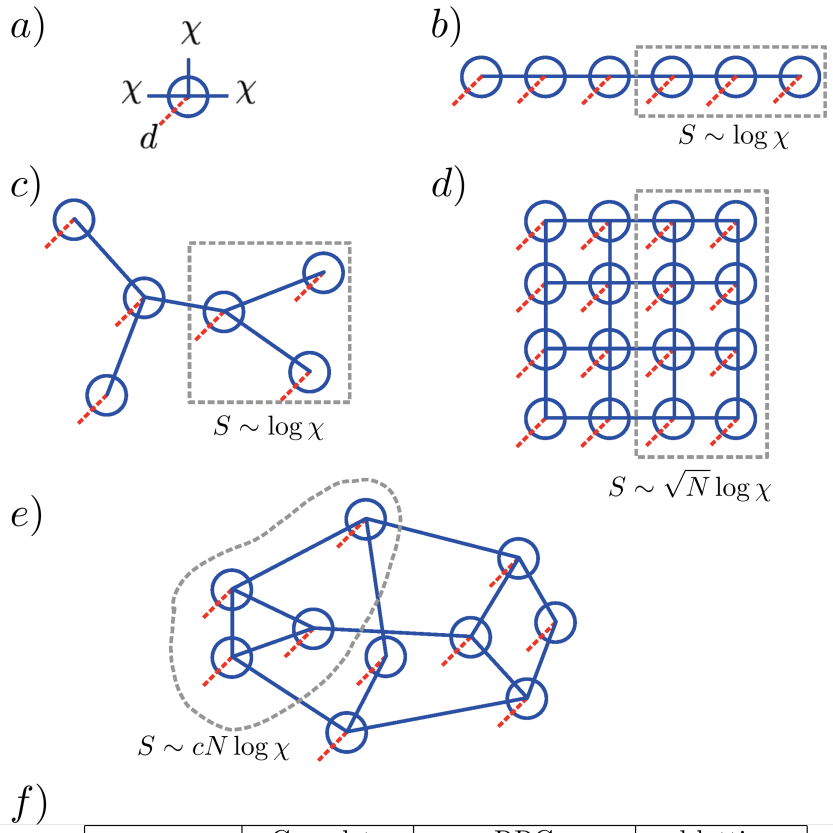

f)

	Complete	RRG	d-lattice
Diameter	2	$\log N$	$N^{1/d}$
Expansion	$\mathcal{O}(1)$	$\mathcal{O}(1)$	0
Cycles	at all scales	few short cycles	at all scales
Degree	$\mathcal{O}(N)$	$\mathcal{O}(1)$	$\mathcal{O}(1)$

Figure 5.3: **Tensor networks on generic graphs.** The fundamental component is the on-site tensor **(a)**, with physical dimension d and virtual bond dimension χ. These can be put on any underlying graph: 1-d lattice **(b)**, a tree **(c)**, 2-d lattice **(d)**, and a random regular graph(RRG) **(e)**. We also show the scaling of the maximal entanglement of the tensor network ansatz for a typical fraction of the graph **(b-e)**. On RRG, volume law states can be represented by finite χ tensor networks. In **(f)** we compare the graph properties of a complete graph, random regular graph (RRG) and a d-dimensional lattice. The properties being compared are: diameter or maximal distance between any two vertices, expansion defined in Eq. 5.1, number and type of cycles, and degree or number of neighbors of any vertex.

etry, which is why tree tensor networks (Fig. 5.3c) are efficient ansatz for any tree-like quantum model [303, 304]. However this does not hold true for 2-d lattices on N vertices (Fig. 5.3d). The number of dangling edges of any connected subgraph (or the "surface area") for such lattices can be upto $\sim \sqrt{N}$, which implies that the slowest step for tensor contraction will require manipulating an array of size $\chi^{\sqrt{N}}$ which has an unfavorable exponential scaling. Another way of seeing why contracting 2-d lattices is difficult is by noting that 2-d lattice has cycles at all scales, while tree tensor networks are acyclic, and 1-d lattice has either no cycle (open boundary condition) or one very long cycle (periodic boundary condition).

Lattices are atypical graphs - which can be understood by considering the expansion property of typical graphs. For any subset of vertices $S \subset V$, we define $\mathcal{E}(S)$ to count the number of dangling edges in G with one extremity in S and the other in $V \setminus S$ ($\mathcal{E}(S)$ captures the notion of "surface area" of S). One can formally define an expansion coefficient, which is the minimal ratio of the "surface area" to the volume for any subgraph of G,

$$h(G) = \min_{S} \{\mathcal{E}(S)/|S| \text{ for } \varphi \neq S \subset V \text{ and } |S| \leq N/2\}. \tag{5.1}$$

For lattices, $h(G) \to 0$ as $N \to \infty$, i.e. the volume scales faster than the "surface area". However, generic graphs have positive "expansion", which can be formalized by considering a probabilistic scheme to construct generic graphs, namely random regular graphs [305]. A random regular graph is a graph drawn from a probability space $\mathcal{G}_{N,r}$, which are all r-regular graphs on N vertices. It can be shown that a random regular graph is an expander graph for large N with high probability, i.e. they have positive expansion, $h(G) = c > 0$ [305]. Note, these graphs are sparse and the number of edges only scales linearly with N, since the graph is $r-$regular.

From this general definition, it would seem that manipulations of tensor networks defined on such expander graphs would be prohibitively inefficient, as a naive contraction will now have to deal with matrix multiplication over an index that scales as badly as $\chi^{\mathcal{O}(N)}$. At the same time, because of the underlying graph structure, a tensor network defined on such a graph can represent a volume law entangled state with even a finite bond dimension χ. The entanglement of a subregion of the tensor network satisfies, $S \leq cN \log \chi$, where c is the expansion, and hence the maximal entanglement scales as a volume-law. For $\chi > e^{\log 2/c}$, the above tensor network bound exceeds the universal bound $S(A) \leq |A| \log 2$. This suggests that with $\chi \sim e^{\log 2/c}$ but independent of N one can already represent nearly maximally entangled state on asymptotically large contiguous subsystems. Hence, we expect that highly entangled states on such graphs can be represented with very modest bond dimension.

However, generic expander graphs are also locally tree-like, which arises due to their sparsity. Typical graphs of $\mathcal{G}_{N,r}$ have a small number of short cycles. In fact, asymptotically $N \to \infty$, the number of cycles of length i behaves as independent Poisson random variable with mean $(r-1)^i/(2i)$. Note, however that the diameter of an expander graph is $\sim \log N$, so for a given sized graph, the cycles of size $\log N$ must exist. Still, starting from any vertex, at large N one has to go farther and farther to see any cycles at all, which makes these graphs 'locally' tree-like.

This locally tree-like feature is special to expander graphs, which is not present for d-dimensional lattices. We find that this property actually allows us to contract tensor networks defined on such graphs efficiently.

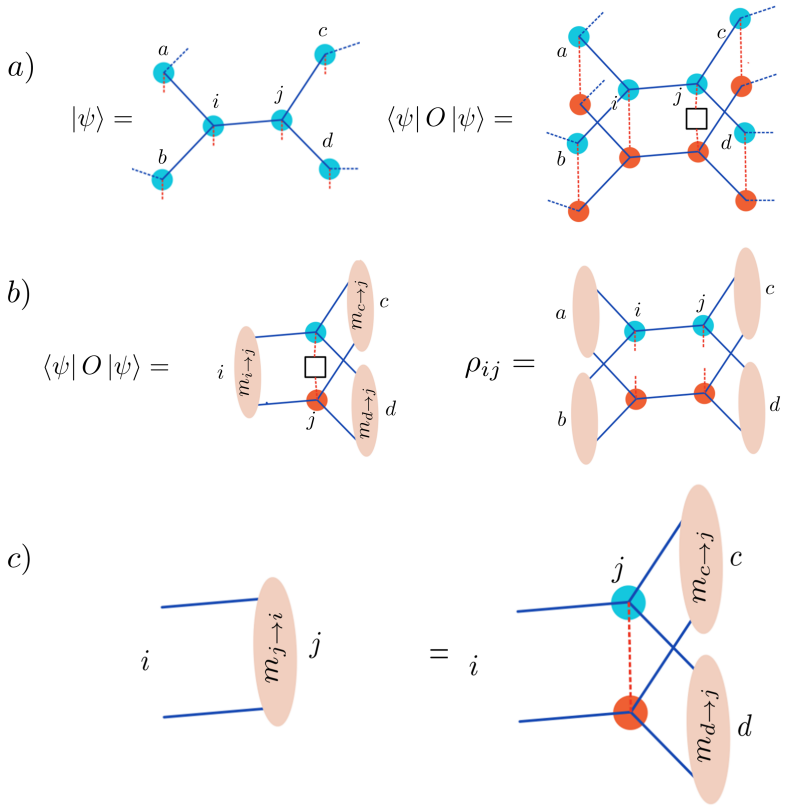

Figure 5.4: **Belief propagation algorithm to contract tensor network on a graph. (a)** shows a patch of the tensor network state $|\psi\rangle$. Expectation value of any local operator O can be computed by considering $|\psi\rangle$ and its conjugated copy and contracting them. These can be equivalently computed using the message tensors, as shown in **(b)**. The reduced density matrix ρ_{ij} of the state $|\psi\rangle$ for two nearest neighbor sites in terms of the local message tensors is shown as well. **(c)** pictorially depicts the central BP equation Eq. 5.2, which is iterated (as in Eq.5.3) to find fixed points of the message tensors.

5.3 Belief propagation method to contract tensors

We now describe the belief propagation algorithm for contracting tensor networks, following the method introduced in [296]. Suppose we are given a tensor network state $|\psi\rangle$ defined on an underlying graph G. Computing the norm $\langle\psi|\,\psi\rangle$ or expectation value of an operator $\langle\psi|\,\mathcal{O}\,|\psi\rangle$ requires us to take two copies of the tensor network (one with a complex conjugate), stack them and introduce the operator $\mathcal{O}$ if necessary, and trace over the physical legs (see Fig. 5.4a). The resulting network is a double-edged factor graph [296], and we will use BP to compute its marginals, which in our case corresponds to the local reduced density matrices.

We define a 'message' tensor $m_{a\to b}$ corresponding to each directed edge connecting two vertices $a, b \in G$, with an added direction $a \to b$. $m_{a\to b}(x, x')$ is a $\chi \times \chi$ dimensional tensor which corresponds to the contraction of the tensor and its conjugate for all sites in G which are connected to b via a. In $m_{a\to b}(x, x')$, (x, x') refer to the indices corresponding to the virtual bonds along ab of the tensor $|\psi\rangle$ and its conjugate, which also makes the matrix $m_{a\to b}$ positive semi-definite. By this definition, one can set up a recursive self-consistency relation that relates the message tensor to their nearest neighbor state tensor ψ_i and the next-nearest neighbor message tensors,

$$m_{i\to j} = \mathrm{Tr}\left(\psi_i \psi_i^* \prod_{k\in\mathcal{N}_i\setminus j} m_{k\to i}\right). \tag{5.2}$$

Here, $\mathcal{N}_i \setminus j$ refers to the neighboring vertices of i apart from j. The self consistency Eq. 5.2 can be pictorially represented as shown in Fig. 5.4c.

Note, the definition of $m_{a\to b}$ as the result of the contraction of the tensor network connected to b 'via' a only makes sense when the underlying graph has no closed chain connecting a and

b, i.e. the graph is a tree. However, the recursive definition Eq. 5.2 is a consistent definition for a positive definite message tensor that works for any graph. Our goal is to access self-consistent message tensors that satisfy the recursive equation Eq. 5.2 by the Belief Propagation algorithm, and then identify that as the result of an actual contraction of the tensor network. In order to do that, we simply iterate the self consistency equation, starting from some initial choice of positive semi-definite message tensors for each directed edge of the graph at $t = 0$. At any subsequent time-step, we get message tensors,

$$m_{i\to j}^{[t+1]} = Tr\left(\psi_i \psi_i^* \prod_{k\in\mathcal{N}_i\setminus j} m_{k\to i}^{[t]}\right). \tag{5.3}$$

We look for fixed points of this iterative algorithm. Note that this can be an uncontrolled step, and in general we are neither guaranteed that a fixed point exists, nor that the fixed point corresponds to the correct marginal contraction. Furthermore, there is a 'gauge' freedom in the definition of the message tensor, as many message tensors can correspond to the contraction of the same tensor network state. However, for tree-like graphs, this is guaranteed to converge to the result from the contracted tensor. As was pointed by [296], even on a 2-d lattice where there is a proliferation of short cycles, this algorithm can return good approximate answers.

Extracting local reduced density matrices is straightforward once we have the self-consistent message tensors, and only requires local contraction of the state tensor with the message tensor, as shown for a neighboring 2-site reduced density matrix in Fig. 5.4b.

The central BP equation for tensor network contraction Eq. 5.3, for an underlying graph with cycles is a version of the loopy-BP algorithm. As mentioned in the introduction, while loopy-BP is not guaranteed to succeed, it has been shown to work extremely well in many practi-

cal scenario. Perhaps its most useful application lies in the decoding of low-density-parity-check (LDPC) codes [306]. Importantly, LDPC codes are asymptotically locally-tree like, hence the effective 'Bethe' or tree-approximation inherent in the BP algorithm works well there.

Motivated by this observation, we employ the BP algorithm to access local expectation values for tensor networks defined on random regular graphs. The intuition is as follows: consider a state on the graph G with correlation length ξ. Typical lengths of cycles on random regular (and in general sparse expander) graphs is $\sim \log N$. Hence, if $\xi < \log N$, the state is expected to look tree-like, and the BP algorithm should converge to the right answer. Crucially, in sparse expander graphs the typical cycle length diverges in the thermodynamic limit, so one can expect successful contraction of a wide scale of states which are not just short-range correlated.

5.4 Graph states and square root states

In this section we demonstrate the usefulness of this method to extract local information from a class of tensor network states defined on sparse graphs. We introduce a class of tensor network states for qudits with local Hilbert space dimension d which can be efficiently represented as a tensor network with bond dimension $\chi = d$ on any underlying graph G,

$$|\psi\rangle \sim \sum_{\{s\}} \left(\prod_{ab \in \text{Edge}_G} M(s_a, s_b) \right) |\{s\}\rangle \,, \tag{5.4}$$

where s_a is a basis of the d-dimensional local qudit Hilbert space. These states can be called generalized graph states. We consider the following decomposition of the $d \times d$ dimensional matrix $M = AA^T$. Now, the state in Eq. 5.4 can be constructed out of the A matrices explicitly and locally. Consider a vertex $a \in G$, with degree r. Consider the generalized identity tensor

$I_{s,\alpha_1,..,\alpha_r} = \delta_{s\alpha_1}\delta_2...\delta_{s\alpha_r}$, where the s index refers to the physical qudit index and α_i refer to the r virtual indices. Now we can multiply the A matrices to I to get the local tensors T corresponding to the state in Eq. 5.4,

$$I_{s\alpha_1...\alpha_r} =$$

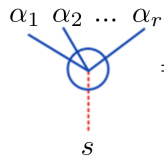

$$= \delta_{s\alpha_1}\delta_{s\alpha_2}...\delta_{s\alpha_r}$$

$$T_{s\alpha_1...\alpha_r} =$$

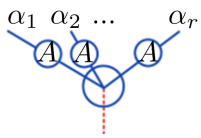

(5.5)

5.4.1 Square root states of classical models

Consider a classical Ising model on any generic graph,

$$H_c = -J \sum_{i,j\in\mathcal{N}_i} s_i s_j, \tag{5.6}$$

with the partition function $\mathcal{Z}(\beta) = \sum_{\{s\}} e^{-\beta H_c}$.

We consider the square root state associated with it [67],

$$|\psi\rangle = \frac{1}{\sqrt{\mathcal{Z}(\beta)}} \sum_{\{s\}} e^{+\frac{\beta J}{2}\sum_{i,j\in\mathcal{N}_i} s_i s_j} |\{s\}\rangle \,. \tag{5.7}$$

We denote the Pauli spin operators as X, Y, Z and the identity operator as $\mathbf{1}$. These states are called square root states, since these can be understood to be the square root of the Ising model partition function; in fact if we consider the unnormalized state, $|\tilde{\psi}\rangle = \sum_{\{s\}} e^{+\frac{\beta J}{2}\sum_{i,j\in\mathcal{N}_i} s_i s_j} |\{s\}\rangle$,

the classical partition function is equal to its norm $\mathcal{Z}(\beta) = \langle\tilde{\psi}|\tilde{\psi}\rangle$. Expectation value of any classical operator (i.e. an operator constructed out of Z_i operators) in the state $|\psi\rangle$ is equal to an averaged classical statistical quantity,

$$\langle\psi| Z_a |\psi\rangle = \langle Z_a\rangle_{H_c} = \frac{\mathrm{Tr}_{\{s_i\}} Z_i e^{-\beta H_c(\{s_i\})}}{\mathrm{Tr}_{\{s_i\}} e^{-\beta H_c(\{s_i\})}}. \tag{5.8}$$

The latter can be estimated by classical Monte Carlo methods, so we can access the expectation value of classical operators easily. However, accessing quantum operators, for example $\langle X_a\rangle$ is not possible using a naive Monte Carlo approach.

The square root state in Eq. 5.7 can be shown to be the ground state of a parent quantum Hamiltonian defined on the graph,

$$H = \sum_a \left[-X_a + e^{-\beta J Z_a \sum_{b\in\mathcal{N}_a} Z_b}\right]. \tag{5.9}$$

It also corresponds to a general graph state defined in Eq. 5.4, with $\chi = d = 2$,

$$M(s_a, s_b) = \begin{pmatrix} \exp \beta J/2 & \exp -\beta J/2 \\ \exp -\beta J/2 & \exp \beta J/2 \end{pmatrix} \tag{5.10}$$

and the corresponding A defined by $AA^T = M$ can be computed straight-forwardly. We study the expectation values of 'classical' Z and the 'quantum' X operators averaged over all sites of the graph using the BP contraction method. The results are shown in Fig. 5.5, where the underlying graph is taken to be an instance of random regular graph $\mathcal{G}_{N=100,r=3}$.

We plot $\overline{|Z_a|}$, which is the absolute value of the expectation of Z_a operators averaged over

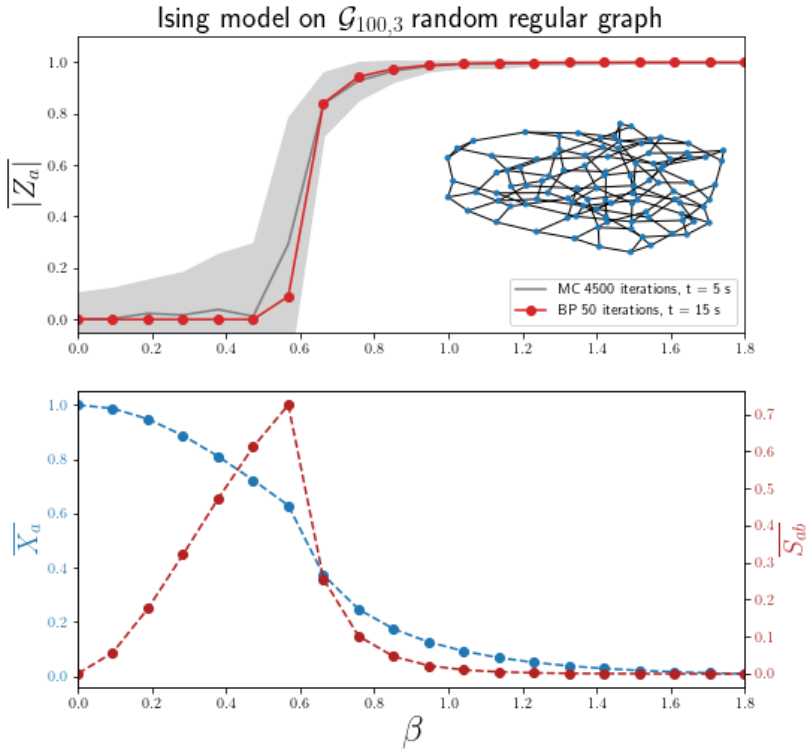

Figure 5.5: **Expectation values of local operators of Ising model square root states**, defined in Eq. 5.7, on a random regular graph from the ensemble $\mathcal{G}_{100,3}$ [inset]. J is set to be 1. In the **top** panel, absolute value of local Z operator averaged over the vertices of the graph is plotted as a function of β. Since this is a classical observable, it can be estimated by straight-forward Monte Carlo sampling (MC), which is shown with the error bar estimate from the average. The BP result is shown in red, which matches the MC estimate. In the **bottom** panel we show the BP result of the site-averaged X operator and the edge-averaged entanglement entropy of reduced density matrix of nearest neighbor sites. These expectation values are inaccessible to simple MC sampling of the classical model.

all vertices of the graph, as a function of the inverse temperature β that is a parameter in the theory. Since this quantity can be directly computed using Monte-Carlo sampling on the original Ising model, we get an independent check for the BP method. We find that $\overline{|Z_a|}$ is an order parameter for the phase transition in the classical model that occurs from the paramagnetic phase at low β to an ordered ferromagnetic phase at high β, and the results are consistent between the BP and the MC answers across all β. However, using the BP messages, we can also compute the averaged $\overline{X_a}$ expectation values, and the averaged entanglement of 2-site reduced density matrices on all edges $ab \in G$. Note, these quantities are not easily accessible via naive Monte Carlo sampling of the classical model, which shows an application of the BP method of tensor network contraction. We discuss the convergence issues and the 'gauge' freedom of the BP message tensors in Sec. 5.6.1.

5.4.2 Graph states on sparse graphs

Graph states in quantum computing [307] are generalizations of cluster states which are resources for measurement-based quantum computing [308]. Importantly for this work, graph states are a kind of generalized graph state as defined in Eq. 5.4.

Graph state $|G\rangle$ is pure state on N qubits for a graph G on N vertices. We start with the product state $(|0\rangle + |1\rangle)^{\otimes N}/2^{N/2}$, and apply the controlled phase gate $U = |0\rangle\langle 0| \otimes \mathbf{I} + |1\rangle\langle 1| \otimes Z$ to any pair of qubits on vertices connected by the edges in G. It can be easily shown that in our definition of generalized graph states in Eq. 5.4, $|G\rangle$ corresponds to,

$$|G\rangle \equiv M(s_a, s_b) = \begin{pmatrix} 1 & 1 \\ 1 & -1 \end{pmatrix}. \tag{5.11}$$

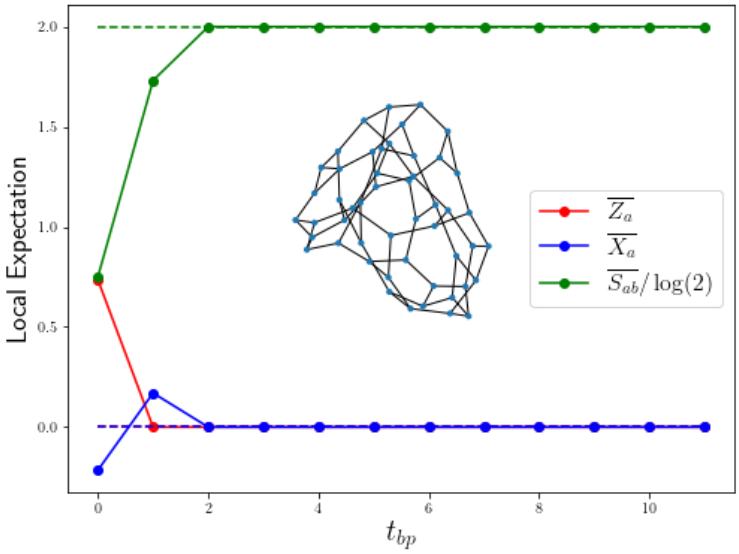

Figure 5.6: **Local expectation values of graph states** defined on a $\mathcal{G}_{50,3}$ random regular graph, as a function of the number of BP steps. The BP steps converge to the correct expectation value for the 1-body and 2-body expectation values after 3 steps.

Hence $|G\rangle$ is efficiently represented by a $\chi = 2$ bond dimension tensor network state defined on any graph G. Graph states form an important class of multi-party entangled states.

We can estimate the local expectation values of $|G\rangle$ defined on random regular graphs using the BP algorithm. On a 3-regular graph, the expectation value of any of the local Pauli operators X, Y, Z is 0, and the entanglement of any reduced density matrix on an edge is $2 \log 2$, which is confirmed as the fixed point after ~ 3 BP steps, as shown in Fig. 5.6.

These results demonstrate the utility of the BP algorithm in accessing local expectation values of a class of entangled states defined on graphs. Next, we introduce a variational algorithm which uses the BP algorithm as a subroutine, to approximately determine the ground state energy and prepare an approximate ground state of a quantum model defined on a sparse graph.

5.5 Variational preparation of ground states of sparse graph Hamiltonians

Suppose we are given a graph G and a Hamiltonian defined on it, $H = -\sum_{a,b\in\mathcal{N}_a} h_{ab}$. Our goal is access the ground state $|\psi_{GS}\rangle$ of this H, and estimate its energy, E_{GS}. Note, given a tensor network state $|\psi\rangle$, the estimation of its energy can be achieved by computing energy functionals over 2-body local reduced density matrices along the edges, $\langle\psi| H |\psi\rangle = \sum_{ab} \langle\psi| h_{ab} |\psi\rangle$, which can be estimated using the BP algorithm. This suggests a variational method to prepare an approximate ground state.

We first start with an initial state $|\psi_{in}\rangle$. At each variational step, we perform a fixed number of BP iterations to access the approximate message tensors. Next, we fix the message tensors $\{m\}$, and locally update the state tensor $|\psi\rangle$ by gradient descent to minimize the energy functional, $|\psi\rangle \to |\psi\rangle - \alpha\nabla H\left(|\psi\rangle, \{m\}\right)$, where the gradient of the energy functional is computed using fixed messages $\{m\}$ obtained beforehand. These two steps are repeated until the energy of the state reaches a steady value. The pseudocode is provided here,

Algorithm 1 Variational TN ground state preparation

```
Initialize state |ψ⟩ = |ψ_in⟩
while t < t_var do
    while τ < t_bp do
        BP on |ψ⟩: messages {m[τ+1]} = BP_|ψ⟩({m[τ]})
    end while
    while n < n_gd do
        Gradient descent: |ψ⟩ → |ψ⟩ − γ∇H(|ψ⟩, {m[t_bp]})
    end while
end while
```

A comment on the variational method: it does not guarantee physically realistic local expectation values during the variational steps. The quantum states are always tensor network states and hence physical, however the BP steps are iterated for a prefixed finite time and not until they

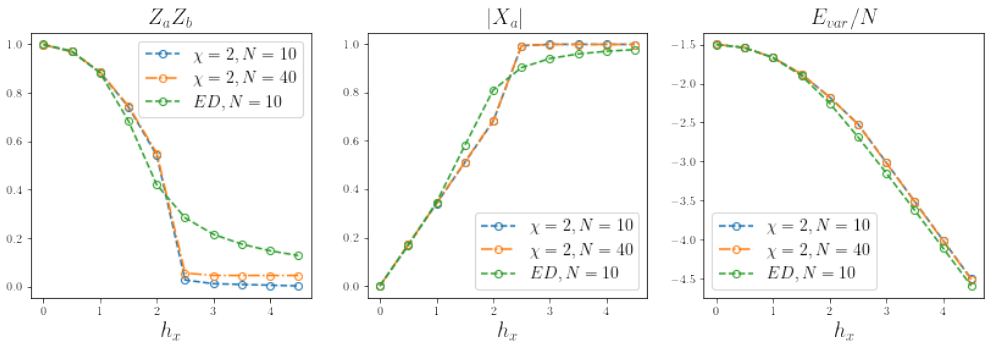

Figure 5.7: **Quantum Ising model on a random regular graph**. We variationally access the local order parameters and the energy density for both $N = 10$ and $N = 40$ sized random regular graphs $\mathcal{G}_{N,r=3}$, with tensor network states with $\chi = 2$. The results are also compared with the $N = 10$ exact diagonalization data.

have converged on to the messages corresponding to the tensor network states.

As a demonstration we consider a random regular graph drawn from $\mathcal{G}_{N,r=3}$, and define a nearest neighbor mixed-field Ising Hamiltonian, with edge terms, $h_{ab} = Z_aZ_b$ and vertex terms, $h_a = 2X_a + 0.5Z_a$. We consider the following parameters for the variational procedure, $t_{bp} = 5, n_{gd} = 10, \gamma = 0.01$, and the initial states are chosen to be either product states or high temperature square root states of the classical Ising Hamiltonian Eq. 5.7.

The results are shown in Fig. 5.2 in Sec. 5.1, which is a benchmark study for $N = 10$ for which the exact ground state can obtained by exact diagonalization. We plot the estimated ground state energy, and the fidelity of the obtained state with the exact ground state for two different bond dimensions $\chi = 1, 2$. We find that with $\chi = 2$ the energy of the variational state is indistinguishable from the exact ground state energy, and the overlap with the exact ground state also is significantly higher than any random state. This suggests that we have variationally prepared a $\chi = 2$ tensor network state which is very close to the exact ground state of the Hamiltonian. This method can be readily generalized to $N = 40$ which takes < 20 minutes on a standard 16 GB laptop to run (see results in Fig. 5.1); however these sizes are inaccessible to

exact diagonalization.

Variational ground state preparation on quantum graphical models using quantum belief propagation has been studied before [309, 310]. On the other hand, variational tensor network ground states have also been studied on tree lattices [311, 312], where the tensor network contraction is simple because of the lack of cycles or loops. Using the formulation of BP for tensor network states, our method leads to approximate tensor network representation of the whole ground state, from which correlation functions may be estimated.

As another demonstration, we consider the quantum Ising model with transverse field,

$$H = -\sum_{ab} \left(Z_a Z_b + h_x X_a \right), \tag{5.12}$$

and access local expectation values of $Z_a Z_b$, X_a, and the energy density, as a function of h_x, shown in Fig. 5.7. This model undergoes the standard $\mathbb{Z}_2$ symmetry breaking quantum phase transition. We find that the variational method works well in the gapped ferromagnetic ($h_x \ll 1$) and the paramagnetic ($h_x \gg 1$) phases, but deviates from the finite size exact diagonalization data near the transition. Interestingly, the local order parameters and the energy density accessed using the BP method show the same results for both the $N = 10$ and $N = 40$ sized graphs return similar values. This indicates that the BP method is able to access the local properties of the large-N graph even with the small finite sized numerics. The results indicate there is a phase transition at $2 \leq h_x \leq 3$. In the ferromagnetic phase of the transverse field Ising model the variational method produces a state in the 'degenerate' ground space, which is in general an uncontrolled superposition of the two lowest lying states; however the local order parameters do not distinguish between the states (see discussion in Sec. 5.6.2).

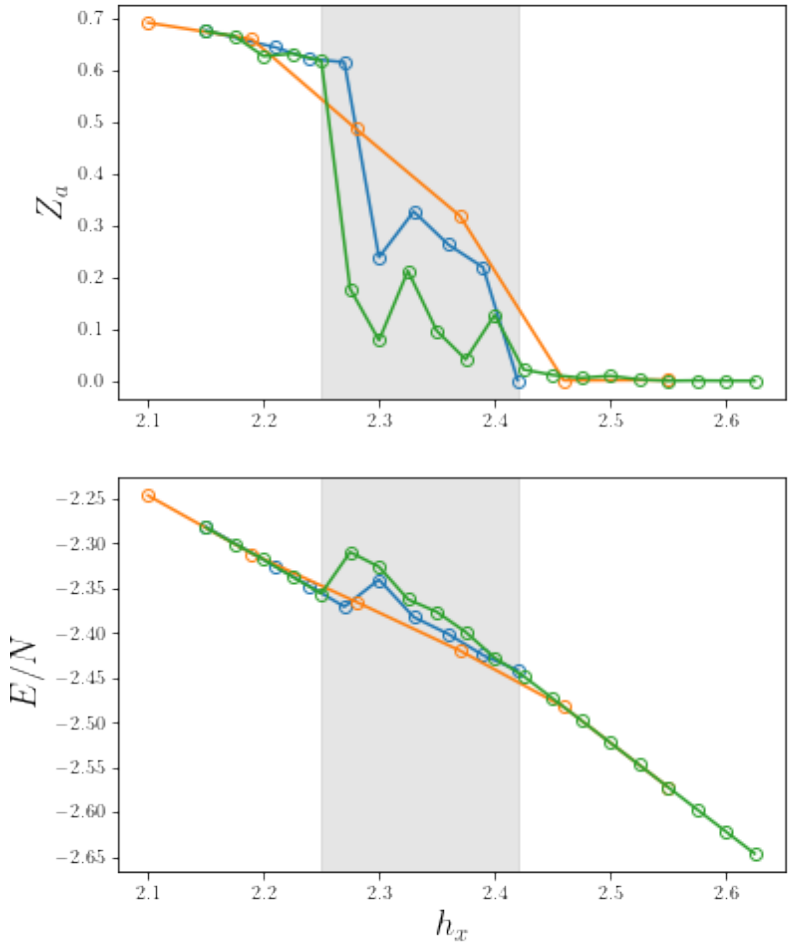

Figure 5.8: **Quantum Ising model near criticality.** We consider the transverse field quantum Ising model on a random regular graph $\mathcal{G}_{40,3}$, and plot the local order parameter Z_a averaged over all sites, and the energy density as a function of the field h_x. The different traces are different runs of the variational algorithm, starting with slightly different initial states, and running for a constant number of iterations which converge away from the critical point.

In Fig. 5.8 we zoom into the critical region, and access the local order parameter Z_a (averaged over all sites) and the energy density. In [311], this model was studied on Bethe lattices using imaginary time evolution, and the phase transition was characterized to be mean-field like. In the random regular case, we find that the variational method slows down considerably near the critical point, and we are not able to access consistent results after a finite number of iterations ($t_{var} = 15$) when we start with distinct initial states. Fig. 5.8 indicates that the phase transition occurs at $2.25 \leq h_x \leq 2.45$, but we are not able to characterize the critical properties of the transition using the variational method for tensor networks with $\chi = 2$.

In a Bethe lattice with degree 3, which is locally similar to the random regular graph $\mathcal{G}_{N,3}$ at large N, bond dimension 2 is enough to asymptotically represent maximally entangled states on large enough subregions. However, the variational method we have studied is a local update method, which is presumably why it fails to approximate the long-range correlated state near the critical point. The sparse graph model is mean-field like, which implies that the physics near the critical point is governed by the uniform spatial zero-mode. One can consider a uniform ansatz for the variational update which will work better for accessing the critical properties of the transition. Also, one can use better variational methods to tackle the issue of small gaps and slow convergence, such as stochastic versions of gradient descent or simulated annealing.

5.6 Details of the numerical implementation

In this section we provide details of some of the numerical observations behind the results in the main paper. We will also discuss convergence and related issues.

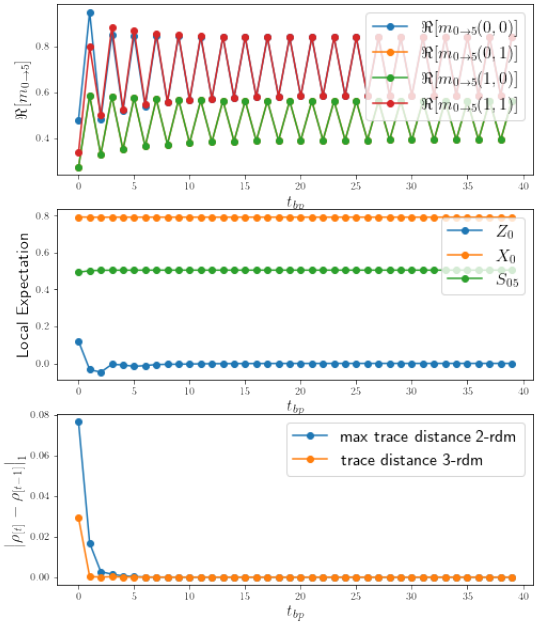

Figure 5.9: Convergence of BP messages and local expectation values with BP for Square root state with $\beta = 0.4J^{-1}$ on a $\mathcal{G}_{20,3}$ random regular graph.

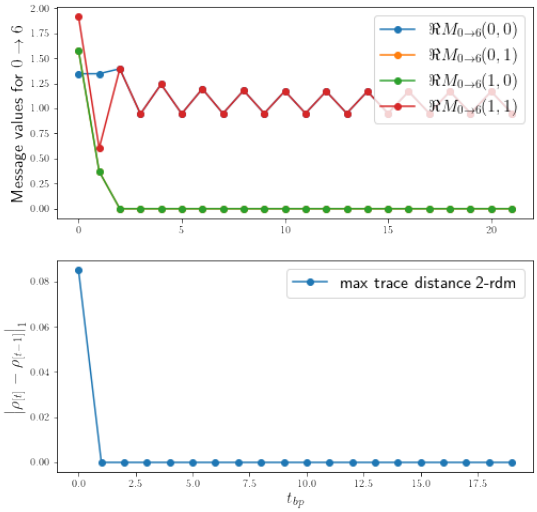

Figure 5.10: Convergence of BP messages and local expectation values with BP for a graph state on a $\mathcal{G}_{20,3}$ random regular graph.

5.6.1 Graph states and Square root states

Here we show the convergence results for the message tensors and local expectation values of the square root states of classical Ising model (Eq. 5.7) and the graph states (Eq. 5.11), both of which are exact tensor network states with $\chi = 2$.

In Fig. 5.9 we study the square root state at $\beta = 0.4J^{-1}$. In the top panel of Fig. 5.9 we plot the message tensors $m_{a\to b}$ (we show only the real part) of a particular directed edge in the graph, with the iterations of the BP algorithm. It is evident that the entries of the message tensors settle into a limit cycle after a few rounds of BP. In the middle panel of Fig. 5.9, we plot the expectation value of local operators (X_a and Z_b, on the site connected by the edge under consideration), and the entanglement entropy S_{ab} of the edge. In the lower panel of Fig. 5.9, we plot the the trace distance between subsequent BP iterations of the reduced density matrices of any 2 and 3 body continuous subregions. For the 2-body reduced density matrix we consider the maximal value of the trace distance over all edges, while for the 3-body reduced density matrix we only consider a particular set of 3 connected neighbors). The middle and lower panels show that the local expectation values have converged, and the reduced density matrices have converged in trace distance. The limit cycle of the message tensor indicates that there exist a notion of 'gauge' equivalence between different message tensors which lead to the same expectation values.

Similar feature can be seen in the convergence study for graph states on a random regular graph $\mathcal{G}_{40,3}$, as shown in Fig. 5.10. Here also the entries of the message tensor show a limit cycle behavior which also coincides with a convergence of reduced density matrices.

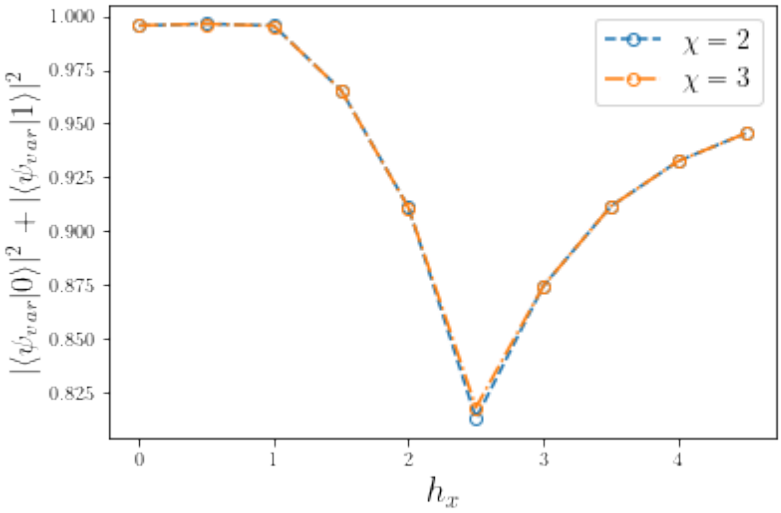

Figure 5.11: Fidelity of variational state in transverse field Ising model on a random regular graph $\mathcal{G}_{20,3}$. The overlap of the variational tensor network wavefunction ψ_{var} with $\chi = 2$ and the two lowest energy states (which are accessed by exact diagonalization) is shown as a function of the transverse field h_x.

5.6.2 Variational ground state of the transverse field Ising model

Here we show details of the fidelity of variational ground state preparation for the transverse field quantum Ising model on a random regular graph. In Fig. 5.11 we plot the overlap of the variational wavefunction ψ_{var} with the two lowest energy states (which are accessed by exact diagonalization) is shown as a function of the transverse field h_x. The reason we choose the first two low energy states is because in the ferromagnetic phase they are separated by a very small gap, and the variational method in general creates an uncontrolled superposition of the two 'degenerate' ground states. We find that the variational method projects to the ground space very effectively in the ferromagnetic and asymptotically in the paramagnetic phase, while showing a cusp near the transition. This also indicates that the $\chi = 2$ ansatz is not sufficient near the critical point, which is associated with long-range critical correlations.

5.7 Discussion

In this work we have demonstrated that tensor networks on generic graphs can be contracted using the belief propagation algorithm, and these work very well for studying quantum systems defined on locally tree-like graphs. We demonstrated the usefulness of such a method by using it extract local information of tensor network states defined on such graphs, such as graph states and square root state of classical Ising model. We also developed a variational method to prepare an approximate ground state of a gapped quantum spin model defined on random regular graphs. We then used this method to also study the phase diagram of the quantum Ising model with transverse fields.

These results open up several new avenues of research. Firstly, there may be application of more developed BP algorithms [313, 314] to study tensor network states on graphs with short loops and 2-d tensor network states with short correlation length. In particular, these modified BP algorithms can tackle short loops efficiently: in gapped local systems one can systematically increase the maximal short loop size until it crosses the correlation length, and obtain accurate contraction of PEPS tensor network states. Systematic study of the limitation of the BP algorithm in contracting tensor network states might also shed light on the exotic nature of the states, for e.g. spin glass order.

Another direction of study would be to study time evolution of sparse graph tensor network states under a Hamiltonian defined on the graph, by using BP in tandem with algorithms such as the density matrix renormalization group (DMRG). These will be useful for studying both dynamics as well as accessing the ground state via imaginary time evolution. One restriction to this is the process of mid-circuit truncation of the graph tensor network states, which is not

guaranteed to be an appropriate truncation of entanglement when there are loops. One direction of approach would be to use the BP algorithm for efficient truncation of graph tensor network states [315], which would be an essential step towards accurate DMRG on such graphs. At the same time, even naive truncation of the tensor network may already be sufficient for sparse graphical models, as they are locally-tree like. On a related note, studying quantum many-body systems on such expander graphs may lead to new physical insights about the nature of the nature of the many-body groundstates and its associated quantum error correction, inspired by novel quantum error-correcting LDPC codes which are under intense recent study in the quantum information community [316].

Simulating real time evolution using tensor networks on lattice systems is generally limited by the entanglement and the bond dimension. However, as mentioned in Sec. 5.2, the graph structure of 'expander' graphs allow for an efficient representation of highly entangled states with only modest bond dimensions. Hence, one should in principle be able to track entanglement build-up for long times with only polynomial resources. This is also a promising direction of future studies.

Another interesting question would be to explore tensor network states associated with multi-body spin and fermionic Hamiltonians on graphs. The variational method for accessing the ground state lends itself naturally to Hamiltonians with multi-body terms. On the other hand, one can also set up a fermionic tensor network states by using parity symmetric tensors and fermionic SWAP gates [317]. This suggests a pathway towards simulating interacting fermionic models on sparse graphs.

Chapter 6: Conclusions

"Are we nearly there yet?" asked Tiny Dragon.

Big Panda smiled. "I hope not."

- Big Panda and Tiny Dragon, James Norbury.

6.1 What have we learned?

In this thesis we have uncovered a number of results at the intersection of quantum many-body physics and quantum information. The core results include:

- A tensor-network based numerical method to access OTOCs in quantum spin chains.
- Evidence of disorder-induced transition in the speed of quantum information propagation in quantum spin systems.
- A thorough study of the thermal regulator dependence of information scrambling, with a new understanding of the limitations of the thermal bound on chaos.
- A solvable model of measurement-induced entanglement transition, with a simple effective field theory for the transition.
- Novel entanglement phases in quantum circuits with measurements and long-range inter-

actions.

- A novel numerical method to study tensor network states on sparse graphs beyond lattices.

In conjunction with a number of recent works on these topics, these results have helped clarify a number of existing questions, and have posed several new questions in the field.

6.2 Where do we go from here?

The most exciting part of any scientific exercise is to dream of newer vistas which open up. In this last section, I take the opportunity to lay out a path for future research along the directions pursued in this dissertation.

- Is the dramatic transition in the speed of quantum information a finite size and finite time effect? More generally, it is an important outstanding question to determine if many-body localization is a genuine phase of matter separated from the ergodic phase by a quantum phase transition.

- Can the effective field theories for Rényi entropy in the hybrid models generalized to von Neumann entropies? While many-body localization and measurement-induced phase transition can both be understood under the broad umbrella of dynamically generated entanglement phases, they are distinguished by the presence of a simple effective theory for the measurement-induced phase transition (MIPT), and a much less established theoretical understanding of many-body localization (MBL). The theoretical understanding of MIPT provides much confidence for the presence of the phase transition, which has been a contentious topic for MBL, as the numerical experiments are limited to small system sizes. It

remains an outstanding question to explore whether a theory of the von Neumann entropy changes our understanding of the measurement-induced phases and phase transitions.

- Can we classify the different entanglement phases possible under generic quantum channels? Much of quantum and classical many-body physics have been about the classification of equilibrium phases of matter. A similar classification of states prepared by generic quantum channels will be an overarching and ambitious question to explore in the future.

- Do the entanglement phases in measurement-induced dynamics survive noise and decoherence? This question is relevant beyond the whimsy of the theorist: it is an important question to address given the very real possibility that such physics may soon be simulated in the laboratory. Furthermore, this physics is intimately related to questions of error thresholds and fault tolerance in quantum computation.

- In the age of quantum simulation, we are not restricted to quantum many-body physics on lattices. What phenomena can we uncover when we go beyond lattices, into the realm of generic graphs? What does quantum many-body physics on sparse graphs tell us about the physics of error correction on these graphical models?

- Many of the problems addressed in this thesis have been posed using the lens of entanglement and information scrambling. More recently, attempts have been made to understand the complexity of states and phases in many-body physics. In this regard, it remains an exciting direction to consider how notions of complexity may be able to shed light on our understanding of quantum many-body phenomena.

The twentieth century had two revolutions in our understanding of the world, through the

development of quantum mechanics, and information and computation theory. It is perhaps no surprise that our efforts to unify the two have led us to the unknown territories in our understanding of nature. Much still remains to be explored and enjoyed!

Appendix A: Chapter 2:

A.1 Spectral representation and the generalized Wightman function

From the definition of the generalized Wightman function in Eq. 2.20, we go to the Fourier space, and expand in terms of many body eigenstates $|n\rangle$ with energy E_n and momentum P_n,

$$\mathcal{G}^{\alpha}_{W}(\omega,\mathbf{k}) = \frac{1}{(2\pi)^3}\int dt e^{i\omega t}\int d^2x \sum_{mn}\langle n|\rho^{\alpha}\phi(t,\mathbf{x})|m\rangle\langle m|\rho^{1-\alpha}\phi(0,\mathbf{0})|n\rangle. \tag{A.1}$$

In Heisenberg representation, $\phi(t,\mathbf{x}) = e^{-iPx}e^{iHt}\phi(0,\mathbf{0})e^{iPx}e^{-iHt}$. This allows us to write the spectral representation of the generalized Wightman function,

$$\mathcal{G}^{\alpha}_{W}(\omega,\mathbf{k}) = \frac{1}{Z}\sum_{mn}|\langle n|\phi|m\rangle|^2\delta\left(\omega-(E_m-E_n)\right)\delta\left(\mathbf{k}-(P_m-P_n)\right)e^{-\beta(\alpha E_n+(1-\alpha)E_m)}. \tag{A.2}$$

The spectral function can be similarly expanded in the spectral representation,

$$A(\omega,\mathbf{k}) = \frac{1}{Z}\sum_{mn}|\langle n|\phi|m\rangle|^2\delta\left(\omega-(E_m-E_n)\right)\delta\left(\mathbf{k}-(P_m-P_n)\right)e^{-\beta E_n}\left(1-e^{-\beta\omega}\right). \tag{A.3}$$

Comparing the two spectral representations, we get the following relation,

$$\mathcal{G}_W^{\alpha}(\omega, \mathbf{k}) = \frac{A(\omega, \mathbf{k})}{2 \sinh \frac{\beta\omega}{2}} e^{\left(\alpha - \frac{1}{2}\right)\beta\omega}. \tag{A.4}$$

A.2 Polarization bubble calculation

T=0

At $T = 0$, the polarization bubble can be evaluated exactly, by changing the Matsubara sum to an integral,

$$\Pi^{T=0}(i\nu_n, \mathbf{q}) = \frac{1}{2} \int_{\mathbf{k}} \int_{\mathbf{R}-(-\epsilon,\epsilon)} \frac{d\omega}{2\pi} \frac{1}{(\omega + \nu_n)^2 + (\mathbf{k}+\mathbf{q})^2 + m^2} \frac{1}{\omega^2 + \mathbf{k}^2 + m^2}. \tag{A.5}$$

The retarded Polarization bubble is obtained by analytically continuing to real frequencies, $\Pi(\mathbf{q}, i\nu_n \to \nu + i0^+)$. The integral can be exactly evaluated, and we obtain,

$$\Pi_R^{T=0}(\nu, \mathbf{q}) = \frac{1}{8\pi} \frac{1}{\sqrt{\mathbf{q}^2 - \nu^2}} \arctan \frac{\sqrt{\mathbf{q}^2 - \nu^2}}{2m}. \tag{A.6}$$

For $\nu^2 \geq \mathbf{q}^2 + 4m^2$,

$$\begin{aligned} Im[\Pi_R^{T=0}(\nu + i0^+, \mathbf{q},)] &= -\frac{1}{16\sqrt{\nu^2 - \mathbf{q}^2}} \\ Re[\Pi_R^{T=0}(\nu + i0^+, \mathbf{q})] &= \frac{1}{16\pi\sqrt{\nu^2 - \mathbf{q}^2}} \log\left(\frac{\sqrt{\nu^2 - \mathbf{q}^2} + 2m}{\sqrt{\nu^2 - \mathbf{q}^2} - 2m}\right). \end{aligned} \tag{A.7}$$

For $\nu^2 < \mathbf{q}^2 + 4m^2$,

$$\begin{aligned} Im[\Pi_R^{T=0}(\nu + i0^+, \mathbf{q})] &= 0 \\ Re[\Pi_R^{T=0}(\nu + i0^+, \mathbf{q})] &= \frac{1}{8\pi} \frac{1}{\sqrt{\mathbf{q}^2 - \nu^2}} \arctan \frac{\sqrt{\mathbf{q}^2 - \nu^2}}{2}. \end{aligned} \tag{A.8}$$

Finite T

Here, we obtain the low temperature correction to the $T = 0$ polarization. At finite T, we introduce the function $b(z) = (e^{\beta z} - 1)^{-1}$ and the ϕ polarization bubble can be calculated,

$$\begin{aligned} \Pi(i\nu_n, \mathbf{q}) &= \frac{T}{2} \sum_{i\omega_n} \int_{\mathbf{k}}^{\Lambda} \frac{1}{(\omega_n + \nu_n)^2 + \epsilon_{\mathbf{k}+\mathbf{q}}^2} \frac{1}{\omega_n^2 + \epsilon_{\mathbf{k}}^2} \\ &= \frac{1}{2} \int_{\mathbf{k}}^{\Lambda} \oint \frac{dz}{2\pi i} b(z) \frac{1}{(z + i\omega_n)^2 - \epsilon_{\mathbf{k}+\mathbf{q}}^2} \frac{1}{z^2 - \epsilon_{\mathbf{k}}^2} \\ &= -\frac{1}{2} \int_{\mathbf{k}}^{\Lambda} \frac{1}{4\epsilon_{\mathbf{k}}\epsilon_{\mathbf{k}+\mathbf{q}}} \left[\frac{b(\epsilon_{\mathbf{k}}) - b(\epsilon_{\mathbf{k}+\mathbf{q}})}{\epsilon_{\mathbf{k}} - \epsilon_{\mathbf{k}+\mathbf{q}} + i\nu_n} - \frac{b(\epsilon_{\mathbf{k}}) + b(\epsilon_{\mathbf{k}+\mathbf{q}})}{\epsilon_{\mathbf{k}} + \epsilon_{\mathbf{k}+\mathbf{q}} + i\nu_n} \right. \\ &\left. - \frac{b(-\epsilon_{\mathbf{k}}) + b(\epsilon_{\mathbf{k}+\mathbf{q}})}{\epsilon_{\mathbf{k}} + \epsilon_{\mathbf{k}+\mathbf{q}} - i\nu_n} - \frac{b(\epsilon_{\mathbf{k}}) - b(\epsilon_{\mathbf{k}+\mathbf{q}})}{\epsilon_{\mathbf{k}+\mathbf{q}} - \epsilon_{\mathbf{k}} + i\nu_n} \right] \end{aligned} \tag{A.9}$$

Using $b(-z) = -b(z) - 1$ and for our hierarchy of scales, $b(\epsilon_{\mathbf{k}}) \approx e^{-\beta\epsilon_{\mathbf{k}}} << 1$ for any $\mathbf{k}$, we can replace $b(-z) \to -1$. The retarded polarization bubble is obtained by analytically continuing from the imaginary Matsubara frequency to real frequency, $\Pi(i\nu_n, \mathbf{q}) \to \Pi_R(\nu + i0^+, \mathbf{q})$. Using Cauchy imaginary value theorem, the imaginary part can be obtained to be (restricting to $\nu > 0$)

$$Im[\Pi_R(\nu + i0^+, \mathbf{q})] = \frac{1}{2} \int_{\mathbf{k}}^{\Lambda} \frac{\pi}{4\epsilon_{\mathbf{k}}\epsilon_{\mathbf{k}+\mathbf{q}}} \left[\delta(\epsilon_{\mathbf{k}} + \epsilon_{\mathbf{k}+\mathbf{q}} - \nu) + 2 \left(e^{-\beta\epsilon_{\mathbf{k}+\mathbf{q}}} - e^{-\beta\epsilon_{\mathbf{k}}} \right) \delta(\epsilon_{\mathbf{k}+\mathbf{q}} - \epsilon_{\mathbf{k}} + \nu) \right]. \tag{A.10}$$

The first term is the $T = 0$ result, which was also obtained in the previous paragraph. At finite T, the only modification is the second term, which we now evaluate.

In order to evaluate this integral, we need to impose the delta function condition. First we shift the $\mathbf{k}$ integral to $\mathbf{k} + \mathbf{q}/2$. We also change notation $\epsilon_\pm = \epsilon_{\mathbf{k}\pm\mathbf{q}/2}$. The delta function conditions are then, $\epsilon_+ + s\epsilon_- = s\nu$, for $s = -1$. Imposing the delta function condition, we get, $k^* = \frac{\nu}{2}\sqrt{\frac{\nu^2-q^2-4m^2}{\nu^2-q^2\cos^2\theta}}$, and $\epsilon^*_\pm = \mp\nu/2 - k^* q\cos\theta/\nu$. For this to be consistent with the positivity of $\epsilon_\pm$, $\theta \in (\pi - \cos^{-1}\nu/q, \pi + \cos^{-1}\nu/q)$.

Now, by change of variable in the delta function,

$$\delta\left(\nu + \epsilon_+ - \epsilon_-\right) = |\nabla f(\mathbf{k})|^{-1}_{k=k^*}\,\delta(k-k^*) \text{ where,}$$
$$f(\mathbf{k}) = \sqrt{(\mathbf{k}+\mathbf{q}/2)^2+m^2} - \sqrt{(\mathbf{k}-\mathbf{q}/2)^2+m^2} + \nu.$$

We then do the radial k integral, by setting $k \to k^*$. In order to do the θ integral, we can employ the Laplace method, as the integrand has the exponential factor, $e^{\frac{\beta q\cos\theta\sqrt{q^2-\nu^2+4m^2}}{2\sqrt{q^2\cos^2\theta-\nu^2}}}$, and $\beta m >> 1$. The exponent has a maxima at $\theta = \pi$, which lies in the allowed domain of θ. Doing the integral, we get the full correction, for $\nu < q$,

$$Im\Pi_R(\nu,\mathbf{q}) = \frac{1}{8\pi}\sqrt{\frac{4\pi}{\beta}}\sinh\left(\frac{\beta\nu}{2}\right)\left(\frac{1}{q^2\left(4m^2-\nu^2+q^2\right)\left(q^2-\nu^2\right)}\right)^{1/4} e^{-\frac{\beta q}{2}\sqrt{\frac{4m^2-\nu^2+q^2}{q^2-\nu^2}}} \tag{A.11}$$

A.3 Self Energy calculation

To study the temperature dependent relaxation time of the bosonic quasiparticles, we need to evaluate the self energy of ϕ. The relevant diagrams are shown in Fig. 2.15. The imaginary part

of the self energy has contribution only from the first diagram in Fig. 2.15, and can be evaluated to give,

$$Im[\Sigma_R(\omega + i0^+, \mathbf{q})] = -\frac{1}{N}\int_{\mathbf{k}} \frac{\sinh \beta\omega/2}{4\epsilon_{\mathbf{k}} \sinh \beta\epsilon_{\mathbf{k}}/2} \times \left[\frac{Im[\Pi_R^{-1}(\epsilon_k - \omega, \mathbf{k} - \mathbf{q})]}{\sinh[\beta(\epsilon_k - \omega)/2]} + \frac{Im[\Pi_R^{-1}(-\epsilon_k - \omega, \mathbf{k} - \mathbf{q})]}{\sinh[-\beta(\epsilon_k + \omega)/2]}\right]. \tag{A.12}$$

Note, at low temperature, the second term in the imaginary part of the self-energy can be ignored. Recalling the definition of the Wightman function, we have,

$$Im[\Sigma_R(\omega + i0^+, \mathbf{q})] \approx \frac{1}{N}\int_{\mathbf{k}} \frac{\sinh \beta\omega/2}{4\epsilon_{\mathbf{k}} \sinh \beta\epsilon_{\mathbf{k}}/2} G^{(1/2)}_{W,\lambda}\left(\epsilon_k - \omega, \mathbf{k} - \mathbf{q}\right). \tag{A.13}$$

The inverse lifetime, or the relaxation rate of ϕ can be written in terms of the imaginary part of the self energy,

$$\Gamma_{\mathbf{q}} = \frac{Im[\Sigma_R(\epsilon_{\mathbf{q}}, \mathbf{q})]}{2\epsilon_q} = \frac{1}{2N}\int_{\mathbf{k}}^{\Lambda} \frac{\sinh\left(\beta\epsilon_{\mathbf{q}}/2\right)}{\sinh\left(\beta\epsilon_{\mathbf{k}}/2\right)} \mathcal{R}^{(1/2)}_{1+}(\mathbf{k}, \mathbf{q}), \text{ where we have defined,}$$
$$\mathcal{R}^{(1/2)}_{1+}(\mathbf{k}, \mathbf{q}) = \frac{G^{(1/2)}_{W,\lambda}\left(\epsilon_k - \epsilon_q, \mathbf{k} - \mathbf{q}\right)}{4\epsilon_k\epsilon_q}. \tag{A.14}$$

Note, $|\epsilon_k - \epsilon_q| < |\mathbf{k} - \mathbf{q}|$. The Wightman function $\mathcal{G}^{(1/2)}_{W,\lambda}(\epsilon_k - \epsilon_q, \mathbf{k} - \mathbf{q})$ can be expressed as

$$\frac{-Im[\mathcal{G}_R((\epsilon_k - \epsilon_q, \mathbf{k} - \mathbf{q})]}{\sinh \beta(\epsilon_{\mathbf{k}} - \epsilon_{\mathbf{q}})/2},$$

where, $Im[\mathcal{G}_R]$ is given by $Im[\Pi_R^{-1}] = -\frac{Im[\Pi_R]}{Re[\Pi_R]^2 + Im[\Pi_R]^2}$. From the calculations in Sec. A.2, one can read off the expression for $Im[\Pi_R]$ which is exponentially suppressed in βm. In the denominator, any temperature dependence can be ignored, because of the leading $T = 0$ behavior

of $Re[\Pi_R]$. Thus, we have the following approximation for $\mathcal{R}_1(\mathbf{k},\mathbf{q})$,

$$\mathcal{R}_{1+}^{(1/2)}(\mathbf{k},\mathbf{q}) \approx \frac{1}{8\pi}\sqrt{\frac{4\pi}{\beta m}}\frac{1}{4\epsilon_{\mathbf{k}}\epsilon_{\mathbf{q}}}\exp\left(-\frac{\beta|\mathbf{k}-\mathbf{q}|\sqrt{(\mathbf{k}-\mathbf{q})^2-\left(\epsilon_{\mathbf{k}}-\epsilon_{\mathbf{q}}\right)^2+4m^2}}{2\sqrt{(\mathbf{k}-\mathbf{q})^2-\left(\epsilon_{\mathbf{k}}-\epsilon_{\mathbf{q}}\right)^2}}\right)\times \left(\frac{\left(|\mathbf{k}-\mathbf{q}|^2-(\epsilon_{\mathbf{k}}-\epsilon_{\mathbf{q}})^2\right)^{3/4}}{|\mathbf{k}-\mathbf{q}|^{1/2}\left(4m^2-(\epsilon_{\mathbf{k}}-\epsilon_{\mathbf{q}})^2+|\mathbf{k}-\mathbf{q}|^2\right)^{1/4}}\right)\frac{64\pi^2}{\arctan^2\frac{\sqrt{\left(|\mathbf{k}-\mathbf{q}|^2-(\epsilon_{\mathbf{k}}-\epsilon_{\mathbf{q}})^2\right)}}{2}}. \tag{A.15}$$

At low temperature, the relaxation rate can be approximated by the Laplace method, since the integrand has a factor exponential in βm (arising from both the prefactor $\sinh$ and $\mathcal{R}_1$ functions in Eq. A.14).

We define the phase coherence inverse time scale as, $\tau_\phi^{-1} = \Gamma_{\mathbf{q}=\mathbf{0}}$ [149], which can be evaluated,

$$\Gamma_0 = \frac{1}{\tau_\phi} \approx \frac{2\pi}{N\beta}e^{-\beta m}. \tag{A.16}$$

The momentum dependent $\Gamma_{\mathbf{q}}$ can be evaluated numerically,

$$\Gamma_{\mathbf{q}} \approx \frac{1}{2N}e^{\beta\epsilon_{\mathbf{q}}/2}\int_{\mathbf{k}} e^{-\beta\epsilon_{\mathbf{k}}/2}\mathcal{R}_{1+}^{(1/2)}(\mathbf{k},\mathbf{q}). \tag{A.17}$$

A.4 Ladder calculation in different contours

The ladder calculation sets up a diagrammatic calculation of the squared commutator in terms of retarded Green functions and Wightman functions of the fields ϕ and λ. Here we give a sketch of how it works, following [114], while also extending their results to the unregulated squared commutator.

Consider the generalized squared commutator,

$$C_{(\alpha)}(t,\mathbf{x}) = -\frac{1}{N^2}\sum_{ab} Tr\left(\rho^{\alpha}[\phi_{a,0}(t,\mathbf{x}),\phi_{b,0}(0,\mathbf{0})]\rho^{(1-\alpha)}[\phi_{a,0}(t,\mathbf{x}),\phi_{b,0}(0,\mathbf{0})]\right). \tag{A.18}$$

To go to the interaction representation for the ϕ fields, we introduce time evolution operators in the interaction picture,

$$U_I = \mathcal{T}\exp\left(\frac{i}{2\sqrt{N}}\sum_a \int_0^t ds \int_{\mathbf{x}} \lambda_0(s,\mathbf{x})\phi_0^2(s,\mathbf{x})\right), \tag{A.19}$$

where the subscript 0 indicates that the fields time evolve under the non-interacting part of the Hamiltonian. We further drop the factors of N and the index structure to obtain,

$$C_{(\alpha)}(t,\mathbf{x}) \sim -Tr\left(\rho^{\alpha}[U_I^{\dagger}\phi_0(t,\mathbf{x})U_I,\phi_0(0,\mathbf{0})]\rho^{(1-\alpha)}[U_I^{\dagger}\phi_0(t,\mathbf{x})U_I,\phi_0(0,\mathbf{0})]\right). \tag{A.20}$$

By expanding up to second order of λ, we get,

$$\begin{aligned} U_I^{\dagger}\phi_0(t)U_I \approx \phi_0(t) + \frac{i}{2}\int_0^t ds\left[\phi_0(t),\lambda_0(s)\phi_0^2(s)\right] + \\ \left(\frac{i}{2}\right)^2 \int_0^t ds_1 \int_0^{s_1} ds_2 \left[\left[\phi_0(t),\lambda_0(s_1)\phi_0^2(s_1)\right],\phi_0(t),\lambda_0(s_2)\phi_0^2(s_2)\right] + ..., \end{aligned} \tag{A.21}$$

where we have suppressed the spatial dimension.

By combining fields from both 'sides of the ladder' in the expanded expression Eq. A.20, we get the two distinct types of rungs - the contributions which are called the Type I and Type II rungs in Sec. 2.3.2. The contour dependence appears in the form of the contour dependence of the Wightman functions. For example, the Type I rung is a contour dependent λ-Wightman function,

$Tr\,(\rho^{\alpha}\lambda_0(s)\rho^{1-\alpha}\lambda_0(s'))$, or, $\mathcal{G}^{(\alpha)}_{W,\lambda}(s-s')$. Similarly, for Type II, we get the corresponding contour dependent Wightman functions.

A.5 Kernel functions at low temperature

A.5.0.1 $\mathcal{R}_1^{(1/2)}$ kernel

We already calculated the $\mathcal{R}^{(1/2)}_{1+}$ kernel in Sec. A.3, as given in Eq. A.15. We now calculate $\mathcal{R}^{(1/2)}_{1-}$ at low temperatures,

$$\begin{aligned}\mathcal{R}^{(1/2)}_{1-}(\mathbf{p}',\mathbf{p}) &:= \frac{\mathcal{G}^{(1/2)}_{W,\lambda}(-\epsilon_{\mathbf{p}\prime}-\epsilon_{\mathbf{p}})}{4\epsilon_{\mathbf{p}\prime}\epsilon_{\mathbf{p}}} \\ &\approx \frac{1}{2\epsilon_{\mathbf{p}\prime}\epsilon_{\mathbf{p}}} e^{-\frac{\beta(\epsilon_{\mathbf{p}}+\epsilon_{\mathbf{p}\prime})}{2}} \frac{Im\Pi^{T=0}_R(\epsilon_{\mathbf{p}\prime}+\epsilon_{\mathbf{p}},\mathbf{p}\prime-\mathbf{p})}{\left|\Pi_R(\epsilon_{\mathbf{p}\prime}+\epsilon_{\mathbf{p}},\mathbf{p}\prime-\mathbf{p})\right|^2} \\ &= \frac{1}{32\epsilon_{\mathbf{p}\prime}\epsilon_{\mathbf{p}}} e^{-\frac{\beta(\epsilon_{\mathbf{p}}+\epsilon_{\mathbf{p}\prime})}{2}} \frac{1}{\sqrt{(\epsilon_{\mathbf{p}}+\epsilon_{\mathbf{p}\prime})^2-(\mathbf{p}\prime-\mathbf{p})^2}} \frac{1}{\left|\Pi^{T=0}_R(\epsilon_{\mathbf{p}\prime}+\epsilon_{\mathbf{p}},\mathbf{p}\prime-\mathbf{p})\right|^2}.\end{aligned} \tag{A.22}$$

$\mathcal{R}^{(1/2)}_{1-}(\mathbf{p}',\mathbf{p})$ is exponentially suppressed unless $p,p' << 1$, while $\mathcal{R}^{(1/2)}_{1+}(\mathbf{p}',\mathbf{p})$ is exponentially suppressed unless $|\mathbf{p}'-\mathbf{p}| << 1$. Furthermore, even in the domain where both the exponents are comparable, it can be numerically verified that $\mathcal{R}^{(1/2)}_{1-}(\mathbf{p}',\mathbf{p})$ is negligible compared to $\mathcal{R}^{(1/2)}_{1+}(\mathbf{p}',\mathbf{p})$. Hence for the ladder calculation, we ignore $\mathcal{R}_{1-}$.

A.5.0.2 $\mathcal{R}_2^{(1/2)}$ kernel

In order to evaluate the $\mathcal{R}^{(1/2)}_2$ integration, we first need an expression for $\mathcal{G}^{(1/2)}_{\text{eff}}$ that was defined in Eq. 2.31. For results correct to the required order of $1/N$, it is enough to consider $\mathcal{G}^{(1/2)}_W(\omega) \sim \mathcal{Q}(\omega)A^{(0)}(\omega)$, where $A^{(0)}$ is the bare ϕ spectral function, given in Eq. 2.19. We

have also defined the function, $\mathcal{Q}(\omega) = [2\sinh(\beta\omega/2)]^{-1}$. Inserting the spectral function in the expression for $\mathcal{G}_W^{(1/2)}(\omega''-\omega, \mathbf{p}''-\mathbf{p})\mathcal{G}_W(\omega'-\omega'', \mathbf{p}'-\mathbf{p}'')$ in Eq. 2.31, allows us to integrate over ω''. We introduce notation $x = \mathbf{p}' - \mathbf{p}$, $y = \frac{\mathbf{p}'+\mathbf{p}}{2}$ and $\overline{\omega} = \omega' - \omega$. We also denote $\epsilon_{x/2\pm\mathbf{p}''} =: \epsilon_\pm$. We now have the following expression for $\mathcal{G}_{\text{eff}}^{(1/2)}$,

$$\begin{aligned}\mathcal{G}_{\text{eff}}^{(1/2)}(\omega', \omega, \mathbf{p}', \mathbf{p}) = \frac{1}{2N}\int_{\mathbf{p}''} \frac{\pi}{\epsilon_+\epsilon_-}\Bigg(&\mathcal{Q}(\epsilon_+)\mathcal{Q}(\overline{\omega}-\epsilon_+)\mathcal{G}_{R,\lambda}(-\omega-\epsilon_+, -\mathbf{p}''-y)\mathcal{G}_{R,\lambda}(\omega+\epsilon_+, \mathbf{p}''+y) \\ &[\delta(\overline{\omega}-\epsilon_+-\epsilon_-) - \delta(\overline{\omega}-\epsilon_++\epsilon_-)] \\ - \quad &\mathcal{Q}(-\epsilon_+)\mathcal{Q}(\overline{\omega}+\epsilon_+)\mathcal{G}_{R,\lambda}(-\omega+\epsilon_+, -\mathbf{p}''-y)\mathcal{G}_{R,\lambda}(\omega-\epsilon_+, \mathbf{p}''+y) \\ &[\delta(\overline{\omega}+\epsilon_+-\epsilon_-) - \delta(\overline{\omega}+\epsilon_++\epsilon_-)]\Bigg).\end{aligned} \tag{A.23}$$

In this expression, because of the delta functions, one can replace the arguments of $\mathcal{Q}$ by $\pm\epsilon_\pm$. Note, at low temperature, $\mathcal{Q}(\epsilon_\pm) \approx e^{-\beta\epsilon_\pm/2}$, and $\mathcal{Q}(-\epsilon_\pm) \approx -e^{-\beta\epsilon_\pm/2}$. We can also use the fact that $\mathcal{G}_{R,\lambda}(\omega, -\mathbf{q}) = \mathcal{G}_{R,\lambda}(\omega, \mathbf{q})$, and that the real and imaginary parts of $\mathcal{G}_{R,\lambda}(\omega, \mathbf{q})$ are even and odd functions of ω respectively. This allows for the following simplification,

$$\begin{aligned}&\mathcal{G}_{R,\lambda}(-\omega+\epsilon_+, -\mathbf{p}''-y)\mathcal{G}_{R,\lambda}(\omega-\epsilon_+, \mathbf{p}''+y) \\ &\qquad = \frac{1}{Re[\Pi_R(\omega-\epsilon_+, \mathbf{p}''+y)]^2 + Im[\Pi_R(\omega-\epsilon_+, \mathbf{p}''+y)]^2} \\ &\qquad \approx \frac{1}{|\Pi_R^{T=0}(\omega-\epsilon_+, \mathbf{p}''+y)|^2}.\end{aligned} \tag{A.24}$$

We finally arrive at a simple expression for $\mathcal{G}_{\text{eff}}^{(1/2)}$,

$$\mathcal{G}_{\text{eff}}^{(1/2)}(\omega', \omega, \mathbf{p}', \mathbf{p}) = \frac{1}{2N} \int_{\mathbf{p}''} \frac{\pi e^{-\frac{\beta(\epsilon_+ + \epsilon_-)}{2}}}{\epsilon_+ \epsilon_-}$$
$$\Bigg(\left|\Pi_R^{T=0}(\omega + \epsilon_+, \mathbf{p}'' + y)\right|^{-2} \left[\delta(\overline{\omega} - \epsilon_+ - \epsilon_-) + \delta(\overline{\omega} - \epsilon_+ + \epsilon_-)\right] \tag{A.25}$$
$$\left|\Pi_R^{T=0}(\omega - \epsilon_+, \mathbf{p}'' + y)\right|^{-2} \left[\delta(\overline{\omega} + \epsilon_+ - \epsilon_-) + \delta(\overline{\omega} + \epsilon_+ + \epsilon_-)\right] \Bigg).$$

A.5.0.3 $\mathcal{R}_{2+}^{(1/2)}$ kernel

For $\mathcal{R}_{2+}^{(1/2)}$, the relevant function is $\mathcal{G}_{\text{eff}}^{(1/2)}(\epsilon_{\mathbf{p}'}, \epsilon_{\mathbf{p}}, \mathbf{p}', \mathbf{p})$, where $\overline{\omega} = \epsilon_{\mathbf{p}'} - \epsilon_{\mathbf{p}}$, and $\mathbf{x} = \mathbf{p}' - \mathbf{p}$. The only delta functions in the equation above that can be satisfied are $\delta(\overline{\omega} + \epsilon_+ - \epsilon_-)$ and $\delta(\overline{\omega} - \epsilon_+ + \epsilon_-)$. We can impose the delta function to do the p'' radial integration, which fixes the radial component at $p''_*(\theta) = \frac{\overline{\omega}}{2}\sqrt{\frac{\overline{\omega}^2 - x^2 - 4m^2}{\overline{\omega}^2 - x^2\cos^2\theta}}$, where θ is the angle with $\mathbf{x}$. This can be followed by the angular integration approximated by the Laplace method, since there is an exponential factor with large βm in the exponent. The calculation closely follows the evaluation of $Im\Pi_R$ at finite

T in Appendix A.2. The final expression for $\mathcal{R}_{2+}^{(1/2)}$ is,

$$\mathcal{R}_{2+}^{(1/2)}(\mathbf{p}',\mathbf{p}) \approx \frac{1}{8\pi}\sqrt{\frac{4\pi}{\beta m}}\frac{1}{4\epsilon_{\mathbf{p}'}\epsilon_{\mathbf{p}}}\exp\left(-\frac{\beta|\mathbf{p}'-\mathbf{p}|\sqrt{(\mathbf{p}'-\mathbf{p})^2-(\epsilon_{\mathbf{p}'}-\epsilon_{\mathbf{p}})^2+4m^2}}{2\sqrt{(\mathbf{p}'-\mathbf{p})^2-(\epsilon_{\mathbf{p}'}-\epsilon_{\mathbf{p}})^2}}\right)\times$$
$$\left(\frac{1}{|\mathbf{p}'-\mathbf{p}|^{1/2}\left(4m^2-(\epsilon_{\mathbf{p}'}-\epsilon_{\mathbf{p}})^2+|\mathbf{p}'-\mathbf{p}|^2\right)^{1/4}\left(|\mathbf{p}'-\mathbf{p}|^2-(\epsilon_{\mathbf{p}'}-\epsilon_{\mathbf{p}})^2\right)^{1/4}}\right)\times$$
$$\left(\left|\Pi_R^{T=0}\left(\frac{\epsilon_{\mathbf{p}'}+\epsilon_{\mathbf{p}}}{2}-\frac{xp_*''(\theta=\pi)}{\overline{\omega}},\frac{\mathbf{p}'+\mathbf{p}}{2}+p_*''(\theta=\pi)\right)\right|^{-2}\right.$$
$$\left.+\left|\Pi_R^{T=0}\left(\frac{\epsilon_{\mathbf{p}'}+\epsilon_{\mathbf{p}}}{2}+\frac{xp_*''(\theta=0)}{\overline{\omega}},\frac{\mathbf{p}'+\mathbf{p}}{2}+p_*''(\theta=0)\right)\right|^{-2}\right). \tag{A.26}$$

A.5.0.4 $\mathcal{R}_{2-}^{(1/2)}$ kernel

We can similarly evaluate the $\mathcal{R}_{2-}^{(1/2)}$, for which the relevant function is $\mathcal{G}_{\text{eff}}(-\epsilon_{\mathbf{p}'},\epsilon_{\mathbf{p}},\mathbf{p}',\mathbf{p})$. We further define, $\overline{\omega}=\epsilon_{\mathbf{p}'}+\epsilon_{\mathbf{p}}$, and $\mathbf{x}=\mathbf{p}'-\mathbf{p}$. The only delta function in the equation above that can be satisfied is $\delta(\overline{\omega}-\epsilon_+-\epsilon_-)$. We can impose the delta function to do the p'' radial integration, which fixes the radial component at $p_*''(\theta)=\frac{\overline{\omega}}{2}\sqrt{\frac{\overline{\omega}^2-x^2-4m^2}{\overline{\omega}^2-x^2\cos^2\theta}}$. This brings an exponential factor of $e^{-\frac{\beta(\epsilon_{\mathbf{p}'}+\epsilon_{\mathbf{p}})}{2}}$ to the expression for $\mathcal{R}_{2-}^{(1/2)}$, and hence $\mathcal{R}_{2-}^{(1/2)}(\mathbf{p}',\mathbf{p})$ is substantial only at $p,p'<<1$. The approximate expression (after the angular integration) is,

$$\mathcal{R}_{2-}^{(1/2)}(\mathbf{p}',\mathbf{p}) \approx \frac{1}{8\epsilon_{\mathbf{p}'}\epsilon_{\mathbf{p}}}e^{-\frac{\beta(\epsilon_{\mathbf{p}'}+\epsilon_{\mathbf{p}})}{2}}\frac{\sqrt{\overline{\omega}^2-4m^2}}{\overline{\omega}^2}\left|\Pi_R^{T=0}\left(\frac{\epsilon_{\mathbf{p}}-\epsilon_{\mathbf{p}'}}{2},\frac{\sqrt{\overline{\omega}^2-4m^2}}{2}\right)\right|^{-2}. \tag{A.27}$$

Numerically, it can be verified that $\mathcal{R}^{(1/2)}_{2-}(\mathbf{p}', \mathbf{p})$ can always be ignored with respect to $\mathcal{R}^{(1/2)}_{2+}(\mathbf{p}', \mathbf{p})$, for similar reasons as $\mathcal{R}_1$. Hence, for the ladder calculation, we can ignore $\mathcal{R}_{2-}(\mathbf{p}', \mathbf{p})$.

A.6 Details of numerics of ladder calculation

Here we provide some details of the numerical computation of the ladder sum. We fix the mass as $m = 1$, and do all the calculation in these units. Having determined the approximate values of the kernel functions $\mathcal{R}_{1,2}$, we need to discretize the 2D momentum space to set up the matrix form of the kernel integration. For that purpose, we set up a hard momentum cut-off of $|\mathbf{p}_x|, |\mathbf{p}_y| \leq 1$. The choice is justified for the kernel in rescaled momenta, which is exponentially suppressed - $\exp(-|\mathbf{p} - \mathbf{p}'|^2/8)$. Next, we create 2D grid of momenta, with the momentum interval dp determined by the number of points that we consider - 40 by 40, 50 by 50 and 60 by 60 grids. Next, we set up the matrix form of the kernel, $\hat{K}_{\mathbf{p}'\mathbf{p}} = dp^2 \hat{\mathcal{K}}(\mathbf{p}', \mathbf{p})$, given in Eq. 2.38. The matrices are of sizes, 1600 by 1600, 2500 by 2500, and 3600 by 3600, respectively. In constructing the matrix, we need to evaluate $\Gamma_{\mathbf{p}}$ by performing a 2D integration (in Eq. 2.29) within the grid area ($|\mathbf{p}_x|, |\mathbf{p}_y| \leq 1$). We find the maximum magnitude eigenvalue of the matrix, and find that the largest magnitude eigenvalue has a positive real part, thereby resulting in exponential growth. The eigenvalues are then extrapolated to the $dp \to 0$ limit by a linear extrapolation. Errors in the estimation are denoted as the errorbars for this eigenvalue (see Fig. A.1).

In Fig. A.2, we study the external momentum dependence of the largest magnitude eigenvalue of the kernel equation $\lambda_L(u)$ at non zero external momentum u. The real part of $\lambda_L(u)$ shows a quadratically decreasing behavior, $\lambda_0 - \lambda_2 u^2$ even at significantly high u, while the the imaginary part shows a linear behavior, $\lambda_i u$. At $u = 0$, the eigenvalue is real and positive.

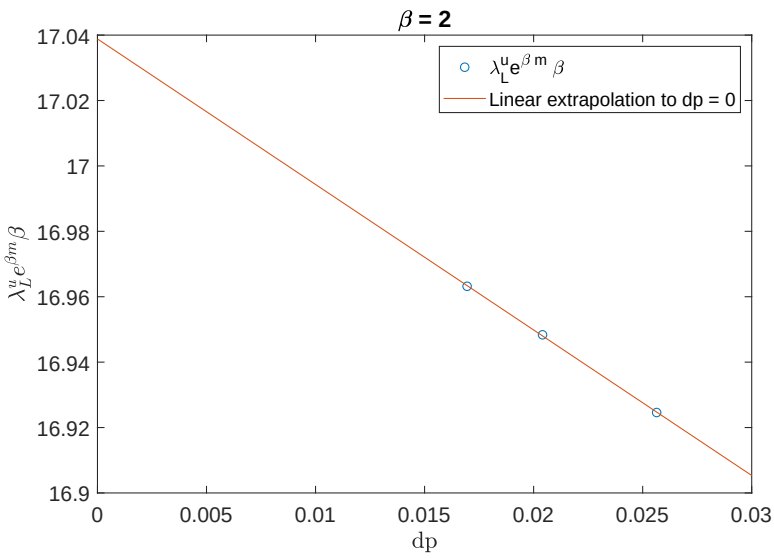

Figure A.1: The maximum eigenvalue $\lambda_L e^{\beta m}\beta$ is determined by taking the linear extrapolation of $\lambda_L e^{\beta m}\beta$ at each grid interval dp to $dp \to 0$. The error is determined as the uncertainty in the extrapolation from its 95% confidence interval. The graph here is shown for the unregulated calculation at $\beta = 2$.

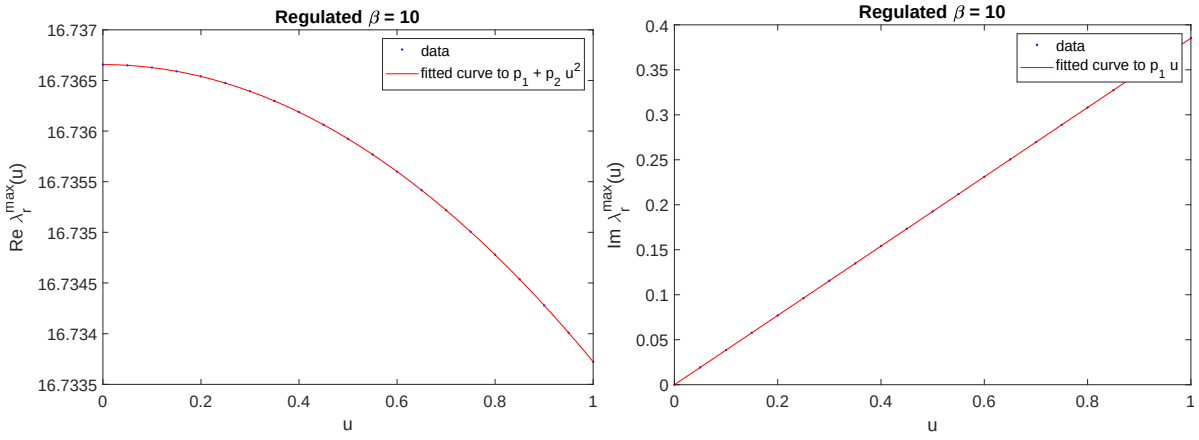

Figure A.2: A sample fit of the numerically obtained $\lambda_L^r(u)$, at $\beta = 10$. m is chosen to be 1. The real part is fit to $f(u) = \lambda_0 - \lambda_2 u^2$, while the imaginary part is fit to $f(u) = \lambda_i u$, and the fit works very well even at quite large u.

Appendix B: Chapter 3:

B.1 Physical interpretation of the different averaged observables

Here we discuss the issue of extracting the averaged purities $\overline{\Pi_Q}, \langle \Pi_Q \rangle$ from experiments. A flowchart describing the experimental protocol is provided in Fig. B.1.

To measure the purity Π_Q, the experimenter first fixes the unitary circuit elements (1), and the measurement bases σ^y_{aux} (3), yielding a single circuit realization with disorder coefficients $\mathbf{J}, \mathbf{n}$. The experimenter then prepares the initial maximally-entangled state $\rho_0 = |\Psi_0\rangle \langle \Psi_0|$ and applies an alternating sequence of unitary and weak-measurement layers to the system Q as described in Sec. IIA. As discussed in the main text, weak measurements on the system are performed by coupling the system to auxiliary qubits and projectively measuring the auxiliary system. In principle, the experimenter can record the measurement results on a classical memory, and the resulting quantum states can be stored in a quantum memory. At this point the experimentalist keeps all resulting quantum states, even if the measurement results are not all $+1$.

Due to the unpredictability of these measurement outcomes, for each given realization $\mathbf{J}, \mathbf{n}$ of the circuit, there will be a collection of quantum trajectories, which we label $\mathbf{T} = \mathbf{T}(\mathbf{J}, \mathbf{n}, \mathbf{m})$, where $\mathbf{m}$ is the record of measurement outcomes. Each trajectory performs a non-unitary operation on the state, $|\Psi_{QR}\rangle = \mathbf{T} |\Psi_0\rangle$ which is an unnormalized pure state, and each trajectory

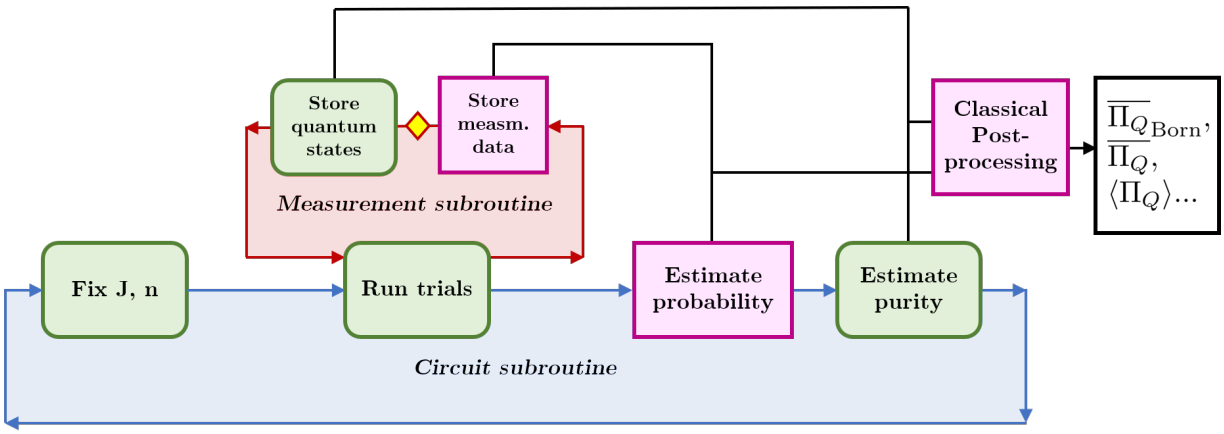

Figure B.1: **Experimental protocol to simulate the various averaged purities.** The protocol is composed of two subroutines - 'circuit' (blue) and 'measurement' (red). Sampling of circuit realizations is done in the blue subroutine, which calls the sampling of measurement trajectories in the red subroutine. For each run of the measurement subroutine, the measurement data is stored classically, and the resulting quantum state is stored in a quantum memory depending on whether we want to simulate the Born probability or post-selected trajectories (this choice is represented by the diamond in the circuit). For each run of the circuit subroutine, purity can be estimated by doing SWAP tests on identical copies of the stored quantum states and the corresponding probabilities can be estimated by processing the classical data of measurement records. To estimate either of these quantities, the typical number of runs of the measurement subroutine scales exponentially with the number of measurements, i.e. exponentially with the 'volume' of the circuit. All quantum processes in the protocol are denoted by 'green' rounded boxes and all classical processes are denoted by 'pink' boxes. Finally, once enough statistics is collected, the 'classical' data of purity and the probability for each circuit/measurement can be post-processed (as described in the text) to give us $\overline{(\Pi_Q)}_{\text{Born}}$, $\overline{\Pi_Q}$, $\langle\Pi_Q\rangle$ or any other simple averaged purity-like quantities.

occurs with the Born probability $P[\mathbf{T}] = \langle \Psi_{QR} | \Psi_{QR} \rangle$. Now, given a sample set of classical data (collection of measurement records), one can estimate the Born probability $P[\mathbf{T}]$. For a system in an initially mixed state, one would start with a prior of 1/2 for each measurement, which would be updated based on the actual outcomes corresponding to the circuit realization and the measurement randomness.

Using the quantum memory which stores the obtained quantum states, the experimenter can access the purity of the state. Once enough copies of each state are obtained, the experimenter can perform SWAP tests on the copies of the states to obtain the purity. The purity for each trajectory is given by

$$\Pi_Q[\mathbf{T}] = \frac{Z_2[\mathbf{T}]}{P^2[\mathbf{T}]}, \tag{B.1}$$

where $Z_2 = \mathrm{Tr}\left[\tilde{\rho}_Q^2\right]$, for the unnormalized reduced density matrix on the system, $\tilde{\rho}_Q = \mathrm{Tr}_R\left[|\Psi_{QR}\rangle \langle \Psi_{QR}|\right]$. The estimate from experiments improves with the number of copies, but these copies are hard to obtain, requiring a typical number of trials that scales exponentially with the number of measurements as discussed in section IIB of the main text. In the simplified setup we consider for our analytical calculation, we require the state to be stored only for specific measurement records $\mathbf{m}$, where the auxiliary qubit measurement only gives the result $+1$.

Now the experimenter can repeat the whole sub-routine, by sampling different circuit realizations, $V = V(\mathbf{J}, \mathbf{n})$, with an underlying probability distribution, $\pi(V(\mathbf{J}, \mathbf{n}))$. For our analytical computation, we considered an analytically-tractable Gaussian probability distributions over the coefficients $\mathbf{J}, \mathbf{n}$ as described in Sec. IIA. While repeating the experiment to collect data, there can be some simplifications due to symmetries in the circuit: for example, applying a weak-measurement layer with the disorder coefficient $\mathbf{n}$ and obtaining a $+1$ outcome on the

auxiliary qubit is equivalent to using a disorder coefficient $-\mathbf{n}$ with an overall negative sign and obtaining the result -1.

Armed with the probability distribution of states and the purities, one can estimate a family of observables, related to different kinds of averages of the purity. Firstly, the Born probability averaged purity is given by,

$$\overline{(\Pi_Q)}_{\text{Born}} = \sum_{V,\mathbf{T}} \pi(V) P\left[\mathbf{T}\right] \Pi_Q\left[\mathbf{T}\right] \tag{B.2}$$

In our setup with post-selection, one can avoid averaging with the Born probability $P[\mathbf{T}]$, by averaging the purity Π_Q only over post-selected trajectories with the desired measurement record $\mathbf{m} = +1$. In this case, there is a single post-selected trajectory for each choice of circuit realization, with a single value of $\Pi_Q(V)$, $Z_2(V)$ and $P^2(V)$. In this case, the circuit-averaged purity for the post-selected trajectories is given by,

$$\overline{\Pi_Q} = \sum_{V} \pi(V) \Pi_Q(V). \tag{B.3}$$

Both the Born and post-selected averaged purity considered above are difficult to access analytically, as one needs to average the ratio of two multi-replica quantities. In principle one could access the disorder-averaged ratio $\overline{Z_2/P^2}$ by studying the path-integral representation of $\overline{Z_2 P^{2n}}$ analytically continued to $n = -1$. This can be difficult because one would typically need to access the expression over the entire domain of n in order to take the analytic continuation.

However, by classical post-processing of the probability data, we can access the analytically-

tractable re-weighted purity $\langle Z_2\rangle/\langle P^2\rangle$ studied in this work. To do so, we first define a re-weighted probability,

$$\mathcal{N}(V) = \frac{\pi(V)\times P^2(V)}{\mathcal{N}_0}, \tag{B.4}$$

with $\mathcal{N}_0 = \sum_V \pi(V)P^2(V)$ to ensure that the probabilities sum to 1. In an experiment, $\mathcal{N}(V)$ can be estimated with just the classical information of the measurement records. Now we consider the purity averaged over this re-weighted probability,

$$\langle \Pi_Q\rangle = \sum_V \mathcal{N}(V)\Pi_Q(V) = \frac{\sum_V \pi(V)Z_2(V)}{\sum_V \pi(V)P^2(V)} = \frac{\langle Z_2\rangle}{\langle P^2\rangle}, \tag{B.5}$$

which being an average of ratios is analytically accessible, and is the quantity we compute in this work. From an experimental point of view, although this estimation requires classical post-processing, it doesn't require any more quantum resources than the other two averages (in fact it requires fewer quantum resources than the Born-averaged quantity due to post-selection and selective storage of quantum states).

B.2 Derivation of general (p, q) path integral

Here we derive a path integral representation for general (p, q) hybrid Brownian circuits probed by the nth moment of the unnormalized density matrix $Z_n = \langle \mathrm{Tr}\left[\tilde{\rho}_Q^n\right]\rangle$. To compute this object, we introduce n copies of the system Q and reference R, and calculate the expectation value of the generalized n-system SWAP operator as shown in Fig. B.2a. Using the circuit identities in Fig. 3.2 and introducing factors of iY as in section IIC of the main text, we can

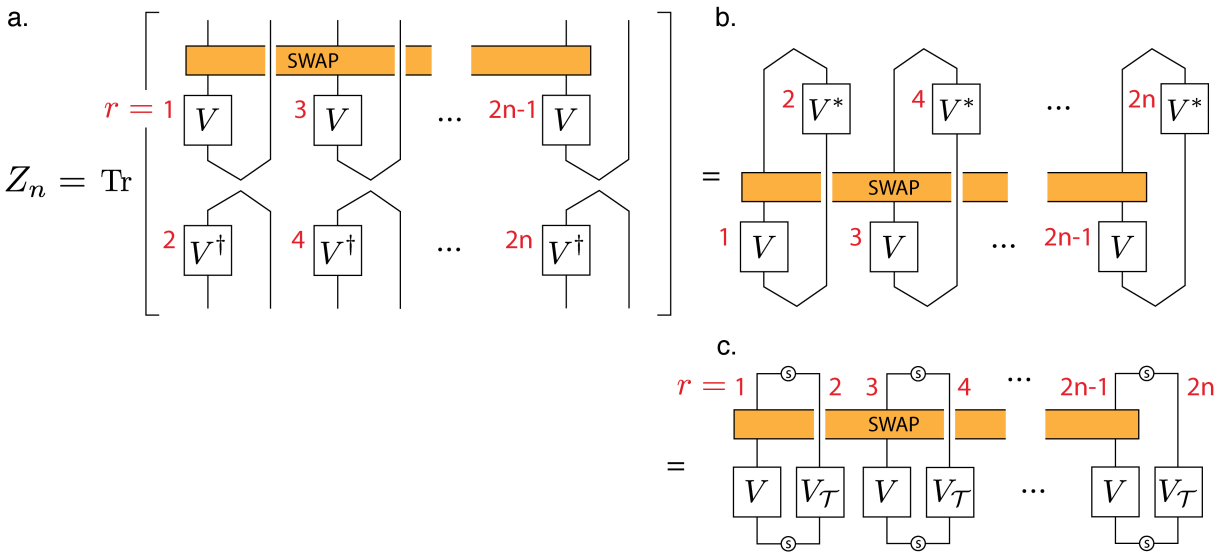

Figure B.2: **Partition function Z_n for the nth moment of the density matrix.** The nth-order Rényi entropy $S_Q^{(n)} = -\ln \mathrm{Tr}\left[\rho_Q^n\right]$ is defined in terms of the nth moment of the system density matrix ρ_Q. The associated circuit for computing the nth moment $\mathrm{Tr}\left[\tilde{\rho}_Q^n\right]$ of the unnormalized density matrix $\tilde{\rho}_Q$ can be transformed into pure-state dynamics on $2n$ replicas $r = 1, 2, \ldots, 2n$ with nontrivial boundary conditions at times $t = 0, T$ coming from the generalized n-system SWAP operator (orange).

bring this circuit to the form shown in Fig. B.2c describing pure-state dynamics on $2n$ replicas $r = 1, 2, \ldots, 2n$ with evolution operator

$$\mathbb{V} = V \otimes V_\mathcal{T} \otimes \cdots \otimes V \otimes V_\mathcal{T}. \tag{B.6}$$

and generalized SWAP boundary condition at $t = T$ which cyclically permutes the n odd replicas $r = 1, 3, \ldots, 2n-1$. The associated probability $P^n = \langle \mathrm{Tr}\left[\tilde{\rho}_Q\right]^n \rangle$ is described by the same circuit but with trivial boundary condition at $t = T$.

The operators V can be constructed by stacking any sequence of unitary Brownian layers or weak-measurement Brownian layers to give a variety of interaction and damping terms in the final action. Regardless of the particular choice of unitary and weak measurement dynamics,

we always choose Brownian coefficients $J_{ij}^{\alpha\beta}(t), n_i^{\alpha}(t), \ldots$ for these layers that are statistically uncorrelated in time. As a result, the disorder average factorizes over the different timesteps Δt and we may compute the disorder average over each layer independently as shown in Fig. 3.2c. We therefore first consider contributions to the effective action from unitary p-body Brownian circuit layers in Sec. B.2.0.1. We then consider contributions from non-unitary q-body Brownian circuit layers in Sec. B.2.0.2. Finally, we combine these results in Sec. B.2.0.3 to give a path integral expression in Eq. (B.31) for Z_n for general (p, q) hybrid Brownian models.

B.2.0.1 p-body Brownian interactions

Unitary Brownian dynamics are generated by p-body spin interactions $U(t) = \exp[-iH(t)\Delta t/2]$ with time-dependent Hamiltonian

$$H(t) = \sum_{\substack{i_1<\ldots<i_p \\ \alpha_1\ldots\alpha_p}} J_{i_1\ldots i_p}^{\alpha_1\ldots\alpha_p}(t)\, S_{i_1}^{\alpha_1} S_{i_2}^{\alpha_2} \cdots S_{i_p}^{\alpha_p} \tag{B.7}$$

where the S_i^{α} are $\mathrm{SU}(2)$ spin-S degrees of freedom on sites $i = 1, \ldots, N$ and the Brownian coefficients $J_{i_1\ldots i_p}^{\alpha_1\ldots\alpha_p}(t)$ are white-noise-correlated Gaussian random variables

$$\begin{aligned} &\left\langle J_{i_1\ldots i_p}^{\alpha_1\ldots\alpha_p}(t) J_{i'_1\ldots i'_p}^{\alpha'_1\ldots\alpha'_p}(t') \right\rangle_{\mathbf{J}} \\ &\quad = \frac{J}{N^{p-1}(S+1)^{2p}} \delta(t-t') \delta_{i_1 i'_1} \cdots \delta^{\alpha_1\alpha'_1} \cdots \end{aligned} \tag{B.8}$$

where the normalization $1/N^{p-1}(S+1)^{2p}$ ensures that the Hamiltonian $H(t)$ is extensive and independent of spin size. We regulate the delta function via the replacement $\delta(t-t') \approx \delta_{tt'}(\Delta t/2)^{-1}$ and consider the limit $\Delta t \to 0$. Note that under the time-reversal operation $\mathcal{T}$ the Hamiltonian

and unitary operator transform as

$$H_{\mathcal{T}}(t) = (-1)^p H(t)$$
$$U_{\mathcal{T}}(t) = \exp\left[i(-1)^p H(t)\Delta t/2\right]. \tag{B.9}$$

Expanding this layer to second order in Δt and performing the disorder average over the Brownian coefficients $J^{\alpha_1\ldots\alpha_p}_{i_1\ldots i_p}(t)$ we find

$$\begin{aligned}\langle U \otimes U_{\mathcal{T}} \otimes \cdots \otimes U \otimes U_{\mathcal{T}} \rangle_{\mathbf{J}} &\approx \left\langle \left(1 - iH\frac{\Delta t}{2} - \frac{1}{2}H^2\frac{\Delta t^2}{4}\right) \otimes \left(1 + iH_{\mathcal{T}}\frac{\Delta t}{2} - \frac{1}{2}H_{\mathcal{T}}^2\frac{\Delta t^2}{4}\right) \otimes \cdots \right\rangle_{\mathbf{J}} \\ &= \left\langle \left(1 - iH\frac{\Delta t}{2} - \frac{1}{2}H^2\frac{\Delta t^2}{4}\right) \otimes \left(1 + i(-1)^p H\frac{\Delta t}{2} - \frac{1}{2}H^2\frac{\Delta t^2}{4}\right) \otimes \cdots \right\rangle_{\mathbf{J}} \\ &= 1 - \frac{\Delta t^2}{4}\sum_{r<s}\mu_{rs}^p \left\langle H^r H^s \right\rangle_{\mathbf{J}} - \frac{1}{2}\frac{\Delta t^2}{4}\sum_r \left\langle (H^r)^2 \right\rangle_{\mathbf{J}} \end{aligned} \tag{B.10}$$

where $H^{r,s}$ denote copies of the Hamiltonian (B.7) acting on replicas $r, s = 1, \ldots, 2n$, and we have defined

$$\mu_{rs}^p \equiv \begin{cases} (-1)^{r+s} & p \text{ even} \\ 1 & p \text{ odd}. \end{cases} \tag{B.11}$$

Evaluating the disorder average, we find

$$\begin{aligned}\langle H^r H^s\rangle_{\mathbf{J}} \frac{\Delta t^2}{4} &= \frac{J\Delta t}{N^{p-1}(S+1)^{2p}} \frac{1}{2p!} \\ &\quad \times \sum_{\substack{i_1 \ldots i_p \\ \alpha_1 \ldots \alpha_p}} \left(S_{i_1}^{\alpha_1,r} S_{i_1}^{\alpha_1,s}\right) \cdots \left(S_{i_p}^{\alpha_p,r} S_{i_p}^{\alpha_p,s}\right) \\ &= \frac{J\Delta t}{N^{p-1}(S+1)^{2p}} \frac{N^p}{2p!} \left(\frac{1}{N}\sum_i \mathbf{S}_i^r \cdot \mathbf{S}_i^s\right)^p \end{aligned} \tag{B.12}$$

as an operator equation, where the additional factor of $1/p!$ comes from converting the ordered sum in Eq. (B.7) to an unordered sum. The disorder-averaged Brownian circuit layer can therefore be written as a propagator:

$$\begin{aligned}\langle U \otimes U_{\mathcal{T}} \otimes \cdots \otimes U \otimes U_{\mathcal{T}}\rangle_{\mathbf{J}} &\approx e^{-N I_p(t)\Delta t} \\ I_p(t) &\equiv n \frac{JS^p}{2p!(S+1)^p} \\ &\quad + \sum_{r<s} \mu_{rs}^p \frac{J}{2p!(S+1)^{2p}} \left(\frac{1}{N}\sum_i \mathbf{S}_i^r \cdot \mathbf{S}_i^s\right)^p \end{aligned} \tag{B.13}$$

to lowest order in Δt, which holds as an operator equation.

B.2.0.2 q-body Brownian measurements

Consider making a weak measurement of a Hermitian q-body operator

$$\mathcal{O}(t) = \sum_{\substack{i_1 < \ldots < i_q \\ \alpha_1 \ldots \alpha_q}} \mathcal{O}_{i_1 \ldots i_q}^{\alpha_1 \ldots \alpha_q}(t)\; S_{i_1}^{\alpha_1} \cdots S_{i_q}^{\alpha_q} \tag{B.14}$$

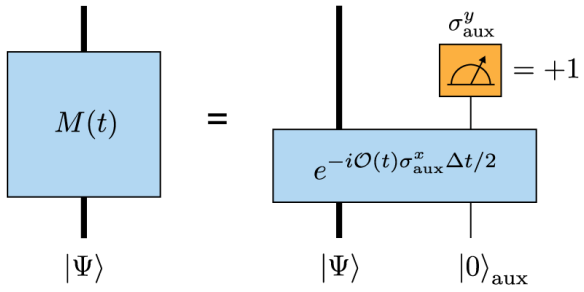

Figure B.3: **Brownian weak measurement protocol.** The operator $M(t)$ weakly measures the Brownian operator $\mathcal{O}(t)$ by coupling it to an auxiliary qubit $|\psi\rangle_{\text{aux}}$ for a time $\Delta t/2$ (blue) and projectively measuring the auxiliary qubit in the σ^y_{aux} basis, post-selecting for $+1$ results (orange). Due to the coupling between the system $|\Psi\rangle$ and auxiliary qubit $|\psi\rangle_{\text{aux}}$ this projective measurement alters the many-body state $|\Psi\rangle \to M(t)\,|\Psi\rangle$.

at some time t during the circuit evolution. For the moment we leave the coefficients $\mathcal{O}^{\alpha_1\ldots\alpha_q}_{i_1\ldots i_q}(t)$ of this operator unspecified. This q-body operator is the analogue of the 1-body spin operators $\mathcal{O}(t) = \sum_{i,\alpha} n^\alpha_i(t) S^\alpha_i$ weakly measured in the $(2,1)$ model described in section II of the main text. To measure this operator we introduce an auxiliary qubit initialized in $|\psi\rangle_{\text{aux}} = |0\rangle_{\text{aux}}$ and couple it to $\mathcal{O}$ via a unitary interaction

$$\exp\left[-i\mathcal{O}(t)\sigma^x_{\text{aux}}\Delta t/2\right]|\Psi\rangle\,|0\rangle_{\text{aux}} \tag{B.15}$$

for a short time $\Delta t/2$, where $|\Psi\rangle$ is the state of the system prior to the weak measurement and σ^x_{aux} is the Pauli-x operator acting on the auxiliary qubit. By projectively measuring the auxiliary qubit in the eigenbasis of σ^y_{aux} and post-selecting only for $+1$ results, the original state is transformed to

$$|\Psi\rangle \to M(t)\,|\Psi\rangle \equiv \left(1 - \mathcal{O}\frac{\Delta t}{2} - \frac{1}{2}\mathcal{O}^2\frac{\Delta t^2}{4} + \cdots\right)|\Psi\rangle \tag{B.16}$$

to lowest order in Δt. The circuit diagram for this measurement protocol is shown in Fig. B.3. The strength of the measurement is controlled by the magnitude of the operator $|\mathcal{O}(t)|$ in units of

the timestep $\Delta t/2$. Under the time-reversal operation $\mathcal{T}$ the operators $\mathcal{O}(t)$ and $M(t)$ transform as

$$\begin{aligned}\mathcal{O}_{\mathcal{T}}(t) &= (-1)^q \mathcal{O}(t) \\ M_{\mathcal{T}}(t) &= \left(1 - (-1)^q \mathcal{O}\frac{\Delta t}{2} - \frac{1}{2}\mathcal{O}^2\frac{\Delta t^2}{4} + \cdots\right).\end{aligned} \tag{B.17}$$

We now apply weak-measurement operators $M(t)$ in the circuit at each odd timestep $t = (2m+1)\Delta t/2$ and take the operator coefficients to be white-noise-correlated Gaussian random variables

$$\begin{aligned}&\left\langle \mathcal{O}^{\alpha_1\ldots\alpha_q}_{i_1\ldots i_q}(t)\mathcal{O}^{\alpha'_1\ldots\alpha'_q}_{i'_1\ldots i'_q}(t')\right\rangle_{\mathbf{O}} \\ &\qquad = \frac{\gamma}{N^{q-1}(S+1)^{2q}}\delta(t-t')\delta_{i_1 i'_1}\cdots\delta^{\alpha_1\alpha'_1}\cdots\end{aligned} \tag{B.18}$$

whose strength is controlled by the parameter γ. As before, the delta function can be regulated by the replacement $\delta(t-t') \approx \delta_{tt'}(\Delta t/2)^{-1}$. Performing the disorder average over the coefficients $\mathcal{O}^{\alpha_1\ldots\alpha_p}_{i_1\ldots i_p}(t)$ in the $2n$-replica system we find

$$\begin{aligned}\langle M\otimes M_{\mathcal{T}}\otimes\cdots\otimes M\otimes M_{\mathcal{T}}\rangle_{\mathbf{O}} &\approx \left\langle\left(1-\mathcal{O}\frac{\Delta t}{2}-\frac{1}{2}\mathcal{O}^2\frac{\Delta t^2}{4}\right)\otimes\left(1-\mathcal{O}_{\mathcal{T}}\frac{\Delta t}{2}-\frac{1}{2}\mathcal{O}^2_{\mathcal{T}}\frac{\Delta t^2}{4}\right)\otimes\cdots\right\rangle_{\mathbf{O}} \\ &= \left\langle\left(1-\mathcal{O}\frac{\Delta t}{2}-\frac{1}{2}\mathcal{O}^2\frac{\Delta t^2}{4}\right)\otimes\left(1-(-1)^q\mathcal{O}\frac{\Delta t}{2}-\frac{1}{2}\mathcal{O}^2\frac{\Delta t^2}{4}\right)\otimes\cdots\right\rangle_{\mathbf{O}} \\ &= 1+\frac{\Delta t^2}{4}\sum_{r<s}\chi^q_{rs}\left\langle\mathcal{O}^r\mathcal{O}^s\right\rangle_{\mathbf{O}} - \frac{1}{2}\frac{\Delta t^2}{4}\sum_r\left\langle(\mathcal{O}^r)^2\right\rangle_{\mathbf{O}}\end{aligned} \tag{B.19}$$

where we have defined

$$\chi^q_{rs} \equiv \mu^{q+1}_{rs} = \begin{cases} 1 & q \text{ even} \\ \\ (-1)^{r+s} & q \text{ odd} \end{cases} \tag{B.20}$$

similar to Eq. (B.11). Evaluating the disorder average, we find

$$\begin{aligned} \langle \mathcal{O}^r \mathcal{O}^s \rangle_{\mathbf{O}} \frac{\Delta t^2}{4} &= \frac{\gamma \Delta t}{N^{q-1}(S+1)^{2q}} \frac{1}{2q!} \sum_{\substack{i_1 \dots i_q \\ \alpha_1 \dots \alpha_q}} \left(S^{\alpha_1, r}_{i_1} S^{\alpha_1, s}_{i_1} \right) \cdots \left(S^{\alpha_q, r}_{i_q} S^{\alpha_q, s}_{i_q} \right) \\ &= \frac{\gamma \Delta t}{N^{q-1}(S+1)^{2q}} \frac{N^q}{2q!} \left(\frac{1}{N} \sum_i \mathbf{S}^r_i \cdot \mathbf{S}^s_i \right)^q \end{aligned} \tag{B.21}$$

as an operator equation. The disorder-averaged Brownian-measurement circuit layer can therefore be written as a propagator:

$$\begin{aligned} \langle M \otimes M_{\mathcal{T}} \otimes \cdots \otimes M \otimes M_{\mathcal{T}} \rangle_{\mathbf{O}} &\approx e^{-N I_q(t) \Delta t} \\ I_q(t) \equiv n \frac{\gamma S^q}{2q!(S+1)^q} &- \sum_{r<s} \chi^q_{rs} \frac{\gamma}{2q!(S+1)^{2q}} \left(\frac{1}{N} \sum_i \mathbf{S}^r_i \cdot \mathbf{S}^s_i \right)^q \end{aligned} \tag{B.22}$$

to lowest order in Δt, which holds as an operator equation. Comparing Eqs. (B.13) and (B.22), we conclude that the q-body Brownian measurement propagator is nearly identical to the unitary p-body propagator – the only differences are in the numerical coefficients μ^p_{rs}, χ^q_{rs} and in the overall sign of the interaction term.

B.2.0.3 Coherent spin state path integral

We now stack a repeating sequence of p-body Brownian interactions and q-body Brownian measurements, insert resolutions of the identity between each layer, and take the limit $\Delta t \to 0$ with T fixed to express the dynamics as a path integral over $2nN$ unit-norm $\mathrm{SO}(3)$ spins $\mathbf{S}_i^r$, using spin coherent states as the basis. The completeness relation for the coherent states for a single spin is given by,

$$\mathbb{I} = \int \frac{2S+1}{4\pi} d\mathbf{\Omega}_i \left|\mathbf{\Omega}_i\right\rangle \left\langle\mathbf{\Omega}_i\right| . \tag{B.23}$$

To turn the spins into coherent states, we use the upper symbols for single spin-S Pauli operators [318],

$$S_i^\alpha = \int \frac{2S+1}{4\pi} d\mathbf{\Omega}_i \left|\mathbf{\Omega}_i\right\rangle \left\langle\mathbf{\Omega}_i\right| (S+1)\Omega_i^\alpha \tag{B.24}$$

$$(S_i^\alpha)^2 = \int \frac{2S+1}{4\pi} d\mathbf{\Omega}_i \left|\mathbf{\Omega}_i\right\rangle \left\langle\mathbf{\Omega}_i\right| \left[(S+1)\left(S+\frac{3}{2}\right)(\Omega_i^\alpha)^2 - \frac{S+1}{2}\right] . \tag{B.25}$$

We introduce a measure for the coherent spin states in the path integral,

$$\mathcal{D}\Omega_i^r = \prod_{t_n} \frac{2S+1}{4\pi} d\mathbf{\Omega}_{i,t_n}^r \langle \mathbf{\Omega}_{i,t_{n+1}}^r | \mathbf{\Omega}_{i,t_n}^r \rangle, \tag{B.26}$$

such that it includes the overlap of spin coherent states at discrete times t_n and t_{n+1}. (Explicit evaluation of these overlap terms leads to 'kinetic energy' or Berry-phase terms $\sim \Omega\partial_t\Omega$ in the path integral [224]; the above choice of integration measure allows us to keep these time-dependent terms implicit, but the reader should keep in mind that these terms are always present.)

In terms of the coherent states, the action for $2n$ copies, combining both scrambling and measurement can be defined as follows,

$$\langle V \otimes V_{\mathcal{T}} \otimes \cdots \otimes V \otimes V_{\mathcal{T}} \rangle_{\mathbf{J},\mathbf{O}} = e^{-NI[\mathbf{\Omega}](t)\Delta t}$$

$$I[\mathbf{\Omega}] = \int_0^T dt \left[\frac{nJS^p}{2p!(S+1)^p} + \frac{n\gamma S^q}{2q!(S+1)^q} + \frac{J}{2p!} \sum_{r<s} \mu_{rs}^p \left(\frac{1}{N} \sum_i \mathbf{\Omega}_i^r \cdot \mathbf{\Omega}_i^s \right)^p \right.$$
$$\left. - \frac{\gamma}{2q!} \sum_{r<s} \chi_{rs}^q \left(\frac{1}{N} \sum_i \mathbf{\Omega}_i^r \cdot \mathbf{\Omega}_i^s \right)^q \right]. \tag{B.27}$$

To deal with the non-linear interactions in $\mathbf{\Omega}_i^r \cdot \mathbf{\Omega}_i^s$, we introduce decoupling fields $F_{rs}(t)$ and $G_{rs}(t)$ with the following operator identity,

$$\mathbb{I} = \int \mathcal{D}F_{rs}\mathcal{D}G_{rs} \exp\left[iN \int_0^T dt\ F_{rs} \left(G_{rs} - \frac{1}{N} \sum_i \mathbf{\Omega}_i^r \cdot \mathbf{\Omega}_i^s \right) \right] \tag{B.28}$$

We can now treat F_{rs} and G_{rs} as the dynamical fields for the problem which couple different replicas r, s, and integrate out the spins, which gives us a propagator for spin problem. Note, we actually have a N-spin propagator when we evaluate the $\mathbf{\Omega}$ path integral. However, since all the sites i are identical and have been decoupled by the disorder average, we can rewrite the $2nN$-spin problem as the N-th power of a $2n$-spin problem,

$$\int \prod_{i,r} \mathcal{D}\Omega_i^r \exp\left(-\sum_{r<s} iF_{rs} \sum_i \mathbf{\Omega}_i^r \cdot \mathbf{\Omega}_i^s \right) = \int \prod_r \left(\mathcal{D}\Omega^r\right)^N \exp\left(-N \sum_{r<s} iF_{rs} \mathbf{\Omega}^r \cdot \mathbf{\Omega}^s \right). \tag{B.29}$$

where the new single-site integration measure is

$$\mathcal{D}\Omega^r = \prod_{t_n} \frac{2S+1}{4\pi} d\mathbf{\Omega}_{t_n}^r \left\langle \mathbf{\Omega}_{t_{n+1}}^r | \mathbf{\Omega}_{t_n}^r \right\rangle \tag{B.30}$$

Putting it all together, along with the boundary conditions for the spin propagator, we get the action density

$$I[F_{rs}, G_{rs}] = I_0 + I_1 - \ln K(\psi_0, \psi_T, T) \qquad \text{where}$$

$$\begin{aligned} I_0 &\equiv JT\frac{nS^p}{2p!(S+1)^p} + \gamma T\frac{nS^q}{2q!(S+1)^q} \\ I_1 &\equiv \int_0^T dt\left[\frac{J}{2p!}\sum_{r<s}\mu_{rs}^p G_{rs}^p - \sum\frac{\gamma}{2q!}\sum_{r<s}\chi_{rs}^q G_{rs}^q - i\sum_{r<s}F_{rs}G_{rs}\right] \\ K(\psi_0, \psi_T, T) &\equiv \langle\psi_T|\exp\left[-\int_0^T dt\sum_{r<s}\frac{iF_{rs}}{(S+1)^2}\mathbf{S}^r\cdot\mathbf{S}^s\right]|\psi_0\rangle \end{aligned} \tag{B.31}$$

Since the propagator K is composed of $\mathrm{SU}(2)$-symmetric Heisenberg couplings, the dynamics of the propagator are highly constrained. For $S = 1/2$ and $n = 2$ we showed in the main text that these constraints reduce the dynamics to a two-dimensional subspace; we expect similar constraints to simplify the problem for more general cases, but this remains a problem for future work.

B.3 Replica symmetry

As discussed in the main text, the microscopic bulk dynamics $\mathbb{V} = V^{(1)}\otimes V_{\mathcal{T}}^{(2)}\otimes V^{(3)}\otimes V_{\mathcal{T}}^{(4)}$ on replicas $r = 1, 2, 3, 4$ for $n = 2$ is manifestly invariant under the replica symmetry group

$$G = (S_2 \times S_2) \rtimes \mathbb{Z}_2 \tag{B.32}$$

where the inner $S_2 \cong \mathbb{Z}_2$ groups denote the permutation groups on replicas $1, 3$ and $2, 4$ with generators $\sigma = (13)$, $\sigma' = (24)$, respectively, where we use standard cycle notation in this section to represent permutations of replicas. The outer $\mathbb{Z}_2$ in the semidirect product is generated by $\tau = \mathcal{T}(12)(34)$, where the operation $\mathcal{T}$ represents time-reversal $V \leftrightarrow V_{\mathcal{T}}$ on all four replicas. Under the semidirect product, the generator τ simply exchanges the generators σ, σ':

$$\sigma' = \tau\sigma\tau. \tag{B.33}$$

Explicitly, these generators act on the bulk dynamics as

$$\begin{aligned}
\sigma\left(V^{(1)} \otimes V_{\mathcal{T}}^{(2)} \otimes V^{(3)} \otimes V_{\mathcal{T}}^{(4)}\right) &= V^{(3)} \otimes V_{\mathcal{T}}^{(2)} \otimes V^{(1)} \otimes V_{\mathcal{T}}^{(4)} \\
\sigma'\left(V^{(1)} \otimes V_{\mathcal{T}}^{(2)} \otimes V^{(3)} \otimes V_{\mathcal{T}}^{(4)}\right) &= V^{(1)} \otimes V_{\mathcal{T}}^{(4)} \otimes V^{(3)} \otimes V_{\mathcal{T}}^{(2)} \\
\tau\left(V^{(1)} \otimes V_{\mathcal{T}}^{(2)} \otimes V^{(3)} \otimes V_{\mathcal{T}}^{(4)}\right) &= V^{(2)} \otimes V_{\mathcal{T}}^{(1)} \otimes V^{(4)} \otimes V_{\mathcal{T}}^{(3)}
\end{aligned} \tag{B.34}$$

where superscripts denote replica indices $r = 1, 2, 3, 4$. The replica symmetry group G for $n = 2$ is isomorphic to the dihedral group $D_4 = \mathrm{Dih}_4$ (the group of symmetries of the geometrical square) via the representation

$$G = \left\langle a, b | a^4 = b^2 = 1, bab = a^{-1} \right\rangle \tag{B.35}$$

with the identification $a = \tau\sigma$ and $b = \sigma$.

While the bulk dynamics $\mathbb{V}$ are invariant under the full group G, the boundary conditions at $t = 0, T$ break this down to a subgroup $H \subset G$ generated by the mutually-commuting operators

τ, c, where

$$c = \sigma\tau\sigma = ba = \mathcal{T}(14)(23) \tag{B.36}$$

corresponds to a 'reflection' $1234 \leftrightarrow 4321$ in replica space followed by time-reversal $\mathcal{T}$ on all replicas. This subgroup is isomorphic to the Klein four-group $H \cong \mathbb{Z}_2 \times \mathbb{Z}_2$ composed of the four elements $\{e, \tau, c, \tau c\}$ with e the identity element. Left-multiplication by $\sigma = b$ yields the left coset $\sigma H = \{\sigma, \sigma\tau, \sigma c, \sigma\tau c\}$, and together the left cosets $H, \sigma H$ generate the full group G. In this sense, the generator $\sigma = b$ represents the $\mathbb{Z}_2$ symmetry that is explicitly broken by the boundary conditions and spontaneously broken in the bulk.

For $n > 2$ the replica symmetry group is

$$G = (S_n \times S_n') \rtimes \mathbb{Z}_2 \tag{B.37}$$

where $S_n = S_{135\ldots}, S_n' = S_{246\ldots}$ are the order-$n!$ symmetric groups on replicas $r = 1, 3, 5, \ldots$ and $r = 2, 4, 6, \ldots$ with generators σ, σ', respectively. Similar to above, the outer $\mathbb{Z}_2$ is generated by an element $\tau = \mathcal{T}(12)(34)\cdots(2n{-}1\ 2n)$ that exchanges the generators $\sigma' = \tau\sigma\tau$. The boundary conditions at $t = 0, T$ break this bulk symmetry down to a subgroup $H \subset G$ that depends on the details of the boundary states.

Because they contain the time-reversal operation $\mathcal{T}$, which itself contains the complex conjugation operation $*$, the operators τ, c are *antilinear* operators on the Hilbert space of quantum states, in contrast to the generators σ, σ' which are conventional linear operators [219]. Whereas conventional linear operators (as their name suggests) are linear in their arguments:

$$\sigma\left(\alpha\left|\psi\right\rangle + \beta\left|\psi'\right\rangle\right) = \alpha\sigma\left|\psi\right\rangle + \beta\sigma\left|\psi'\right\rangle \tag{B.38}$$

antilinear operators are antilinear in their arguments:

$$\tau\left(\alpha\left|\psi\right\rangle+\beta\left|\psi'\right\rangle\right)=\alpha^{*}\tau\left|\psi\right\rangle+\beta^{*}\tau\left|\psi'\right\rangle \tag{B.39}$$

where complex conjugation of the c-numbers α,β arises due to the complex conjugation in the definition of time-reversal $\mathcal{T}$. The antilinearity of τ, c leads to restrictions on the spectrum of the operator $\mathbb{V}$ via the same mechanism that guarantees the reality of eigenvalues of certain non-Hermitian Hamiltonians in PT-symmetric quantum mechanics [225, 226].

Here we show that an operator $\mathbb{V}$ with *unbroken PT symmetry* has a real spectrum, while an operator with *broken PT symmetry* has a spectrum consisting of complex-conjugate pairs. Assume that there is an antilinear operator τ that commutes with the operator $\mathbb{V}$:

$$[\tau,\mathbb{V}]=0 \tag{B.40}$$

and suppose $\left|\Psi\right\rangle$ is an eigenstate of $\mathbb{V}$ with eigenvalue V:

$$\mathbb{V}\left|\Psi\right\rangle=V\left|\Psi\right\rangle. \tag{B.41}$$

Multiplying this eigenvalue equation on the left by τ and using the fact that $\tau V = V^{*}\tau$ by antilinearity of τ, along with the commutativity of $\tau,\mathbb{V}$, we find that $\left|\Psi'\right\rangle = \tau\left|\Psi\right\rangle$ is also an eigenstate of $\mathbb{V}$ with eigenvalue V^{*}:

$$\mathbb{V}\left|\Psi'\right\rangle=V^{*}\left|\Psi'\right\rangle. \tag{B.42}$$

Hence any eigenstate $|\Psi\rangle$ of $\mathbb{V}$ with eigenvalue V is always accompanied by a second eigenstate $\tau|\Psi\rangle$ with eigenvalue V^*.

This shows that the spectrum of any PT-symmetric operator $\mathbb{V}$ always consists of complex-conjugate pairs V, V^*, but there is no guarantee that these eigenvalues lie on the real line. To guarantee reality of the spectrum one requires the additional assumption that the eigenstate $|\Psi\rangle$ is simultaneously also an eigenstate of τ:

$$\tau|\Psi\rangle = \lambda|\Psi\rangle\,. \tag{B.43}$$

If τ were a conventional linear operator, this would follow immediately from the commutativity of $\tau, \mathbb{V}$ (B.40); but when τ is antilinear this is an additional independent assumption. Because τ is antilinear the eigenvalue λ can be any pure phase $\lambda = e^{i\phi}$ but we may always appropriately redefine the eigenstate $|\Psi\rangle$ such that $\lambda = 1$ [219, 225, 226]. In this case we have $|\Psi'\rangle = \tau|\Psi\rangle = |\Psi\rangle$ and therefore by combining Eqs. (B.41) and (B.42) we immediately obtain $V = V^*$. Thus, if $|\Psi\rangle$ is a simultaneous eigenstate of both τ and $\mathbb{V}$, then its eigenvalue V is real.

If all of the eigenstates of $\mathbb{V}$ are also eigenstates of the antilinear operator τ then the spectrum is guaranteed to be real by the above arguments and we say that the PT symmetry of $\mathbb{V}$ is *unbroken*. Conversely, if there are eigenstates of $\mathbb{V}$ that are not eigenstates of τ, then the spectrum consists of complex-conjugate pairs and we say that the PT symmetry of $\mathbb{V}$ is *broken*.

B.4 Simplification of the path integral at saddle point

We introduce symmetric and anti-symmetric fields defined as

$$F_a^{\pm} = \frac{2}{9}(iF_{12} \pm iF_{34}),\ G_a^{\pm} = \frac{9}{2}(G_{12} \pm G_{34})$$
$$F_b^{\pm} = \frac{2}{9}(iF_{14} \pm iF_{23}),\ G_b^{\pm} = \frac{9}{2}(G_{14} \pm G_{23})$$
$$F_c^{\pm} = \frac{2}{9}(iF_{13} \pm iF_{24}),\ G_c^{\pm} = \frac{9}{2}(G_{13} \pm G_{24}).$$

This re-definition simplifies the 4-replica propagator, as the only fields appearing in the propagator are the symmetric combinations, $F^+_{a,b,c}$. This implies that the saddle-point equations of motion for the anti-symmetric fields $F^-_{a,b,c}$ set $G^-_{a,b,c} = 0$, which reduces the number of fields to consider down from 12 to 6. Since all the anti-symmetric fields are thus integrated away, we drop the $\pm$ superscript and define $G_{a,b,c} = G^+_{a,b,c}$ (and similarly for the F fields).

In terms of these fields, the action density can be rewritten as,

$$I = \int_0^T dt \left[\frac{J}{162}\left(-G_a^2 - G_b^2 + G_c^2\right) - \frac{\gamma}{9}\left(-G_a - G_b + G_c\right) \right.$$
$$\left. -F_a G_a - F_b G_b - F_c G_c \right] - \ln K. \tag{B.44}$$

The saddle-point equations of motion corresponding to this action are given by,

$$-\frac{J}{81}G_{a,b} + \frac{\gamma}{9} = F_{a,b}$$
$$\frac{J}{81}G_c - \frac{\gamma}{9} = F_c,\ \ G_{a,b,c} = -\frac{d\ln K}{dF_{a,b,c}} \tag{B.45}$$

The G fields can thus be integrated out by replacing them with the saddle-point solutions. We can also rewrite the action in terms of the magnetic field variables $\vec{B}$. The B_0 field can also be

integrated out since it appears in a quadratic form.

Finally we have a path integral over just two fields, with the action,

$$
\begin{aligned}
I = \int_0^T dt \left[\frac{27 B_x^2}{4J} - \frac{81 B_z^2}{4J} + B_z(1+18\gamma) - \frac{J}{72} \right. \\
\left. - \frac{4\gamma^2}{J} - \frac{\gamma}{2} \right] - \ln K \\
K = \langle \psi_T | \exp \left[\frac{1}{2} \int_0^T dt \left(B_x \sigma_x + B_z \sigma_z \right) \right] | \psi_0 \rangle \, .
\end{aligned} \tag{B.46}
$$

We need to determine the integral contour such that the integral is converged. This implies that B_x is to be integrated from $-\infty \to \infty$, while B_z is to be integrated along the imaginary axis, $-i\infty \to i\infty$.

Note that until now we have not made any assumptions about the time dependence of the fields. This simplified expression for the path integral over just 2 fields follows naturally from the symmetry of the 4-spin Hamiltonian and the fact that the boundary states belong to a particular spin sector.

B.5 Numerical gradient descent

We can estimate the time dependent solutions to Eq. (C.47) by performing numerical gradient descent on discretized field configurations of B_x and B_z. For this section in order to perform gradient descent over real valued B_x and B_z fields we change the definition of B_z to an imaginary 'magnetic field', iB_z. The action is given by,

$$I = \int_0^T dt \left[\frac{27B_x^2}{4J} + \frac{81B_z^2}{4J} + iB_z(1+18\gamma) - \frac{J}{72} - \frac{4\gamma^2}{J} - \frac{\gamma}{2} \right] - \ln K$$
$$K = \langle \psi_T | \exp \left[\frac{1}{2} \int_0^T dt \left(B_x \sigma_x + iB_z \sigma_z \right) \right] |\psi_0\rangle . \tag{B.47}$$

For the gradient descent, we consider units where $Jdt = 0.05$. In Figs. 6 and 7 we consider total times of $2430Jt$ and $3240Jt$ respectively. Starting from the bulk saddle-point configurations we perform the gradient descent with the action given in Eq. (B.47) until the difference in action is below a threshold of $\delta I \sim 10^{-7}$. Each of the configurations in Fig. 3.6 require ~ 10000 iterations of the gradient descent to reach the required threshold. For Fig. 3.7a, we initialize the configuration of the fields to correspond to the instanton configuration in Eq. (3.46) and find that the action is already below the threshold for gradient descent.

To explore the subsystem purity phase diagram Fig. 3.10, we perform numerical gradient with the k dependent action with the propagator given by Eq. (3.53). For $\gamma < \gamma_c$ but close to criticality, we consider the two configurations in Fig. 3.10b(iii-iv) and perform gradient descent to find local minima near these solutions, for a range of $k \in 0.50, 0.501, .., 0.51$ as shown in Fig. B.4. We then interpolate to find the value of k for which the two configurations exchange in total action, which is the numerical estimation of k_c, used to plot Fig. 3.11. The error bars are the errors due to the resolution of the k values considered for the numerics.

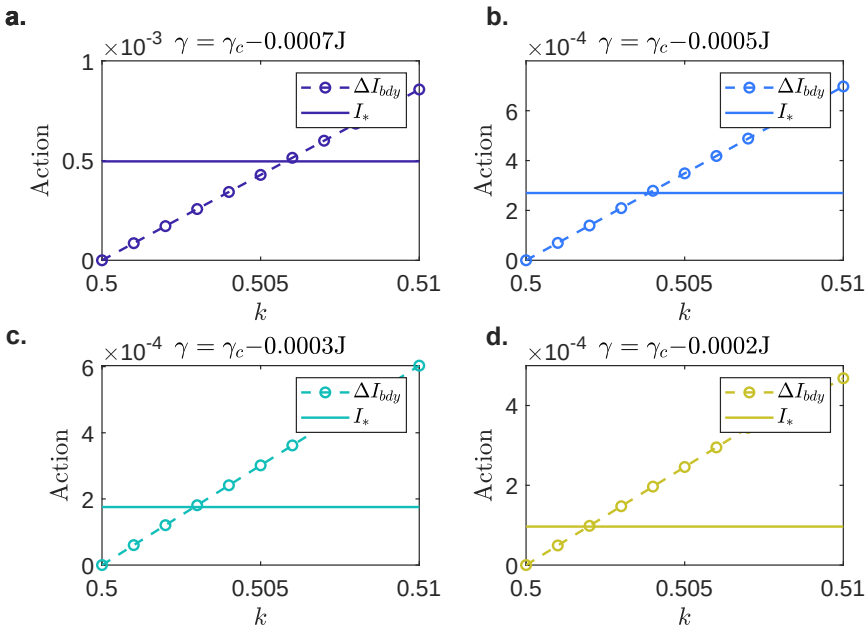

Figure B.4: **Subsystem purity critical exponent μ from gradient descent numerics.** The critical subsystem fraction $k_c(\gamma)$ is identified for measurement rates $\gamma < \gamma_c$ just below the critical point by finding points in the k, γ plane where the boundary action ΔI_{bdy} is equal to the single-instanton action I_*.

B.6 Exact diagonalization

Numerical simulations of the hybrid dynamics for small system sizes N confirm the presence of a long-lived mixed phase as shown in Fig. 3.8 of the main text. These data were obtained by numerically simulating the $(2, 1)$ hybrid Brownian model on $N = |Q| = 6$ qubits maximally entangled with $|R| = 6$ reference qubits using the Krylov subspace method [230, 231, 232].

We plot the results of these numerical simulations in Fig. B.5, which shows the entropy $-\ln \Pi_Q = -\ln Z_2/P^2$ as a function of time, averaged over 50 circuit realizations. We perform the disorder average in two different ways: the 'physical' disorder average $\langle Z_2/P^2 \rangle$ that one obtains from the Born rule (purple); and the 'tractable' disorder average $\langle Z_2 \rangle / \langle P^2 \rangle$ studied in this work (green). At low measurement rates γ we find that these two ways of doing the disorder

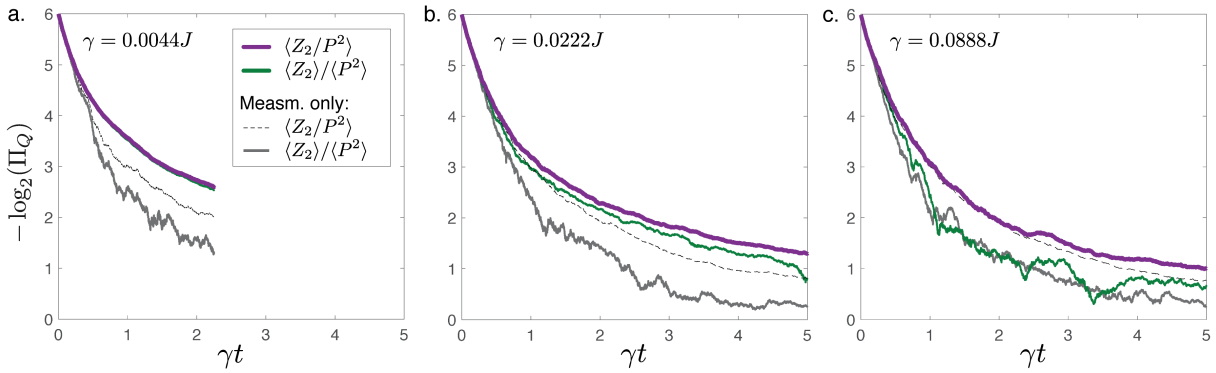

Figure B.5: **Disorder averaging in exact diagonalization numerics.** (a) Far below the critical point, the two averaging protocols (purple, green) yield nearly identical results in numerical simulations with $N = 6$ qubits averaged over 50 circuit realizations. (b) Closer to the critical point the two estimates begin to diverge, while above the critical point (c) they disagree sharply. Nevertheless, both disorder averages appear to faithfully diagnose the transition when compared to the respective disorder averages performed in circuits featuring measurements only (dotted grey, solid grey).

average give nearly identical answers (Fig. B.5a), while they disagree for higher values of γ (Figs. B.5b-c). Both disorder averages, however, deviate substantially from the corresponding curves computed in measurement-only circuits (dotted black, solid black), indicating that both disorder averages are sensitive to the purification transition.

Our exact diagonalization calculations are limited to short simulation times and values of γ/J that are not too small. At small γ one must distinguish the phase from the initial exponential decay, necessitating simulation times longer than $t > 1/\gamma$; accessing these long timescales is challenging for exact diagonalization due to the propagation of successive errors in the Krylov approximation. Specifically, numerical accuracy of the Krylov algorithm requires $\epsilon = \sqrt{J\delta t} \ll 1$ (the square root comes from the fact that J controls the variance of the couplings in Eq. (3.2), not the standard deviation). Together with the requirement $t > 1/\gamma$ this gives a lower bound

$$\frac{t}{\delta t} > \frac{1}{\epsilon^2}\frac{J}{\gamma} \tag{B.48}$$

on the number of timesteps $t/\delta t$ required to access the mixed phase given fixed numerical precision ϵ and phase parameter γ/J. Our simulation for $\gamma = 0.0044J$ above, for example, has $\epsilon \approx 0.16$ and $J/\gamma = 225$, requiring on the order of $t/\delta t \approx 10^4$ timesteps or more to access the mixed phase.

B.7 Continuous Monitoring of Disordered Spin Observables with Optical Cavities

While the projective qubit model introduced in Appendix B.2.0.2 is conceptually useful for deriving the effective weak measurement operator $M(t)$, high-fidelity single-site projective measurements are challenging to implement experimentally. Fortunately, such high-fidelity single-qubit projective measurements are not strictly necessary for our scheme to work. Instead, one can generate equivalent weak measurement dynamics by continuously monitoring the collective spin operator $\mathcal{O} = \sum_{i,\alpha} n_i^\alpha S_i^\alpha$ directly. Such collective spin variables can be monitored naturally in state-of-the-art cavity quantum electrodynamics setups by coupling a quasi-one-dimensional cold atomic ensemble to the optical mode of an all-to-all optical cavity [188, 212, 319, 320, 321, 322].

In such a cavity setup, each spin $\mathbf{S}_i$ is encoded into the electronic states of the ith atom, which resides at position z_i along the longitudinal cavity axis. The atoms act like a spin-dependent refractive index for the cavity mode, which causes the cavity resonance to shift by an amount proportional to the total magnetization $S^z_{\text{Tot}} = \sum_i S^z_i$ [319, 320, 321]. By probing the cavity with near-resonant light we can therefore continuously monitor the total spin projection S^z_{Tot}. If the atoms are coupled unequally to the cavity mode, the shift in cavity resonance is instead proportional to the disordered magnetization $\tilde{S}^z_{\text{Tot}} = \sum_i n_i S^z_i$, where the weights n_i are determined by

the coupling between the ith atom and the cavity mode. These couplings can be modified by shifting the physical locations of the atoms relative to the cavity mode, or by applying nonuniform local ac Stark shifts to the ensemble. Further, one can couple different spin components S_i^α to the cavity mode by applying additional non-uniform magnetic fields or optical drive fields to rotate the local coordinate frame at each atomic site z_i. The combination of these tools in principle allows for continuous monitoring of disordered spin-linear operators of the form $\mathcal{O} = \sum_{i,\alpha} n_i^\alpha S_i^\alpha$ without requiring single-site projective measurements of single qubits.

Appendix C: Chapter 4:

C.1 Setup of the Rényi entropy calculation

In the main part of the paper we focus on a 1-dimensional lattice of size L with periodic boundary conditions, however the results can be readily extended to higher dimensions. For the spin model, each spin operator is labeled as $\mathcal{S}_{ri\alpha}$, with i and α denoting the intra-cluster label and spin direction respectively, while r refers to the position label of the cluster in the chain, and a similar labeling applies to the fermions.

The dofs in Q (vectors in the Hilbert space $\mathcal{H}$) undergo a non-unitary random evolution $V(t)$. The randomness comes from the Brownian nature of the unitary evolution that we consider in our setup. Under this evolution, a density matrix (when viewed as vector in the doubled Hilbert space $|\rho\rangle\rangle$) evolves as, $|\rho\rangle\rangle \to V(t) \otimes V^*(t) \, |\rho\rangle\rangle$, which generates an unnormalized state because of the non-unitary evolution. We want to study the entanglement properties of the subsystem A for this state, a particular diagnostic of which is the Rényi-n entropy of the normalized reduced density matrix ρ_A,

$$S_A^{(n)} = \frac{1}{1-n} \mathbb{E} \log \frac{\mathrm{Tr}\left[\rho_A^n(t)\right]}{\mathrm{Tr}\left[\rho_A(t)\right]^n}, \tag{C.1}$$

where $\mathbb{E}$ refers to the averaging over the realizations of the random circuit $V(t)$.

Estimating the actual Rényi-2 entropy averaged over the randomness requires taking a non-trivial replica limit since this is an average of a ratio of two multi-replica quantities. Instead, we will calculate the quasi Rényi-2 entropy [264], which is the ratio of the averages,

$$\hat{S}_A^{(n)} = \frac{1}{1-n} \log \frac{\mathbb{E}\mathrm{Tr}\left[\rho_A^n(t)\right]}{\mathbb{E}\mathrm{Tr}\left[\rho_A(t)\right]^n} \tag{C.2}$$

This quantity, while distinct from the disorder averaged Rényi-n entropy, is easier to calculate. In this work we focus on estimating $\hat{S}_A^{(2)}$, for which it is convenient to consider the dynamics in 4 replicas of the Hilbert space $\mathcal{H}^{(4)}$. We use a $1, 2, 3, 4$ notation: $1, 2$ $(3, 4)$ denote the first (second) replica, and $1, 3$ $(2, 4)$ denote the forward (backward) evolution. In $\mathcal{H}^{(4)}$ the time evolution is given by $\mathbf{V}(t) = V^{(1)}(t) \otimes V^{(2)*}(t) \otimes V^{(3)}(t) \otimes V^{(4)*}(t)$, and the normalization factor is given by $\mathcal{N}(\rho) = \sqrt{\langle\langle \mathcal{I}| \mathbf{V}(t) |\rho\rangle\rangle |\rho\rangle\rangle}$. To define $|\mathcal{I}\rangle\rangle \in \mathcal{H}^{(4)}$, we first define two normalized states,

$$|+\rangle\rangle \sim \sum_{ab=0,1} |aabb\rangle\rangle \tag{C.3}$$

$$|-\rangle\rangle \sim \sum_{ab=0,1} |abba\rangle\rangle, \tag{C.4}$$

which leads to the definition, $|\mathcal{I}\rangle\rangle = \bigotimes_{i,r} |+\rangle\rangle$. This definition ensures that the normalization factor is the usual norm of a state. In our setup, the system dofs in Q are initially maximally entangled with NL qubits in a reference R. The corresponding initial state for Q in $\mathcal{H}^{(4)}$ is $|\rho\rangle\rangle \otimes |\rho\rangle\rangle = |\mathcal{I}\rangle\rangle$.

We further define a SWAP state in $\mathcal{H}^{(4)}$ as,

$$|\mathcal{S}_A\rangle\rangle = \bigotimes_{i,r\in A} |-\rangle\rangle \bigotimes_{i,r\in A^c=Q-A} |+\rangle\rangle, \tag{C.5}$$

and the quasi Rényi-2 entropy is given by,

$$\exp\left(-\hat{S}_A^{(2)}\right) = \frac{\langle\langle \mathcal{S}_A| \mathbb{E}\mathbf{V}(t) |\mathcal{I}\rangle\rangle}{\langle\langle \mathcal{I}| \mathbb{E}\mathbf{V}(t) |\mathcal{I}\rangle\rangle}. \tag{C.6}$$

The quasi-entropy can be simulated in a quntum experiment with extra classical post-processing and no extra quantum resources over estimating the usual Rényi entropy [4].

C.1.1 Relation between the quasi Rényi, Rényi, and von Neumann entropies

One can show that the Rényi entropy and the quasi Rényi entropy can be treated as a part of the same family of generalized entropic quantities. Consider the generalized function,

$$\chi_A^{(nm)} = \frac{1}{m(1-n)} \log \frac{\mathbb{E}\left(\mathrm{Tr}\left[\rho_A^n\right]\right)^m}{\mathbb{E}\left(\mathrm{Tr}\left[\rho_A\right]\right)^{nm}} \tag{C.7}$$

One can show,

$$\chi_A^{(nm)}\big|_{m\to 0} = S_A^{(n)} \tag{C.8}$$

$$\chi_A^{(nm)}\big|_{m\to 1} = \hat{S}_A^{(n)}. \tag{C.9}$$

Intriguingly, one can also extract the von Neumann entropy directly from the quasi Rényi entropy. First let us define the normalized density matrix, $\tilde{\rho}_A = \rho_A/\mathrm{Tr}\left[\rho_A\right]$. The probability of

each trajectory is given by $\mathrm{Tr}\left[\rho_A\right]$. The trajectory averaged von-Neumann entropy is given by,

$$\overline{S_A} = -\mathbb{E}\big[\mathrm{Tr}\left[\rho_A\right]\mathrm{Tr}\left[\tilde{\rho}_A \log \tilde{\rho}_A\right]\big]. \tag{C.10}$$

We find that the trajectory averaged von-Neumann entropy is the $n \to 1$ limit of the quasi-Renyi entropy,

$$\hat{S}_A^{(n\to 1)} = \overline{S_A}. \tag{C.11}$$

Let us sketch this proof.

$$\begin{aligned}
\overline{S_A} &= -\mathbb{E}\big[\mathrm{Tr}\left[\rho_A \log \rho_A\right] - \mathrm{Tr}\left[\rho_A\right]\log \mathrm{Tr}\left[\rho_A\right]\big] \\
&= -\partial_n \mathbb{E}\big[\mathrm{Tr}\left[\rho_A^n\right] - \left(\mathrm{Tr}\left[\rho_A\right]\right)^n\big]\Big|_{n\to 1} \\
&= -\partial_n \left[\frac{\mathbb{E}\mathrm{Tr}\left[\rho^n\right]}{\mathbb{E}\left(\mathrm{Tr}\left[\rho_A\right]\right)^n}\right]\Bigg|_{n\to 1} \text{(using } \mathbb{E}\mathrm{Tr}\left[\rho_A\right] = 1\text{)} \\
&= \frac{1}{1-n}\log \frac{\mathbb{E}\mathrm{Tr}\left[\rho^n\right]}{\mathbb{E}\left(\mathrm{Tr}\left[\rho_A\right]\right)^n}\Bigg|_{n\to 1} \\
&= \hat{S}_A^{(n\to 1)}.
\end{aligned}$$

Hence we find that although the quasi Rényi and the averaged Rényi entropies are different replica limits of a generalized entropy function, a particular replica limit of the quasi Rényi entropy can access the physical von Neumann entropy of the state generated by the hybrid circuit.

C.2 Path integral representation of the replicated dynamics

In this section of the Appendix we show how to derive the spin path integral for the replicated dynamics and derive Eqs. 4,5 and 6 in the main text.

C.2.1 Measurement model in the Brownian spin model

A random 1-body operator at a given time, $\mathcal{O}(t) = \sum_{i,\alpha} n_i^\alpha(t)\mathcal{S}_{i\alpha}$ is coupled to an auxiliary qubit via the interaction,

$$\exp\left[-i\frac{\Delta t}{2}\mathcal{O}(t)\sigma^x_{\text{aux}}\right]|\Psi\rangle\,|0\rangle_{\text{aux}}\,, \tag{C.12}$$

with $|\Psi\rangle$ being the state of the system. After this coupling, the auxiliary qubit is measured in the σ^y_{aux} basis, and only $+1$ results are post-selected. Under this dynamics, the system deterministically evolves with a non-unitary evolution operator $M(t)$,

$$|\Psi\rangle \to M(t)\,|\Psi\rangle = \left(1 - \frac{1}{2}\mathcal{O}\Delta t - \frac{1}{8}\mathcal{O}^2\Delta t^2 + \cdots\right)|\Psi\rangle\,. \tag{C.13}$$

C.2.2 Integrating out disorder and spin path integral

The Brownian disorders are explicitly given by,

$$\begin{aligned}
&\mathbb{E}\left[n_i^\alpha(t)n_j^\beta(t')\right] = \frac{\gamma}{(\mathcal{S}+1)^2}\frac{\delta_{tt'}}{\Delta t/2}\delta_{ij}\delta^{\alpha\beta},\\
&\mathbb{E}\left[J_{ij\alpha\beta}(t)J_{kl\mu\rho}(t')\right] = \frac{J}{N(\mathcal{S}+1)^4}\frac{\delta_{tt'}}{\Delta t/2}\delta_{ik}\delta_{jl}\delta_{\alpha\mu}\delta_{\beta\rho},\\
&\mathbb{E}\left[\tilde{J}^{r_1r_2}_{ij\alpha\beta}(t)\tilde{J}^{r_1'r_2'}_{kl\mu\rho}(t')\right] = \frac{gJ_{r_1r_2}}{N(\mathcal{S}+1)^4}\frac{\delta_{tt'}}{\Delta t/2}\delta_{r_1r_1'}\delta_{r_2r_2'}\delta_{ik}\delta_{jl}\delta_{\alpha\mu}\delta_{\beta\rho}.
\end{aligned}$$

We want to write down a path integral expression for the averaged circuit evolution in n replicated copies of the physical system, which includes $2n$ copies of the circuit (counting the

time-reversed copies). This quantity,

$$\mathbf{V}(t) = \mathbb{E}\left[V^{(1)}(t) \otimes V^{(2)*}(t) \otimes \ldots V^{(2n-1)}(t) \otimes V^{(2n)*}(t)\right], \tag{C.14}$$

can give us access to the n-th Rényi entropies, and in particular, the $n = 2$ result corresponds to the Rényi-2 entropy that we consider in this paper. Let u, v denote the replica index. The time evolution operator in any given copy is generated by an interaction Hamiltonian and a non-unitary evolution generated by a weak measurement followed by post-selection, as described in the main text. Schematically this can be expressed as,

$$V^{(u)}(\Delta t) \sim \exp\left[-\frac{i\Delta t}{2}\left(H^{(u)}(t) - i\mathcal{O}^{(u)}(t)\right)\right], \tag{C.15}$$

where the $H^{(u)}$ and $\mathcal{O}^{(u)}$ are the Hamiltonian and the measured operator (in replica u) respectively. These operators are taken to be Brownian in our model, which implies that the time evolution is uncorrelated in the time direction. However the randomness is same for each replica, which implies that in $\mathbf{V}$ different replicas become correlated when the disorder is integrated away, using the Gaussian nature of the Brownian variables defined in Eq. 3 of the main text. One way to derive this is by expanding the evolution in each time step in the product in (C.15) to second order in Δt, and collecting terms like $\mathbb{E}\left[H^{(u)}H^{(v)}\right]$, $\mathbb{E}\left[H^{(u)}H^{(u)}\right]$ or $\mathbb{E}\left[\mathcal{O}^{(u)}\mathcal{O}^{(v)}\right]$ together. This procedure is discussed in detail in the Appendix B of [4]. Exponentiating back, one obtains that $\mathbf{V}(\Delta t) \sim \exp\left(-NI_n(t)\Delta t\right)$. The variances of the random terms have been scaled in a way that the exponential comes with a prefactor of N. Dropping some constant terms (which arise from the intra-replica terms) $I_n(t)$ is given by,

$$
\begin{aligned}
I_n(t) = \Bigg[& \sum_{\substack{r \\ u<v}} (-1)^{u+v} \frac{J}{4(\mathcal{S}+1)^4} \left(\frac{1}{N} \sum_i \mathcal{S}^u_{ri} \cdot \mathcal{S}^v_{ri} \right)^2 \\
& + \sum_{\substack{r \neq r' \\ u<v}} (-1)^{u+v} \frac{g J_{rr'}}{2(\mathcal{S}+1)^4} \left(\frac{1}{N} \sum_i \mathcal{S}^u_{ri} \cdot \mathcal{S}^v_{ri} \right) \left(\frac{1}{N} \sum_i \mathcal{S}^u_{r'i} \cdot \mathcal{S}^v_{r'i} \right) \\
& - \sum_{\substack{r \\ u<v}} (-1)^{u+v} \frac{\gamma}{2(\mathcal{S}+1)^2} \left(\frac{1}{N} \sum_i \mathcal{S}^u_{ri} \cdot \mathcal{S}^v_{ri} \right) \Bigg].
\end{aligned} \tag{C.16}
$$

In this expression the spin operator $\mathcal{S}$ refers to the spin operator at time t.

We can now stack $\mathbf{V}_u(\Delta t)$ at different times by repeating sequence of the Brownian interactions and measurements, insert resolutions of the identity between each layer, and take the limit $\Delta t \to 0$ with T fixed to express $\mathbb{V}(t)$ as a path integral over $2nN$ unit-norm $\mathrm{SO}(3)$ spins $\mathcal{S}^u_{ri}$, using spin coherent states as the basis. The completeness relation for the coherent states for a single spin is given by,

$$
\mathbb{I} = \int \frac{2\mathcal{S}+1}{4\pi} d\mathbf{\Omega}_i \left| \mathbf{\Omega}_i \right\rangle \left\langle \mathbf{\Omega}_i \right| . \tag{C.17}
$$

To turn the spins into coherent states, we use the upper symbols for single spin-S Pauli operators [318],

$$
\mathcal{S}_{i\alpha} = \int \frac{2\mathcal{S}+1}{4\pi} d\mathbf{\Omega}_i \left| \mathbf{\Omega}_i \right\rangle \left\langle \mathbf{\Omega}_i \right| (\mathcal{S}+1) \Omega_{i\alpha} \tag{C.18}
$$

$$
(\mathcal{S}_{i\alpha})^2 = \int \frac{2\mathcal{S}+1}{4\pi} d\mathbf{\Omega}_i \left| \mathbf{\Omega}_i \right\rangle \left\langle \mathbf{\Omega}_i \right| \left[(\mathcal{S}+1) \left(\mathcal{S} + \frac{3}{2} \right) (\Omega_{i\alpha})^2 - \frac{\mathcal{S}+1}{2} \right], \tag{C.19}
$$

and introduce a measure for the coherent spin states in the path integral,

$$\mathcal{D}\Omega^u_{ri} = \prod_{t_n} \frac{2\mathcal{S}+1}{4\pi} d\mathbf{\Omega}^u_{r,i,t_n} \langle \mathbf{\Omega}^u_{r,i,t_{n+1}} | \mathbf{\Omega}^u_{r,i,t_n} \rangle, \tag{C.20}$$

with implicit time dependent terms.

In terms of the coherent states $\mathbb{V}(t)$ is given by a path integral,

$$\begin{aligned}
\mathbf{V}(t) &= \mathbb{E}\left[V \otimes V_{\mathcal{T}} \otimes \cdots \otimes V \otimes V_{\mathcal{T}}\right] = e^{-NI[\mathbf{\Omega}]} \\
I[\mathbf{\Omega}] &= \int_0^T dt \Bigg[\frac{J}{4} \sum_{\substack{r \\ u<v}} (-1)^{u+v} \left(\frac{1}{N} \sum_i \mathbf{\Omega}^u_{ri} \cdot \mathbf{\Omega}^v_{ri} \right)^2 \\
&\quad + \sum_{\substack{r \neq r' \\ u<v}} (-1)^{u+v} \frac{g J_{rr'}}{2} \left(\frac{1}{N} \sum_i \mathbf{\Omega}^u_{ri} \cdot \mathbf{\Omega}^v_{ri} \right) \left(\frac{1}{N} \sum_i \mathbf{\Omega}^u_{r'i} \cdot \mathbf{\Omega}^v_{r'i} \right) \\
&\quad - \sum_{\substack{r \\ u<v}} (-1)^{u+v} \frac{\gamma}{2(S+1)^2} \left(\frac{1}{N} \sum_i \mathbf{\Omega}^u_{ri} \cdot \mathbf{\Omega}^v_{ri} \right) \Bigg]
\end{aligned} \tag{C.21}$$

To decouple the non-linear interactions in $\mathbf{\Omega}^u_{ri} \cdot \mathbf{\Omega}^v_{ri}$, we introduce Hubbard Stratonovich type fields which couple different replicas $F^{(r)}_{uv}$ and $G^{(r)}_{uv}$, satisfying the operator identity,

$$1 = \left(\prod_{r,u<v} \int \mathcal{D}F^{uv}_r \mathcal{D}G^{uv}_r \right) \exp\left[iN \int_0^T dt F^{uv}_r \left(G^{uv}_r - \frac{1}{N} \sum_i \mathbf{\Omega}^u_{ri} \cdot \mathbf{\Omega}^v_{ri} \right) \right]. \tag{C.22}$$

The action can thus be re-written as,

$$I[F,G,\mathbf{\Omega}] = \int dt \Bigg[\sum_{\substack{r \\ u<v}} \frac{(-1)^{u+v} J}{4} \left(G_r^{uv}\right)^2 + \sum_{\substack{r\neq r' \\ u<v}} \frac{(-1)^{u+v} g J_{rr'}}{2} \left(G_r^{uv}\right)\left(G_{r'}^{uv}\right) - \sum_{\substack{r \\ u<v}} \frac{(-1)^{u+v}\gamma}{2} \left(G_r^{uv}\right) - \sum_{\substack{r \\ u<v}} \left(iF_r^{uv} G_r^{uv}\right) + \sum_{\substack{r \\ u<v}} iF_r^{uv} \left(\frac{1}{N} \sum_i \mathbf{\Omega}_{ri}^u \cdot \mathbf{\Omega}_{ri}^v \right) \Bigg] \tag{C.23}$$

Note that (C.23) is applicable in any general dimensions, where the position label $r \in \mathbb{Z}^d$ can be identified as a d dimensional vector, with L being the linear size along each dimension.

C.2.3 Field theory with periodic boundary condition

We can further simplify (C.23) by assuming periodic boundary condition and going to momentum space. We also assume that the interaction $J_{rr'}$ is translationally invariant and even, i.e. $J_{rr'} \sim J_{|r-r'|}$.

We consider discrete d-dimensional cubic lattice in the space $\mathbb{Z}^d$ with L being the linear extent of the cube. In the limit $L \gg 1$, the momentum space domain is $k \in \{0, 2\pi\}^d$. We use the following schematic definitions,

$$\begin{aligned} G_k &= \sum_{r\in\mathbb{Z}^d} e^{-ik\cdot r} G_r \\ G_r &= \frac{1}{(2\pi)^d} \int_0^{2\pi} \cdots \int_0^{2\pi} dk_1 \cdots dk_d e^{ik\cdot r} G_k \equiv \int đ^d k e^{ik\cdot r} G_k \\ \frac{1}{(2\pi)^d} \sum_{r\in\mathbb{Z}^d} e^{ik\cdot r} &= \delta(k) \ , \ \int đ^d k e^{ikr} = \delta_{r,0}. \end{aligned} \tag{C.24}$$

We also introduce the notation,

$$\Omega_r^{uv} = \frac{1}{N}\sum_i \mathbf{\Omega}_{ri}^u \cdot \mathbf{\Omega}_{ri}^v. \tag{C.25}$$

In momentum space, we can rewrite Eq. C.23 can be rewritten as (dropping the constant terms),

$$I[F,G,\mathbf{\Omega}] = \int dt \int đ^d k \sum_{u<v} \left[\frac{(-1)^{u+v}}{4} \left(\hat{J}_k G_k^{uv} G_{-k}^{uv} - 4\pi\gamma G_k^{uv}\delta(k) \right) - iF_k^{uv} G_{-k}^{uv} + iF_k^{uv}\Omega_{-k}^{uv} \right],$$
$$\text{where, } \hat{J}_k = J + \sum_{r\in\mathbb{Z}^d} e^{-ik\cdot r} J_{|r|} \tag{C.26}$$

Note that all the G_k^{uv} fields can be integrated out, by satisfying the equations of motion,

$$\begin{aligned} G_k^{uv} &= (-1)^{u+v}\frac{2iF_k^{uv}}{\hat{J}_k} && \text{for } k \neq 0, \\ G_0^{uv} &= \frac{2\pi\gamma}{\hat{J}_0} + (-1)^{u+v}\frac{2iF_0^{uv}}{\hat{J}_0} && \text{for } k = 0. \end{aligned} \tag{C.27}$$

Integrating out the G fields, we get (again dropping constant terms),

$$I[F,\mathbf{\Omega}] = \int dt \int đ^d k \sum_{u<v} \left[-\frac{(-1)^{u+v}}{\hat{J}_k} \left(iF_k^{uv}\right)\left(iF_{-k}^{uv}\right) - \frac{2\pi\gamma}{\hat{J}_0}\left(iF_k^{uv}\right)\delta(k) + iF_k^{uv}\Omega_{-k}^{uv} \right]. \tag{C.28}$$

Going back to real space, we get,

$$I[F,\mathbf{\Omega}] = \int dt \sum_{\substack{r \\ u<v}} \left[-(-1)^{u+v} \sum_{r'} \mathcal{J}_{rr'} \left(iF_r^{uv}\right)\left(iF_{r'}^{uv}\right) - \frac{\gamma}{\hat{J}_0}\left(iF_r^{uv}\right) + \left(iF_r^{uv}\right)\Omega_r^{uv} \right], \tag{C.29}$$

with an effective real space interaction $\mathcal{J}_{rr'}$ given by,

$$\mathcal{J}_{rr'} = \int đ^d k \frac{e^{ik\cdot(r-r')}}{\hat{J}_k}. \tag{C.30}$$

By identifying the last term in (C.29) as a partition function for the spins with external fields iF, one gets the Eq. 4 in the main text.

C.2.4 Effective real space interaction

(C.29) holds for any general number of dimensions. The microscopic interaction between the spins i.e. $J_{rr'}$ can be Fourier transformed to give the momentum space interaction $\hat{J}_k$ between the G fields. This can then be transformed to an interaction $\mathcal{J}_{rr'}$ between the iF fields via (C.30).

Here we consider two forms of the interaction, nearest neighbor (NN) or power-law interacting (PL). In the main text results are used for the PL case. Including the on-site term, the real space interaction between spins in a d-dimensional lattice is defined as follows,

$$J_{rr'} = \begin{cases} J\left(\delta_{r,r'} + g\sum_i \left(\delta_{r,r'+e_i} + \delta_{r,r'-e_i}\right)\right) & \text{(NN)} \\ J\left(\delta_{r,r'} + g\left(1-\delta_{r,r'}\right)\frac{1}{|r-r'|^{2\alpha}}\right) & \text{(PL)}. \end{cases} \tag{C.31}$$

Here e_i is a d-dimensional vector $\{0, 0, .., i, .., 0\}$ with 1 in the i-th position.

The momentum space interaction is given by its discrete-time Fourier transform,

$$\hat{J}_k = \begin{cases} J\left(1 + 2g\sum_i \cos k_i\right) & \text{(NN)} \\ J\left(1 + g\sum_{s\neq 0} \frac{e^{-ik\cdot s}}{|s|^{2\alpha}}\right) & \text{(PL).} \end{cases} \tag{C.32}$$

To get the effective real space interaction $\mathcal{J}$ between the replica fields iF, one has to take the Fourier transform of $\hat{J}_k^{-1}$. This can be done exactly for $d = 1$.

C.2.4.1 d=1

In $d = 1$ we have,

$$\hat{J}_k = \begin{cases} J\left(1 + 2g\cos k\right) & \text{(NN)} \\ J\left(1 + g\left(\text{Li}_{2\alpha}\left(e^{-ik}\right) + \text{Li}_{2\alpha}\left(e^{ik}\right)\right)\right) & \text{(PL),} \end{cases} \tag{C.33}$$

where $\text{Li}_n(z)$ is the Polylogarithm function. For large α, $\text{Li}_{2\alpha}(z) \to z$, and $\hat{J}_k$ reduces to the Nearest Neighbor case.

In the NN case, the real space interaction between the replica fields is given by,

$$\mathcal{J}_{rr'}^{\text{NN}} = \int_0^{2\pi} \frac{dk}{2\pi} \frac{e^{ik(r-r')}}{1 + 2g\cos k}. \tag{C.34}$$

Changing the variables to $z = e^{ik}$, we get contour integral defined along the unit circle in the complex z-plane, with two isolated poles along the negative real axis. Performing the contour

integral picks up the pole within the unit circle and one obtains,

$$\mathcal{J}^{\text{NN}}_{rr'} = \frac{(-1)^{r-r'}}{\sqrt{1-4g^2}} e^{-\text{acosh}\frac{1}{2g}|r-r'|}. \tag{C.35}$$

In the PL case, with the same change of variables, the real space interaction is given by the following contour integral defined along the unit circle,

$$\mathcal{J}^{\text{PL}}_{rr'} = \int_{\mathcal{C}} \frac{dz}{2\pi i} \frac{z^{r-r'-1}}{1+g\left(\text{Li}_{2\alpha}(z)+\text{Li}_{2\alpha}(1/z)\right)}. \tag{C.36}$$

For large enough g (including $g=1$) there is an isolated pole along the negative real axis within the unit circle, and a branch cut due to the $\text{Li}_{2\alpha}(1/z)$ term along the positive real axis $z \in (0,\infty)$. The pole gives an exponential decay like the NN case, while we will show that the branch cut contribution leads to a power law interaction.

Deforming the contour to hug the branch cut, the integral is proportional to the discontinuity along the branch cut ($\int_{0+i\varepsilon}^{1+i\varepsilon} - \int_{0-i\varepsilon}^{1-i\varepsilon}$), which for the function $\text{Li}_{2\alpha}(1/z)$ is proportional to $\log^{2\alpha-1}(1/z)$. Thus we get,

$$\mathcal{J}^{\text{PL}}_{rr'} = \text{Pole contribution} - \int_0^1 dz z^{r-r'-1} \log^{2\alpha-1}(z) g(z), \tag{C.37}$$

where $g(z)$ is a smooth function. For large $|r-r'|$ the integrand is heavily suppressed away from $z=1$, so we can change variables $z \sim e^{-w}$, and after dropping the regular terms, we have an

integral,

$$\int_0^\infty dw e^{-w|r-r'|} w^{2\alpha-1} \sim |r-r'|^{-2\alpha}, \text{ for } |r-r'| \gg 1.$$

Along with the pole contribution we thus get the effective real space interaction,

$$\mathcal{J}_{rr'}^{\text{PL}} \sim (-1)^{r-r'} e^{-\mu|r-r'|} - (1-\delta_{rr'}) \frac{1}{|r-r'|^{2\alpha}}. \tag{C.38}$$

At large $|r-r'|$, $\mathcal{J}_{rr'} \sim |r-r'|^{-2\alpha}$, as was noted in the main text.

C.2.4.2 General d

In this section we will derive the effective real space interaction in any general dimension, d.

For the NN case, we have,

$$\mathcal{J}_{rr'}^{\text{NN}} = \int đ^d k \frac{e^{ik\cdot(r-r')}}{1+2g\sum_i \cos k_i}, \tag{C.39}$$

which can be expanded around $k_i = \pi$. Furthermore, we can consider $r-r'$ to be along a

particular dimension, say 1. With these manipulations we get,

$$\begin{aligned}\mathcal{J}^{\text{NN}}_{rr'} &\sim \int_{-\pi}^{+\pi} đ^d k \frac{e^{ik_1(r-r')}}{1+\tilde{g}\sum_i k_i^2} \\ &\sim \int_0^{\infty} dk k^{d-2} \int đk_1 \frac{e^{ik_1(r-r')}}{1+k_1^2+k^2} \\ &\sim \int_0^{\infty} \frac{k^{d-2}}{\sqrt{1+k^2}} e^{-\sqrt{1+k^2}|r-r'|} \sim e^{-\mu|r-r'|}. \end{aligned} \tag{C.40}$$

For the PL case, one needs to evaluate,

$$\mathcal{J}^{\text{PL}}_{rr'} \sim \int đ^d k \frac{e^{ik\cdot s}}{1+g\sum_{u\neq 0}\frac{e^{-ik\cdot u}}{|u|^{2\alpha}}}. \tag{C.41}$$

Firstly we have,

$$\sum_{u\neq 0}\frac{e^{-ik\cdot u}}{|u|^{2\alpha}} \sim \int' đ^d u \frac{e^{-ik\cdot u}}{|u|^{2\alpha}} \sim k^{2\alpha-d}. \tag{C.42}$$

With this, we can expand the function to be Fourier Transformed at small k,

$$\mathcal{J}^{\text{PL}}_{rr'} \sim \int đ^d k e^{ik\cdot s}\left(1-gk^{2\alpha-d}\right) \sim \delta(s) - g|s|^{-2\alpha}. \tag{C.43}$$

These results generalize C.38 for any general dimension.

C.3 Saddle point analysis of the mean field

C.3.1 Effective Bulk Action and saddle points

The mean-field action in Eq. (C.29) (equivalent to Eq. 4 in the main text), describes the dynamics of $4L$ spins $\mathbf{S}_r^u$ interacting via Heisenberg couplings $\mathbf{S}_r^u \cdot \mathbf{S}_r^v$. Because these coupling terms are manifestly symmetric under global $\mathrm{SU}(2)$ rotations, the action $I = I[iF_r^{uv}]$ is also $\mathrm{SU}(2)$ invariant. In fact, because the interaction terms are separable $\sum_r \ln \mathcal{K}_r$ in the space coordinate r, the action I is invariant under all *local* $\mathrm{SU}(2)$ rotations generated by the total spin operators $\mathbf{S}_r^{\mathrm{Tot}} = \sum_u \mathbf{S}_r^u$ within each cluster r. At the same time, the boundary conditions generated by the EPR pairs and SWAP operator force the system to form $\mathrm{SU}(2)$ spin singlets at times $t = 0, T$. Together, these facts constrain the dynamics within each cluster r to live entirely in the spin-singlet subspace $\mathbf{S}_r^{\mathrm{Tot}} = 0$ for each $r = 1, \ldots, L$. Thus, each cluster r supports a single replica qubit or r-bit spanned by the states $|\uparrow\rangle_r, |\downarrow\rangle_r$.

The underlying $\mathrm{SU}(2)$ symmetry significantly simplifies the problem. For $n = 2$ the propagator $\mathcal{K}_r$ in each two-dimensional r-bit subspace simplifies to

$$\mathcal{K}_r = \langle \psi_T | \exp\left[\frac{1}{2}\int_0^T dt\, \left(\phi_r(t)\sigma_r^x + \Theta_r(t)\sigma_r^z\right)\right] |\psi_0\rangle\, e^{BT/2} \tag{C.44}$$

where $\sigma_r^{x,z}$ are the 2×2 Pauli matrices acting on the r-bit $|\uparrow\rangle_r, |\downarrow\rangle_r$ subspace. The fields $\phi_r(t), \Theta_r(t)$ are linear combinations of the mean fields

$$\begin{aligned} \phi_r &= \frac{2}{3\sqrt{3}}\left(iF_r^{12} + iF_r^{34} - iF_r^{14} - iF_r^{23}\right) \\ \Theta_r &= \frac{2}{9}\sum_{u<v} iF_r^{uv} - \frac{2}{3}\left(iF_r^{13} + iF_r^{24}\right) \end{aligned} \tag{C.45}$$

and where terms proportional to the identity within the r-bit subspace have been collected into the term

$$B = \frac{2}{9L} \sum_{r,u<v} iF_r^{uv}. \tag{C.46}$$

The time- and space-dependent bulk fields $\phi_r(t), \Theta_r(t)$ encode the relevant mean-field dynamics of the r-bits in each cluster r. In general these fields must execute nontrivial motions in the bulk in order to satisfy the non-equal boundary conditions $|\psi_0\rangle, |\psi_T\rangle$. By contrast, the remaining fields in the action appear simply as quadratic Gaussian fields and may therefore be trivially integrated out of the path integral, leading to the effective action

$$\begin{aligned} \mathbb{E}\mathrm{Tr}\left[\rho_A^2(t)\right] \text{ or } \mathbb{E}\mathrm{Tr}\left[\rho_A(t)\right]^2 &= \int \mathcal{D}\phi\mathcal{D}\Theta \exp\left[-NI[\phi,\Theta]\right] \\ I[\phi,\Theta] &= \sum_r \int_0^T dt \left[\sum_{r'} \frac{27\mathcal{J}_{rr'}}{16}\left(\phi_r\phi_{r'} - 3\Theta_r\Theta_{r'}\right) + \Theta_r\left(1 + \frac{9\gamma}{\hat{J}_0}\right)\right] - \sum_r \ln \mathcal{K}_r. \end{aligned} \tag{C.47}$$

with the propagator $\mathcal{K}_r$ given in Eq. (C.44), and where we have dropped additive constant terms.

To understand the saddle points of the action $I[\phi,\Theta]$ we first consider the bulk mean-field limit in which the fields are independent of space and time: $\phi_r(t) = \phi, \Theta_r(t) = \Theta$. In this case the propagator $\mathcal{K}_r$ is dominated at long times by the ground state of the r-bit effective Hamiltonian $\phi\sigma_r^x + \Theta\sigma_r^z$, which yields

$$\sum_r \ln \mathcal{K}_r = \frac{LT}{2}\sqrt{\phi^2 + \Theta^2} + \frac{BLT}{2}. \tag{C.48}$$

By substituting this into Eq. (C.47) (and again dropping additive constant terms) we obtain the time- and space-independent effective bulk action,

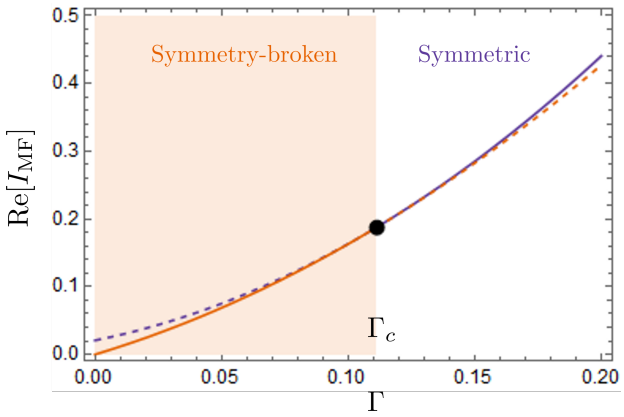

Figure C.1: Action cost for symmetric and symmetry-broken phases. Below the critical point $\Gamma < \Gamma_c$, the action cost $\mathrm{Re}[I_{MF}]$ is minimized by the symmetry-broken saddle points (solid orange) relative to the symmetric saddle point (dashed purple). Above the critical point $\Gamma > \Gamma_c$ the path integral is dominated by the symmetric saddle point (solid purple) because the symmetry-broken saddles (dashed orange) are imaginary and therefore do not contribute to the integral (see Fig. C.2).

$$I_{\mathrm{MF}}[\phi, \Theta] = NTL\left[\mathcal{J}\left(\phi^2 - 3\Theta^2\right) - 9\left(\Gamma + \frac{1}{9}\right)\Theta - \frac{1}{2}\sqrt{\phi^2 + \Theta^2}\right], \tag{C.49}$$

where we have defined $\Gamma \equiv \frac{\gamma}{\hat{J}_0}$ and $\mathcal{J} \equiv 27/16 \sum_{s\in\mathbb{Z}} \mathcal{J}_{r(r+s)}$.

Saddle point analysis of this action [4] reveals a phase transition at $\Gamma_c = 1/9$. For $\Gamma > \Gamma_c$ the action is dominated by the symmetric saddle point with $\phi^* = 0$ and $\Theta^* = -3(\Gamma_c + 2\Gamma)/4\mathcal{J}$. By contrast, for $\Gamma < \Gamma_c$, the action is dominated by the symmetry-broken saddle-point where the field ϕ^* is non-zero and comes in a pair, $\phi^* \propto \pm\sqrt{\Gamma_c - \Gamma}$, while $\Theta^* = -9(\Gamma_c + \Gamma)/8\mathcal{J}$. The replica permutation $1 \leftrightarrow 3$ is equivalent to $\phi \leftrightarrow -\phi$ symmetry, which is spontaneously broken for $\Gamma < \Gamma_c$.

Note, γ_c is given by $\Gamma_c \hat{J}_0 \sim \Gamma_c \left(1 + g \sum_{s\neq 0} |s|^{-2\alpha}\right) \approx \Gamma_c \left(1 + g \int' d^d s |s|^{-2\alpha}\right)$. Thus γ_c diverges when $2\alpha < d$, when the system effectively becomes all-to-all.

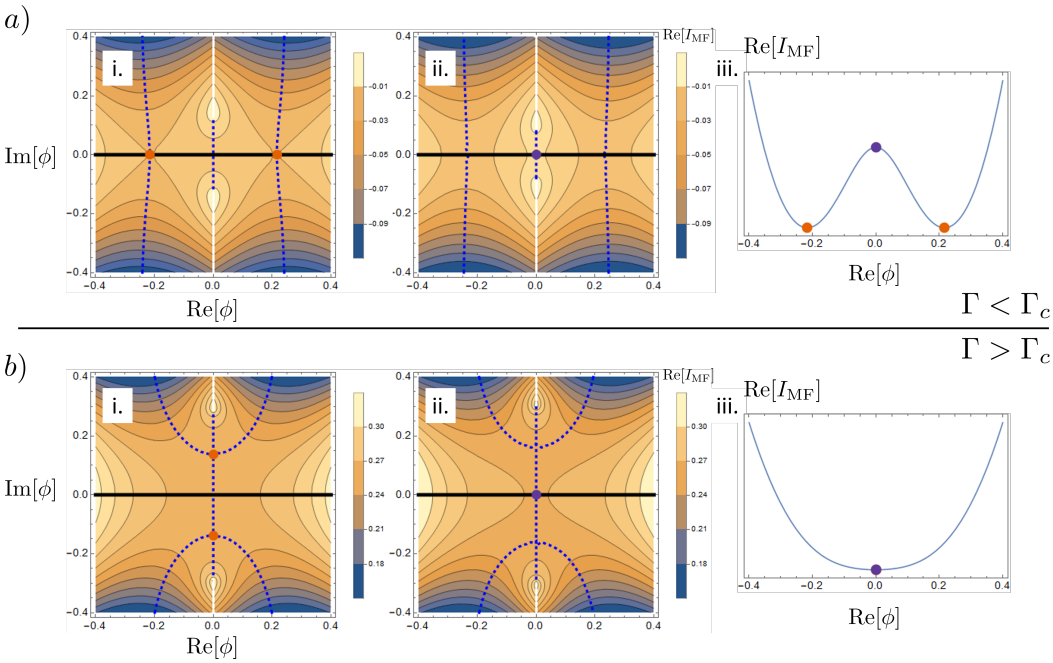

Figure C.2: Saddle-point integration contours. (a) Below the critical point, both the symmetry-broken saddle points (i., orange dots) and the symmetric saddle point (ii., purple dot) lie along the real axis of integration (solid black). In this case all three saddle points contribute to the integral, but the symmetry-broken saddle points dominate because they minimize the action $\mathrm{Re}[I_{\mathrm{MF}}]$. (b) Above the critical point, the symmetry-broken saddle points (i., orange dots) lie on the imaginary axis and therefore do not contribute to the integral. Therefore the integral is dominated by the symmetric saddle point (ii., purple dot). Dotted blue lines show contours of steepest ascent / descent.

C.3.2 Effective Field Theory Near Criticality

In the previous analysis we understood the bulk mean-field physics of the model by ignoring the space- and time- dependence of the fields $\phi_r(t), \Theta_r(t)$. Here we restore the space- and time-dependence and study the model near the critical point. In this limit we can transform the effective r-bit action Eq. (C.47) into a ϕ^4 field theory with long-range interactions. In particular, near the critical point the dynamics is governed entirely by the small fluctuations of the symmetry-breaking field $\phi_r(t)$. In the following we expand the action $I[\phi, \Theta]$ in fluctuations of this small parameter to obtain an effective long-range ϕ^4 field theory for the system.

First we evaluate the leading term of the effective action $I[\phi, \Theta]$ in Eq. (C.47), corresponding to the long-range power-law interactions. Substituting $\mathcal{J}_{rr'} = \mathcal{J}^{\mathrm{PL}}_{rr'}$ from Eq. (C.38), we obtain

$$\begin{aligned}\sum_{r'}(-1)^{r-r'}e^{-\mu|r-r'|}\phi_r\phi_{r'} &\approx \sum_{q\in\mathbb{Z}}(-1)^q e^{-\mu|q|}\phi_r^2 + \sum_{q\in\mathbb{Z}}(-1)^q\frac{q^2}{2}e^{-\mu|q|}\phi_r\partial_r^2\phi_r + O(\phi_r\partial_r^4\phi_r)\\ &\approx \frac{(1-e^{-\mu})}{(1+e^{-\mu})}\phi_r^2 - \frac{e^{-2\mu}\,(1-e^{-\mu})}{(1+e^{-\mu})^3}\phi_r\partial_r^2\phi_r \end{aligned} \tag{C.50}$$

and

$$\sum_{r'}(1-\delta_{rr'})\frac{1}{|r-r'|^{2\alpha}}\phi_r\phi_{r'} \to \int_s' \frac{1}{|r-s|^{2\alpha}}\phi_r\phi_s \tag{C.51}$$

in the continuum limit, where the delta-function term $1-\delta_{rr'}$ is responsible for the UV cut-off in the continuum integral $\int_s' = \int_{\mathbb{R}\setminus(r-\varepsilon,r+\varepsilon)} ds$. Here we have assumed that the parameter μ is large such that the exponential $e^{-\mu|q|}$ decays rapidly and suppresses higher derivative terms e.g.

$\phi_r \partial_r^4 \phi_r$. Next, we fix $\Theta_r(t) = \Theta = -3(\Gamma_c + 2\Gamma)/4\mathcal{J}$ to its saddle-point value and expand the propagators $\ln \mathcal{K}_r$ in the small parameter $\phi_r(t)$ [4]:

$$\begin{aligned}\ln \mathcal{K}_r &= \ln 2 \cosh \frac{\Theta T}{2} + \frac{1}{8} \int dt_1 dt_2 \phi_r(t_1) \phi_r(t_2) e^{-|\Theta||t_1 - t_2|} - \int dt \frac{\phi_r^4}{16 |\Theta|^3} + O(\phi_r^6) \\ &\approx \int dt \left[\frac{\phi_r \partial_t^2 \phi_r}{4 |\Theta|^3} + \frac{\phi_r^2}{4 |\Theta|} - \frac{\phi_r^4}{16 |\Theta|^3} \right] + \text{const.} \end{aligned} \tag{C.52}$$

Finally, summing the results, taking the continuum limit, and ignoring additive constants, we find the near-critical Landau-Ginzburg effective field theory

$$\frac{I_{\text{eff}}[\phi]}{N} = \frac{1}{4 |\Theta|^3} \int_{t,r} dt dr \left[-\phi_r \left(\partial_t^2 + \beta \partial_r^2 \right) \phi_r - b \int_s' \frac{\phi_r \phi_s}{|r - s|^{2\alpha}} - \frac{\delta}{2} \phi_r^2 + \frac{\phi_r^4}{4} \right], \tag{C.53}$$

for small fluctuations $\phi_r(t)$ around the critical point. Here we have introduced the numerical coefficients

$$\begin{aligned} \beta &= 4 |\Theta|^3 \frac{27J}{16} \frac{e^{-2\mu} (1 - e^{-\mu})}{(1 + e^{-\mu})^3} \\ b &= 4 |\Theta|^3 \frac{27J}{16} \\ \delta &= 8 |\Theta|^3 \left(\frac{1}{4 |\Theta|} - \frac{27J}{16} \frac{(1 - e^{-\mu})}{(1 + e^{-\mu})} \right). \end{aligned} \tag{C.54}$$

By rescaling space and b we can get rid of the β parameter, and end up with the Landau-Ginzburg theory in Eq. 6 in the main text.

C.4 Scaling of entanglement entropy in the symmetry broken phase

In this section we derive results for $d = 1$.

C.4.1 Nearest Neighbor model

For the NN case, the power law term in the action is absent and we will be working with the short-range action,

$$I[\phi] = \int dt \int dr \left[-\phi \left(\partial_t^2 + \beta \partial_r^2 \right) \phi - \frac{\delta}{2} \phi^2 + \frac{\phi^4}{4} \right], \tag{C.55}$$

C.4.1.1 Entropy of a maximally mixed initial state

The SWAP action acts on the whole spatial slice, and we need to only solve for the equations of motion with the time derivative,

$$\partial_t^2 \phi = -\delta \phi + \phi^3. \tag{C.56}$$

For $\delta < 0$, we have an instanton-like solution,

$$\phi^*(r,t) = \sqrt{\delta} \tanh \left[\sqrt{\frac{\delta}{2}} (t - t_0) \right]. \tag{C.57}$$

Hence for $\delta > 0$, we have the following scaling of the quasi-entropy of the full system,

$$\hat{S}_Q^{(2)} \sim N \left(I[\phi^*] - I[\sqrt{\delta}] \right) \sim N L \delta^{3/2} + ... \tag{C.58}$$

The correction to this term will be given by the fluctuations of the domain wall within periodic boundary condition, which was estimated using Capillary Wave Theory in [173]. For

$T \gg \sqrt{L}$, this will be given by,

$$-\log\frac{T}{\sqrt{L}} - \log\sqrt{\frac{\beta N\delta^{3/2}}{12\pi}} \sim -\log\frac{T}{\sqrt{L}} + \text{const.} \tag{C.59}$$

C.4.1.2 Sub-system entropy

For a subsystem between the region r_1 and r_2, the domain wall must be pinned to the future time boundary at r_1 and r_2. We assume the solution of the fields is of the form,

$$\phi^*(r,t) = \sqrt{\delta}\tanh\left[\sqrt{\frac{\delta}{2}}\left(t - y(r)\right)\right], \tag{C.60}$$

where $y(r)$ is the 'height' of the domain wall (or equivalently the position of the instanton). Due to the boundary pinning effect, $y(r)$ must be $\epsilon \to 0$ at $r = r_1$ and $r = r_2$. The action for the quasi-entropy is given by a functional of $y(r)$,

$$\begin{aligned} I[y(r)] &= I[\phi^*] - I[\sqrt{\delta}] \\ &= \int dt \int dr\delta^2 \Bigg[\left(1 + \beta y'(r)^2\right) \text{sech}^2\sqrt{\frac{\delta}{2}}(t-y) - \frac{1}{4}\left(3 + 4\beta y'(r)^2\right)\text{sech}^4\sqrt{\frac{\delta}{2}}(t-y) \\ &+ \frac{\beta}{\sqrt{2\delta}} y''(r)\text{sech}^2\sqrt{\frac{\delta}{2}}(t-y)\text{tanh}\sqrt{\frac{\delta}{2}}(t-y)\Bigg] \end{aligned}$$

Rescale the time variable,

$$z = \sqrt{\frac{\delta}{2}}(t - y(r)).$$

The limits for z integration are approximately $0 \to \infty$. The action for quasi-entropy is thus given by,

$$I[y(r)] \sim \delta^{3/2} \int dr \int dz \left[\left(1 + \beta y'(r)^2\right) \text{sech}^2 z - \frac{1}{4} \left(3 + 4\beta y'(r)^2\right) \text{sech}^4 z + \mathcal{O}(y''(r)) \right]$$
$$\sim \delta^{3/2} \int dr \left(1 + \frac{\beta}{6} y'(r)^2 + \mathcal{O}(y''(r)\right). \tag{C.61}$$

We can ignore the $\mathcal{O}(y''(r))$ term as it is irrelevant under RG flow, since $[y] = 1$ and $[y''] = -1$. Thus, the quasi-entropy is thus given by,

$$\hat{S}^{(2)}(A) = -\ln \int \mathcal{D}(y(r)) \exp\left[-N\delta^{3/2} \int_A dr \left(1 + \frac{\beta}{6} y'(r)^2\right)\right] \tag{C.62}$$
$$= N\delta^{3/2}|A| - \ln \int \mathcal{D}(y(r)) \exp\left[-\frac{\beta N \delta^{3/2}}{6} \int_A dr \left(y'(r)^2\right)\right] \tag{C.63}$$

This is exactly the action conjectured by Li and Fisher and solved using Capillary Wave Theory in [173]. Using their result, the quasi-entropy is given by,

$$\hat{S}_A^{(2)} \approx N\delta^{3/2}|A| + \frac{3}{2}\ln|A| - \ln\left[\sqrt{\frac{2}{\pi}}\epsilon^2 \left(\frac{\beta N \delta^{3/2}}{6}\right)^{3/2}\right] \tag{C.64}$$
$$= N\delta^{3/2}|A| + \frac{3}{2}\ln|A| + \text{const...} \tag{C.65}$$

The approximations a la Li and Fisher [173] behind this are $|A| \ll L$, $\sqrt{A} \ll T$, and for a spatial lattice cut-off, ϵ, such that, $\epsilon \ll \sqrt{|A|/(\beta N \delta^{3/2})}$. Note, we further have our large N approximation, $T \lesssim \text{poly}(N)$. These can all be satisfied in the regime, $\sqrt{A} \ll T \lesssim \text{poly}(N)$. The logarithmic correction term is $1/N$ suppressed in our model.

C.4.2 Power Law model

In the symmetry broken phase, the field theory is given by,

$$I[\phi] = \int dtdr \left[-\phi \left(a\, \partial_t^2 + \beta\, \partial_r^2 \right) \phi - b \int' ds \frac{\phi_r \phi_s}{|r-s|^{2\alpha}} - \frac{\delta\, \phi^2}{2} + \frac{u\, \phi^4}{4} \right], \tag{C.66}$$

for $\delta > 0$.

By appropriate rescaling of the fields, we can rewrite the field theory as,

$$I[\phi] = \int dtdr \left[-\phi \left(\partial_t^2 + \beta\, \partial_r^2 \right) \phi - b \int' ds \frac{\phi_r \phi_s}{|r-s|^{2\alpha}} - \frac{\delta\, \phi^2}{2} + \frac{\phi^4}{4} \right], \tag{C.67}$$

The ϕ equation of motion is given by,

$$\partial_t^2 \phi_r + \beta \partial_r^2 \phi_r = -\delta \phi_r + \phi_r^3 - \int' ds \phi_s \frac{1}{|r-s|^{2\alpha}}. \tag{C.68}$$

C.4.2.1 Total Entropy of the maximally mixed initial state

In this case, the saddle point configuration will be independent of space, and the equation of motion can be simplified to be,

$$\partial_t^2 \phi = -\delta_\alpha \phi + \phi^3, \tag{C.69}$$

$$\text{where, } \delta_\alpha = \delta + \int' ds \frac{1}{|r-s|^{2\alpha}}. \tag{C.70}$$

The phase transition is effected by taking $\delta_\alpha \to 0$. The static solutions of this equation is,

$$\phi = \pm\sqrt{\delta_\alpha}, \tag{C.71}$$

and the instanton solution is,

$$\phi^* = \sqrt{\delta_\alpha}\tanh\sqrt{\frac{\delta_\alpha}{2}}(t - t_0). \tag{C.72}$$

As before, the entropy of the whole system will be given by,

$$\hat{S}_Q^{(2)} \sim NL\delta_\alpha^{3/2} - \log\frac{T}{\sqrt{L}} + \text{const.} \tag{C.73}$$

C.4.2.2 Subsystem entropy

For general long-range interactions, there can't be a simple capillary wave picture, as the gradient expansion doesn't converge for $2\alpha < 3$. For the effectively short-ranged case $2\alpha > 3$, the story is the same as for the nearest neighbor model.

In absence of a controlled analytical calculation, we can make reasonable estimates of the energy of a domain wall pinned to the future boundary at a subsystem A. First we estimate the energy of a flat domain wall of length A and width w, for a microscopic model with the same low-energy action as the long range ϕ^4 model. One such model is a classical Ising model in 2D, with long range interaction along one direction (space) and short range interaction along the other

direction (time), with a Hamiltonian,

$$H = -\sum_t \sum_r J S_{r,t} S_{r,t+1} - \sum_t \sum_{r \neq s} \frac{K}{|r-s|^{2\alpha}} S_{r,t} S_{s,t} \text{ with } J, K > 0. \tag{C.74}$$

The energy of a flat domain wall of length $|A|$ and width w is given by,

$$E_{\text{dw}} = |A|J + wK \left(\sum_{r \in L, s \in L} - \sum_{r \in A, s \in A} - \sum_{r \in A^c, s \in A^c} + 2 \sum_{r \in A, s \in A^c} \right) \frac{1}{|r-s|^{2\alpha}} \tag{C.75}$$

We can change the sums into integrals with a regulator ε, and this is given by,

$$E_{\text{dw}} = |A|J + wK \int'_{r \in A, s \in A^c} dr ds \frac{1}{|r-s|^{2\alpha}} + \text{const.} \sim |A|J + wK \left(|A|^{2-2\alpha} - \varepsilon^{2-2\alpha} \right) + \text{const.} \tag{C.76}$$

Here we have assumed $L >> |A| >> \varepsilon$.

In this simple estimate we can't estimate the optimal width of the domain wall, w. However this already suggests that w will not scale with $|A|$, and should instead be given by the time-like correlation length in this model, $w \sim \xi_t$. Hence for $2\alpha \leq 2$, we get a power-law correction to the volume law entropy, which is distinct from the logarithmic correction that one obtained for the nearest neighbor / short-ranged case. In the large-N model, the interactions J, K scale with N. The entropy of a small subregion is hence given by,

$$\hat{S}_A^{(2)} \sim N|A|\delta_\alpha^{3/2} + \xi_t N |A|^{2-2\alpha} + \mathcal{O}(1/N). \tag{C.77}$$

Any corrections due to the fluctuations of the domain wall will be 1/N suppressed as in the

local case.

C.5 Brownian SYK details

In this section we derive the Landau-Ginzburg effective action for the monitored Brownian SYK model. The Brownian Gaussian random couplings in the unitary part is defined by the parameters,

$$\mathbb{E}\left[J^{r_1 r_2}_{a,ij}(t_1)J^{r'_1 r'_2}_{a',ij}(t_2)\right] = \frac{J_{rr'}}{2N}\frac{\delta_{t_1 t_2}}{\Delta t}\delta_{aa'}\delta^{r_1,r'_1}\delta^{r_2,r'_2},$$
$$\mathbb{E}\left[U^{r}_{a,j_1\ldots j_q}(t_1)U^{r'}_{a',j_1\ldots j_q}(t_2)\right] = \frac{2^{q-2}(q-1)!U}{N^{q-1}}\frac{\delta_{t_1 t_2}}{\Delta t}\delta_{aa'}\delta^{r,r'}.$$

.

The measurement part for the flavor i at the site x can be cast into,

$$\begin{aligned}\sum_{\nu=1}^{2} M^{x,i}_{\nu}\otimes M^{x,i\dagger}_{\nu}\otimes M^{x,i}_{\nu}\otimes M^{x,i\dagger}_{\nu} = &\left(1-\frac{s^2}{2}\sum_{u=1}^{4}\pi^{+,u}_{x,i}+s^4\otimes_{u=1}^{4}\pi^{+,u}_{x,i}\right)\\ \approx &\exp\left(-\frac{s^2}{2}\sum_{u}\pi^{+,u}_{x,i}\right)\\ = &\exp\frac{\delta t\gamma}{2}\sum_{u} i\psi^{u}_{x,L,i}\psi^{u}_{x,R,i},\end{aligned} \tag{C.78}$$

where we have used the relation $\pi^{+}_{x,a,j}+\pi^{-}_{x,a,j}=1$ and also introduced $u=1,...,4$ to denote the four copies of the tensor product. To derive the above equation, we assume $s\ll 1$ and keep orders up to $O(s^2)$. In the last line we introduce $\gamma = s^2/\delta t$, and when the continuum limit is taken, γ is kept fixed. All the constants are neglected because they will not affect the dynamics. The effect of monitoring every Majorana species i at every site x is described by

$$\exp\left(\frac{\gamma}{2}\int dt\sum_{x,\alpha,i} i\psi^{\alpha}_{x,L,i}\psi^{\alpha}_{x,R,i}\right), \tag{C.79}$$

where we implicitly sum over all infinitesimal time steps to arrive at the time integral for a time evolution.

Due to the large-N structure in both Hamiltonian in Eq. 10 in the main text and monitoring part (C.79), we can introduce the bilocal field,

$$G^{uv}_{ab,r}(t,t') = \frac{1}{N}\sum_j \psi^u_{r,a,j}(t)\psi^v_{r,b,j}(t'), \tag{C.80}$$

to rewrite the Majorana field with the help of the following identity

$$1 = \int d\Sigma \exp \int dt_1 dt_2 \Big[-\frac{N}{2}\Sigma^{uv}_r(t_1,t_2)\Big(G^{uv}_r(t_1,t_2) - \frac{1}{N}\sum_i \psi^u_{r,i}(t_1)\psi^v_{r,i}(t_2)\Big)\Big], \tag{C.81}$$

where $\Sigma^{uv}_{ab,r}(t,t')$ is the self-energy. It is a standard approach for the SYK model [25], which is then generalized to the four contours with monitoring part [265]. With a slight modification that replace the nearest-neighbor hopping to a power-law hopping, the large-N action in the replica space reads

$$\begin{aligned} -\frac{I}{N} \;=\; & \sum_r \Big[\frac{1}{2}\mathrm{Tr}\log\left((-1)^{u+1}\partial_t - \Sigma_r\right) - \frac{1}{2}\int_{t,t'} \Sigma^{uv}_{ab,r}G^{uv}_{ab,r} \\ & + \int_{t,t'} \delta(t-t')\Big[\frac{(-1)^{u+v+1}}{4}\delta_{ab}\Big(\sum_{r'} J^{rr'}G^{uv}_{ab,r}G^{uv}_{ab,r'} + \frac{U}{2q}(2G^{uv}_{ab,r})^q\Big) + \frac{i\gamma}{2}G^{uu}_{LR,r}\Big]\Big], \end{aligned} \tag{C.82}$$

where $u, v = 1, ..., 4$ denote the four contours, and $\int_{t,t'} \equiv \int dtdt'$. The summations over a, b and u, v are implicit. Note that the model can be generalized to arbitrary graph with a modification on the hopping term in the second line of (C.82).

Saddle-point analysis can be straightforwardly applied to the large-N action. The Schwinger-

Dyson equation resulted from (C.82) reads

$$\begin{aligned}
[G_r^{-1}]_{ab}^{uv} = & \quad (-1)^{u+1}\delta^{uv}\delta_{ab}\partial_t - \Sigma_{ab,r}^{uv}, \\
\Sigma_{ab,r}^{uv} = & \quad \delta(t-t')\Big[\frac{(-1)^{u+v+1}\delta_{ab}}{2}\Big(\sum_{r'} J_{rr'}2G_{ab,r'}^{uv} + U(2G_{ab,r}^{uv})^{q-1}\Big) + i\gamma\delta^{uv}\frac{\delta_{aL}\delta_{bR}-\delta_{aR}\delta_{bL}}{2}\Big].
\end{aligned} \tag{C.83}$$

For a homogeneous solution in real space, i.e., $G_{ab,r}^{uv} = \bar{G}_{ab}^{uv}$ and $\Sigma_{ab,r}^{uv} = \bar{\Sigma}_{ab}^{uv}$, the Schwinger-Dyson equation is simplified to be

$$\begin{aligned}
[\bar{G}^{-1}]_{ab}^{uv} = & \quad (-1)^{\alpha+1}\delta^{uv}\delta_{ab}\partial_t - \bar{\Sigma}_{ab}^{uv}, \\
\bar{\Sigma}_{ab}^{uv} = & \quad \delta(t-t')\Big[\frac{(-1)^{u+v+1}\delta_{ab}}{2}\Big(\hat{J}2\bar{G}_{ab}^{uv} + U(2\bar{G}_{ab}^{uv})^{q-1}\Big) + i\gamma\delta^{uv}\frac{\delta_{aL}\delta_{bR}-\delta_{aR}\delta_{bL}}{2}\Big],
\end{aligned} \tag{C.84}$$

where $\hat{J} = J\zeta(2\alpha)$, and $\zeta(\alpha) \equiv \sum_{r=1}^{\infty}\frac{1}{r^\alpha}$.

To get the solution, we focus on two contours, $u, v = 1, 2$, because the boundary condition in $\mathrm{Tr}(\rho)^2$ is to connect 1 to 2 and connect 3 to 4 separately. According to Ref. [265], the saddle point solution can be obtained by replacing J to $\hat{J}$,

$$\bar{G}(t_1,t_2) = \begin{cases} \frac{e^{-\frac{\hat{J}+U\lambda^{q-2}}{2}|t_{12}|}}{2}\Big[\mathrm{sgn}(t_{12})\sigma^z - \lambda i\sigma^y + \frac{\tilde{\gamma}\tau^y}{1+\tilde{U}\lambda^{q-2}}\Big], & \tilde{\gamma} < 1, \\ & , \\ \frac{e^{-\frac{\gamma|t_{12}|}{2}}}{2}\left(\mathrm{sgn}(t_{12})\sigma^z + \tau^y\right) & \tilde{\gamma} \geq 1 \end{cases} \tag{C.85}$$

where $t_{12} \equiv t_1 - t_2$ is the time difference, $\tilde{\gamma} \equiv \gamma/\hat{J}$, $\tilde{U} \equiv U/\hat{J}$ and Pauli matrix σ (τ) acts on 1 and 2 contours (L and R chains). The parameter λ is given by

$$(1-\lambda^2)(1+\tilde{U}\lambda^{q-2})^2 = \tilde{\gamma}^2. \tag{C.86}$$

The solution on $3, 4$ contours is the same, consistent with the boundary condition without twist operators. We will discuss the saddle-point solution in more details in the next section.

C.5.1 Landau-Ginzburg effective action and Rényi entropy

The symmetry of the theory is not affected by the power-law hopping. In the following, we discuss the $O(2)$ symmetry and the C_4 symmetry of the noninteracting and interacting SYK models, separately.

C.5.2 Noninteracting SYK_2 model

For Brownian randomness Eq. 11 in the main text, it is legitimate to assume the Green functions are strictly local $G^{uv}_{ab,r}(t,t) \equiv G^{uv}_{ab,r}(t)$ and antisymmetric $G^{uv}_{ab,r}(t) = -G^{vu}_{ba,r}(t)$ [323], so for $U = 0$ the action can be written as

$$-\frac{I}{N} = \frac{1}{2}\mathrm{Tr}\log\left(S\partial_t + \Sigma_r\right) + \int \frac{1}{2}\mathrm{Tr}\Big[\Sigma_{ab,x}G_{ba,x} + \sum_{r'}\frac{J_{rr'}}{4}G_{ab,r}SG_{ba,r'}S + i\frac{\gamma}{2}G_{LR,r}\Big], \tag{C.87}$$

where $S^{uv} = (-1)^u\delta^{uv}$ and the trace in the second line is over the contour indices. The theory is invariant under $O(2) \times O(2)$ transformation, i.e.,

$$G_{ab,x} \to O^{-1}G_{ab,x}O, \quad O^TO = 1, \quad O^TSO = S, \tag{C.88}$$

where O acts identically on the left and right chains. (Without the coupling between the left and the right chains, $\mu = 0$, the action is invariant under two $O(2) \times O(2)$ for the left and the right chains, respectively, $G_{ab,x} \to O_a^{-1}G_{ab,x}O_b$, where $O_a^TO_a = 1, O_a^TSO_a = 1$.) The rotational

symmetry is generated by $\gamma_{(13)}$ and $\gamma_{(24)}$, $\gamma^{uv}_{(ij)} = \delta^{iu}\delta^{jv} - \delta^{ju}\delta^{iv}$, i.e.,

$$O = e^{\theta_{13}\gamma_{(13)}+\theta_{24}\gamma_{(24)}}, \tag{C.89}$$

where θ_{13} denotes the rotation angle between the contour 1 and 3, and θ_{24} denotes the rotation angle between the contour 2 and 4.

The saddle point solution (C.85) for $U = 0$ and $\tilde{\gamma} < 1$ spontaneously breaks the *relative* rotational symmetry. For the noninteracting case, $U = 0$, $\lambda = \sqrt{1-\tilde{\gamma}^2}$. There is one Goldstone mode generated by applying the broken-symmetry generator $\gamma_- \equiv \gamma_{(13)} - \gamma_{(24)}$, i.e.,

$$\delta G_{aa,r}(t) = e^{-\theta_r(t)\gamma_-}\bar{G}_{aa}(t,t)e^{\theta_r(t)\gamma_-} - \bar{G}_{aa}(t,t) \approx \sqrt{1-\tilde{\gamma}^2}\theta_r(t)(\gamma_{(14)} + \gamma_{(23)}), \tag{C.90}$$

where $\theta_r(t)$ denotes the Goldstone mode. In contrast, when $\tilde{\gamma} > 1$, this $O(2)$ symmetry is unbroken and the replicated theory is in the gapped phase.

Again, with a slight modification the effective theory for the Goldstone mode reads [265],

$$\frac{I_{\text{eff}}}{N} = \frac{\rho}{2}\sum_k \int_\Omega \left(\frac{\Omega^2}{\gamma^2} + (1-\epsilon_k)\right)|\theta_k(\Omega)|^2, \tag{C.91}$$

where $\theta_k = \frac{1}{\sqrt{L}}\sum_r \theta_r e^{-ikr}$ is the Fourier transform of the lattice site, and

$$\epsilon_k \equiv \frac{1}{\zeta(2\alpha)}\sum_{r=1}^{\infty}\frac{\cos kr}{r^{2\alpha}}, \tag{C.92}$$

resulted from the power-law hopping. Similar results have been obtained in Ref. [267]. Notice that $\epsilon_{k=0} = 1$ consistent with $\theta_k(\Omega)$ being a Goldstone mode. The stiffness $\rho = \hat{J}(1-\tilde{\gamma}^2)$

vanishes at $\tilde{\gamma} = 1$, indicating that the transition occurs at $\gamma = \hat{J}$.

C.5.3 Interacting SYK$_4$ model

Now we discuss the interacting case $\tilde{U} > 0$. The parameter λ is determined by (C.86). For small $\tilde{U}$, $\lambda = \sqrt{1-\tilde{\gamma}^2}[1+\tilde{\gamma}^2(1-\tilde{\gamma}^2)^{q/2-2}\tilde{U} + O(\tilde{U}^2)]$ is well defined when $\tilde{\gamma} < 1$, and vanishes continuous as $\tilde{\gamma} \to 1$. In the following we will focus on $q = 4$, while our results are true for generic q. At the critical point,

$$\lambda^2\big((2\tilde{U}-1) + (\tilde{U}^2 - 2\tilde{U})\lambda^2 - \tilde{U}^2\lambda^4\big) = 0, \tag{C.93}$$

which shows that for $\tilde{U} > 1/2$ there are two degenerate distinct physical solutions indicating a discontinuous jump. Thus, the condition for a continuous transition is $2U < \hat{J}$. On the other hand, when $\gamma \geq \hat{J}$, the solution is same as the noninteracting case (C.85) at $\tilde{\gamma} \geq 1$.

What symmetry out of $O(2) \times O(2)$ is preserved for $\tilde{U} > 0$? It is easy to show that the symmetry reduces to $C_4 \times C_4$, satisfying the condition $((O^{-1})^{uu'})^{q/2} S^{u'v'} (O^{v'v})^{q/2} = S^{uv}$. The generator is still given by $\gamma_{(13)}$ and $\gamma_{(24)}$ but the rotation angle is restricted to multiples of $\pi/2$. The relative rotation symmetry is spontaneously broken by nonzero λ in (C.85) when $\gamma < J$. Namely, λ serves as an order parameter of the C_4 symmetry breaking transition. With a slight modification that replaces $\cos k$ to ϵ_k and J to $\hat{J}$, the Landau-Ginzburg effective theory reads

$$\frac{I_{\text{eff}}}{N} = \frac{1}{2}\sum_{i=1,2;k}\int_\Omega \left(\frac{\Omega^2}{\gamma} + \hat{J}(1-\epsilon_k)\right)|\phi_{i,k}(\Omega)|^2 + \sum_r \int_t \left(\frac{\gamma-\hat{J}}{2}\vec{\phi}_r^2 + \frac{\gamma}{8}\vec{\phi}_r^4 - \frac{U}{4}(\phi_{1,r}^4 + \phi_{2,r}^4)\right), \tag{C.94}$$

where $\phi_1 = \delta G^{12} + \delta G^{34}$ and $\phi_2 = \delta G^{14} + \delta G^{23}$ transform like a vector under the relative

C_4 rotation. (In this case we have $\delta G^{12}_{RR} = \delta G^{12}_{LL}$, $\delta G^{34}_{RR} = \delta G^{34}_{LL}$, $\delta G^{14}_{RR} = \delta G^{14}_{LL}$, $\delta G^{23}_{RR} = \delta G^{23}_{LL}$. So we omit the subscript of the left and right chains.) This theory features a second order transition if $2U < \gamma$, and a first order one if $2U > \gamma$, consistent with the analysis (C.93) of the saddle-point solution at the transition $\gamma = \hat{J}$.

Bibliography

[1] S. Kumar, K. Maiti, S. Bhattacharya, D. Banerjee, K. C. Das, and R. Bhattacharya. M ossbauer studies on the precipitates of fe(oh)3 and kfeiii[feii(cn)6]. *Physica Status Solidi (a)*, 144(1), July 1994.

[2] Subhayan Sahu, Shenglong Xu, and Brian Swingle. Scrambling dynamics across a thermalization-localization quantum phase transition. *Phys. Rev. Lett.*, 123:165902, Oct 2019.

[3] Subhayan Sahu and Brian Swingle. Information scrambling at finite temperature in local quantum systems. *Physical Review B*, 102(18), nov 2020.

[4] Gregory S. Bentsen, Subhayan Sahu, and Brian Swingle. Measurement-induced purification in large-n hybrid brownian circuits, sep 2021.

[5] Subhayan Sahu, Shao-Kai Jian, Gregory Bentsen, and Brian Swingle. Entanglement phases in large-n hybrid brownian circuits with long-range couplings. 2021.

[6] Subhayan Sahu and Brian Swingle. Efficient tensor network simulation of quantum many-body physics on sparse graphs. 2022.

[7] P. W. Anderson. More is different. *Science*, 177(4047):393–396, 1972.

[8] Bei Zeng, Xie Chen, Duan-Lu Zhou, and Xiao-Gang Wen. Quantum information meets quantum matter – from quantum entanglement to topological phase in many-body systems. 2015.

[9] Matthew B. Hastings and Tohru Koma. Spectral gap and exponential decay of correlations. *Communications in Mathematical Physics*, 265(3):781–804, aug 2006.

[10] Luca D'Alessio, Yariv Kafri, Anatoli Polkovnikov, and Marcos Rigol. From quantum chaos and eigenstate thermalization to statistical mechanics and thermodynamics. *Advances in Physics*, 65(3):239–362, may 2016.

[11] Pavan Hosur, Xiao-Liang Qi, Daniel A. Roberts, and Beni Yoshida. Chaos in quantum channels. *J. High Energy Phys.*, 2016(2):4, Feb 2016.

[12] A Kitaev. A simple model of quantum holography. *A simple model of quantum holography, KITP strings seminar and Entanglement 2015 program*, 2015.

[13] Daniel A. Roberts and Brian Swingle. Lieb-robinson bound and the butterfly effect in quantum field theories. *Phys. Rev. Lett.*, 117:091602, Aug 2016.

[14] E.H. Lieb and D.W. Robinson. The finite group velocity of quantum spin systems. *Communications in Mathematical Physics*, 28(251–257), 1972.

[15] Adam Nahum, Sagar Vijay, and Jeongwan Haah. Operator Spreading in Random Unitary Circuits. *Phys. Rev. X*, 8(2):021014, apr 2018.

[16] Shenglong Xu and Brian Swingle. Locality, Quantum Fluctuations, and Scrambling. *arXiv:1805.05376*, 2018.

[17] P. W. Anderson. Absence of diffusion in certain random lattices. *Phys. Rev.*, 109:1492–1505, Mar 1958.

[18] Dmitry A. Abanin, Ehud Altman, Immanuel Bloch, and Maksym Serbyn. Colloquium : Many-body localization, thermalization, and entanglement. *Reviews of Modern Physics*, 91(2), may 2019.

[19] Dries Sels and Anatoli Polkovnikov. Dynamical obstruction to localization in a disordered spin chain. *Physical Review E*, 104(5), nov 2021.

[20] Juan Maldacena, Stephen H. Shenker, and Douglas Stanford. A bound on chaos. *J. High Energy Phys.*, 2016(8), 2016.

[21] Yaodong Li, Xiao Chen, and Matthew P. A. Fisher. Quantum zeno effect and the many-body entanglement transition. *Phys. Rev. B*, 98:205136, Nov 2018.

[22] Brian Skinner, Jonathan Ruhman, and Adam Nahum. Measurement-induced phase transitions in the dynamics of entanglement. *Phys. Rev. X*, 9:031009, Jul 2019.

[23] Michael J. Gullans and David A. Huse. Dynamical purification phase transition induced by quantum measurements. *Phys. Rev. X*, 10:041020, Oct 2020.

[24] Subir Sachdev. Bekenstein-hawking entropy and strange metals. *Phys. Rev. X*, 5:041025, Nov 2015.

[25] Juan Maldacena and Douglas Stanford. Remarks on the sachdev-ye-kitaev model. *Phys. Rev. D*, 94:106002, Nov 2016.

[26] Patrick Hayden and John Preskill. Black holes as mirrors: quantum information in random subsystems. *Journal of High Energy Physics*, 2007(09):120–120, sep 2007.

[27] Nima Lashkari, Douglas Stanford, Matthew Hastings, Tobias Osborne, and Patrick Hayden. Towards the fast scrambling conjecture. *Journal of High Energy Physics*, 2013(4), Apr 2013.

[28] Gregory Bentsen, Yingfei Gu, and Andrew Lucas. Fast scrambling on sparse graphs. *Proceedings of the National Academy of Sciences*, 116(14):6689–6694, Mar 2019.

[29] Shenglong Xu, Leonard Susskind, Yuan Su, and Brian Swingle. A sparse model of quantum holography, 2020.

[30] M. S. Leifer and D. Poulin. Quantum Graphical Models and Belief Propagation. *Annals of Physics*, 323(8):1899–1946, August 2008.

[31] Marc Mézard and Andrea Montanari. *Information, Physics, and Computation*. Oxford Graduate Texts. Oxford University Press, Oxford, 2009.

[32] D. M. Basko, I. L. Aleiner, and B. L. Altshuler. Metal-insulator transition in a weakly interacting many-electron system with localized single-particle states. *Annals of Physics*, 321(5):1126–1205, 2006.

[33] Vadim Oganesyan and David A. Huse. Localization of interacting fermions at high temperature. *Phys. Rev. B*, 75:155111, Apr 2007.

[34] I. V. Gornyi, A. D. Mirlin, and D. G. Polyakov. Interacting electrons in disordered wires: Anderson localization and low-t transport. *Phys. Rev. Lett.*, 95:206603, Nov 2005.

[35] Arijeet Pal and David A. Huse. Many-body localization phase transition. *Phys. Rev. B*, 82:174411, Nov 2010.

[36] Marko Žnidarič, Tomaž Prosen, and Peter Prelovšek. Many-body localization in the Heisenberg XXZ magnet in a random field. *Phys. Rev. B*, 77(6):064426, feb 2008.

[37] Jens H. Bardarson, Frank Pollmann, and Joel E. Moore. Unbounded growth of entanglement in models of many-body localization. *Phys. Rev. Lett.*, 109(1):1–5, 2012.

[38] Maksym Serbyn, Z. Papić, and Dmitry A. Abanin. Universal slow growth of entanglement in interacting strongly disordered systems. *Phys. Rev. Lett.*, 110(26):260601, jun 2013.

[39] Bela Bauer and Chetan Nayak. Area laws in a many-body localized state and its implications for topological order. *J. Stat. Mech.: Theory Exp.*, 2013(9), 2013.

[40] Ehud Altman and Ronen Vosk. Universal Dynamics and Renormalization in Many-Body-Localized Systems. *Annu. Rev. Condens. Matter Phys*, 6(1):383–409, mar 2015.

[41] Maksym Serbyn, Z. Papić, and Dmitry A. Abanin. Local conservation laws and the structure of the many-body localized states. *Phys. Rev. Lett.*, 111:127201, Sep 2013.

[42] Ronen Vosk, David A. Huse, and Ehud Altman. Theory of the many-body localization transition in one-dimensional systems. *Phys. Rev. X*, 5(3):1–14, 2015.

[43] David A. Huse, Rahul Nandkishore, and Vadim Oganesyan. Phenomenology of fully many-body-localized systems. *Phys. Rev. B*, 90(17):1–5, 2014.

[44] Brian Swingle. A simple model of many-body localization. *arXiv:1307.0507*, 2013.

[45] Kartiek Agarwal, Sarang Gopalakrishnan, Michael Knap, Markus Müller, and Eugene Demler. Anomalous diffusion and Griffiths effects near the many-body localization transition. *Phys. Rev. Lett.*, 114(16):1–6, 2015.

[46] Kartiek Agarwal, Ehud Altman, Eugene Demler, Sarang Gopalakrishnan, David A. Huse, and Michael Knap. Rare-region effects and dynamics near the many-body localization transition. *Ann. Phys. (Berl.)*, 529(7):1600326, jul 2017.

[47] David J. Luitz, Nicolas Laflorencie, and Fabien Alet. Many-body localization edge in the random-field Heisenberg chain. *Phys. Rev. B*, 91(8):1–5, 2015.

[48] Rahul Nandkishore and David A. Huse. Many-Body Localization and Thermalization in Quantum Statistical Mechanics. *Annu. Rev. Condens. Matter Phys*, 6(1):15–38, mar 2015.

[49] Andrew C. Potter, Romain Vasseur, and S. A. Parameswaran. Universal properties of many-body delocalization transitions. *Phys. Rev. X*, 5:031033, Sep 2015.

[50] Dmitry A. Abanin and Papić Zlatko. Recent progress in many-body localization. *Ann. Phys. (Berl.)*, 529(7):1700169, 2017.

[51] John Z. Imbrie. Diagonalization and many-body localization for a disordered quantum spin chain. *Phys. Rev. Lett.*, 117:027201, Jul 2016.

[52] John Z. Imbrie. On many-body localization for quantum spin chains. *J. Stat. Phys.*, 163(5):998–1048, Jun 2016.

[53] David A. Huse, Rahul Nandkishore, Vadim Oganesyan, Arijeet Pal, and S. L. Sondhi. Localization-protected quantum order. *Phys. Rev. B*, 88:014206, Jul 2013.

[54] Anushya Chandran, Vedika Khemani, C. R. Laumann, and S. L. Sondhi. Many-body localization and symmetry-protected topological order. *Phys. Rev. B*, 89:144201, Apr 2014.

[55] David Pekker, Gil Refael, Ehud Altman, Eugene Demler, and Vadim Oganesyan. Hilbert-glass transition: New universality of temperature-tuned many-body dynamical quantum criticality. *Phys. Rev. X*, 4:011052, Mar 2014.

[56] Jonas A. Kjäll, Jens H. Bardarson, and Frank Pollmann. Many-body localization in a disordered quantum ising chain. *Phys. Rev. Lett.*, 113:107204, Sep 2014.

[57] Tarun Grover. Certain General Constraints on the Many-Body Localization Transition. *arXiv:1405.1471*, 2014.

[58] Yasaman Bahri, Ronen Vosk, Ehud Altman, and Ashvin Vishwanath. Localization and topology protected quantum coherence at the edge of hot matter. *Nat. Commun.*, 6:7341, 2015.

[59] Vedika Khemani, S. P. Lim, D. N. Sheng, and David A. Huse. Critical properties of the many-body localization transition. *Phys. Rev. X*, 7, 2017.

[60] Antonio Rubio-Abadal, Jae-yoon Choi, Johannes Zeiher, Simon Hollerith, Jun Rui, Immanuel Bloch, and Christian Gross. Probing many-body localization in the presence of a quantum bath. *arXiv:1805.00056*, 2018.

[61] Henrik P. Lüschen, Pranjal Bordia, Sebastian Scherg, Fabien Alet, Ehud Altman, Ulrich Schneider, and Immanuel Bloch. Observation of Slow Dynamics near the Many-Body Localization Transition in One-Dimensional Quasiperiodic Systems. *Phys. Rev. Lett.*, 119(26):260401, dec 2017.

[62] Henrik P. Lüschen, Pranjal Bordia, Sean S. Hodgman, Michael Schreiber, Saubhik Sarkar, Andrew J. Daley, Mark H. Fischer, Ehud Altman, Immanuel Bloch, and Ulrich Schneider. Signatures of many-body localization in a controlled open quantum system. *Phys. Rev. X*, 7(1):011034, mar 2017.

[63] Stephen H. Shenker and Douglas Stanford. Black holes and the butterfly effect. *J. High Energy Phys.*, 2014(3), 2014.

[64] Patrick Hayden and John Preskill. Black holes as mirrors: quantum information in random subsystems. *J. High Energy Phys.*, 2007(09):120, 2007.

[65] Yasuhiro Sekino and Leonard Susskind. Fast scramblers. *J. High Energy Phys.*, 2008(10):065, 2008.

[66] A I Larkin and Yu N Ovchinnikov. Quasiclassical Method in the Theory of Superconductivity. *Soviet Physics JETP*, 28(6):1200–1205, 1969.

[67] Brian Swingle, Gregory Bentsen, Monika Schleier-Smith, and Patrick Hayden. Measuring the scrambling of quantum information. *Phys. Rev. A*, 94(4):1–6, 2016.

[68] Guanyu Zhu, Mohammad Hafezi, and Tarun Grover. Measurement of many-body chaos using a quantum clock. *Phys. Rev. A*, 94(6):35–38, 2016.

[69] Norman Y. Yao, Fabian Grusdt, Brian Swingle, Mikhail D. Lukin, Dan M. Stamper-Kurn, Joel E. Moore, and Eugene A. Demler. Interferometric Approach to Probing Fast Scrambling. *arXiv:1607.01801*, 2016.

[70] Nicole Yunger Halpern. Jarzynski-like equality for the out-of-time-ordered correlator. *Phys. Rev. A*, 95(1):1–9, 2017.

[71] A Bohrdt, C B Mendl, M Endres, and M Knap. Scrambling and thermalization in a diffusive quantum many-body system. *New Journal of Physics*, 19(6):063001, jun 2017.

[72] Jun Li, Ruihua Fan, Hengyan Wang, Bingtian Ye, Bei Zeng, Hui Zhai, Xinhua Peng, and Jiangfeng Du. Measuring out-of-time-order correlators on a nuclear magnetic resonance quantum simulator. *Phys. Rev. X*, 7(3):1–12, 2017.

[73] Martin Garttner, Justin G. Bohnet, Arghavan Safavi-Naini, Michael L. Wall, John J. Bollinger, and Ana Maria Rey. Measuring out-of-time-order correlations and multiple quantum spectra in a trapped-ion quantum magnet. *Nat. Phys.*, 13(8):781–786, 2017.

[74] Ken Xuan Wei, Chandrasekhar Ramanathan, and Paola Cappellaro. Exploring Localization in Nuclear Spin Chains. *Phys. Rev. Lett.*, 120(7):70501, 2018.

[75] Eric J. Meier, Jackson Ang'ong'a, Fangzhao Alex An, and Bryce Gadway. Exploring quantum signatures of chaos on a Floquet synthetic lattice. *arXiv:1705.06714*, 2017.

[76] Naoto Tsuji, Philipp Werner, and Masahito Ueda. Exact out-of-time-ordered correlation functions for an interacting lattice fermion model. *Phys. Rev. A*, 95:011601, Jan 2017.

[77] Justin Dressel, José Raúl González Alonso, Mordecai Waegell, and Nicole Yunger Halpern. Strengthening weak measurements of qubit out-of-time-order correlators. *Phys. Rev. A*, 98:012132, Jul 2018.

[78] Xinfang Nie, Bo-Bo Wei, Xi Chen, Ze Zhang, Xiuzhu Zhao, Chudan Qiu, Yu Tian, Yunlan Ji, Tao Xin, Dawei Lu, and Jun Li. Experimental observation of equilibrium and dynamical quantum phase transitions via out-of-time-ordered correlators. *Physical Review Letters*, 124(25), jun 2020.

[79] Nicole Yunger Halpern, Brian Swingle, and Justin Dressel. Quasiprobability behind the out-of-time-ordered correlator. *Phys. Rev. A*, 97:042105, Apr 2018.

[80] Manoj K. Joshi, Andreas Elben, Benoî t Vermersch, Tiff Brydges, Christine Maier, Peter Zoller, Rainer Blatt, and Christian F. Roos. Quantum information scrambling in a trapped-ion quantum simulator with tunable range interactions. *Physical Review Letters*, 124(24), jun 2020.

[81] Bing Chen, Xianfei Hou, Feifei Zhou, Peng Qian, Heng Shen, and Nanyang Xu. Detecting the out-of-time-order correlations of dynamical quantum phase transitions in a solid-state quantum simulator. *Applied Physics Letters*, 116(19):194002, may 2020.

[82] Xiao Mi et al. Information scrambling in quantum circuits. *Science*, 374(6574):1479–1483, dec 2021.

[83] Jochen Braumüller et al. Probing quantum information propagation with out-of-time-ordered correlators. *Nature Physics*, 18(2):172–178, dec 2021.

[84] Bhuvanesh Sundar, Andreas Elben, Lata Kh Joshi, and Torsten V Zache. Proposal for measuring out-of-time-ordered correlators at finite temperature with coupled spin chains. *New Journal of Physics*, 24(2):023037, feb 2022.

[85] Michael R. Geller, Andrew Arrasmith, Zoë Holmes, Bin Yan, Patrick J. Coles, and Andrew Sornborger. Quantum simulation of operator spreading in the chaotic ising model. *Physical Review E*, 105(3), mar 2022.

[86] Alaina M. Green, A. Elben, C. Huerta Alderete, Lata Kh Joshi, Nhung H. Nguyen, Torsten V. Zache, Yingyue Zhu, Bhuvanesh Sundar, and Norbert M. Linke. Experimental measurement of out-of-time-ordered correlators at finite temperature. *Physical Review Letters*, 128(14), apr 2022.

[87] Shahaf Asban, Konstantin E. Dorfman, and Shaul Mukamel. Interferometric spectroscopy with quantum light: Revealing out-of-time-ordering correlators. *The Journal of Chemical Physics*, 154(21):210901, jun 2021.

[88] Christian K. Burrell and Tobias J. Osborne. Bounds on the speed of information propagation in disordered quantum Spin chains. *Phys. Rev. Lett.*, 99(16):1–4, 2007.

[89] Brian Swingle and Debanjan Chowdhury. Slow scrambling in disordered quantum systems. *Phys. Rev. B*, 95(6):1–7, 2017.

[90] Yichen Huang, Yong Liang Zhang, and Xie Chen. Out-of-time-ordered correlators in many-body localized systems. *Ann. Phys. (Berl.)*, 529(7):1600318, jul 2017.

[91] Ruihua Fan, Pengfei Zhang, Huitao Shen, and Hui Zhai. Out-of-time-order correlation for many-body localization. *Sci. Bull.*, 62(10):707–711, may 2017.

[92] Rong Qiang He and Zhong Yi Lu. Characterizing many-body localization by out-of-time-ordered correlation. *Phys. Rev. B*, 95(5):054201, feb 2017.

[93] Yu Chen. Universal Logarithmic Scrambling in Many Body Localization. *arXiv:1608.02765*, 2016.

[94] Xiao Chen, Tianci Zhou, David A. Huse, and Eduardo Fradkin. Out-of-time-order correlations in many-body localized and thermal phases. *Ann. Phys. (Berl.)*, 529(7):1600332, jul 2017.

[95] Kevin Slagle, Zhen Bi, Yi Zhuang You, and Cenke Xu. Out-of-time-order correlation in marginal many-body localized systems. *Phys. Rev. B*, 95(16):1–7, 2017.

[96] Marko Žnidarič, Antonello Scardicchio, and Vipin Kerala Varma. Diffusive and Subdiffusive Spin Transport in the Ergodic Phase of a Many-Body Localizable System. *Phys. Rev. Lett.*, 117(4):1–6, 2016.

[97] Ilia Khait, Snir Gazit, Norman Y. Yao, and Assa Auerbach. Spin transport of weakly disordered Heisenberg chain at infinite temperature. *Phys. Rev. B*, 93(22):224205, jun 2016.

[98] David J. Luitz and Yevgeny Bar Lev. Information propagation in isolated quantum systems. *Phys. Rev. B*, 96(2):1–6, 2017.

[99] Adam Nahum, Jonathan Ruhman, and David A. Huse. Dynamics of entanglement and transport in 1D systems with quenched randomness. *Phys. Rev. B*, 98:035118, Jul 2018.

[100] Shenglong Xu and Brian Swingle. Accessing scrambling using matrix product operators. *arXiv:1802.00801*, 2018.

[101] Cheng Ju Lin and Olexei I. Motrunich. Out-of-time-ordered correlators in a quantum Ising chain. *Phys. Rev. B*, 97(14):1–17, 2018.

[102] Vedika Khemani, David A. Huse, and Adam Nahum. Velocity-dependent Lyapunov exponents in many-body quantum, semi-classical, and classical chaos. *arXiv:1803.05902*, 2018.

[103] Juan Jose Mendoza-Arenas, Marko Znidaric, Vipin Kerala Varma, John Goold, Stephen R. Clark, and Antonello Scardicchio. Asymmetry in energy versus spin transport in certain interacting, disordered systems. *arXiv:1803.11555*, 2018.

[104] Guifré Vidal. Efficient simulation of one-dimensional quantum many-body systems. *Phys. Rev. Lett.*, 93:040502, Jul 2004.

[105] Guifré Vidal. Efficient classical simulation of slightly entangled quantum computations. *Phys. Rev. Lett.*, 91:147902, Oct 2003.

[106] Andrew John Daley, Corinna Kollath, Ulrich Schollwöck, and Guifré Vidal. Time-dependent density-matrix renormalization-group using adaptive effective hilbert spaces. *J. Stat. Mech.: Theory Exp.*, 2004(04):P04005, 2004.

[107] Steven R. White and Adrian E. Feiguin. Real-time evolution using the density matrix renormalization group. *Phys. Rev. Lett.*, 93:076401, Aug 2004.

[108] C. W. von Keyserlingk, Tibor Rakovszky, Frank Pollmann, and S. L. Sondhi. Operator Hydrodynamics, OTOCs, and Entanglement Growth in Systems without Conservation Laws. *Phys. Rev. X*, 8(2):021013, apr 2018.

[109] Winton Brown and Omar Fawzi. Scrambling speed of random quantum circuits. 2012.

[110] Nima Lashkari, Douglas Stanford, Matthew Hastings, Tobias Osborne, and Patrick Hayden. Towards the fast scrambling conjecture. *Journal of High Energy Physics*, 2013(4), Apr 2013.

[111] Stephen H. Shenker and Douglas Stanford. Stringy effects in scrambling. *Journal of High Energy Physics*, 2015(5), May 2015.

[112] Juan Maldacena and Douglas Stanford. Remarks on the sachdev-ye-kitaev model. *Phys. Rev. D*, 94:106002, Nov 2016.

[113] Alexei Kitaev and S. Josephine Suh. The soft mode in the sachdev-ye-kitaev model and its gravity dual. *Journal of High Energy Physics*, 2018(5), May 2018.

[114] Debanjan Chowdhury and Brian Swingle. Onset of many-body chaos in the $o(n)$ model. *Phys. Rev. D*, 96:065005, Sep 2017.

[115] Brian Swingle, Gregory Bentsen, Monika Schleier-Smith, and Patrick Hayden. Measuring the scrambling of quantum information. *Phys. Rev. A*, 94:040302, Oct 2016.

[116] Guanyu Zhu, Mohammad Hafezi, and Tarun Grover. Measurement of many-body chaos using a quantum clock. *Phys. Rev. A*, 94:062329, Dec 2016.

[117] Norman Y. Yao, Fabian Grusdt, Brian Swingle, Mikhail D. Lukin, Dan M. Stamper-Kurn, Joel E. Moore, and Eugene A. Demler. Interferometric approach to probing fast scrambling. 2016.

[118] Nicole Yunger Halpern. Jarzynski-like equality for the out-of-time-ordered correlator. *Phys. Rev. A*, 95:012120, Jan 2017.

[119] Michele Campisi and John Goold. Thermodynamics of quantum information scrambling. *Phys. Rev. E*, 95:062127, Jun 2017.

[120] Beni Yoshida and Alexei Kitaev. Efficient decoding for the hayden-preskill protocol. 2017.

[121] B. Vermersch, A. Elben, L. M. Sieberer, N. Y. Yao, and P. Zoller. Probing scrambling using statistical correlations between randomized measurements. *Phys. Rev. X*, 9:021061, Jun 2019.

[122] Xiao-Liang Qi, Emily J. Davis, Avikar Periwal, and Monika Schleier-Smith. Measuring operator size growth in quantum quench experiments. 2019.

[123] Martin Gärttner, Justin G. Bohnet, Arghavan Safavi-Naini, Michael L. Wall, John J. Bollinger, and Ana Maria Rey. Measuring out-of-time-order correlations and multiple quantum spectra in a trapped-ion quantum magnet. *Nature Physics*, 13(8):781–786, May 2017.

[124] Ken Xuan Wei, Chandrasekhar Ramanathan, and Paola Cappellaro. Exploring localization in nuclear spin chains. *Phys. Rev. Lett.*, 120:070501, Feb 2018.

[125] Jun Li, Ruihua Fan, Hengyan Wang, Bingtian Ye, Bei Zeng, Hui Zhai, Xinhua Peng, and Jiangfeng Du. Measuring out-of-time-order correlators on a nuclear magnetic resonance quantum simulator. *Phys. Rev. X*, 7:031011, Jul 2017.

[126] Eric J. Meier, Jackson Ang'ong'a, Fangzhao Alex An, and Bryce Gadway. Exploring quantum signatures of chaos on a floquet synthetic lattice. *Phys. Rev. A*, 100:013623, Jul 2019.

[127] K. A. Landsman, C. Figgatt, T. Schuster, N. M. Linke, B. Yoshida, N. Y. Yao, and C. Monroe. Verified quantum information scrambling. *Nature*, 567(7746):61–65, Mar 2019.

[128] Ken Xuan Wei, Pai Peng, Oles Shtanko, Iman Marvian, Seth Lloyd, Chandrasekhar Ramanathan, and Paola Cappellaro. Emergent prethermalization signatures in out-of-time ordered correlations. *Phys. Rev. Lett.*, 123:090605, Aug 2019.

[129] Xinfang Nie, Ze Zhang, Xiuzhu Zhao, Tao Xin, Dawei Lu, and Jun Li. Detecting scrambling via statistical correlations between randomized measurements on an nmr quantum simulator. 2019.

[130] Efim B. Rozenbaum, Sriram Ganeshan, and Victor Galitski. Lyapunov exponent and out-of-time-ordered correlator's growth rate in a chaotic system. *Phys. Rev. Lett.*, 118:086801, Feb 2017.

[131] Tianrui Xu, Thomas Scaffidi, and Xiangyu Cao. Does scrambling equal chaos? *Phys. Rev. Lett.*, 124:140602, Apr 2020.

[132] Daniel E. Parker, Xiangyu Cao, Alexander Avdoshkin, Thomas Scaffidi, and Ehud Altman. A universal operator growth hypothesis. *Phys. Rev. X*, 9:041017, Oct 2019.

[133] Chaitanya Murthy and Mark Srednicki. Bounds on chaos from the eigenstate thermalization hypothesis. *Phys. Rev. Lett.*, 123:230606, Dec 2019.

[134] Yunxiang Liao and Victor Galitski. Nonlinear sigma model approach to many-body quantum chaos: Regularized and unregularized out-of-time-ordered correlators. *Phys. Rev. B*, 98:205124, Nov 2018.

[135] Aurelio Romero-Bermúdez, Koenraad Schalm, and Vincenzo Scopelliti. Regularization dependence of the otoc. which lyapunov spectrum is the physical one? *Journal of High Energy Physics*, 2019(7), Jul 2019.

[136] Igor L. Aleiner, Lara Faoro, and Lev B. Ioffe. Microscopic model of quantum butterfly effect: Out-of-time-order correlators and traveling combustion waves. *Annals of Physics*, 375:378–406, Dec 2016.

[137] Aavishkar A. Patel, Debanjan Chowdhury, Subir Sachdev, and Brian Swingle. Quantum butterfly effect in weakly interacting diffusive metals. *Phys. Rev. X*, 7:031047, Sep 2017.

[138] Shenglong Xu and Brian Swingle. Locality, quantum fluctuations, and scrambling. *Phys. Rev. X*, 9:031048, Sep 2019.

[139] Vedika Khemani, David A. Huse, and Adam Nahum. Velocity-dependent lyapunov exponents in many-body quantum, semiclassical, and classical chaos. *Physical Review B*, 98(14), Oct 2018.

[140] Xizhi Han and Sean A. Hartnoll. Quantum Scrambling and State Dependence of the Butterfly Velocity. *SciPost Phys.*, 7:45, 2019.

[141] Michael M. Wolf, Frank Verstraete, Matthew B. Hastings, and J. Ignacio Cirac. Area laws in quantum systems: Mutual information and correlations. *Phys. Rev. Lett.*, 100:070502, Feb 2008.

[142] Kévin Hémery, Frank Pollmann, and David J. Luitz. Matrix product states approaches to operator spreading in ergodic quantum systems. *Phys. Rev. B*, 100:104303, Sep 2019.

[143] Subir Sachdev. *Quantum Phase Transitions*. Cambridge University Press, Cambridge, 2011.

[144] Douglas Stanford. Many-body chaos at weak coupling. *Journal of High Energy Physics*, 2016(10):9, Oct 2016.

[145] Julia Steinberg and Brian Swingle. Thermalization and chaos in qed_3. *Phys. Rev. D*, 99:076007, Apr 2019.

[146] Gong Cheng and Brian Swingle. Chaos in a quantum rotor model. 2019.

[147] Yahya Alavirad and Ali Lavasani. Scrambling in the dicke model. *Phys. Rev. A*, 99:043602, Apr 2019.

[148] Yingfei Gu and Alexei Kitaev. On the relation between the magnitude and exponent of otocs. *Journal of High Energy Physics*, 2019(2), Feb 2019.

[149] Andrey V. Chubukov, Subir Sachdev, and Jinwu Ye. Theory of two-dimensional quantum heisenberg antiferromagnets with a nearly critical ground state. *Phys. Rev. B*, 49:11919–11961, May 1994.

[150] Bryce Kobrin, Zhenbin Yang, Gregory D. Kahanamoku-Meyer, Christopher T. Olund, Joel E. Moore, Douglas Stanford, and Norman Y. Yao. Many-Body Chaos in the Sachdev-Ye-Kitaev Model. feb 2020.

[151] Huzihiro Araki. Gibbs states of a one dimensional quantum lattice. *Communications in Mathematical Physics*, 14(2):120–157, jun 1969.

[152] Patrick Hayden, Sepehr Nezami, Xiao-Liang Qi, Nathaniel Thomas, Michael Walter, and Zhao Yang. Holographic duality from random tensor networks. *Journal of High Energy Physics*, 2016(11), Nov 2016.

[153] Adam Nahum, Sagar Vijay, and Jeongwan Haah. Operator spreading in random unitary circuits. *Phys. Rev. X*, 8:021014, Apr 2018.

[154] Tianci Zhou and Adam Nahum. Emergent statistical mechanics of entanglement in random unitary circuits. *Phys. Rev. B*, 99:174205, May 2019.

[155] Romain Vasseur, Andrew C. Potter, Yi-Zhuang You, and Andreas W. W. Ludwig. Entanglement transitions from holographic random tensor networks. *Phys. Rev. B*, 100:134203, Oct 2019.

[156] Nicholas Hunter-Jones. Unitary designs from statistical mechanics in random quantum circuits. *arXiv:1905.12053*, 2019.

[157] Javier Lopez-Piqueres, Brayden Ware, and Romain Vasseur. Mean-field entanglement transitions in random tree tensor networks. *Phys. Rev. B*, 102:064202, Aug 2020.

[158] Amos Chan, Rahul M. Nandkishore, Michael Pretko, and Graeme Smith. Unitary-projective entanglement dynamics. *Phys. Rev. B*, 99:224307, Jun 2019.

[159] Yaodong Li, Xiao Chen, and Matthew P. A. Fisher. Measurement-driven entanglement transition in hybrid quantum circuits. *Phys. Rev. B*, 100:134306, Oct 2019.

[160] M. Szyniszewski, A. Romito, and H. Schomerus. Entanglement transition from variable-strength weak measurements. *Phys. Rev. B*, 100:064204, Aug 2019.

[161] Dorit Aharonov. Quantum to classical phase transition in noisy quantum computers. *Phys. Rev. A*, 62:062311, Nov 2000.

[162] Yimu Bao, Soonwon Choi, and Ehud Altman. Theory of the phase transition in random unitary circuits with measurements. *Phys. Rev. B*, 101:104301, Mar 2020.

[163] Chao-Ming Jian, Yi-Zhuang You, Romain Vasseur, and Andreas W. W. Ludwig. Measurement-induced criticality in random quantum circuits. *Phys. Rev. B*, 101:104302, Mar 2020.

[164] Ruihua Fan, Sagar Vijay, Ashvin Vishwanath, and Yi-Zhuang You. Self-organized error correction in random unitary circuits with measurement. *arXiv:2002.12385*, 2020.

[165] Yaodong Li, Xiao Chen, Andreas WW Ludwig, and Matthew Fisher. Conformal invariance and quantum non-locality in hybrid quantum circuits. *arXiv:2003.12721*, 2020.

[166] Soonwon Choi, Yimu Bao, Xiao-Liang Qi, and Ehud Altman. Quantum error correction in scrambling dynamics and measurement-induced phase transition. *Phys. Rev. Lett.*, 125:030505, Jul 2020.

[167] Aidan Zabalo, Michael J. Gullans, Justin H. Wilson, Sarang Gopalakrishnan, David A. Huse, and J. H. Pixley. Critical properties of the measurement-induced transition in random quantum circuits. *Phys. Rev. B*, 101:060301, Feb 2020.

[168] Qicheng Tang and W. Zhu. Measurement-induced phase transition: A case study in the nonintegrable model by density-matrix renormalization group calculations. *Phys. Rev. Research*, 2:013022, Jan 2020.

[169] Xhek Turkeshi, Rosario Fazio, and Marcello Dalmonte. Measurement-induced criticality in $(2+1)$-dimensional hybrid quantum circuits. *Phys. Rev. B*, 102:014315, Jul 2020.

[170] Lei Zhang, Justin A. Reyes, Stefanos Kourtis, Claudio Chamon, Eduardo R. Mucciolo, and Andrei E. Ruckenstein. Nonuniversal entanglement level statistics in projection-driven quantum circuits. *Phys. Rev. B*, 101:235104, Jun 2020.

[171] Shimpei Goto and Ippei Danshita. Measurement-induced transitions of the entanglement scaling law in ultracold gases with controllable dissipation. *Phys. Rev. A*, 102:033316, Sep 2020.

[172] Jason Iaconis, Andrew Lucas, and Xiao Chen. Measurement-induced phase transitions in quantum automaton circuits. *Phys. Rev. B*, 102:224311, Dec 2020.

[173] Yaodong Li and Matthew P. A. Fisher. Statistical mechanics of quantum error correcting codes. *Phys. Rev. B*, 103:104306, Mar 2021.

[174] Adam Nahum, Sthitadhi Roy, Brian Skinner, and Jonathan Ruhman. Measurement and entanglement phase transitions in all-to-all quantum circuits, on quantum trees, and in landau-ginsburg theory. *PRX Quantum*, 2:010352, Mar 2021.

[175] Sagar Vijay. Measurement-driven phase transition within a volume-law entangled phase. *arXiv:2005.03052*, 2020.

[176] Chunxiao Liu, Pengfei Zhang, and Xiao Chen. Non-unitary dynamics of sachdev-ye-kitaev chain. *arXiv:2008.11955*, 2020.

[177] Xiangyu Cao, Antoine Tilloy, and Andrea De Luca. Entanglement in a fermion chain under continuous monitoring. *arXiv:1804.04638*, 2018.

[178] Xiao Chen, Yaodong Li, Matthew P. A. Fisher, and Andrew Lucas. Emergent conformal symmetry in nonunitary random dynamics of free fermions. *Phys. Rev. Research*, 2:033017, Jul 2020.

[179] Michael J. Gullans and David A. Huse. Scalable probes of measurement-induced criticality. *Phys. Rev. Lett.*, 125:070606, Aug 2020.

[180] Niels Bohr et al. *The quantum postulate and the recent development of atomic theory*, volume 3. Printed in Great Britain by R. & R. Clarke, Limited, 1928.

[181] Howard M Wiseman and Gerard J Milburn. *Quantum measurement and control*. Cambridge university press, 2009.

[182] John Archibald Wheeler and Wojciech Hubert Zurek. *Quantum theory and measurement*, volume 53. Princeton University Press, 2014.

[183] Howard M Wiseman and Gerard J Milburn. Quantum theory of optical feedback via homodyne detection. *Physical Review Letters*, 70(5):548, 1993.

[184] Howard M Wiseman and Gerard J Milburn. Quantum theory of field-quadrature measurements. *Physical review A*, 47(1):642, 1993.

[185] HM Wiseman and GJ Milburn. Interpretation of quantum jump and diffusion processes illustrated on the bloch sphere. *Physical Review A*, 47(3):1652, 1993.

[186] HM Wiseman and GJ Milburn. Squeezing via feedback. *Physical Review A*, 49(2):1350, 1994.

[187] Tony E Lee and Ching-Kit Chan. Heralded magnetism in non-hermitian atomic systems. *Physical Review X*, 4(4):041001, 2014.

[188] Giovanni Barontini, Leander Hohmann, Florian Haas, Jérôme Estève, and Jakob Reichel. Deterministic generation of multiparticle entanglement by quantum zeno dynamics. *Science*, 349(6254):1317–1321, 2015.

[189] Wojciech Kozlowski, Santiago F Caballero-Benitez, and Igor B Mekhov. Non-hermitian dynamics in the quantum zeno limit. *Physical Review A*, 94(1):012123, 2016.

[190] Gabriel Mazzucchi, Wojciech Kozlowski, Santiago F Caballero-Benitez, Thomas J Elliott, and Igor B Mekhov. Quantum measurement-induced dynamics of many-body ultracold bosonic and fermionic systems in optical lattices. *Physical Review A*, 93(2):023632, 2016.

[191] JJWH Sørensen, Mogens Dalgaard, Alexander Holm Kiilerich, Klaus Mølmer, and JF Sherson. Quantum control with measurements and quantum zeno dynamics. *Physical Review A*, 98(6):062317, 2018.

[192] Jonathan A Gross, Carlton M Caves, Gerard J Milburn, and Joshua Combes. Qubit models of weak continuous measurements: Markovian conditional and open-system dynamics. *Quantum Science and Technology*, 3(2):024005, 2018.

[193] DA Ivanov, T Yu Ivanova, SF Caballero-Benitez, and IB Mekhov. Feedback-induced quantum phase transitions using weak measurements. *Physical review letters*, 124(1):010603, 2020.

[194] Katrin Kroeger, Nishant Dogra, Rodrigo Rosa-Medina, Marcin Paluch, Francesco Ferri, Tobias Donner, and Tilman Esslinger. Continuous feedback on a quantum gas coupled to an optical cavity. *New Journal of Physics*, 22(3):033020, 2020.

[195] Yohei Fuji and Yuto Ashida. Measurement-induced quantum criticality under continuous monitoring. *Phys. Rev. B*, 102:054302, Aug 2020.

[196] Alberto Biella and Marco Schiró. Many-body quantum zeno effect and measurement-induced subradiance transition. *Quantum*, 5:528, 2021.

[197] Shao-Kai Jian, Zhi-Cheng Yang, Zhen Bi, and Xiao Chen. Yang-lee edge singularity triggered entanglement transition. *arXiv:2101.04115*, 2021.

[198] Xhek Turkeshi, Alberto Biella, Rosario Fazio, Marcello Dalmonte, and Marco Schiro. Measurement-induced entanglement transitions in the quantum ising chain: From infinite to zero clicks. *arXiv:2103.09138*, 2021.

[199] Matteo Ippoliti and Vedika Khemani. Postselection-free entanglement dynamics via spacetime duality. *Phys. Rev. Lett.*, 126:060501, Feb 2021.

[200] Matteo Ippoliti, Tibor Rakovszky, and Vedika Khemani. Fractal, logarithmic and volume-law entangled non-thermal steady states via spacetime duality. *arXiv:2103.06873*, 2021.

[201] Ali Lavasani, Yahya Alavirad, and Maissam Barkeshli. Measurement-induced topological entanglement transitions in symmetric random quantum circuits. *Nature Physics*, pages 1–6, 2021.

[202] Shengqi Sang and Timothy H Hsieh. Measurement protected quantum phases. *arXiv:2004.09509*, 2020.

[203] Matteo Ippoliti, Michael J. Gullans, Sarang Gopalakrishnan, David A. Huse, and Vedika Khemani. Entanglement phase transitions in measurement-only dynamics. *Phys. Rev. X*, 11:011030, Feb 2021.

[204] Nicolai Lang and Hans Peter Büchler. Entanglement transition in the projective transverse field ising model. *Phys. Rev. B*, 102:094204, Sep 2020.

[205] Ali Lavasani, Yahya Alavirad, and Maissam Barkeshli. Topological order and criticality in (2+1)d monitored random quantum circuits. *arXiv:2011.0659*, 2021.

[206] Yimu Bao, Soonwon Choi, and Ehud Altman. Symmetry enriched phases of quantum circuits. *arXiv:2102.09164*, 2021.

[207] Brian Swingle, Gregory Bentsen, Monika Schleier-Smith, and Patrick Hayden. Measuring the scrambling of quantum information. *Phys. Rev. A*, 94:040302, Oct 2016.

[208] Gregory Bentsen, Tomohiro Hashizume, Anton S. Buyskikh, Emily J. Davis, Andrew J. Daley, Steven S. Gubser, and Monika Schleier-Smith. Treelike interactions and fast scrambling with cold atoms. *Phys. Rev. Lett.*, 123:130601, Sep 2019.

[209] Emily J. Davis, Gregory Bentsen, Lukas Homeier, Tracy Li, and Monika H. Schleier-Smith. Photon-mediated spin-exchange dynamics of spin-1 atoms. *Phys. Rev. Lett.*, 122:010405, Jan 2019.

[210] Waseem S Bakr, Jonathon I Gillen, Amy Peng, Simon Fölling, and Markus Greiner. A quantum gas microscope for detecting single atoms in a hubbard-regime optical lattice. *Nature*, 462(7269):74–77, 2009.

[211] Jacob F Sherson, Christof Weitenberg, Manuel Endres, Marc Cheneau, Immanuel Bloch, and Stefan Kuhr. Single-atom-resolved fluorescence imaging of an atomic mott insulator. *Nature*, 467(7311):68–72, 2010.

[212] Sebastien Gleyzes, Stefan Kuhr, Christine Guerlin, Julien Bernu, Samuel Deleglise, Ulrich Busk Hoff, Michel Brune, Jean-Michel Raimond, and Serge Haroche. Quantum jumps of light recording the birth and death of a photon in a cavity. *Nature*, 446(7133):297–300, 2007.

[213] Rajibul Islam, Ruichao Ma, Philipp M Preiss, M Eric Tai, Alexander Lukin, Matthew Rispoli, and Markus Greiner. Measuring entanglement entropy in a quantum many-body system. *Nature*, 528(7580):77–83, 2015.

[214] Artur K. Ekert, Carolina Moura Alves, Daniel K. L. Oi, Michał Horodecki, Paweł Horodecki, and L. C. Kwek. Direct estimations of linear and nonlinear functionals of a quantum state. *Phys. Rev. Lett.*, 88:217901, May 2002.

[215] Ryszard Horodecki, Paweł Horodecki, Michał Horodecki, and Karol Horodecki. Quantum entanglement. *Rev. Mod. Phys.*, 81:865–942, Jun 2009.

[216] A. J. Daley, H. Pichler, J. Schachenmayer, and P. Zoller. Measuring entanglement growth in quench dynamics of bosons in an optical lattice. *Phys. Rev. Lett.*, 109:020505, Jul 2012.

[217] Andrzej Jamiołkowski. Linear transformations which preserve trace and positive semidefiniteness of operators. *Reports on Mathematical Physics*, 3(4):275–278, 1972.

[218] Man-Duen Choi. Completely positive linear maps on complex matrices. *Linear algebra and its applications*, 10(3):285–290, 1975.

[219] Fritz Haake. *Quantum signatures of chaos*. Springer, 2010.

[220] Marc Mézard, Giorgio Parisi, and Miguel Angel Virasoro. *Spin glass theory and beyond: An Introduction to the Replica Method and Its Applications*, volume 9. World Scientific Publishing Company, 1987.

[221] Tommaso Castellani and Andrea Cavagna. Spin-glass theory for pedestrians. *Journal of Statistical Mechanics: Theory and Experiment*, 2005(05):P05012, 2005.

[222] Subir Sachdev and Jinwu Ye. Gapless spin-fluid ground state in a random quantum heisenberg magnet. *Phys. Rev. Lett.*, 70:3339–3342, May 1993.

[223] F. T. Arecchi, Eric Courtens, Robert Gilmore, and Harry Thomas. Atomic coherent states in quantum optics. *Phys. Rev. A*, 6:2211–2237, Dec 1972.

[224] Eduardo Fradkin. *Field theories of condensed matter physics*. Cambridge University Press, 2013.

[225] Carl M. Bender and Stefan Boettcher. Real spectra in non-hermitian hamiltonians having pt symmetry. *Phys. Rev. Lett.*, 80:5243–5246, Jun 1998.

[226] Carl M Bender. Introduction to pt-symmetric quantum theory. *Contemporary physics*, 46(4):277–292, 2005.

[227] Sarang Gopalakrishnan and Michael J Gullans. Entanglement and purification transitions in non-hermitian quantum mechanics. *arXiv:2012.01435*, 2020.

[228] Antonio M García-García, Yiyang Jia, Dario Rosa, and Jacobus JM Verbaarschot. Replica symmetry breaking and phase transitions in a pt symmetric sachdev-ye-kitaev model. *arXiv:2102.06630*, 2021.

[229] Jean Zinn-Justin. *Quantum field theory and critical phenomena*. Clarendon Press, Oxford, 2002.

[230] Cornelius Lanczos. *An iteration method for the solution of the eigenvalue problem of linear differential and integral operators*. United States Governm. Press Office Los Angeles, CA, 1950.

[231] Tae Jun Park and JC Light. Unitary quantum time evolution by iterative lanczos reduction. *The Journal of chemical physics*, 85(10):5870–5876, 1986.

[232] Jörg Liesen and Zdenek Strakos. *Krylov subspace methods: principles and analysis*. Oxford University Press, 2013.

[233] Bunji Sakita. *Quantum theory of many variable systems and fields*, volume 1. World Scientific Publishing Company, 1985.

[234] Harald JW Müller-Kirsten. *Introduction to Quantum Mechanics: Schrödinger Equation and Path Integral*. World Scientific Publishing Company, 2006.

[235] Ehud Altman et al. Quantum simulators: Architectures and opportunities. *PRX Quantum*, 2:017003, Feb 2021.

[236] Zachary Eldredge, Zhe-Xuan Gong, Jeremy T. Young, Ali Hamed Moosavian, Michael Foss-Feig, and Alexey V. Gorshkov. Fast quantum state transfer and entanglement renormalization using long-range interactions. *Physical Review Letters*, 119(17), Oct 2017.

[237] Takuro Matsuta, Tohru Koma, and Shu Nakamura. Improving the lieb–robinson bound for long-range interactions. *Annales Henri Poincaré*, 18(2):519–528, Oct 2016.

[238] Minh C. Tran, Chi-Fang Chen, Adam Ehrenberg, Andrew Y. Guo, Abhinav Deshpande, Yifan Hong, Zhe-Xuan Gong, Alexey V. Gorshkov, and Andrew Lucas. Hierarchy of linear light cones with long-range interactions. *Physical Review X*, 10(3), Jul 2020.

[239] Tianci Zhou, Shenglong Xu, Xiao Chen, Andrew Guo, and Brian Swingle. Operator lévy flight: Light cones in chaotic long-range interacting systems. *Phys. Rev. Lett.*, 124:180601, May 2020.

[240] Chi-Fang Chen and Andrew Lucas. Finite speed of quantum scrambling with long range interactions. *Physical Review Letters*, 123(25), Dec 2019.

[241] Tomotaka Kuwahara and Keiji Saito. Strictly linear light cones in long-range interacting systems of arbitrary dimensions. *Physical Review X*, 10(3), Jul 2020.

[242] Minh C. Tran, Andrew Y. Guo, Abhinav Deshpande, Andrew Lucas, and Alexey V. Gorshkov. Optimal state transfer and entanglement generation in power-law interacting systems. *Physical Review X*, 11(3), Jul 2021.

[243] Minh C. Tran, Andrew Y. Guo, Christopher L. Baldwin, Adam Ehrenberg, Alexey V. Gorshkov, and Andrew Lucas, 2021.

[244] K. Aikawa, A. Frisch, M. Mark, S. Baier, A. Rietzler, R. Grimm, and F. Ferlaino. Bose-einstein condensation of erbium. *Phys. Rev. Lett.*, 108:210401, May 2012.

[245] M. Saffman, T. G. Walker, and K. Mølmer. Quantum information with rydberg atoms. *Rev. Mod. Phys.*, 82:2313–2363, Aug 2010.

[246] Joseph W. Britton, Brian C. Sawyer, Adam C. Keith, C.-C. Joseph Wang, James K. Freericks, Hermann Uys, Michael J. Biercuk, and John J. Bollinger. Engineered two-dimensional ising interactions in a trapped-ion quantum simulator with hundreds of spins. *Nature*, 484(7395):489–492, Apr 2012.

[247] Bo Yan, Steven A. Moses, Bryce Gadway, Jacob P. Covey, Kaden R. A. Hazzard, Ana Maria Rey, Deborah S. Jin, and Jun Ye. Observation of dipolar spin-exchange interactions with lattice-confined polar molecules. *Nature*, 501(7468):521–525, Sep 2013.

[248] N.Y. Yao, L. Jiang, A.V. Gorshkov, P.C. Maurer, G. Giedke, J.I. Cirac, and M.D. Lukin. Scalable architecture for a room temperature solid-state quantum information processor. *Nature Communications*, 3(1), Jan 2012.

[249] J. S. Douglas, H. Habibian, C.-L. Hung, A. V. Gorshkov, H. J. Kimble, and D. E. Chang. Quantum many-body models with cold atoms coupled to photonic crystals. *Nature Photonics 2015 9:5*, 9(5):326–331, apr 2015.

[250] C. Monroe, W. C. Campbell, L.-M. Duan, Z.-X. Gong, A. V. Gorshkov, P. W. Hess, R. Islam, K. Kim, N. M. Linke, G. Pagano, P. Richerme, C. Senko, and N. Y. Yao. Programmable quantum simulations of spin systems with trapped ions. *Rev. Mod. Phys.*, 93:025001, Apr 2021.

[251] M Buchhold, Y Minoguchi, A Altland, and S Diehl. Effective theory for the measurement-induced phase transition of dirac fermions. *arXiv preprint arXiv:2102.08381*, 2021.

[252] 2021.

[253] Yaodong Li, Sagar Vijay, and Matthew Fisher. Entanglement domain walls in monitored quantum circuits and the directed polymer in a random environment. *arXiv preprint arXiv:2105.13352*, 2021.

[254] Maxwell Block, Yimu Bao, Soonwon Choi, Ehud Altman, and Norman Yao, 2021.

[255] Takaaki Minato, Koudai Sugimoto, Tomotaka Kuwahara, and Keiji Saito, 2021.

[256] Thomas Müller, Sebastian Diehl, and Michael Buchhold, 2021.

[257] Anders Søndberg Sørensen and Klaus Mølmer. Entangling atoms in bad cavities. *Phys. Rev. A*, 66:022314, Aug 2002.

[258] Kristian Baumann, Christine Guerlin, Ferdinand Brennecke, and Tilman Esslinger. Dicke quantum phase transition with a superfluid gas in an optical cavity. *Nature*, 464(7293):1301–1306, Apr 2010.

[259] Ian D. Leroux, Monika H. Schleier-Smith, and Vladan Vuletić. Implementation of cavity squeezing of a collective atomic spin. *Phys. Rev. Lett.*, 104:073602, Feb 2010.

[260] Justin G. Bohnet, Brian C. Sawyer, Joseph W. Britton, Michael L. Wall, Ana Maria Rey, Michael Foss-Feig, and John J. Bollinger. Quantum spin dynamics and entanglement generation with hundreds of trapped ions. *Science*, 352(6291):1297–1301, Jun 2016.

[261] E Urban, Todd A Johnson, T Henage, L Isenhower, DD Yavuz, TG Walker, and M Saffman. Observation of rydberg blockade between two atoms. *Nature Physics*, 5(2):110–114, 2009.

[262] L. I. R. Gil, R. Mukherjee, E. M. Bridge, M. P. A. Jones, and T. Pohl. Spin squeezing in a rydberg lattice clock. *Phys. Rev. Lett.*, 112:103601, Mar 2014.

[263] Shao-Kai Jian and Brian Swingle. Phase transition in von neumann entanglement entropy from replica symmetry breaking. *arXiv:2108.11973*, 2021.

[264] John Napp, Rolando L. La Placa, Alexander M. Dalzell, Fernando G. S. L. Brandao, and Aram W. Harrow, 2020.

[265] Shao-Kai Jian, Chunxiao Liu, Xiao Chen, Brian Swingle, and Pengfei Zhang, 2021.

[266] Matthew B. Hastings, Iván González, Ann B. Kallin, and Roger G. Melko. Measuring renyi entanglement entropy in quantum monte carlo simulations. *Physical Review Letters*, 104(15), Apr 2010.

[267] Pengfei Zhang, Chunxiao Liu, Shao-Kai Jian, and Xiao Chen, 2021.

[268] Michael E. Fisher, Shang-keng Ma, and B. G. Nickel. Critical exponents for long-range interactions. *Phys. Rev. Lett.*, 29:917–920, Oct 1972.

[269] J. Sak. Recursion relations and fixed points for ferromagnets with long-range interactions. *Phys. Rev. B*, 8:281–285, Jul 1973.

[270] Miguel F. Paulos, Slava Rychkov, Balt C. van Rees, and Bernardo Zan. Conformal invariance in the long-range ising model. *Nuclear Physics B*, 902:246–291, Jan 2016.

[271] Xin Chen, Ruihua Fan, Yiming Chen, Hui Zhai, and Pengfei Zhang. Competition between chaotic and nonchaotic phases in a quadratically coupled sachdev-ye-kitaev model. *Phys. Rev. Lett.*, 119:207603, Nov 2017.

[272] Xue-Yang Song, Chao-Ming Jian, and Leon Balents. Strongly correlated metal built from sachdev-ye-kitaev models. *Phys. Rev. Lett.*, 119:216601, Nov 2017.

[273] HM Wiseman. Quantum trajectories and quantum measurement theory. *Quantum and Semiclassical Optics: Journal of the European Optical Society Part B*, 8(1):205, 1996.

[274] Intuitively, this symmetry transformation can be understood as rotating between contour 2 and 4 while keeping $1, 3$ fixed.

[275] H. A. Bethe and William Lawrence Bragg. Statistical theory of superlattices. *Proceedings of the Royal Society of London. Series A - Mathematical and Physical Sciences*, 150(871):552–575, July 1935. Publisher: Royal Society.

[276] M. Mézard and G. Parisi. The bethe lattice spin glass revisited. *The European Physical Journal B*, 20(2):217–233, mar 2001.

[277] Antoine Georges, Gabriel Kotliar, Werner Krauth, and Marcelo J. Rozenberg. Dynamical mean-field theory of strongly correlated fermion systems and the limit of infinite dimensions. *Rev. Mod. Phys.*, 68:13–125, Jan 1996.

[278] C. R. Laumann, S. A. Parameswaran, S. L. Sondhi, and F. Zamponi. AKLT models with quantum spin glass ground states. *Physical Review B*, 81(17), may 2010.

[279] C. R. Laumann, S. A. Parameswaran, and S. L. Sondhi. Absence of goldstone bosons on the bethe lattice. *Physical Review B*, 80(14), oct 2009.

[280] Alicia J. Kollár, Mattias Fitzpatrick, and Andrew A. Houck. Hyperbolic lattices in circuit quantum electrodynamics. *Nature*, 571(7763):45–50, jul 2019.

[281] J. Ignacio Cirac, David Pé rez-García, Norbert Schuch, and Frank Verstraete. Matrix product states and projected entangled pair states: Concepts, symmetries, theorems. *Reviews of Modern Physics*, 93(4), dec 2021.

[282] Román Orús. A practical introduction to tensor networks: Matrix product states and projected entangled pair states. *Annals of Physics*, 349:117–158, oct 2014.

[283] Ian Affleck, Tom Kennedy, Elliott H. Lieb, and Hal Tasaki. Rigorous results on valence-bond ground states in antiferromagnets. *Phys. Rev. Lett.*, 59:799–802, Aug 1987.

[284] Steven R. White. Density matrix formulation for quantum renormalization groups. *Phys. Rev. Lett.*, 69:2863–2866, Nov 1992.

[285] Guifré Vidal. Efficient classical simulation of slightly entangled quantum computations. *Physical Review Letters*, 91(14), oct 2003.

[286] F. Verstraete and J. I. Cirac. Renormalization algorithms for quantum-many body systems in two and higher dimensions. 2004.

[287] Norbert Schuch, Michael M. Wolf, Frank Verstraete, and J. Ignacio Cirac. Computational complexity of projected entangled pair states. *Phys. Rev. Lett.*, 98:140506, Apr 2007.

[288] V. Murg, F. Verstraete, and J. I. Cirac. Variational study of hard-core bosons in a two-dimensional optical lattice using projected entangled pair states. *Phys. Rev. A*, 75:033605, Mar 2007.

[289] H. C. Jiang, Z. Y. Weng, and T. Xiang. Accurate determination of tensor network state of quantum lattice models in two dimensions. *Phys. Rev. Lett.*, 101:090603, Aug 2008.

[290] Michael P. Zaletel and Frank Pollmann. Isometric tensor network states in two dimensions. *Physical Review Letters*, 124(3), jan 2020.

[291] Laurens Vanderstraeten, Lander Burgelman, Boris Ponsioen, Maarten Van Damme, Bram Vanhecke, Philippe Corboz, Jutho Haegeman, and Frank Verstraete. Variational contractions of projected entangled-pair states. 2021.

[292] Judea Pearl. Fusion, propagation, and structuring in belief networks. *Artificial Intelligence*, 29(3):241–288, September 1986.

[293] Jonathan S Yedidia, William T Freeman, Yair Weiss, et al. Understanding belief propagation and its generalizations. *Exploring artificial intelligence in the new millennium*, 8(236-239):0018–9448, 2003.

[294] Frank R Kschischang, Brendan J Frey, and H-A Loeliger. Factor graphs and the sum-product algorithm. *IEEE Transactions on information theory*, 47(2):498–519, 2001.

[295] Elina Robeva and Anna Seigal. Duality of graphical models and tensor networks. 2017.

[296] R. Alkabetz and I. Arad. Tensor networks contraction and the belief propagation algorithm. *Physical Review Research*, 3(2), Apr 2021.

[297] L. De Cesare, K. Lukierska Walasek, and K. Walasek. Cavity-field approach to quantum spin glasses: The ising spin glass in a transverse field. *Phys. Rev. B*, 45:8127–8130, Apr 1992.

[298] M. B. Hastings. Quantum belief propagation: An algorithm for thermal quantum systems. *Physical Review B*, 76(20), nov 2007.

[299] David Poulin and Ersen Bilgin. Belief propagation algorithm for computing correlation functions in finite-temperature quantum many-body systems on loopy graphs. *Phys. Rev. A*, 77:052318, May 2008.

[300] C. Laumann, A. Scardicchio, and S. L. Sondhi. Cavity method for quantum spin glasses on the bethe lattice. *Physical Review B*, 78(13), oct 2008.

[301] Florent Krzakala, Alberto Rosso, Guilhem Semerjian, and Francesco Zamponi. Path-integral representation for quantum spin models: Application to the quantum cavity method and monte carlo simulations. *Physical Review B*, 78(13), oct 2008.

[302] Gino Del Ferraro, Chuang Wang, Dani Martí, and Marc Mézard. Cavity method: Message passing from a physics perspective. 2014.

[303] Y.-Y. Shi, L.-M. Duan, and G. Vidal. Classical simulation of quantum many-body systems with a tree tensor network. *Phys. Rev. A*, 74:022320, Aug 2006.

[304] Naoki Nakatani and Garnet Kin-Lic Chan. Efficient tree tensor network states (ttns) for quantum chemistry: Generalizations of the density matrix renormalization group algorithm. *The Journal of chemical physics*, 138(13):134113, 2013.

[305] Béla Bollobás. *Random Graphs*. Cambridge Studies in Advanced Mathematics. Cambridge University Press, 2 edition, 2001.

[306] R.J. McEliece, D.J.C. MacKay, and Jung-Fu Cheng. Turbo decoding as an instance of pearl's "belief propagation" algorithm. *IEEE Journal on Selected Areas in Communications*, 16(2):140–152, 1998.

[307] Marc Hein, Wolfgang Dur, Jens Eisert, Robert Raussendorf, Maarten Van den Nest, and Hans J. Briegel. Entanglement in graph states and its applications. *arXiv: Quantum Physics*, 2006.

[308] H. J. Briegel, D. E. Browne, W. Dür, R. Raussendorf, and M. Van den Nest. Measurement-based quantum computation. *Nature Physics*, 5(1):19–26, jan 2009.

[309] A. Ramezanpour. Cavity approach to variational quantum mechanics. *Physical Review B*, 85(12), mar 2012.

[310] I Biazzo and A Ramezanpour. Low-temperature excitations within the bethe approximation. *Journal of Statistical Mechanics: Theory and Experiment*, 2013(04):P04011, apr 2013.

[311] Daniel Nagaj, Edward Farhi, Jeffrey Goldstone, Peter Shor, and Igor Sylvester. Quantum transverse-field ising model on an infinite tree from matrix product states. *Phys. Rev. B*, 77:214431, Jun 2008.

[312] Peter Lunts, Antoine Georges, E. Miles Stoudenmire, and Matthew Fishman. Hubbard model on the bethe lattice via variational uniform tree states: Metal-insulator transition and a fermi liquid. *Physical Review Research*, 3(2), apr 2021.

[313] S. Yoon, A. V. Goltsev, S. N. Dorogovtsev, and J. F. F. Mendes. Belief-propagation algorithm and the ising model on networks with arbitrary distributions of motifs. *Physical Review E*, 84(4), oct 2011.

[314] Alec Kirkley, George T. Cantwell, and M. E. J. Newman. Belief propagation for networks with loops. *Science Advances*, 7(17):eabf1211, 2021.

[315] Glen Evenbly. Gauge fixing, canonical forms, and optimal truncations in tensor networks with closed loops. *Physical Review B*, 98(8), aug 2018.

[316] Nikolas P. Breuckmann and Jens Niklas Eberhardt. Quantum low-density parity-check codes. *PRX Quantum*, 2(4), oct 2021.

[317] Philippe Corboz, Romá n Orús, Bela Bauer, and Guifré Vidal. Simulation of strongly correlated fermions in two spatial dimensions with fermionic projected entangled-pair states. *Physical Review B*, 81(16), apr 2010.

[318] J Klauder and B Skagerstam. *Coherent States*. World Scientific, 1985.

[319] Monika H Schleier-Smith, Ian D Leroux, and Vladan Vuletić. Squeezing the collective spin of a dilute atomic ensemble by cavity feedback. *Physical Review A*, 81(2):021804, 2010.

[320] Ian D Leroux, Monika H Schleier-Smith, and Vladan Vuletić. Implementation of cavity squeezing of a collective atomic spin. *Physical Review Letters*, 104(7):073602, 2010.

[321] Ian D Leroux, Monika H Schleier-Smith, Hao Zhang, and Vladan Vuletić. Unitary cavity spin squeezing by quantum erasure. *Physical Review A*, 85(1):013803, 2012.

[322] Emily J Davis, Zhaoyou Wang, Amir H Safavi-Naeini, and Monika H Schleier-Smith. Painting nonclassical states of spin or motion with shaped single photons. *Physical review letters*, 121(12):123602, 2018.

[323] Phil Saad, Stephen H. Shenker, and Douglas Stanford, 2019.